Inclusive J/psi production measurement in Pb-Pb collisions at sqrts_NN = 2.76 TeV with the ALICE Muon Spectrometer

Lizardo Valencia Palomo

To cite this version:

Lizardo Valencia Palomo. Inclusive J/psi production measurement in Pb-Pb collisions at sqrts_NN = 2.76 TeV with the ALICE Muon Spectrometer. Other [cond-mat.other]. Université Paris Sud - Paris XI, 2013. English. NNT : 2013PA112137 . tel-01139756

École Doctorale MIPEGE

Inclusive J/ψ production measurement in Pb-Pb collisions at $\sqrt{s_{\mathrm{NN}}} = 2.76$ TeV with the ALICE Muon Spectrometer

Thesis submitted for the degree of
Doctor of Philosophy (Nuclear Physics)
by

Lizardo Valencia Palomo

Defended on September 6th 2013, in front of the jury:

President	T. Suomijarvi	*IPN, Paris-Sud*
Referee	A. Andronic	*GSI*
Referee	O. Drapier	*LLR, École Polytechnique*
Examiner	S. Peigne	*SUBATECH, EMN*
Thesis advisor	B. Espagnon	*IPN, Paris-Sud*
Thesis co-advisor	C. Hadjidakis	*IPN, Paris-Sud*

”Jesus did many other things as well, if every one of them were written down I suppose that even the whole world would not have room for the books that would be written.”

John 21:25

”Muchas otras cosas hizo Jesús, que si se escribiesen una por una creo que ni el mismo mundo podría contener los libros escritos”

Juan 21:25

Acknowledgments

Thanks God for being at my side throughout this journey, without your help nothing would have been possible.

To Jéssica, that has always been with me as a friend, girlfriend and wife through thick and thin. Everything I have achieved is thanks to you.

To my parents, the best models I can have, for supporting me during all my life. Thanks dad, thanks mom, for working so hard for us. Honoring you is my biggest satisfaction.

Jorge and Guillermo, my brothers, that have always protected me. Although the distance I know I can rely on you.

Papá Emo and Mamá Mechita for taking care of your grand children and for being as our parents. Thanks for being a model of love and marriage in modern times.

My aunt Mirna and Fina, uncle Ramón and my cousins Ingrid and Marcy, for enduring me during the years I lived with you.

Anahí and Emiliana, you know all I had to suffer in order to achieve this. Without your help and explanations during the university everything would have been even more difficult.

I did never imagine that studying french would be one of the best decisions of my live, because it was during one of those french lessons where I found Nancy and Marina. Thanks for your support and your friendship, at your side I could laugh or cry without being ashamed.

I keep in my memory many other Mexican friends that, during some time, where a cornerstone of my life. It would be impossible to write down their names, however let me tell you that I will always be thankful for all those moments we shared together.

Bruno, Cynthia and Christophe for allowing me to be part of the ALICE group at the IPNO. Thanks for all the time spent answering my questions and for always supporting me on the job.

Daniel and Zaida, for speaking spanish in a french environment.

To the members of the jury for taking the time to review and comment on my thesis.

To the Subatech group and Roberta Arnaldi, with whom I worked during all my PhD.

During these three years I had opportunity to meet many other people that made my stay in France more comfortable. Specially, I would like to thank Livio Bianchi for being my first friend in this new country.

Doc Andrés, Doc Belmont and Rubén from the IFUNAM for guiding my first steps in the world of the scientific research.

Finally, but not least, I want to thank to the Facultad de Ciencias, Instituto de Física and the UNAM for shaping me as a Physicist and as a human being.

Agradecimientos

Gracias a Dios por haberme acompañado en todo este camino, ya que sin ti nada hubiese sido posible. Te pido Señor me sigas enseñando a hacer tu voluntad.

A Jéssica que ha estado a mi lado como amiga, novia y esposa en las buenas y en las malas. Gracias por ser mi compañera de las mil batallas, eres tu la verdadera artífice de todo lo que hoy estoy logrando. Yo sin ti no soy nada.

A mis padres, por ser mi ejemplo a seguir en la vida. Gracias por apoyarme en todo momento, ya que sin ello nada hubiese sido posible. Gracias mami, gracias papi, por dar hasta el último aliento, día con día, por nosotros sus hijos. Mi maxima satisfacción en la vida es honrarlos y hacerlos sentir orgullosos de mi.

Jorge y Guillermo, mis hermanos, que siempre me han protegido. Se muy bien que, aun en la distancia, se preocupan por mi y que cuento con ustedes en cualquier momento.

Papá Emo y mamá Mechita, por cuidar de sus nietos y ser nuestros segundos padres. Gracias por ser un ejemplo de amor y matrimonio en tiempos modernos.

Mi tía Mirna y Fina, mi tío Ramón y mis primas Ingrid y Marcy, por haberme aguantado durante esos años que viví con ustedes.

Anahí y Emiliana, ustedes más que nadie saben todo lo que me ha costado llegar hasta aquí. Sin su ayuda y explicaciones durante la licenciatura, este camino hubiese sido aun más difícil.

Jamás pensé que estudiar francés fuera una de las mejores desiciones de mi vida, ya que fue precisamente en uno de esos cursos de idioma donde encontré a Nancy y a Marina. Gracias por su apoyo y su amistad, a su lado he podido reir o llorar sin el menor pudor.

Guardo en la memoria a muchos otros amigos de México que en algún momento fueron parte importante de mi vida. Sería imposible para mi enlistar, aquí y ahora, a todos y cada uno de ellos. Sin embargo en mi corazón permanecen y les estoy profundamente agradecido por todo lo que vivimos juntos.

A Bruno, Cynthia y Christophe por permitirme ser parte del grupo ALICE del

IPNO. Gracias por el tiempo que me dieron para responder a mis preguntas y por apoyarme siempre en mi trabajo.

A Daniel y Zaida porque con ellos podía escapar del idioma francés para hablar en español.

A los miembros del jurado por tomarse la molestia de revisar y comentar mi tesis.

Al grupo del Subatech y a Roberta Arnaldi, con quienes trabajé estrechamente durante todo mi doctorado.

Durante estos tres años tuve la fortuna de conocer a mucha gente que me hizo más agradable mi estancia en Francia. En particular quisiera mencionar a Livio Bianchi por ser el primer amigo que hice en este nuevo país.

Al Doc Andrés, Doc Belmont y Rubén del IFUNAM por haber quiado mis primeros pasos dentro del mundo de la investigación científica.

Finalmente quiero agradecer a la Facultad de Ciencias, al Instituto de Física y a la UNAM por haberme forjado como Físico y como persona.

Résumé

La Chromodynamique Quantique prédit que la matière chaude et dense produite en collisions d'ions lourds ultra-relativistes, le Plasma de Quarks et de Gluons (QGP), se conduit comme un état déconfiné de quarks et gluons.

ALICE est la seule expérience au LHC qui a été conçue et construite pour caractériser la physique du QGP. Le spectromètre à muons, un des détecteurs d'ALICE, est utilisé pour mesurer la production de quarkonia à haut rapidité.

Dans la thèse suivante, l'efficacité des chambres de trajectographie du spectromètre à muons est étudiée durant une année de pris des données. Les résultats obtenus des données réelles sont comparées aux simulations pour calculer les incertitudes systématiques des chambres de trajectographie.

Une analyse complète de la production inclusive de $\mathrm{J}/\psi \to \mu^+\mu^-$ dans les collisions Pb-Pb 2011 est également presentée. L'étude inclut l'extraction du signal, la normalisation et les corrections d'acceptance et d'efficacité. Une partie importante est consacrée à quantifier les incertitudes systématiques liées aux différentes sources. Les résultats, R_{AA} et $\langle p_{\mathrm{T}} \rangle$, sont comparés aux mesures de plus basse énergie et aux modèles théoriques.

Abstract

The Standard Model (SM) is the theoretical framework that describes the interplay between the fundamental blocks of the Nature. Within the SM, Quantum Chromodynamics (QCD) is used to study the strong interaction of the elementary particles. At sufficiently high temperatures and pressure, QCD predicts that ordinary nuclear matter undergoes a phase transition. This new state of matter is called Quark Gluon Plasma (QGP) and is characterized by deconfined quarks and gluons.

High energy heavy-ion collisions are used in the laboratory to satisfy the conditions of energy density and temperature necessary to recreate the QGP. A direct observation of the plasma is not possible, among the possible probes of the QGP, heavy quarks are of particular interest because they are produced in the initial hard-scattering processes and experience the whole evolution of the system. In particular the quarkonium family has been proposed as a tool to characterize the QGP: color screening of the heavy quarks potential, due to the deconfined state, would lead to a suppression of quarkonium production. However recent theoretical models indicate that recombination of charm quarks can lead to an enhanced J/ψ production, provided that the overall charm density of the medium at hadronization time is sufficiently high.

The Large Hadron Collider (LHC), located under the French-Swiss border, is the largest and most powerful particle accelerator in the world. There are four main experiments located in the LHC, out of these, A Large Ion Collider Experiment (ALICE) is the only one that was specifically designed and built to focus on the study of heavy-ion collisions. Its goal is to characterize the physics of the QGP, but its programme also includes the study of proton-proton, proton-nucleus and lighter ions collisions.

The ensemble of detectors present in the ALICE experiment can be divided in three groups: the central barrel, forward detectors and the muon spectrometer. The latter is located at forward rapidity ($2.5 < y < 4$) and was designed to measure the quarkonia and low-mass vector mesons production via their dimuon decay channel, but also open heavy flavours through their semimuonic desintegration. The muon spectrometer is made out of absorbers, a dipole magnet, tracking and trigger chambers.

The first set of results in this thesis present the efficiency of the tracking chambers computed, both in real data and simulations, in Pb-Pb and pp collisions at $\sqrt{s_{\mathrm{NN}}} = 2.76$ TeV. The results are available in a run-per-run basis and integrated over the whole data taking period. For the Pb-Pb collisions the efficiency is also measured for different collision centralities and, for the 2011 heavy-ion period only, as a function of the transverse momentum and rapidity. In all cases the effects due to correlated inefficiencies in the tracking chambers are quantified. The comparison of the results obtained in data and simulation are used to assess the systematic uncertainties on the tracking apparatus.

Finally, the second group of results contain the main physics output of the thesis. It describes the complete analysis performed on the 2011 Pb-Pb collisions: signal extraction, acceptance times efficiency corrections, normalization of the data and determination of the systematic uncertainties that arise from difference sources. The results present the J/ψ R_{AA}, $\langle p_{\mathrm{T}} \rangle$ and $\langle p_{\mathrm{T}}^{2} \rangle$ together with a comparison to theoretical models and other experiments.

Contents

List of Figures

List of Tables

Chapter 1

The Quark Gluon Plasma

The present chapter will describe some general concepts used in particle physics and heavy ion collisions. It begins with a brief description of the Standard Model of elementary particles and the quantum field theory of strong interactions. This will lead to the property of confinement and asymptotic freedom and the prediction of a phase transition at extreme conditions of temperature and density. The final sections will overview some recent experimental results on the physics of ultrarelativistic nucleus-nucleus collisions.

1.1 The Standard Model

The Standard Model (SM) is a theory based on the $\mathrm{SU}(3)_\mathrm{C}\times$ $\mathrm{SU}(2)_\mathrm{L}\times$ $\mathrm{U}(1)_\mathrm{Y}$ gauge symmetry. Once these and the quantum numbers have been defined, the Lagrangian is determined by the gauge invariance and renormalization [1]:

$$\mathcal{L}_{\mathrm{SM}} = \mathcal{L}_{\mathrm{Gauge}} + \mathcal{L}_{\mathrm{Matter}} + \mathcal{L}_{\mathrm{Yukawa}} + \mathcal{L}_{\mathrm{Higgs}}. \tag{1.1}$$

The first term contains the kinetic energy of the gauge fields (gluon, weak and hypercharge) and their self interactions.

The next piece is the matter Lagrangian that includes the kinetic energy of the fermions and their interactions with the gauge fields, which are contained in covariant derivatives.

The third component in equation 1.1 is the Yukawa interaction of the Higgs field with the fermions. These 3 × 3 Yukawa matrices give rise to mixing among different generations and contain most of the parameters of the SM.

The final term is the Higgs Lagrangian that contains the kinetic energy of the Higgs field, its gauge interactions and the Higgs potential. It includes the only dimentionful parameter in the SM, its sign is chosen such that Higgs field has a non-zero vacuum-expectation value on the circle of minima in the

Higgs field space. The acquisition of a non-zero vacuum expectation value by the Higgs field breaks the electroweak symmetry and generates masses for the gauge bosons. Recent experimental results [2, 3] at the Large Hadron Collider (LHC) [4] indicate clear evidence for the production of a neutral boson that is compatible with the Standard Model Higgs boson.

Tables 1.1 and 1.2 show the current masses of quarks and leptons present in the SM, they are all fermions with spin 1/2 [5]. In the SM the neutrinos are assumed to have zero mass, but recent experimental evidences have shown the opposite. However, the mass of the neutrinos remain unknown and it is only possible to quote an upper value.

Table 1.3 displays the gauge bosons (spin 1), their electric charge, the force they carry and their masses.

Table 1.1: Quarks of the Standard Model.

Flavour	Mass	Charge (e)
u	$2.3^{+0.7}_{-0.5}$ MeV/c^2	2/3
d	$4.8^{+0.7}_{-0.3}$ MeV/c^2	-1/3
c	1.275 ± 0.025 GeV/c^2	2/3
s	95 ± 5 MeV/c^2	-1/3
t	173.5 ± 0.6 GeV/c^2	2/3
b	4.18 ± 0.03 GeV/c^2	-1/3

Table 1.2: Leptons of the Standard Model.

Flavour	Mass (MeV/c^2)	Charge (e)
e	$0.51 \pm 1.1{\times}10^{-8}$	-1
ν_e	$< 2 \times 10^{-3}$	0
μ	$105.65 \pm 3.5{\times}10^{-6}$	-1
ν_μ	$< 2 \times 10^{-3}$	0
τ	$1\,776.82 \pm 0.16$	-1
ν_τ	$< 2 \times 10^{-3}$	0

Table 1.3: The gauge bosons of the Standard Model.

Boson	Charge (e)	Force	Mass (GeV/c^2)
γ	0	Electromagnetic	0
$W^{\pm}$	± 1	Weak	80.385 ± 0.015
Z^0	0	Weak	91.1876 ± 0.0021
g	0	Strong	0

1.1.1 Quantum Chromodynamics

In 1954 Yang and Mills generalized the gauge transformations to SU(N)[1] non-abelian groups. SU(3) was then used to describe the strong interactions among particles, leading to what it is now called Quantum Chromodynamics (QCD).

In QCD there are three fields for each quark flavour and they are arranged in colour triplets $q_j^{\mathrm{T}} = (q_1, q_2, q_3)$ where the subscript denote the three colour fields. The free Lagrangian is given by [6]:

$$\mathcal{L}_f = \overline{q}_j(i\gamma^\mu \partial_\mu - m)q_j, \tag{1.2}$$

for simplicity only one quark flavour is shown. This equation must remain invariant under the local (gauge) transformation:

$$q(x) \longrightarrow Uq(x) \equiv e^{i\alpha_a(x)\,T_a}\, q(x),$$

with T_{a} (a = 1,...,8) the SU(3) generators: a group of 3 × 3 linearly independent matrices with null trace known as the Gell-Mann matrices, U an arbitrary 3 × 3 unitary matrix and α_a the group parameters.

This is a non-abelian group because not all the generators T_a commute with each other:

$$[T_a, T_b] = i f_{abc} T_c,$$

where f_{abc} are the structure constants of the group. In order to leave equation 1.2 invariant under the desired transformation, it is mandatory to replace the ordinary derivative with a covariant one that is defined as:

$$D_\mu = \partial_\mu + igT_a G^a_\mu.$$

Here g is the QCD gauge coupling constant and G^a_μ, the gluon field of colour a, transforms as:

$$G^a_\mu \longrightarrow G^a_\mu - \frac{1}{g}\,\partial_\mu\,\alpha_a - f_{abc}\,\alpha_b G^c_\mu.$$

The term representing the kinetic energy of the gauge boson is given by $-\frac{1}{4}\,G^a_{\mu\nu}G^{\mu\nu}_a$ where:

$$G^a_{\mu\nu} = \partial_\mu G^a_\nu - \partial_\nu G^a_\mu - g f_{abc} G^b_\mu G^c_\nu. \tag{1.3}$$

The gauge invariant QCD Lagrangian is then written:

---

[1] The group of $n \times n$ unitary matrices with determinant 1.

$$\mathcal{L} = \overline{q}(i\gamma^{\mu}\partial_{\mu} - m)q - g(\overline{q}\gamma^{\mu}T_a q)G^a_{\mu} - \frac{1}{4}G^a_{\mu\nu}G^{\mu\nu}_a.$$

The non-Abelian nature of the field strength tensor $G^a_{\mu\nu}$ is contained in the last term of equation 1.3. The kinetic component of the QCD Lagrangian includes then a self-coupling of the gauge boson up to a fourth degree. This has an important consequence, as will be shown in the next section.

1.2 Phase transition

The QCD gauge coupling constant can be related to the strong coupling constant ($\alpha_s = g^2/4\pi$), in such a way that as long as α_s is small, perturbative QCD (pQCD) can be employed to describe the interactions between quarks and gluons. In this regime, a perturbative expansion in α_s is used to compute different observables, where the first non-zero term of the expansion is the leading order (LO) term. Higher orders include quark and gluon loops, called virtual corrections (left panel of figure 1.1), that produce ultraviolet divergences due to the integration over the full phase space of virtual and real quarks and gluons (momentum of virtual particles can go up to infinity). Another type of divergences are the so-called infrared divergences which arise from the soft or collinear emission of massless gluons (left panel of figure 1.1).

1.2.1 Confinement and asymptotic freedom

In order to get rid of the aforementioned divergences a procedure called renormalisation is applied. In this method the divergent integrals are replaced by finite expressions requiring the introduction of the renormalisation scale μ_R. All renormalised quantities, in particular α_s, will explicitly depend on μ_R, creating a dependence of the strong coupling constant on the energy scale. It is then said that α_s is a running constant and is given by the renormalisation group equation:

$$Q^2 \frac{d\alpha_{\mathrm{s}}}{dQ^2} = \beta(\alpha_s), \tag{1.4}$$

with $Q^2 = \mu_R^2$ the square of the transferred momentum and the β-function a perturbative expansion in α_s, covering its dependency on the chosen scale (Q^2):

$$\beta(\alpha_s) = -\frac{\beta_0}{4\pi}\,\alpha_s^2 - \frac{\beta_1}{8\pi^2}\,\alpha_s^3 - \dots$$

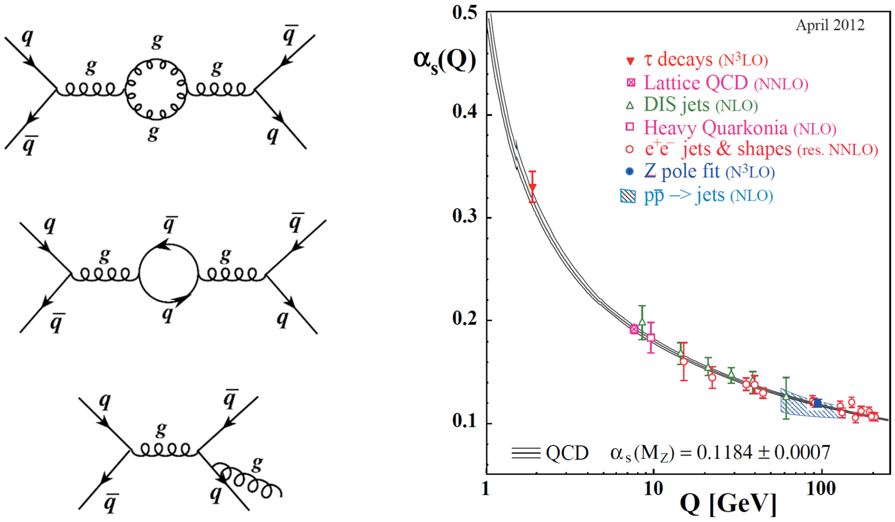

Figure 1.1: *Left:* Examples of divergences at NLO: gluon loop (top), quark loop (middle) and emission of a collinear gluon (bottom). *Right:* Values of α_s as a function of the transferred momentum, the band corresponds to the QCD prediction.

$$\beta_0 = 11 - \frac{2}{3} n_f, \quad \beta_1 = 51 - \frac{19}{3} n_f, \quad \ldots$$

The LO solution to equation 1.4 is given by:

$$\alpha_s(Q^2) = \frac{4\pi}{\beta_0 \ln(Q^2/\Lambda^2_{\mathrm{QCD}})},$$

where $\Lambda_{\mathrm{QCD}} \approx 200$ MeV is the scale at which α_s becomes sufficiently large, imposing a limit on the applicability of pQCD. The right plot of figure 1.1 shows the dependence of the strong coupling constant on the chosen scale [7]. At large Q the value of α_s is small and the quarks can be treated as free (asymptotic freedom). The rise of α_s for small values of Q corresponds to soft and large distance interactions which results in confinement and the invalidation of perturbative calculations.

1.2.2 Lattice QCD

QCD is the correct gauge theory to describe the interactions among partons, but it is not enough, it is also necessary to study the phases of the quark matter. Since equilibrium and phase transitions involve quarks and gluons interacting over a large distance scale, pQCD cannot be applied. Lattice QCD (lQCD), a non perturbative treatment of Quantum Chromodynamics formulated on a

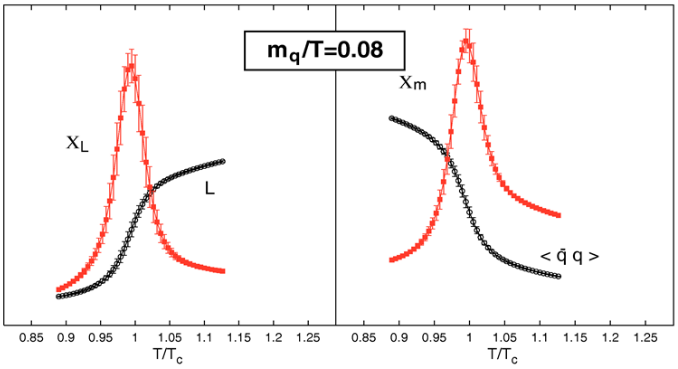

Figure 1.2: Deconfinement and chiral symmetry restoration computed for two quark flavours.

discrete lattice of space-time coordinates and at low baryon densities (μ_B), allows the extraction of the corresponding thermodynamic variables (temperature, volume, etc) by means of the partition function.

In the heavy quark (Q) mass approximation ($m_Q \to \infty$) and zero temperature, confinement can be modelled by assuming a potential that increases linearly with the distance r between a $Q\overline{Q}$ pair. To study the effect of the increasing temperature T one should look to an order parameter called the Wilson line (L) that at finite temperature is related to the free energy ($F_{Q\overline{Q}}(r, T)$) of the system [8]:

$$\exp\left[-\frac{\mathrm{F_{Q\overline{Q}}(r,T)}}{\mathrm{T}}\right] = \langle \mathrm{Tr}L\mathrm{Tr}L^{\dagger}\rangle \to |\langle L\rangle|^2.$$

For large separations $F_{Q\overline{Q}}$ is large and $\langle L\rangle = 0$ at $T < T_\mathrm{C}$ (confinement), where T_C is a critical temperature. When $T > T_\mathrm{C}$ the free energy is finite and $\langle L\rangle > 0$ (deconfinement).

Another order parameter is the effective quark mass, as it is related to the expectation value ($\langle\overline{q}q\rangle$) of the corresponding term in the Lagrangian. In the confined phase the chiral symmetry ($m_\mathrm{q} \to 0$) is spontaneously broken, while in the deconfined phase at high temperatures, its restoration is expected.

Related quantities are the Polyakov loop susceptibility ($\chi_\mathrm{L} \approx \langle L^2\rangle - \langle L\rangle^2$) and the chiral susceptibility ($\chi_\mathrm{m} \approx \partial\langle\overline{\psi}\psi\rangle/\partial m_\mathrm{q}$) that have a maximum at T_C, indicating the point of the phase transition (figure 1.2).

The transition temperature T_C has not been precisely determined, but recent lQCD results have established it between 180 and 200 MeV [9]. In this interval the energy density of the system (ϵ/T^4) increases by the latent heat of deconfinement (left plot of figure 1.3); it grows from a value determined by the degrees of freedom of a hadron gas to a much higher one governed by those from quarks and gluons. The Stefan-Boltzmann limit (SB) for massless non

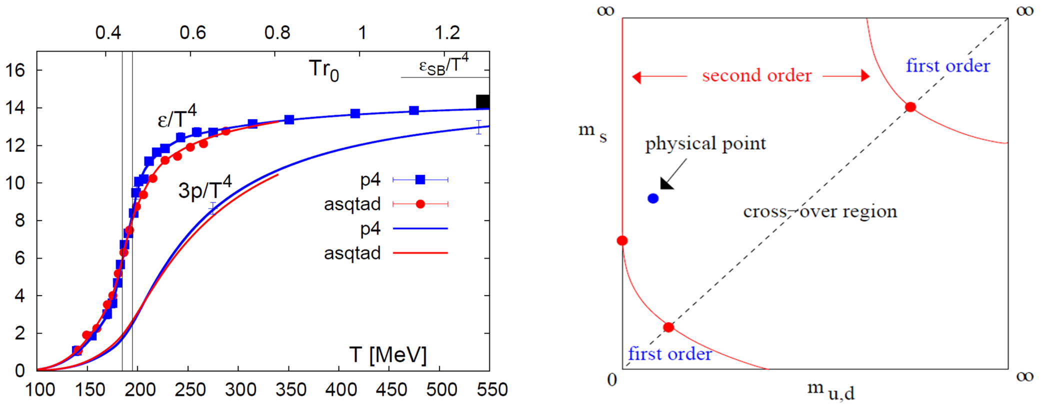

Figure 1.3: *Left:* Energy density and pressure vs temperature, colours refer to different discretizations of the lattice and vertical lines denote the transition region. *Right:* Order of the phase transition for finite temperature and $\mu_{\mathrm{B}} = 0$.

interacting particles is never reached.

This new deconfined state of matter where chiral symmetry is expected to be restored is known as Quark Gluon Plasma (QGP).

The order of the phase transition, strongly dependent on the quark masses, can be seen on the right plot of figure 1.3. A n^{th} order phase transition means that the n^{th} derivative of the free energy, $\partial^n F/\partial T^n$ is discontinuous, while the lower derivatives in T are continuous. Due to the light mass of the u and d quarks and the heavier s quark, the physical point is located in a region indicating that the phase transition is a rapid, but smooth cross-over [10].

1.2.3 QCD phase diagram

A first order phase transition is expected at low temperatures and large μ_B, however it is not clear at which point it would take place since lQCD calculations are not suitable in this regime. It has been predicted that the deep interior of compact stellar objects such as neutron stars would be the relevant place where this dense QCD matter at low temperature could be found [11]. If the baryon density is asymptotically high, weak-coupling QCD analyses indicate that the QCD ground state forms a condensation of quark Cooper pairs, namely the Colour SuperConductivity (CSC).

Figure 1.4 depicts the QCD phase diagram as a function of T and μ_{B}. The critical point marks the end of the first order phase transition (yellow area), giving place to the cross-over phase transition region (at low μ_{B}). The QCD phase diagram tells us that the strongly interacting matter, at extreme conditions of temperature and density, undergoes a phase transition to a state of

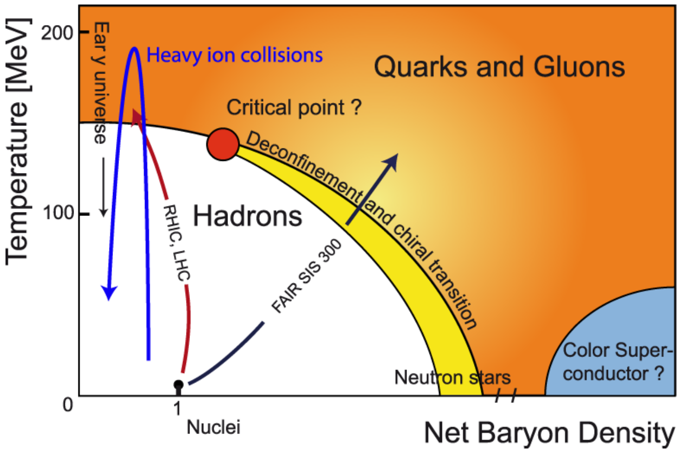

Figure 1.4: QCD phase diagram. The arrows indicate the region probed by the different particle accelerators.

deconfined quarks and gluons. Nowadays, the only way to recreate matter at the corresponding high energy densities in the terrestrial laboratory is by colliding heavy nuclei. In this way, ultrarelativistic heavy ion collisions reproduce the QGP at high temperatures and vanishing net baryon densities.

1.3 Nucleus-nucleus collisions

The process of multiple nucleon-nucleon collisions occurring between two nucleus allows to deposit a large amount of energy in a very small region. This is the key feature of high energy heavy-ion collisions to reach the deconfinement of quarks and gluons.

During these multiple collisions the nucleons lose a fraction of their energy. At low energies, nucleons are stopped in the collision region, giving birth to a state with high μ_B. At very high energies, the nucleons can still have enough momentum to continue with their trajectory and move far away from the interaction point. The energy lost is then deposited in the collision region creating a high energy density nuclear matter with small μ_B.

1.3.1 Space-time evolution

If the energy of the collision is high enough, the QGP can be created. If the plasma reaches the thermal equilibrium, its evolution will follow the laws of thermodynamics. As the system expands its temperature also drops down, giving place to hadronization. The space-time evolution of a high energy heavy-ion collision is the following (figure 1.5):

- Heavy quarks, jets and direct photons are created in the initial hard

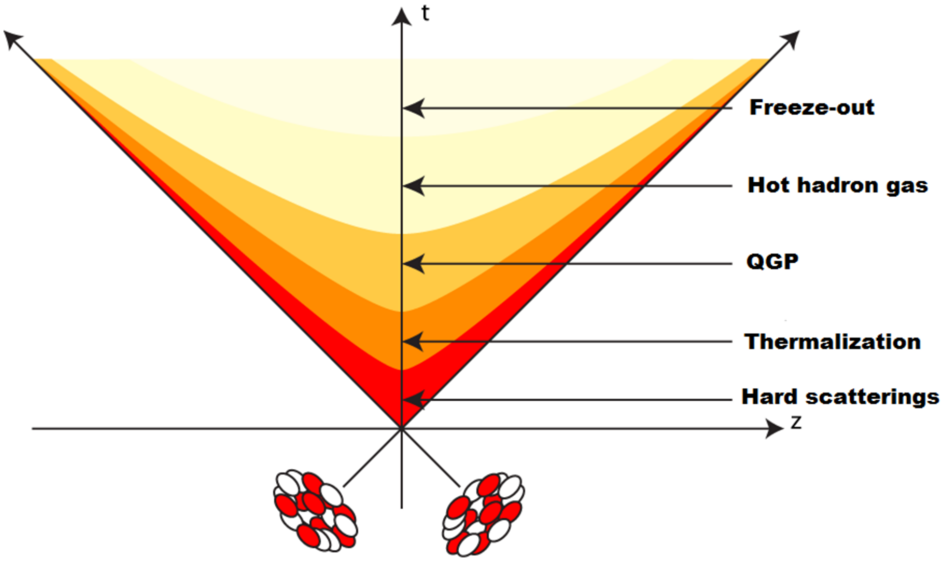

Figure 1.5: Space-time evolution of a high energy heavy-ion collision.

scatterings ($t \approx 0$ fm/c). These processes are well described by pQCD.

- Multiple scatterings among partons and produced particles lead to a rapid increase of entropy which could result in thermalization ($t \approx 1-2$ fm/c).
- The system reaches the deconfined phase ($t \approx 10-15$ fm/c).
- The expanding system cools down and below the critical temperature quarks and gluons become confined into hadrons ($t \approx 20$ fm/c).
- Inelastic processes are reduced until the relative abundance of hadrons is fixed (chemical freeze-out). Finally all the interactions cease and created hadrons stream out (kinetic freeze-out).

1.4 SPS and RHIC results on the QGP

If the QGP is created in a collision of two heavy nuclei, it eventually has to hadronize again. The detectors in the experiments can only measure the hadronic debris and particles created from this collision. A direct observation of the QGP is therefore not possible.

The present section will only review some of the observables that have been studied at the Relativistic Heavy Ion Collider (RHIC) and the Super Proton Synchrotron (SPS) before the LHC era. Results on charmonium production measurements are postponed to the next chapter.

1.4.1 Elliptic flow

In non central nucleus-nucleus collisions[2], the almond shaped overlap zone determines larger pressure gradients along the short axis relative to the long one (left panel of figure 1.6). The consequence is a preferential direction in the particle emission in the space of momenta, by measuring this anisotropy it is possible to retrieve information of the initial QGP state. The azimuthal momentum distribution can be expanded into a Fourier series:

$$\frac{dN}{d\phi} = \frac{N}{2\pi}\left[1 + 2\nu_1\cos(\phi) + 2\nu_2\cos(2\phi) + \ldots\right], \tag{1.5}$$

where ϕ is the azimuthal angle of momentum and ν_n are the Fourier coefficients of the n^{th} harmonic. Due to the symmetry around the y-axis the sine terms vanish. The first and second harmonics, ν_1 and ν_2, are called direct and elliptic flow parameters, respectively.

In general, the fact that flow is observed in the final state hadrons shows that thermalization is rapid, so that hydrodynamics comes into play before the spatial anisotropy of the overlap zone dissipates. At this early stage flow should be proportional to the number of constituent quarks n_q. Figure 1.6 shows the ν_2/n_q vs p_{T}/n_q indicating a poor scaling for $p_{\mathrm{T}}/n_q \lesssim 1$ GeV/c and a much better one for $p_{\mathrm{T}}/n_q \gtrsim 1.3$ GeV/c, albeit with large error bars [12]. However, the ν_2/n_q vs transverse kinetic energy ($KE_{\mathrm{T}} = m_{\mathrm{T}} - m$) shows a good scaling over the entire range of measurements. This is a consequence of perfect fluid hydrodynamics, implying that the viscosity is small and leading to the description of the sQGP (strongly interacting QGP) produced at RHIC as a perfect fluid.

1.4.2 Strangeness enhancement

In A-A collisions the initial content of strangeness is zero because nucleons are only made out of quarks from the first family, so the strange matter that is detected after a nucleus-nucleus collision can only be created by the collision. Besides this, strangeness is a conserved quantity, implying that each strange quark (s) has to be created together with its antiparticle. As mentioned before, the transition from ordinary nuclear matter to the QGP is expected to be accompanied by a restoration of the chiral symmetry, so the threshold energy to produce a $s\bar{s}$ pair would be much lower than in elementary hadronic collisions. As a consequence, the production of (anti)hyperons would be greater in heavy-ion collisions relative to pp or pA. This effect is often called strangeness enhancement.

---

[2] Centrality determination and related quantities are described in appendix A

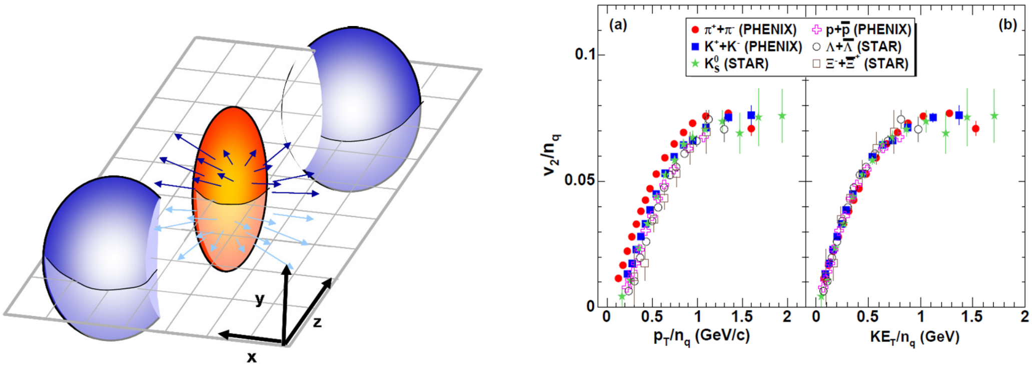

Figure 1.6: *Left:* Almond shaped overlap zone created in a non central A-A collision. *Right:* ν_2/n_q vs p_{T}/n_q and KE_{T}/n_q for identified particle species obtained in minimum bias Au-Au collisions measured by the PHENIX experiment at RHIC.

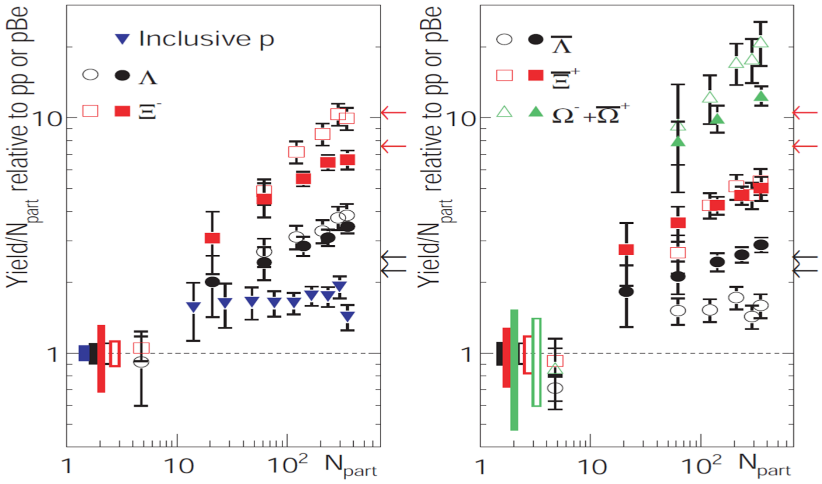

Figure 1.7: Observed (anti)hyperon yields normalized to pp or pBe collisions as a function of the centrality of the collision; open and closed points correspond to measurements performed at SPS and RHIC, respectively. The arrows on the right axis are the predictions from a Grand Canonical formalism for different chemical freeze-out temperatures.

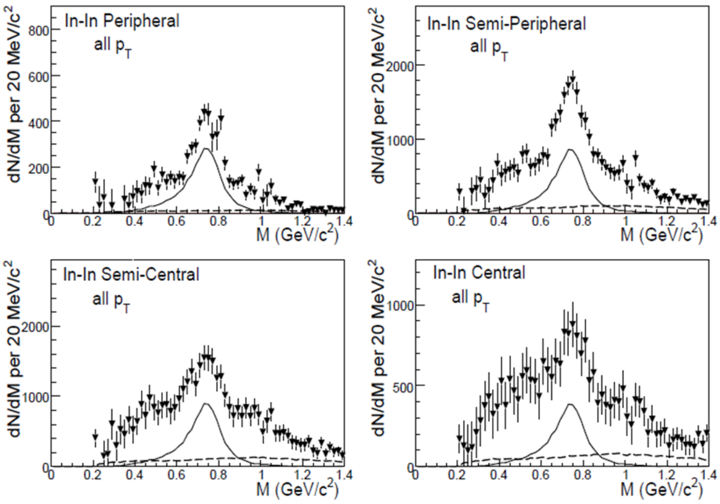

Figure 1.8: Invariant $\rho \to \mu^+\mu^-$ mass spectrum in 158 AGeV In-In collisions for different collision centralities. Dashed line indicates the level of uncorrelated background.

In figure 1.7 it is possible to appreciate the yield of (anti)hyperons compared to pp or pBe that are used as benchmarks. A clear hierarchy in the scale of enhancements, which grows with the increased strangeness content of the baryon, is observed [13].

1.4.3 Resonances

Due to their short lifetime, comparable to the fireball created in a heavy-ion collision, strongly decaying resonances as ρ and ϕ can be used to obtain information on the medium where they disintegrate. Indeed, the decay tracks from a resonance are produced in a dense environment and so they may undergo scattering; if this occurs the reconstructed invariant mass of the resonance will be smeared out (mass and width in-medium modification). Resonances can decay into leptons as well as into hadrons. As leptons do not couple to the strong interaction rescattering is expected to occur at a much lower rate and the resonance can be used to sample all the stages of the interaction. The hadronic decay channel can only allow the reconstruction of resonances from the later stages of the system.

The NA60 experiment at SPS has studied the ρ spectrum for different collision centralities in In-In collisions (figure 1.8). After subtraction of all other sources of opposite sign muon pairs, the invariant mass distribution of the resonance is peaked at the nominal mass value but its width is substantially broadened for increasing centralities. The spectral shape is better reproduced by models which consider in-medium width broadening due to interactions in a hot and dense hadronic medium [14].

NA60 has also measured and compared the decay yield, mass and width of $\phi \to K^+K^-$ and $\phi \to \mu^+\mu^-$ [15]. The obtained yields are in agreement between each other, except for central collisions where a difference in the yields larger than 18% at 95% Confidence Limit (C.L.) in the common p_T range was found. In addition, no modification of the mass and width has been observed as a function of centrality.

1.4.4 Di-hadron azimuthal correlations

The study of the production of high transverse momentum hadrons in heavy ion collisions provides an experimental probe of the QCD matter in the densest stage of the collisions. In particular, two-hadron azimuthal correlations support the assessment of back-to-back, hard-scattered partons that propagate in the medium before fragmenting into jets of hadrons, thereby serving as a tomographic probe of the medium. These events are identified by triggering on a high-p_T hadron (p_T^a), in such a way that its partner is expected in a region of $\Delta\phi \approx \pi$ away (p_T^b).

A typical di-hadron azimuthal correlation in pp and compared to central Au-Au collisions at $\sqrt{s_\mathrm{NN}} = 200$ GeV is shown in figure 1.9. The di-jet structure in pp collision is clearly indicated by the gaussian-like strong azimuthal correlation peaks on the same ($\Delta\phi = \phi_b$ - $\phi_a \approx 0$) and away side ($\Delta\phi \approx \pi$) relative to the triggered particle. In Au-Au events, the widths of the near side (NR) peaks are comparable to those from pp over the full $p_\mathrm{T}^a \otimes p_\mathrm{T}^b$ range. However, the away side peaks are much wider and show a two-lobed structure called the shoulders (SR) at lower p_T^a with a dip at $\phi \approx \pi$, reverting to the more conventional structure of a peak at $\phi \approx \pi$ known as the head (HR) for larger p_T^a [16]. These observations suggest that both the away and near side distributions contain a jet fragmentation (medium-induced) component which dominates at high (low) transverse momentum.

1.4.5 Heavy flavours

As heavy flavours (HF) are produced on a very short time-scale in the initial hard-scattering processes, they experience the whole evolution of the system. For this reason, they can be used as a probe to understand the in-medium partonic energy loss in the dense QCD matter created in a central heavy-ion collision. This energy loss can occur either via inelastic (medium-induced gluon radiation) or elastic (collisional) mechanisms. The amount of energy lost by a parton in a medium is proportional to its Casimir factor (colour charge), implying that quarks would suffer a smaller energy loss than gluons. In addition the dead-cone effect, which prevents the small-angle gluon radiation from

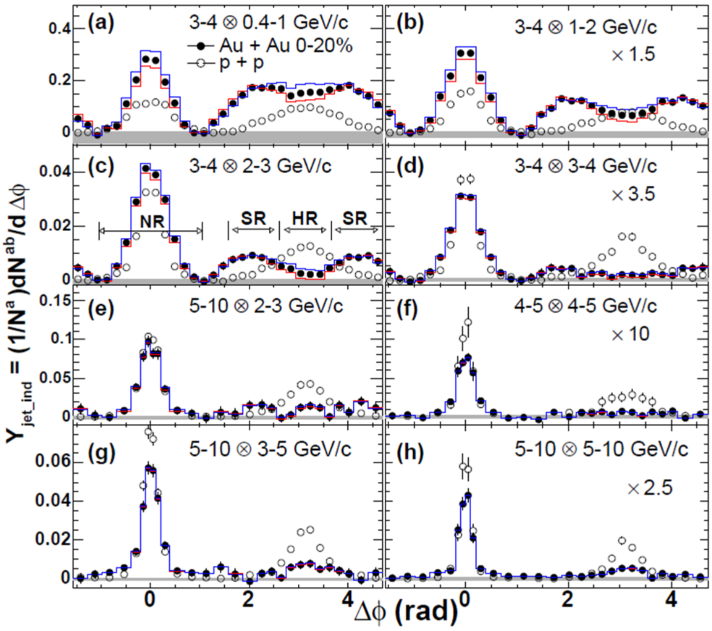

Figure 1.9: Azimuthal correlation yield of jet-induced pairs per trigger for different $p_{\mathrm{T}}^{a} \otimes p_{\mathrm{T}}^{b}$ values. The shaded band is the uncertainty on the combinatorial background subtraction, while the solid lines indicate the uncertainty arising from the elliptic flow.

quarks in a colour charged medium, becomes more important with increasing mass. The QCD energy loss model predicts a $\Delta E_{\mathrm{Q}} < \Delta E_{\mathrm{q}} < \Delta E_{\mathrm{g}}$ hierarchy that can be experimentally verified if $R_{\mathrm{AA}}^{\pi} < R_{\mathrm{AA}}^{\mathrm{D}} < R_{\mathrm{AA}}^{\mathrm{B}}$ is measured. The Nuclear Modification Factor (R_{AA}) is defined as:

$$R_{\mathrm{AA}} = \frac{d^2 N_{\mathrm{AA}}/dp_{\mathrm{T}} d\eta}{\langle N_{\mathrm{coll}} \rangle d^2 N_{\mathrm{pp}}/dp_{\mathrm{T}} d\eta}, \tag{1.6}$$

where $d^2 N_{\mathrm{AA}}/dp_{\mathrm{T}} d\eta$ is the number of measured particles per unit of transverse momentum and pseudorapidity[3] in A-A collisions, $d^2 N_{\mathrm{pp}}/dp_{\mathrm{T}} d\eta$ the number of the same kind of particles measured in pp collisions and $\langle N_{\mathrm{coll}} \rangle$ the mean number of nucleon-nucleon collisions. If $R_{\mathrm{AA}} \approx 1$, then there is no difference between the production in nucleus-nucleus and in pp collisions. But if $R_{\mathrm{AA}} \neq 1$ then it might be an indication of medium induced effects.

Figure 1.10 shows the measured R_{AA} and ν_2^{HF} of non-photonic electrons (electrons from heavy flavours decays) and π^0 as measured by PHENIX in Au-Au collisons at $\sqrt{s_{\mathrm{NN}}} = 200$ GeV. The data shows a suppression of heavy quarks almost at the same level of π^0 at high-p_{T} (within uncertainties), where a large

---

[3] The pseudorapidity is defined as $\eta = -\ln\tan(\theta/2)$, where θ is the polar angle relative to the beam axis.

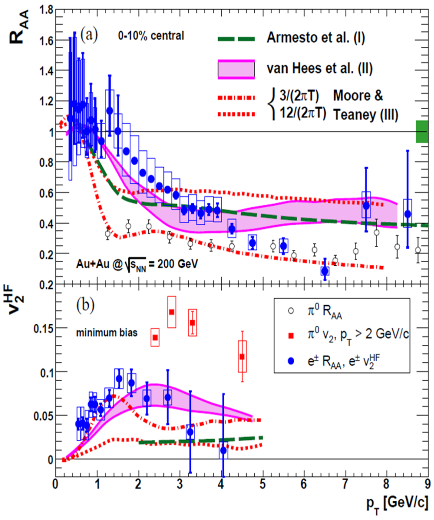

Figure 1.10: R_{AA} and ν_2^{HF} of non-photonic electrons.

fraction of electrons is expected to come from beauty. The large ν_2^{HF} indicates a short charm relaxation time[4], while comparison to theoretical models suggest a viscosity to entropy ratio of the medium near a perfect fluid [17].

1.5 Results from Pb-Pb collisions in ALICE

A Large Ion Collider Experiment (ALICE) [18] is the heavy-ion dedicated experiment of the LHC. In November 2010 the first Pb-Pb collisions took place in three of the four main experiments at the LHC and within days ALICE had the first physics results.

The following is a selection of the published results from the 2010 and 2011 Pb-Pb runs. Studies on charmonium production will be addressed in the next chapter.

1.5.1 Global properties

In the Bjorken approach, once the termalization time (τ_0) has been defined it is then possible to estimate the energy density of the collision with the following formula [19]:

$$\epsilon \geq \frac{3}{2}\langle E_{\mathrm{T}}/N\rangle \frac{dN_{\mathrm{ch}}/d\eta}{\tau_0 \pi R^2},$$

---

[4] Time to approach equilibrium in the medium.

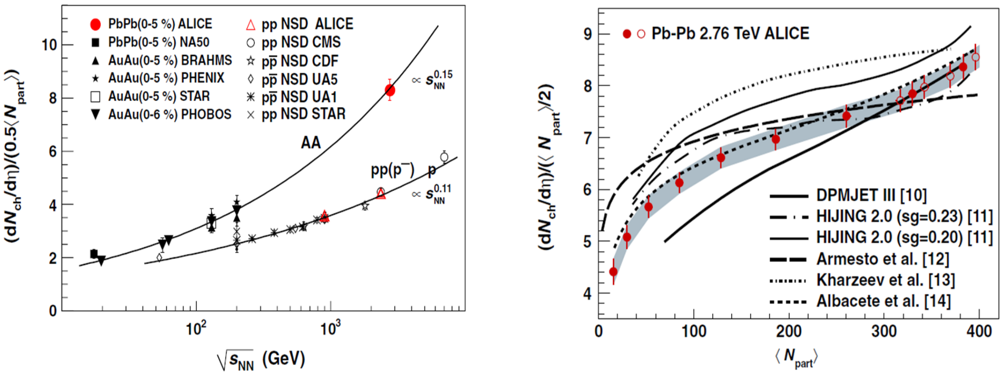

Figure 1.11: *Left:* $dN_{\rm ch}/d\eta/(0.5\ N_{\rm part})$ vs $\sqrt{s_{\rm NN}}$ for different kinds of colliding systems. *Right:* $dN_{\rm ch}/d\eta$ vs $\langle N_{\rm part}\rangle$ compared to theoretical predictions.

where $\langle E_{\rm T}/N\rangle$ is the mean transverse energy per emitted particle (approximately 1 GeV), R the nuclear radius and $dN_{\rm ch}/d\eta$ the number of charged particles produced per unit of pseudorapidity. At the LHC $dN_{\rm ch}/d\eta \approx 1\ 600$ [20], implying that the initial energy density (for $\tau_0 = 1$ fm/c) is about 15 GeV/fm^3. This is a very conservative computation because the termalization time has been considered to be the same at RHIC, although it is expected to be smaller for the LHC.

Left plot of figure 1.11 shows the charged particle multiplicity per participant pair, $dN_{\rm ch}/d\eta/(0.5\ N_{\rm part})$, as a function of $\sqrt{s_{\rm NN}}$ for different colliding systems; the particle production does not follow anymore a logarithmic behaviour but a power law one [20]. On the right plot of the same figure, $dN_{\rm ch}/d\eta/(0.5\ N_{\rm part})$ vs $\langle N_{\rm part}\rangle$ is compared to theoretical predictions [21]. The curve that better reproduces the data is based on a saturation model.

The freeze-out volume (size of the matter at the time when strong interactions cease) and the lifetime of the created system (the time between the collision and freeze-out) can be determined by means of Handbury-Brown-Twiss (HBT) correlations. For identical bosons (fermions), quantum statistics lead to an enhancement (depletion) for particles emitted close-by in phase space modifying the two particle correlation function measured in energy and momentum variables. These are in turn related, via a Fourier transformation, to the space and time distribution of the emitting source.

The HBT correlation results are shown in figure 1.12, the freeze-out volume in the coordinate system is defined by the beam axis ($R_{\rm long}$), the direction along the pair transverse momentum ($R_{\rm out}$) and the perpendicular to the particle pair total $p_{\rm T}$ ($R_{\rm side}$); the lifetime is estimated from the pair-momentum dependence of $R_{\rm long}$ [22]. The pion source radii obtained by ALICE exceed those measured at RHIC by 10-35%, while the homogeneity volume is found

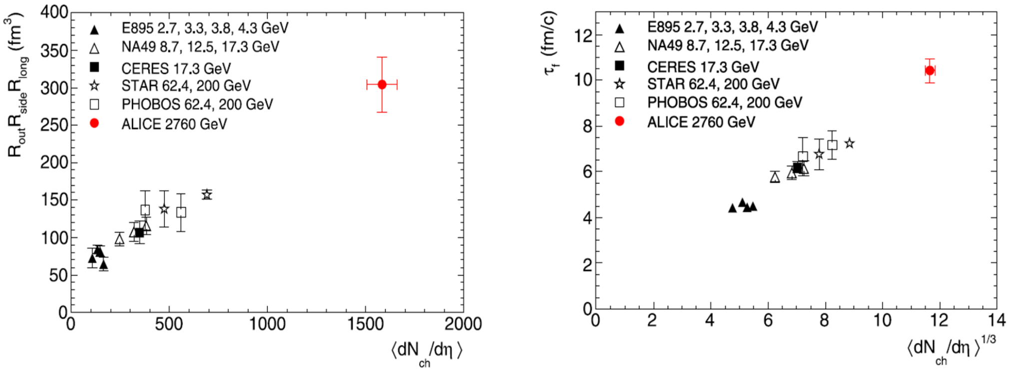

Figure 1.12: Freeze-out volume (*left*) and system lifetime (*right*) compared to lower energy results.

to be larger by a factor of two. The decoupling time for mid rapidity[5] pions exceeds 10 fm/c, which is 40% larger than at RHIC. These results indicate that the fireball created in Pb-Pb collisions at the LHC is hotter, lives longer and expands to a larger size at freeze-out as compared to lower energies.

1.5.2 Elliptic flow

Since the success of the ideal hydrodynamics description of the elliptic flow in Au-Au collisions at RHIC, hydrodynamics is considered as the most appropriate theory to describe a thermalized phase in the time evolution of the system created in a heavy-ion collision. The measured elliptic flow of charged particles in 20-30% centrality class is compared to lower energy results in figure 1.13, it shows a continuous increase in the magnitude of the ν_2. The increase of 30%, relative to Au-Au collisions at $\sqrt{s_{\mathrm{NN}}} = 200$ GeV, is larger than in current ideal hydrodynamic calculations at LHC multiplicities, but in agreement with some models that include viscous corrections [23].

1.5.3 Higher harmonic anisotropic flow

The azimuthal correlation, $C(\Delta\phi)$, observed in the most central collisions (0-1%) for triggered particles in the range $2 < p_{\mathrm{T}} < 3$ GeV with associated particles in $1 < p_{\mathrm{T}} < 2$ GeV for pairs in $|\Delta\eta| > 1$ is shown in figure 1.14. A doubly peaked correlation structure centered opposite to the trigger particle is clearly visible, something that has been interpreted as an indication for various jet-medium modifications as for example the Mach cones. The azimuthal correlation shape expected from ν_2, ν_3, ν_4 and ν_5 (equation 1.5) are evaluated

---

[5] The rapidity $y = \frac{1}{2}\ln\left(\frac{E+p_z}{E-p_z}\right)$ is related to the longitudinal momentum p_z and energy E of a particle.

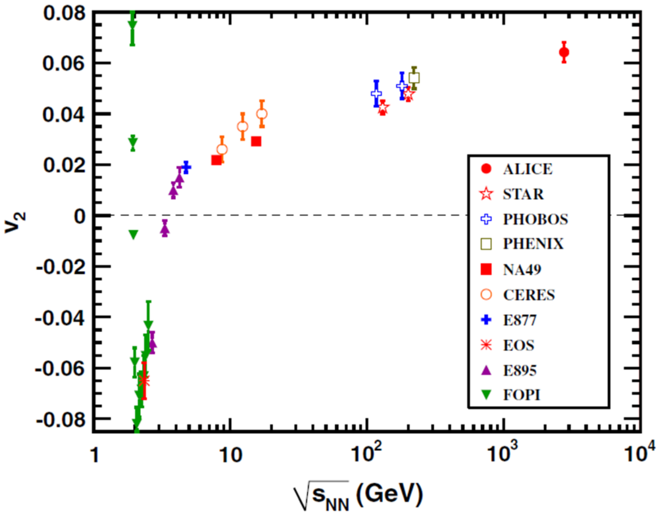

Figure 1.13: ALICE elliptic flow of charged particles in the 20-30% centrality class compared to lower energy results.

at the corresponding transverse momenta with the measured two-particle azimuthal correlation. The combination of these harmonics provides a natural description of the observed structure on the away side [24].

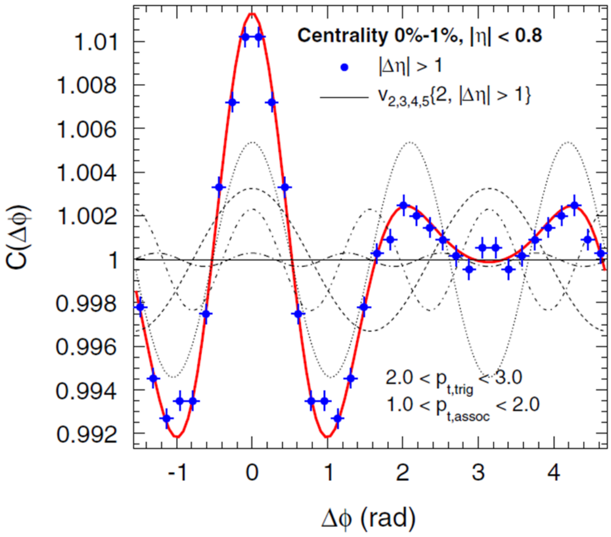

Figure 1.14: The two-particle azimuthal correlation in the 2-3 ⊗ 1-2 GeV range.

1.5.4 High-p_{T} suppression

The fragmentation of high-p_{T} partons originated in the early stages of the nuclear collisions is the main production mechanism for high-p_{T} hadrons. It is expected that the large energy density of the medium created in ultrarelativistic heavy-ion collisions leads to a large energy loss of high-p_{T} partons, specially at the energy scales involved at the LHC. Figure 1.15 compares the inclusive R_{AA} measured at the LHC and at RHIC in the most central collisions, a hint of enhanced energy loss is obtained for Pb-Pb collisions at $\sqrt{s_{\mathrm{NN}}}$ = 2.76 TeV. A rise towards high-p_{T} is already suggested by the highest p_{T} points from PHENIX and STAR, although the large uncertainties do not give a clear trend [25].

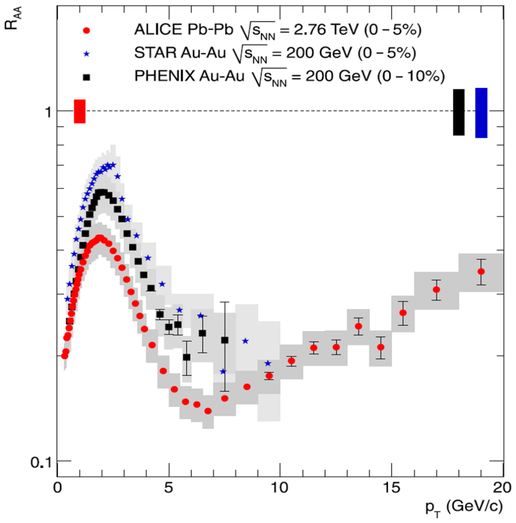

Figure 1.15: R_{AA} of charged particles in the most central collisions measured by ALICE compared to STAR and PHENIX results.

1.5.5 Heavy flavours

Prompt D mesons R_{AA} (D^0, D^+ and D^{*+}) was computed as a function of N_{part} at mid rapidity. The observed suppression increases as a function of the collision centrality and is similar for the three D meson species [26]. An average D mesons R_{AA} vs p_{T} (left plot of figure 1.16) is, within uncertainties, in agreement with the R_{AA} of charged hadrons, with a hint of a smaller suppression. The comparison to non-prompt J/ψ (coming from the decay of B mesons) indicates a possible larger suppression of D mesons. These behaviours may be due to the predicted energy loss hierarchy, but more precise measurements are needed to reduce the uncertainties.

The inclusive production of muons from heavy flavour decays at forward rapidity[6] ($2.5 < y < 4$) exhibits a strong suppression with increasing centrality, reaching a factor of about 3-4 in the most central collisions (right plot of figure 1.16). This suppression is similar to that of D mesons and J/ψ from beauty decays previously mentioned, although the results for single muons from heavy flavours are from a different p_{T} and rapidity region [27].

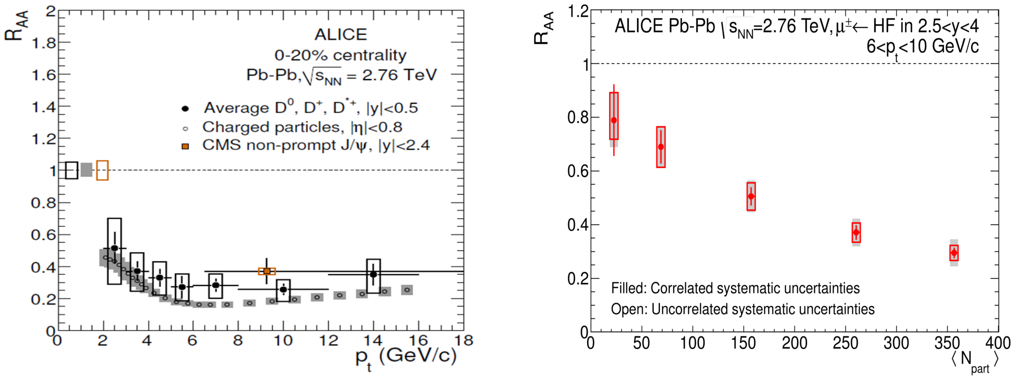

Figure 1.16: *Left*: Average D mesons R_{AA} compared to charged hadrons and non-prompt J/ψ measured by CMS as a function of p_{t} in the most central collisions. *Right*: Nuclear Modification Factor of muons from heavy flavour decays as a function of the centrality.

---

[6] In the ALICE reference frame the muon spectrometer covers a negative η range and consequently has also a negative y range. However, it has been chosen to present the results with a positive y notation.

Chapter 2

Charmonium

The previous chapter presented a general introduction to the physics of high energy heavy-ion collisions. The present chapter will focus on charmonia, the main subject of this thesis. It will begin with a basic historical introduction and a description of the most popular models that describe the production of charmonia in hadronic collisions. Then it will continue with the topic of charmonium suppression as a signature of the QGP and the descriptions of theoretical models that go from suppression to (re)generation. This chapter will finally present the latest results on J/ψ from the ALICE experiment

2.1 A brief history of charmonium

In November 1974 a narrow resonance at 3.1 GeV/c^2 in the $\mu^+ \mu^-$ invariant mass spectrum was observed in proton-beryllium and electron-positron collisions by two independent research groups [28, 29]. The particle was named "J" by the group working in the Alternating Gradient Synchrotron (AGS) at the Brookhaven National Laboratory (BNL) and ψ by those working in the Standford Positron Electron Asymmetric Ring (SPEAR) at the Stanford Linear Accelerator Center (SLAC). The latter name was driven by the topology of the $e^+ e^- \rightarrow \pi^+ \pi^-$ decay. Two years later, when both research group leaders (Ting and Richter) were awarded with the Nobel prize for their simultaneous discovery, the particle was renamed as J/ψ.

However this was not at all an ordinary discovery, as at that time the world was expected to consist of only three light quarks (u, d and s) plus electrons and muons. Soon after the first observation of the new particle it became clear that the J/ψ contained the c quarks predicted by the Glashow-Iliopoulos-Maiani (GIM) mechanism[1]. So, the discovery of the J/ψ added a

---

[1] Introduced in the early 1970′s in order to explain the small branching ratio ($\simeq 10^{-7}$) of $K^0 \rightarrow \mu^+ \mu^-$ according to the models available at that time. The GIM mechanism basically describes the decay as a destructive interference between two indistinguishable decay

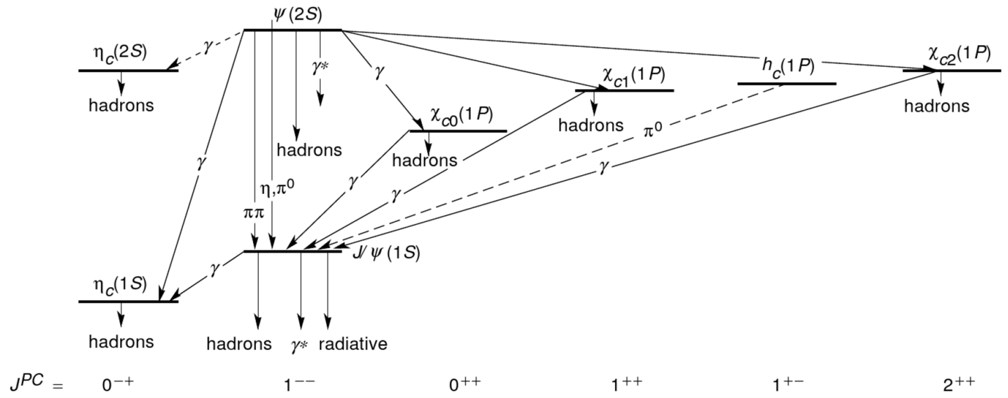

Figure 2.1: Spectroscopy for charmonium states below the open heavy flavour pair production threshold. For each state the following notation is used: n L, with n the principal quantum number and L the orbital angular momentum. In the bottom P indicates the parity and C the charge conjugation.

new particle to the fundamental building blocks of nature.

The November Revolution motivated huge experimental efforts aimed to new discoveries in the c quark sector. Nowadays, all this knowledge of charmonium resonances can be summarized as in figure 2.1.

Because of its large mass ($m_{\mathrm{Q}} \ll \Lambda_{\mathrm{QCD}}$), bound states of $c\bar{c}$ can be treated using a non-relativistic approach with the Cornell potential

$$V(r) = \sigma r - \frac{\alpha}{r} \tag{2.1}$$

where the linearly rising part represents the confining force given in terms of the string tension $\sigma \approx 0.2$ (GeV)^2 that keeps the pair attached to each other. The second term is a coulombian type potential with $\alpha = \pi/12$. In this way it is possible to compute the masses, binding energies and radii of the lowest $c\bar{c}$ bound states, as can be seen in table 2.1 [30]

Table 2.1: Masses, binding energies and radii of charmonium states.

States	J/ψ	χ_c	ψ'
Mass (GeV)	3.10	3.53	3.68
ΔE (GeV)	0.64	0.20	0.05
r_0 (fm)	0.50	0.72	0.90

---

channels. This destructive interference explained the small branching ratio, nevertheless, the additional decay channel implied the existence of a fourth quark.

2.2 Charmonium production

A heavy quarkonium has at least three intrinsic momentum scales [31]: the heavy quark mass m_Q; the momentum of the heavy quark or antiquark in the quarkonium rest frame, which is of the order $m_Q v$; and the binding energy of the heavy quark-antiquark ($Q\overline{Q}$) pair, which is of the order $m_Q v^2$. Here v is the typical velocity of the heavy quark or antiquark in the quarkonium rest frame: $v^2 \approx 0.3$, in natural units, for the J/ψ.

If a heavy quarkomium is produced in a hard scattering process, then, in addition to the intrinsic scales of the quarkonium, the hard scattering scale p enters into the description of the production process. In quarkonium hadroproduction p is usually taken to be of the order of p_{T}, the transverse momentum of the quarkonium.

The production of quarkonium states can be understood in two steps: the production of the $Q\overline{Q}$ pair, which would occur at the scale p, and the subsequent evolution of the $Q\overline{Q}$ pair into the quarkonium, which would involve the smaller dynamical scales $m_Q v$ and $m_Q v^2$. The first step would be calculable in an expansion in powers of $\alpha_{\mathrm{s}}(p)$, while the second step would typically involve inherently nonperturbative physics. The term *short distance* is often used to refer to the momentum scale p (distance scale $1/p$), while the term *long distance* refers to the typical hadronic momentum scales ($m_Q v$, $m_Q v^2$ or Λ_{QCD}).

The separation of the perturbative effects at the scale p from the long distance nonperturbative dynamics is know as *factorization*.

Since the charmonium discovery, many models have been proposed in order to describe and predict its properties (p_{T} distribution, polarization, etc). In the following, the Color Singlet Model (CSM), the Color Evaporation Model (CEM) and the Non-Relativistic QCD (NRQCD)approach are described [32, 33, 34].

2.2.1 Color Singlet Model

The fundamental hypothesis of the CSM is that the angular momentum quantum numbers of the $c\bar{c}$ pair are the same than the produced quarkonium and therefore the initial hard scattering has to produce color singlet $c\bar{c}$ pair.

This model has a very high predictive power as the only input required, apart from the Parton Distribution Functions (PDF) in case of hadronic collisions, is the absolute value of the color singlet $c\bar{c}$ wave function. These quantities can be determined from data or by the application of potential models. Once these quantities are provided, the CSM has no free parameters.

2.2.2 Color Evaporation Model

Charm quarks are produced in primary hard collisions ($t_{c\bar{c}} \approx 1/2m_c \approx 0.1$ fm/c) and in general the $c\bar{c}$ pair is in a color octet state. After a short relaxation time $\tau \approx 1/\sqrt{2m_c\Lambda_{\mathrm{QCD}}} \approx 0.25$ fm/c this pre-resonance neutralises its colour, turning into the physical $c\bar{c}$ resonance. Contrary to the CSM, in the CEM there is no specification about the quantum numbers of the pre-resonance created. So, by construction, the CEM can not predict the polarization of the charmonium state. In case an octet state is created, the colour is neutralized through interactions with the colour field produced by the collision.

The cross section for a charmonium state H is some fraction F_H of the cross section to produce $c\bar{c}$ pairs with invariant mass below the $D\overline{D}$ threshold. However, even if the $c\bar{c}$ invariant mass is less than the heavy meson threshold $2m_D$ the additional energy needed to produce charmed hadrons can be obtained from the non-perturbative colour field. As a consequence, the sum of the fractions F_H of all the charmonium states H can be less than unity. The fractions F_H are assumed to be universal.

A prediction from the CEM is that the ratio of the cross section for any of two charmonium states should be constant, independent of the process and kinematic region. Nevertheless some variations in these ratios have been observed, representing a serious challenge to the CEM.

2.2.3 Non-Relativistic QCD

In this model the physical state H of the charmonium, for $p_{\mathrm{T}} \gtrsim m_H$, is considered as a result of products of NRQCD matrix elements and short distance coefficients:

$$\sigma[H] = \sum_i \sigma_n(\Lambda)\langle\mathcal{O}_n^H\rangle, \tag{2.2}$$

where Λ is the ultraviolet cutoff of the effective theory, $\sigma_n(\Lambda)$ the short distance coefficients and $\mathcal{O}_n^H$ the four-fermion operators.

The short distance coefficients depend on the partonic cross sections to produce a $c\bar{c}$ convoluted with parton distribution functions (if hadrons are present in the initial state). The $c\bar{c}$ pair can be produced in a colour singlet or colour octet state, the spin can be singlet or triplet and it can also have orbital angular momentum.

The vacuum matrix element of the four-fermion operator is the probability for a $c\bar{c}$ pair to form a quarkonium plus anything. These matrix elements are somewhat analogous to the parton FF as they contain all the non-perturbative physics associated with the evolution of the $c\bar{c}$ pair into a charmonium state.

2.3 Charmonium suppression as a signature of the QGP

In 1986 charmonium was proposed to be used as a probe for the matter created in high energy heavy-ion collisions [35]. If the QGP is created, deconfined quarks and gluons are then free to move within a volume of a few fm^3. In this medium, the Cornell potential (equation 2.1) is replaced by [30]:

$$V(r,T) = \frac{\sigma}{\mu}\left\{1 - e^{-\mu r}\right\} - \frac{\alpha}{r}e^{-\mu r}, \tag{2.3}$$

where μ is the screening mass (inverse to the Debye radius) for the medium at temperature T. When the temperature of the QGP is higher than a given dissociation temperature T_d, the c and $\bar{c}$ are screened by the deconfined partons and their binding breaks up. This effect is known as Debye screening and leads to the suppression of charmonium states produced in heavy-ion collisions.

Quantitative results must be obtained by solving the Schrödinger equation with [30]:

$$V(r,T) = F(r,T) - T\left(\frac{\partial F(r,T)}{\partial T}\right) \approx F(r,T),$$

with $F(r,T)$ the free energy of the $c\bar{c}$ pair. On the left of figure 2.2 it is possible to observe that the energy needed to separate the heavy quark pair decreases with increasing temperature, as does the separation distance at which the string breaks. This indicates that with increasing T, the screening reduces the range of the potential. The dissociation temperature is then determined when the bound state vanishes, $\Delta \mathrm{E} = 0$, as can be seen on the right (left) plot of figure 2.2 (figure 2.3) for the case of the J/ψ (ψ' and χ_c).

As different charmonium states have different binding energies (table 2.1) and given the dependence of the screening radius on the temperature of the medium, it is then natural to think that these states have different melting temperatures (table 2.2). A crucial feature of J/ψ suppression by deconfinement is its sequential nature [36]: the dissociation affects first the J/ψ originating from ψ' decay, then those from χ_c and finally the directly produced J/ψ (right plot of figure 2.3).

It is also expected that the effect of charmonium suppression could also manifest itself in the transverse momentum [37]. The basic effect of a nuclear medium on the transverse momentum behaviour of hard processes is a collision broadening of the incident parton momentum; this in turn leads to a broadening of the transverse momentum distribution of the charmonia formed by hard parton interactions.

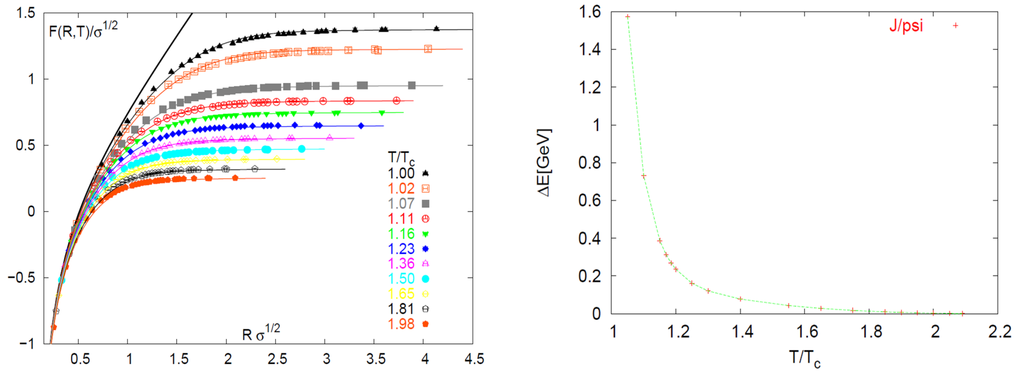

Figure 2.2: *Left*: Free quark energy as a function of the distance times the string tension between the quarks. *Right*: Temperature dependence of the binding energy for the J/ψ.

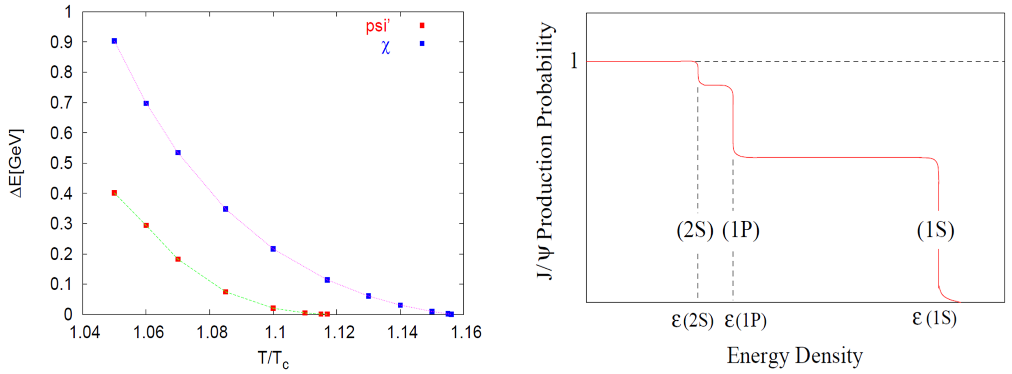

Figure 2.3: *Left*: Temperature dependence of the binding energy for the ψ' and χ_c. *Right*: Sequential suppression of different charmonia states.

Table 2.2: Dissociation temperatures for the different charmonia states.

States	J/ψ	χ_c	ψ'
T_d/T_c	2.10	1.16	1.12

2.4 Cold Nuclear Matter effects

Even if the QGP is not created in heavy-ion collisions, the production of charmonia can be affected by

- Initial state effects: associated to the modification of the PDF of the nucleons in the nucleus.

- Final state effects: corresponding to the interaction of the charmonium state with the surrounding nuclear matter.

The mechanisms responsibles for the modification of the charmonium production in the absence of a QGP in nucleus-nucleus collisions are oftenly called Cold Nuclear Matter (CNM) effects. At the LHC these effects are being quantified by studying pA collisions, while at RHIC d-Au collisions are used.

2.4.1 Initial state effects

At the LHC the production of heavy quarks is dominated by the interactions between gluons. As nucleons are embedded in the nucleus, their gluon distribution functions are modified by the nuclear environment, implying that the gluon PDF in a nucleus is different from the superposition of PDFs of their nucleons [38, 39]. This effect is quantified by the shadowing ratio given by:

$$R_g^A(x,Q^2) = \frac{f_g^A(x,Q^2)}{A\, f_g^{\text{nucleon}}(x,Q^2)},$$

where f_g^A is the PDF of the gluons in the nucleus and f_g^{nucleon} the PDF of the gluons in the nucleon.

Figure 2.4 shows the expected evolution of R_g^A in a lead nucleus as a function of x for different Q^2 values, ranging from 2.25 GeV^2 up to 10^4 GeV^2. It is also visible the x regions accessible at SPS, RHIC and LHC. The x domain where $R_g^A < 1$ is called *shadowing* region, whereas if $R_g^A > 1$ the region is known as anti-*shadowing*. At the LHC the shadowing effect is expected to be strong.

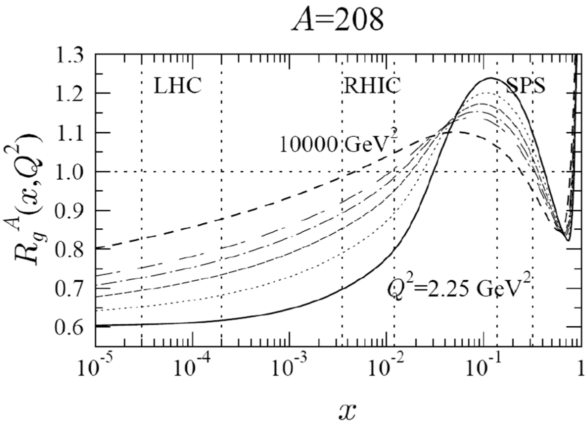

Figure 2.4: R_g^A evolution in a lead nucleus as a function of x for different Q^2 values.

Another initial state effect is called *gluon saturation*, that is also related to the fact that the number of gluons in the wave function of a nucleus at high energies is reduced with respect to the simple addition of the gluon field of the constituent nucleons. However, while the nuclear shadowing is an empiric parametrization fitted to the data, the saturation is a dynamical description via gluon self-interactions that tame the growth of gluons towards high energies [40].

2.4.2 Final state effects

Once the charmonium pre-resonance has been produced it is susceptible to interact with the nuclear environment and as a consequence be dissociated. The survival probability can be parametrised by [41]:

$$S_{\mathrm{abs}}(b) \approx \exp[-\rho_0 \sigma_{abs} \overline{L}],$$

where b is the impact parameter of the collision, σ_{abs} is the absorption cross section, ρ_0 the nuclear matter density and $\overline{L}$ the average length traveled by the J/ψ in the nucleus.

The nuclear absorption depends on the center of mass energy of the collision. At low energies the heavy system undergoes successive interactions with the nucleons in its path, so there is a strong nuclear absorption. At high energies (as in the LHC) the coherence length is large and the projectile interacts with the nucleus as a whole, implying a small nuclear absorption [42].

The $c\bar{c}$ state can also be destroyed by scattering on particles produced during the collision, usually called comovers. At short times, the density of comovers is proportional to the density of participants n_p and decreases with time like t^{-1} as a results of the longitudinal expansion. The survival probability at time t can be expressed as [41]:

$$S_{co}(b) \approx \exp[-\sigma_{\mathrm{co}} \overline{n}_p \log(t/t_0)], \tag{2.4}$$

with σ_{co} an effective cross section and $\overline{n}_p$ the average number of participants. The logarithmic factor accounts for the longitudinal dilution, and t_0 is a given initial time. Unlike nuclear absorption, which takes place at short times, the interaction with comovers continues until the system becomes too dilute.

2.5 From suppression to (re)generation

In a medium formed by the superposition of many nucleon-nucleon (N-N) collisions, such as a QGP, a c quark produced in a given N-N collision can in principle also bind with a $\bar{c}$ from another N-N collision. This can lead to an enhanced J/ψ production (figure 2.5), provided the overall charm density of the medium is sufficiently high, something that is largely favoured at the LHC: $N_{c\bar{c}}$(LHC) $\approx 10 \times N_{c\bar{c}}$(RHIC) per event in central Pb-Pb collisions. If regeneration takes places, then charmonium states can not be considered as a thermometer for the QGP. An important point is that regeneration can take place even if no QGP is created: J/ψ dissociated via CNM effects (comovers) can also recombine.

In the following, models that have a (re)generation component, and that will be later confronted to the experimental data, are described.

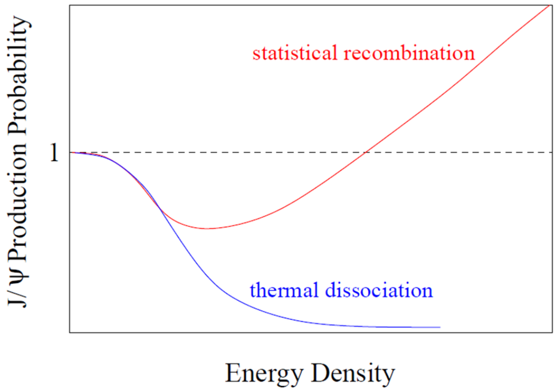

Figure 2.5: Sketch of J/ψ enhancement by recombination.

2.5.1 Statistical Hadronization Model

The Statistical Hadronization Model (SHM) assumes that the total number of charm quarks (N_c) stays constant until hadronization [43]. It also assumes thermal equilibration in the QGP, at least near the critical temperature T_c, and that hadronization of all heavy quarks takes place near the phase boundary, just before the hadron gas formation. The hadron formation from the bulk of heavy quarks is determined using weight functions from a thermal ensemble. Since the number of directly produced charm quarks deviates from the value determined by chemical equilibration, a charm enhancement factor g_c is introduced by the requirement of charm conservation.

The model has the following input parameters [44]:

- Characteristics at chemical freeze-out: temperature, baryochemical potential and volume corresponding to one unit of rapidity. These values are extracted from thermal fits of non-charmed hadrons.
- Charm production cross section in pp collisions: if no experimental results are available, the NLO pQCD calculations are considered. This value is used to calculate the number of directly produced $c\bar{c}$ pairs.

A direct indication of J/ψ generation was found by analyzing the rapidity dependence of the R_{AA} for J/ψ production in Au-Au collisions at $\sqrt{s_{\mathrm{NN}}} = 200$ GeV from PHENIX [45].

2.5.2 Transport Models

In order to extract information about the hot and dense medium created in ultrarelativistic heavy-ion collisions, the J/ψ production process must be treated dynamically. Since the J/ψ are, according to these models, unlikely fully thermalized with the medium, their phase space distribution is governed by a transport equation.

In the model from Zhao et al. ([46]), a rate equation including dissociation and formation components is obtained after integration over the spatial and momentum dependence of the Boltzmann equation. The charmonium binding energy is taken from lQCD results, ensuring a realistic hierarchy between ground and excited states. The initial conditions consist of $\mathrm{d}\sigma_{c\bar{c}}/\mathrm{d}y \approx 0.5$ mb at $y = 3.25$, no nuclear absorption and a shadowing that accounts for 30% of the suppression in the most central Pb-Pb events. The J/ψ from beauty hadrons is estimated as 10% and no b-quenching (suppression of beauty hadrons) is assumed. The evolving medium is modeled by an expanding thermal fireball constrained by hadro-chemestry, hadron yields and spectra. Finally, the quarkonium ground and excited states are evolved with their individual binding energies and reaction rates to account for feed down.

The quarkonium transport equation from Liu et al ([47]) includes, besides the dissociation and regeneration, a term that leads to the leakage effect[2]. The dissociation component includes two steps functions, one of them is controlled by the critical temperature of the deconfinement phase transition and implies that the dissociation happens only in the QGP phase. The second step function is characterized by a dissociation temperature T_d and indicates that any charmonium state cannot survive when $T > T_d$. Input values used are: $\mathrm{d}\sigma_{c\bar{c}}/\mathrm{d}y$ ≈ 0.38 mb at $y = 3.25$, $\sigma_{\mathrm{abs}} = 0$, EKS98 shadowing and the same b-hadron contribution scenario as in the previous model. The b-quenching is assumed to be constant (0.4) in all the p_{T} range.

2.5.3 Comovers plus recombination

Originally, the Comovers Interaction Model used the dissociation of J/ψ by hadronic comovers to explain the suppression observed at SPS. A couple of year later, it failed to describe the results from RHIC as at that moment it

---

[2] The charmonium suppression due to Debye screening is not an instantaneous process, but takes a certain time. During this time, high-p_{T} J/ψ may leak out of the colour deconfined region.

did not consider regeneration. However, the updated version [48] includes recombination to explain the data from the LHC and RHIC.

The comovers plus recombination (CpR) model considers a strong contribution from shadowing as the only initial state effect, does not assume thermal equilibrium of the matter created in the collision (no QGP formation) and a negligible component of nuclear absorption. The survival probability due to hadronic and partonic comovers interaction is similar to the one in equation 2.4, with $\sigma_{co} = 0.65$ mb obtained by fitting low-energy experimental data. The recombination is incorporated by adding a gain term proportional to the square density of open charm produced in the collision and it is considered to be larger at mid rapidity. A decrease of $R_{\rm AA}$ with increasing y may be compensated by the increase of $R_{\rm AA}$ due to a smaller density of comovers at $y \neq 0$, which induces less dissociation.

2.6 RHIC and SPS results on J/ψ in AA collisions

Charmonium production in high energy heavy-ion collisions at the SPS was extensively studied by three different experiments: NA38 [49], NA50 [50, 51] and NA60 [52], all of them performed their measurements in the dimuon decay channel. The reference that was used to quantify the amount of suppression is the Drell-Yan process ($q\bar{q} \rightarrow l^+ \, l^-$), that is expected to scale with the number of binary collisions and not to be affected by a deconfined medium. As an indicator of the centrality of the collision they adopted the length L of the path from the parton collision point through the nuclear matter.

A compilation of results from SPS is shown in figure 2.6, where the red line represents the expectations from the CNM effects. In central collisions (large L values), the NA50 results present a clear suppression (factor of 2), suggesting the creation of a deconfined medium.

At RHIC the PHENIX experiment has studied the J/ψ production both at midrapidity ($|y| < 0.35$) via $e^+ \, e^-$ decay and at forward rapidity ($|y| \in$ [1.2,2.2]) via $\mu^+ \, \mu^-$ decay in Au-Au collisions at $\sqrt{s_{NN}} = 200$ GeV [53]. These measurements were performed as a function of the centrality, rapidity and transverse momentum. An important aspect is that PHENIX found a larger suppression at forward rapidity with respect to mid rapidity (figure 2.7). However, PHENIX results have not been corrected by CNM effects.

This was the picture of the J/ψ in AA collisions before the heavy-ion program of the LHC began in autumn 2010.

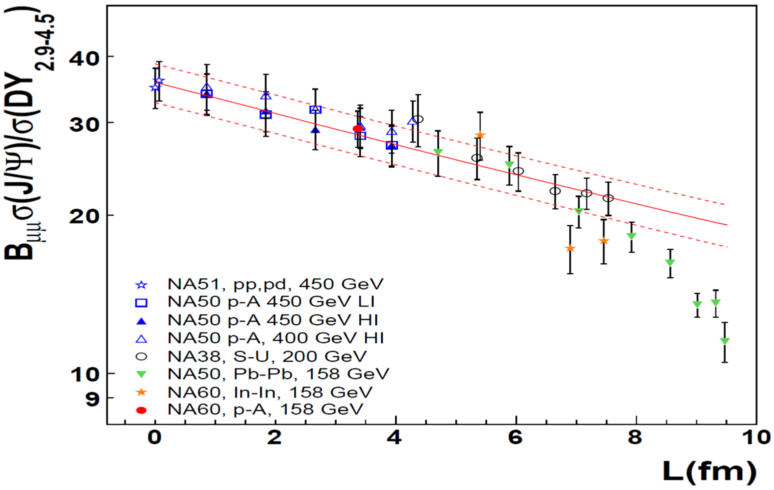

Figure 2.6: Summary of J/ψ over Drell-Yan production cross section as a function of the traversed nuclear matter at SPS [54].

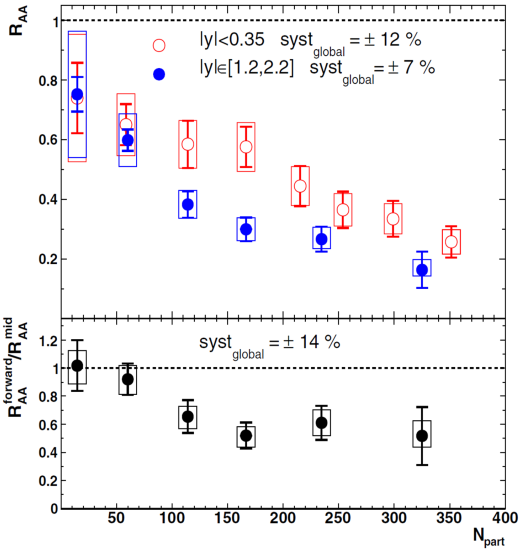

Figure 2.7: R_{AA} vs N_{part} at mid and forward rapidity obtained by the PHENIX experiment in Au-Au collisions at $\sqrt{s_{NN}}$ = 200 GeV.

2.7 ALICE results on J/ψ

In ALICE, heavy quarkonia are measured through their e^+ e^- and μ^+ μ^- decays at mid ($|y| < 0.9$) and forward ($2.5 < y < 4.0$) rapidity, respectively. A key feature of ALICE, making it unique at the LHC, is that it can measure quarkonia down to $p_T = 0$ GeV/c both at forward and mid rapidity.

The following section presents only the published ALICE results on inclusive[3] J/ψ production in pp ($\sqrt{s}$ = 7 and 2.76 TeV) and Pb-Pb ($\sqrt{s_{\mathrm{NN}}}$ = 2.76 TeV) collisions.

2.7.1 pp collisions

The measurement of quarkonium hadroproduction in the new energy domain of the LHC is crucial for a deeper understanding of the physics involved in these processes. Furthermore, low-p_{T} charmonium measurements, in particular at forward rapidity, are sensitive to an unexplored region ($x < 10^{-5}$ at $Q^2 = m^2_{\mathrm{J}/\psi}$) of the gluon distribution function of the proton.

On the left of figure 2.8 the p_{T} and y differential cross section $\mathrm{d}^2\sigma_{\mathrm{J}/\psi}/\mathrm{d}p_{\mathrm{T}}\mathrm{d}y$ at $\sqrt{s} = 7$ TeV is presented [55]. ALICE results are compared to other LHC experiments; notice that at central rapidity ALICE is complementary to ATLAS and CMS. At forward rapidity the comparison to LHCb contains the prompt and non-prompt production and integrated in the range $2.5 < y < 4.0$. Both experiments are in good agreement.

On the right side of figure 2.8, the $\mathrm{d}^2\sigma_{\mathrm{J}/\psi}/\mathrm{d}p_{\mathrm{T}}\mathrm{d}y$ at forward rapidity is shown, both for $\sqrt{s}$ = 7 and 2.76 TeV for the range $0 < p_{\mathrm{T}} < 8$ GeV/c [56]. The coloured bands correspond to the NRQCD predictions containing Color Singlet and Color Octet terms at NLO. The model describes very well the data for $3 < p_{\mathrm{T}} < 8$ GeV/c.

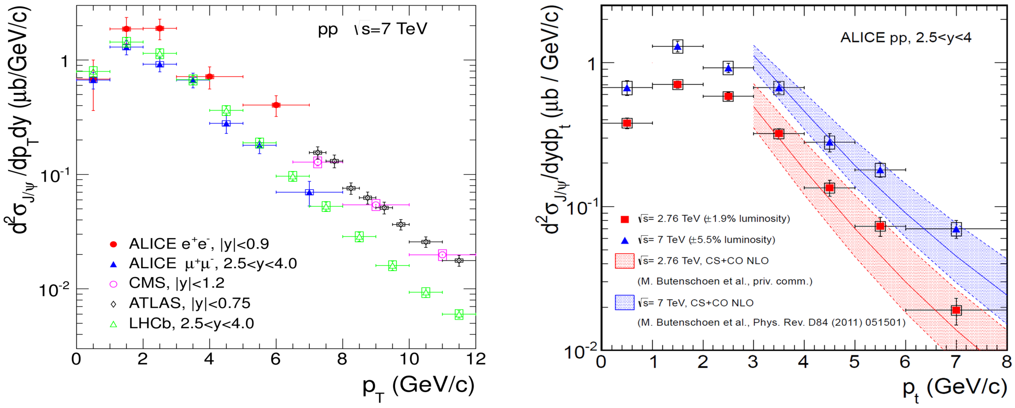

Figure 2.8: $\mathrm{d}^2\sigma_{\mathrm{J}/\psi}/\mathrm{d}p_{\mathrm{T}}\mathrm{d}y$ comparison for different LHC experiments at $\sqrt{s}$ = 7 TeV (*left*) and to NLO NRQCD calculations at $\sqrt{s}$ = 7 and 2.76 TeV (*right*).

---

[3] Except for UPC, where the exclusive photoproduction is measured.

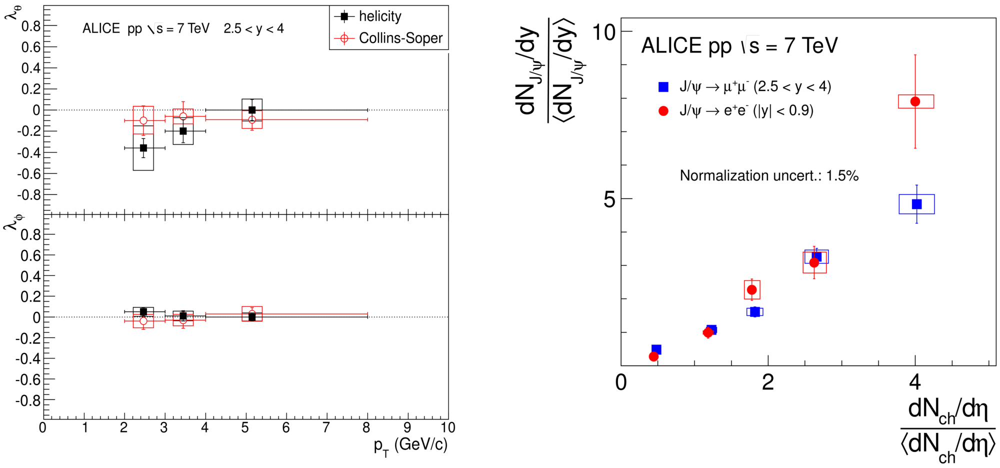

Figure 2.9: *Left*: λ_θ and λ_ϕ as a function of p_T in the HE and CS frames. *Right*: relative J/ψ yield as a function of the relative charged particle multiplicity density.

2.7.1.1 Polarization

Although various theoretical calculations have been able to reproduce the J/ψ p_T spectrum from the LHC experiments, the measurement of the polarization still represents a stringent test for the models as it can confirm or rule out the current QCD approach to charmonium production.

The results on λ_θ and λ_ϕ parameters, which quantify the degree of polarization, are shown on the left panel of figure 2.9 for the Collins-Soper (CS) and helicity (HE) frames [57]. In both frames the parameters are compatible with zero, with a possible hint of longitudinal polarization at low-p_T in the HE frame.

Comparison to LO and NLO predictions from NRQCD and CSM show that none of the models can perfectly describe the experimental results, however, NLO NRQCD is slightly favoured [58].

2.7.1.2 Yield vs event multiplicity

At the unprecedent energies reached at the LHC, pp collisions can have a substantial contribution from Multi Parton Interactions (MPI), which in turn could induce a correlation between the yield of quarkonia and the total charged particle multiplicity. ALICE has performed the first measurement of relative J/ψ production yields $(\mathrm{d}N_{J/\psi}/\mathrm{d}y)/\langle \mathrm{d}N_{J/\psi}/\mathrm{d}y\rangle$ as a function of the relative charged particle multiplicity density $(\mathrm{d}N_{\mathrm{Ch}}/\mathrm{d}\eta)/\langle \mathrm{d}N_{\mathrm{Ch}}/\mathrm{d}\eta\rangle$ as determined in $|y| < 1$ for pp collisions at $\sqrt{s} = 7$ TeV at the LHC.

The right panel of figure 2.9 shows that the relative J/ψ yield follows an approximately linear increase with $(\mathrm{d}N_{\mathrm{Ch}}/\mathrm{d}\eta)/\langle \mathrm{d}N_{\mathrm{Ch}}/\mathrm{d}\eta\rangle$, both at forward and mid rapidity [59]. A possible interpretation is that the J/ψ production is accompanied by a strong hadronic activity. Indeed, the resulting behaviour cannot be reproduced by a $2 \rightarrow 2$ hard partonic scattering scenario as predicted by PYTHIA 6.4.25 in the Perugia 2011 tune, where the J/ψ multiplicity exhibits a decrease with respect to the event multiplicity.

2.7.1.3 Prompt and non-prompt contribution

The inclusive J/ψ yield is composed of three contributions: prompt J/ψ produced directly in the collision, indirect prompt J/ψ (produced via the decay of excited charmonium states as ψ(2S) or χ_{c}) and non-prompt J/ψ from the decay of b-hadrons. The other LHC experiments have separated the prompt and non-prompt J/ψ components, but at mid rapidity ATLAS and CMS have only measured the high-p_{T} ($p_{\mathrm{T}} > 6.5$ GeV/c) part of the $\mathrm{d}\sigma_{\mathrm{J}/\psi}/\mathrm{d}p_{\mathrm{T}}$ distribution.

The measured fraction of non-prompt J/ψ (f_{B}) in $|y| < 0.9$ amounts, from 9% ($1.3 < p_{\mathrm{T}} < 3.0$ GeV/c), up to 31% ($7.0 < p_{\mathrm{T}} < 10.0$ GeV/c) [60]. By combining the measurements of the inclusive J/ψ cross section and the f_{B} value, the prompt J/ψ can be computed as: $\sigma_{\mathrm{prompt\ J}/\psi} = (1 - f_{\mathrm{B}}) \cdot \sigma_{\mathrm{J}/\psi}$.

On the left plot of figure 2.10 the resulting $\mathrm{d}^2\sigma_{\mathrm{prompt\ J}/\psi}/\mathrm{d}p_{\mathrm{T}}\mathrm{d}y$ is shown. ALICE complements ATLAS and CMS results by extending the p_{T} measurements down to $p_{\mathrm{T}} \approx 1$ GeV/c. The total cross section of J/ψ coming from b-hadron decays is extracted by extrapolating the cross section from the measured region down to p_{T} equal to zero using an implementation of pQCD calculations at fixed order with next-to leading-log resummation (FONLL). The right plot of figure 2.10 presents this measurement together with CMS and LHCb data; the experimental values are well described by the FONLL predictions.

2.7.2 Pb-Pb collisions

ALICE has measured the inclusive J/ψ production in Pb-Pb collisions at $\sqrt{s_{NN}} = 2.76$ TeV down to zero transverse momentum in the rapidity range $2.5 < y < 4$ [61]. The Nuclear Modification Factor results assume unpolarized J/ψ production in pp and Pb-Pb collisions.

The resulting R_{AA} vs N_{part}, compared to PHENIX results, is shown on the left panel of figure 2.11. The ALICE centrality integrated value is $R_{\mathrm{AA}}^{0-80\%} = 0.545 \pm 0.032 \pm 0.083$, indicating a clear J/$\psi$ suppression. The contribution from beauty hadron feed-down to the inclusive J/ψ yield in the measured y and p_{T} domain was measured by LHCb to be about 10% in pp collisions at $\sqrt{s} = 7$ TeV. Therefore, the difference between the prompt J/ψ R_{AA} and the present inclusive measurement is expected to not exceed 11% if N_{coll} scaling of

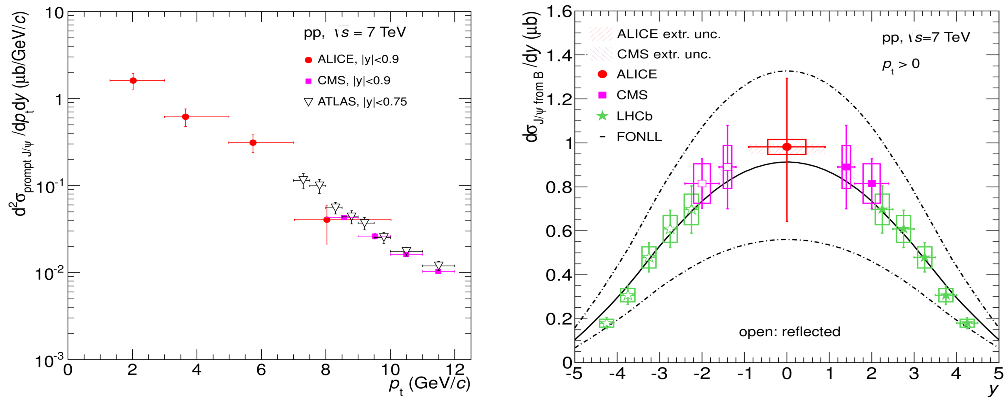

Figure 2.10: *Left*: double differential production cross section of prompt J/ψ as a function of p_T compared to ATLAS and CMS results at mid rapidity. *Right*: cross setion for non-prompt J/ψ production as a function of y compared to FONLL calculations.

beauty production is assumed and shadowing effects are neglected. The comparison to PHENIX measurements at forward rapidity indicate that R_{AA}^{ALICE} $\approx 3 \times R_{AA}^{PHENIX}$ for $N_{part} \gtrsim 180$. In addition, ALICE results do not exhibit a significant centrality dependence.

The right plot of figure 2.11 compares the ALICE results to the Transport and Statistical Hadronization Models, the latter prediction is given for two different values of $d\sigma_{c\bar{c}}/dy$ in absence of a measurement for Pb-Pb collisions. The transport models are shown as a band which connects the results obtained with (lower limit) and without (higher limit) shadowing. The three models can describe the data.

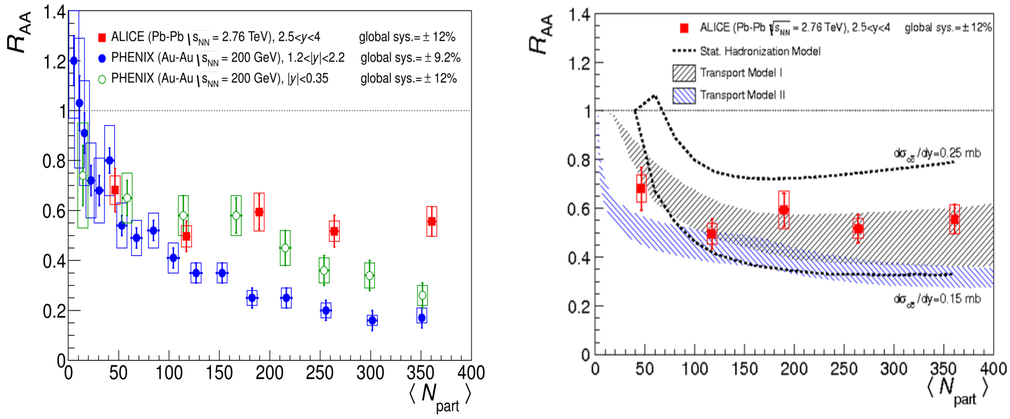

Figure 2.11: ALICE J/ψ R_{AA} from 2010 Pb-Pb collisions compared to PHENIX results (*left*) and theoretical models (*right*).

2.7.2.1 Ultraperipheral collisions

In two photon and photonuclear interactions in ultraperipheral heavy-ion collisions, the nuclei are separated by impact parameters larger than the sum of their radii, therefore hadronic interactions are strongly suppressed. On the other hand the cross section for photon induced reactions is large, as the intensity of the virtual photon flux grows as Z^2, where Z is the charge of the nucleus. The exclusive photoproduction can be coherent or incoherent, in the former the photon couples coherently to all nucleons, it is characterized by the production of low-p_T vector mesons and normally the target nucleus does not break up.

On the left side of figure 2.12 the peak at low-p_T is mainly due to coherent interactions, while the tail extending out to 0.8 GeV/c comes from incoherent production [62]. However, it is important to stress that this high-p_T region may still contain some hadronic interactions, making it difficult to extract the incoherent photoproduction cross section from these data. The right plot of figure 2.12 is the differential cross section of J/ψ photoproduction compared to theoretical models. The differences among models are mainly due to the treatment on photonuclear interaction. The best agreement is found with models where the cross section is proportional to the nuclear gluon distribution squared (RSZ-LTA, AB-EPS09 and AB-EPS08).

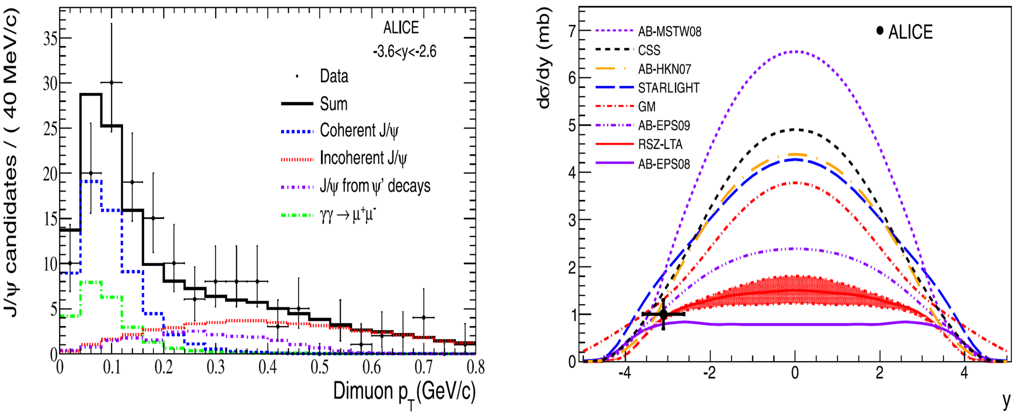

Figure 2.12: *Left*: Dimuon p_T distribution from ultraperipheral collisions. *Right*: Coherent differential cross section of J/ψ photoproduction compared to theoretical models.

Chapter 3

The LHC and the ALICE experiment

This chapter will begin with the description of the experimental apparatus used to study the Quark Gluon Plasma in ALICE. For this reason, it will first summarize the most important characteristics of the LHC and its experiments. Right after this the chapter focus on ALICE, providing a complete description of its detectors and trigger system. Only the Muon Spectrometer and its upgrades are not detailed here as they are the main subject of the next chapter.

3.1 The Large Hadron Collider

The LHC [4] is the largest and most powerful particle accelerator of the world. It is located in a tunnel used by the Large Electron Positron (LEP) collider under the French-Swiss border at a depth of 50 to 175 meters. The LHC has a circumference of 27 kilometers and it was conceived to collide protons and lead ions at a maximum energy of $\sqrt{s} = 14$ TeV and $\sqrt{s_{NN}} = 5.5$ TeV, respectively. The origins of this particle accelerator can be traced back to the mid-eighties, but it was not until 1994 that the project was approved by the CERN Council and its construction started in 2001 after dismantling the LEP.

Finally, the 10th of September 2008 the first proton beam circulated around the entire ring. Unfortunately, a couple of days later an electrical fault ocurred, damaging two dipoles [63]. This incident delayed the LHC operations for more than one year.

Once again, the 20th of November 2009, pilot bunches (a single bunch per beam) circulated in the LHC and three days later the first collisions at $\sqrt{s} = 900$ GeV took place, leading ALICE to provide the first publication of the LHC [64].

Table 3.1: Some LHC nominal proton and lead beam parameters (third and fourth columns). The last column are the actual values used in proton beams.

	Units	Proton	Lead	June 2012
Number of magnets		9593		
Number of dipoles		1232		
Number of quadrupoles		392		
Beam energy	TeV	7	2.76/n	4
Bunches per beam		2808	592	1380
Protons/ions per bunch		1.15x10^{11}	7x10^{7}	1.48x10^{11}
Bunch separation	ns	25	100	50
Luminosity	cm^{-2}s^{-1}	10^{34}	10^{27}	6.8x10^{33}
Beam size at IP[1]	μm	16.7	15.9	19
Beam current	A	0.582	6.12x10^{-3}	0.369

3.1.1 Overview

The LHC is a synchrotron type accelerator that collides two counter-rotating beams in four interaction points along its circumference. It relies on NbTi superconducting magnets cooled by superfluid helium at temperatures below 2 °K, allowing to reach a magnetic field of 8.3 T. Four radio-frequency systems are used to capture, accelerate and store the injected beams.

Besides the collision energy, another key feature of the LHC is the luminosity, defined as:

$$\mathcal{L} = fnN^2/A,$$

with f the revolution frequency, n the number of bunches in both beams, N the number of particles per bunch, A the cross sectional area of the beams and it is usually expressed in cm^{-2}s^{-1}. The number of events per unit of time can be written in terms of the luminosity and the event cross section (σ_{events}) as:

$$N_{\text{event}} = \mathcal{L}\sigma_{\text{event}}.$$

Table 3.1 contains some LHC nominal protons/lead beam parameters and a comparison to the current (June 2012) ones for protons [65, 66]. As can be seen, in some cases (beam size at IP and luminosity) the LHC has already reached its designed performance and in particular for the number of protons per bunch it has surpassed its expectations.

---

[1] IP stands for Interaction Point.

The four interaction points allow the implementation of four main experiments plus two smaller ones:

- A Large Ion Collider Experiment (ALICE): it will be fully detailed in the next section.
- A Toroidal LHC ApparatuS (ATLAS) [67]: its main goal is the discovery/exclusion of the Higgs Boson, supersymmetric particles and extradimensions. It also takes part in the heavy-ion programme.
- Compact Muon Solenoid (CMS) [68]: has exactly the same physics objectives, both in pp and Pb-Pb as ATLAS.
- Large Hadron Collider beauty experiment (LHCb) [69]: a b-physics experiment, it focuses on precise measurements of CP-symmetry violation processes. It does (does not) participate in the data taking of p-Pb (heavy-ion) collisions.
- Large Hadron Collider forward experiment (LHCf) [70]: located closed to the ATLAS experiment, it is designed to study the forward production of neutral particles in pp collisions in order to provide a better understanding of the hadron interaction models used in cosmic ray physics.
- TOTal Elastic and diffractive cross section Measurement (TOTEM) [71]: placed near the CMS facility, aims to measure the total pp cross section, elastic scattering and diffractive processes.

3.1.2 The injection chain

The reason whereby the LHC has such an outstanding performance is, in part, because it profits from an existing complex of accelerators at CERN (figure 3.1). These smaller accelerators work as pre-injectors to the LHC increasing at each step the beam energy.

In the case of the protons the journey is [72]:

1. Source and Radio Frequency Quadrupole (RFQ): protons are produced in a Duoplasmatron by ionisation of hydrogen gas, then the RFQ accelerates the beam to 750 KeV.
2. Linear accelerator (Linac) 2: is an Alvarez type Linac of 30 meters length that accelerates the beam up to 50 MeV.

3. Proton Synchrotron (PS) Booster: synchrotron accelerator with 4 vertically stacked rings, multi-turn injection of Linac beam defines the LHC emittance [2]. It accelerates the beam from 50 MeV to 1.4 GeV.
4. PS: in this step the 25 ns bunch train for the LHC is created. The acceleration is from 1.4 to 25 GeV.
5. Super PS (SPS): this accelerator is similar in size to the Tevatron, but it uses warm magnets, boosting the beam to 450 GeV.

For ions, the path is a little bit different [73]:

1. Electron Cyclotron Resonance (ECR) and RFQ: ^{208}Pb is heated until evaporation inside the ECR chamber filled by a magnetic field. It then ionises the lead vapour until it becomes Pb^{27+} and at this moment the ions are extracted by the RFQ.
2. Linac3: the beam is accelerated up to 4.2 MeV/n and the Pb^{27+} ions are stripped by a carbon foil to become Pb^{54+}.
3. Low Energy Ion Ring (LEIR): its role is to transform the long, low-intensity ion pulses from Linac3 into short bunches using multi-turn injection and accumulation. The output energy of this accelerator is 72.2 MeV/n.
4. PS: it is at this step that the Pb^{54+} ions are fully stripped to Pb^{82+} by an aluminium foil. Once the nominal bunch spacing is reached (100 ns) the beam is extracted to the next accelerator at an energy of 5.9 GeV/n.
5. SPS: the beam is accelerated up to 177 GeV/n and then finally injected into the LHC.

3.1.3 Upgrades

As any other machine, after some years of operations, the LHC will have to be upgraded. For this reason an improvement on the LHC performance, known as High Luminosity LHC [74], will take place after the long shutdown 3 (planned on 2022). The aim is to increase the designed luminosity by a factor of 5-10 times in order to provide 300 fb^{-1}/year during 10-12 years. This has two main purposes: to perform more accurate measurements on the new particles discovered at the LHC and to observe rare processes that occur at rates below the current sensitivity. Among the technological challenges, preliminary studies foresee 12 T superconducting magnets and high radiation-resistant electronics.

---

[2] In a particle accelerator the emittance is a measurement of the spread of the particles in the beam (in position or momentum phase space). The beam size is proportional to the square-root of the emittance.

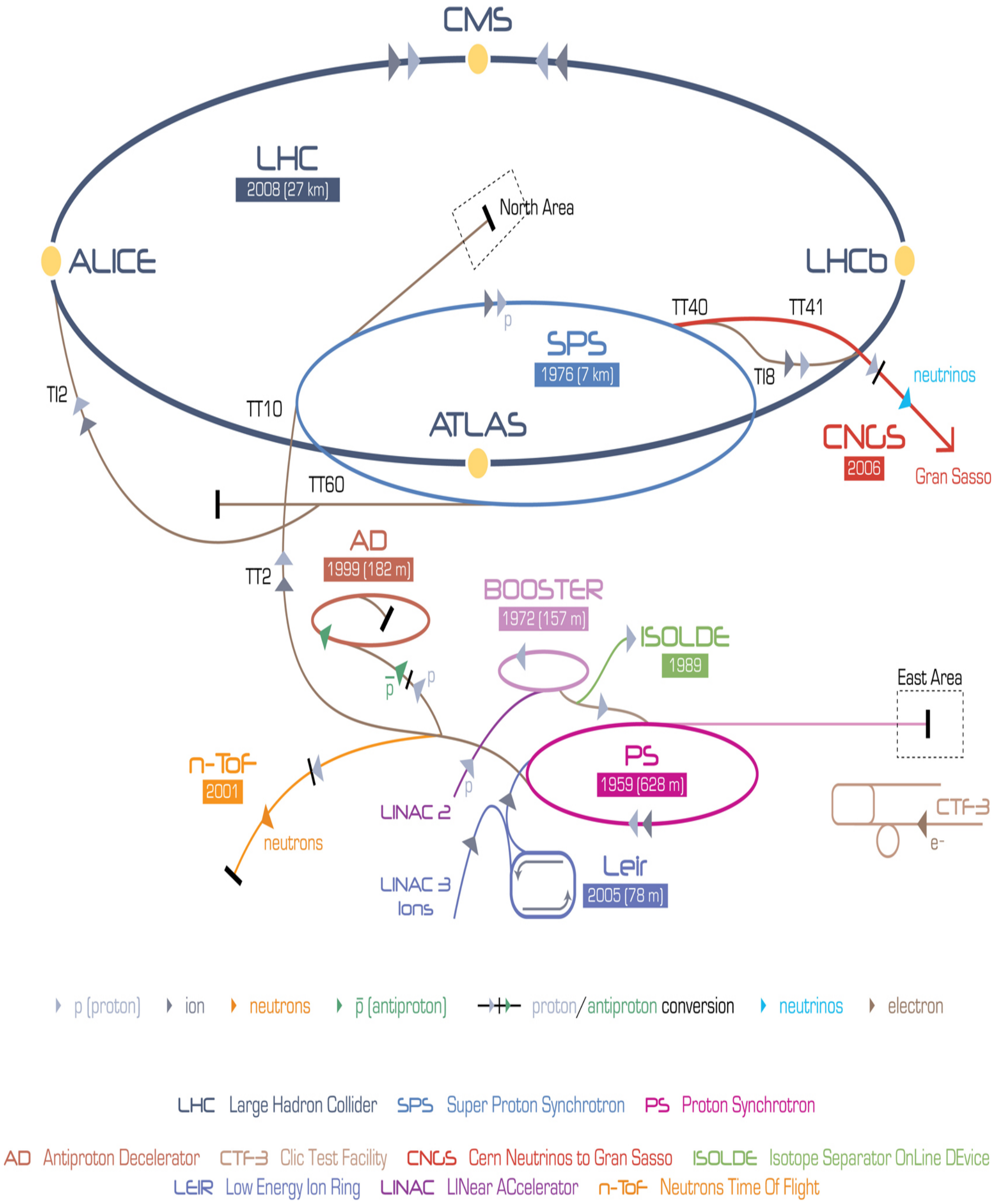

Figure 3.1: The LHC and its preinjectors in CERN's accelerator complex.

3.2 A Large Ion Collider Experiment

Among all the LHC experiments, ALICE [18] is the only one that was designed and built to focus on the study of high energy heavy-ion collisions. Its goal is to characterize the physics of the Quark Gluon Plasma, but its programme also includes proton-proton, proton-nucleus and lighter ions collisions. For this purpose, it has been equipped with 14 detectors in an overall dimension of 16 x 16 x 26 m^3 with a total weight of approximately 10 000 tons (figure 3.2).

As the single dedicated heavy-ion experiment at the LHC, ALICE will cover a wide range of physics observables [75, 76]: global event characteristics, heavy flavour production and jet fragmentation, elliptic flow, quarkonia production, resonance, particle interferometry, etc. Another unique feature of ALICE is that it employs almost all known Particle IDentification (PID) techniques: energy loss ($\mathrm{d}E/\mathrm{dx}$), time of flight, transition and Cherenkov radiation, electromagnetic calorimetry, muon filters and topological decay reconstruction.

The detectors of the ALICE experiment can be divided in three groups:

- Central barrel: detectors contained here cover the polar angle from 45° to 135° and they are embedded in a solenoid magnet originally used in the L3 experiment at LEP. From the inside out the barrel contains the Inner Tracking System (ITS), the Time Projection Chamber (TPC), the Time Of Flight (TOF), the Transition RaDiation (TRD), the High Momentum Particle IDentification (HMPID), the PHOton Spectrometer (PHOS) and the ElectroMagnetic Calorimeter (EMCal). All of them (except HMPID, PHOS and EMCal) cover the full azimuthal angle. Finally the ALICE COsmic Ray DEtector (ACORDE) is located on top of the L3 magnet.

- Forward detectors: a group of smaller detectors located at small angles for global event characterization and triggering: Zero Degrees Calorimeter (ZDC), Photon Multiplicity Detector (PMD), Forward Multiplicity Detector (FMD), V0 and T0.

- Muon spectrometer: it will be extensively described in the next chapter.

Table 3.2 summarizes some geometrical parameters of the central barrel and forward detectors of the ALICE experiment [77].

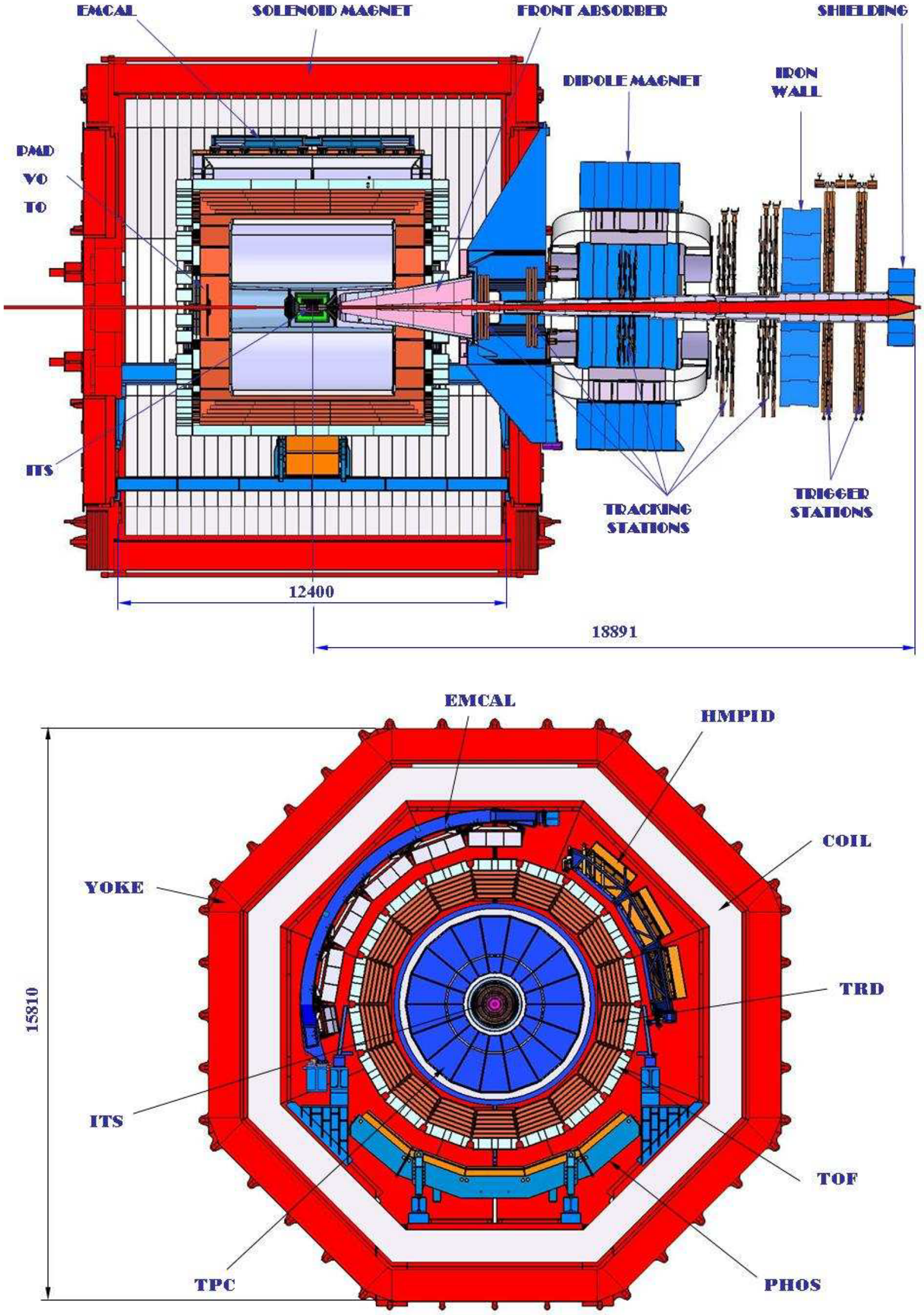

Figure 3.2: 2D ALICE cut views along the yz (upper panel) and the xy (lower panel) directions. The coordinate system is defined as follows: the positive x-axis perpendicular to the beam pipe and pointing to the center of the LHC; the positive y-axis perpendicular to the ground and pointing upward; the positive z-axis is located along the beam pipe and opposite to the Muon Spectrometer.

Table 3.2: A summary of the ALICE detectors. The first column is the name of the detector or subdetector; the second one is the acceptance computed from the nominal interaction point, those without explicit ϕ value cover the full azimuthal angle. The third column indicates the inner and outer radius distance relative to the nominal interaction point for those detectors located in the central barrel, while for the remaining ones it indicates the position along the z axis. The fourth column provides the total area covered by the active detector elements. Finally, the last column is the number of independent electronic readout channels.

Detector	Acceptance (η, ϕ)	Position (m)	Dimension (m^2)	Channels
ITS layer 1,2 (SPD)	$\pm2, \pm1.4$	0.039, 0.076	0.21	9.8 M
ITS layer 3,4 (SDD)	$\pm0.9, \pm0.9$	0.150, 0.239	1.31	133 000
ITS layer 5,6 (SSD)	$\pm0.97, \pm0.97$	0.380, 0.430	5.0	2.6 M
TPC	±0.9 at r=2.8 m	0.848, 2.466	readout 32.5 m^2	557 568
	±1.5 at r=1.4 m		Vol. 90 m^3	
TRD	±0.84	2.90, 3.68	716	1.2 M
TOF	±0.9	3.78	141	157 248
HMPID	±0.6, $1.2° < \phi < 58.8°$	5.0	11	161 280
PHOS	±0.12, $220° < \phi < 320°$	4.6	8.6	17 920
EMCal	±0.7, $80° < \phi < 187°$	4.36	44	12 672
ACORDE	±1.3, $-60° < \phi < 60°$	8.5	43	120
ZDC:ZN	$\lvert\eta\rvert < 8.8$	±116	2×0.0049	10
ZDC:ZP	$6.5 < \lvert\eta\rvert < 7.5$	±116	2×0.027	10
	$-9.7° < \phi < 9.7°$			
ZDC:ZEM	$4.8 < \eta < 5.7$,	7.25	2×0.0049	2
	$-16° < \phi < 16°$ and			
	$164° < \phi < 196°$			
PMD	$2.3 < \eta < 3.7$	3.64	2.59	2 221 184
FMD disc 1	$3.62 < \eta < 5.03$	inner: 3.2	0.266	51 200
FMD disc 2	$1.7 < \eta < 3.68$	inner: 0.834		
		outer: 0.752		
FMD disc 3	$-3.4 < \eta < -1.7$	inner:−0.628		
		outer:−0752		
V0A	$2.8 < \eta < 5.1$	3.4	0.548	32
V0C	$-1.7 < \eta < -3.7$	−0.897	0.315	32
T0A	$4.61 < \eta < 4.92$	3.75	0.0038	12
T0C	$-3.28 < \eta < -2.97$	−0.727	0.0038	12

3.2.1 Inner Tracking System

The main tasks of the ITS [78] are to localize the primary vertex with a resolution better than 100 μm, to reconstruct the secondary vertices from the decays of hyperons and D and B mesons, to track and identify particles with momentum below 200 MeV/c, to improve the momentum and angle resolution for particles reconstructed by the TPC and to reconstruct particles traversing dead regions of the TPC.

The ITS consists of six cylindrical layers of silicon detectors (figure 3.3). The number, position and segmentation of the layers were optimized for efficient track finding and high impact-parameter resolution. In particular, the outer radius is determined by the necessity to match tracks with those from the TPC and the inner radius is the minimum allowed by the beam pipe. The first layer has a more extended pseudo-rapidity acceptance to provide, together with the FMD, continuous coverage for the measurement of charged particles multiplicity.

Because of the high particle density in heavy-ion collisions at the LHC and in order to achieve the required impact parameter resolution, Silicon Pixel Detectors (SPD) have been chosen for the innermost two layers, and Silicon Drift Detectors (SDD) for the following two layers. The two outer layers, where the track density is smaller, are equipped with double-sided Silicon micro-Strip Detectors (SSD). The four outer layers have analogue readout and therefore can be used for particle identification via dE/dx measurement in the non-relativistic ($1/\beta^2$) region. The analogue readout has a dynamic range large enough to provide the dE/dx measurement for low-momentum, highly ionising particles, down to the lowest momentum at which tracks can still be reconstructed. This feature gives the ITS stand-alone capability as a low-p_T particle spectrometer (left plot of figure 3.5).

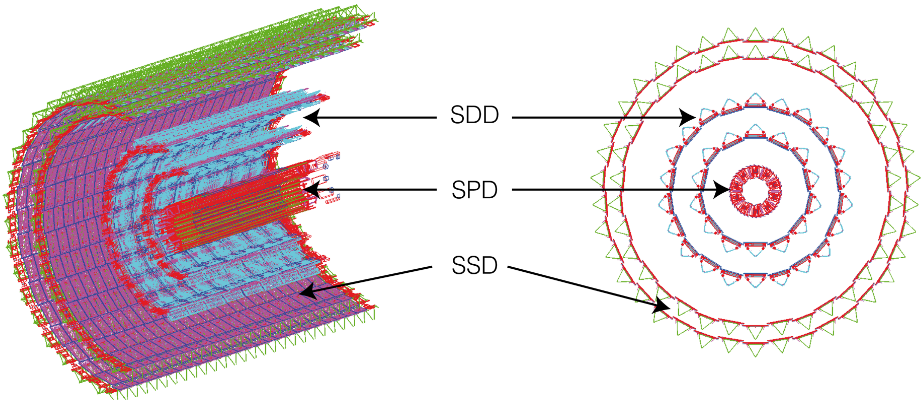

Figure 3.3: The six layers that compose the ITS.

3.2.2 Time Projection Chamber

The TPC [79] is made of a large cylindrical field cage, filled with 90 m^3 of Ne/CO$_2$/N$_2$ (90/10/5). When a charged particle traverses the TPC it ionizes the gas mixture, these electrons are then transported over a distance of up to 2.5 m on either side of the central electrode to the end plates. Multi-wire proportional chambers with cathode pad readout are mounted into 18 trapezoidal sectors at each end plate (figure 3.4). The field cage contains a central high-voltage (100 kV) electrode and two opposite axial potential dividers which create a highly uniform electrostatic field, resulting in a maximum drift time of about 90 μs.

It is the main tracking detector of the central barrel and is optimised to provide, together with the other central barrel detectors, charged-particle momentum measurements with good two-track separation, particle identification, and vertex determination (right plot of figure 3.5). It covers a broad p_{T} range: from 0.1 up to 100 GeV/c.

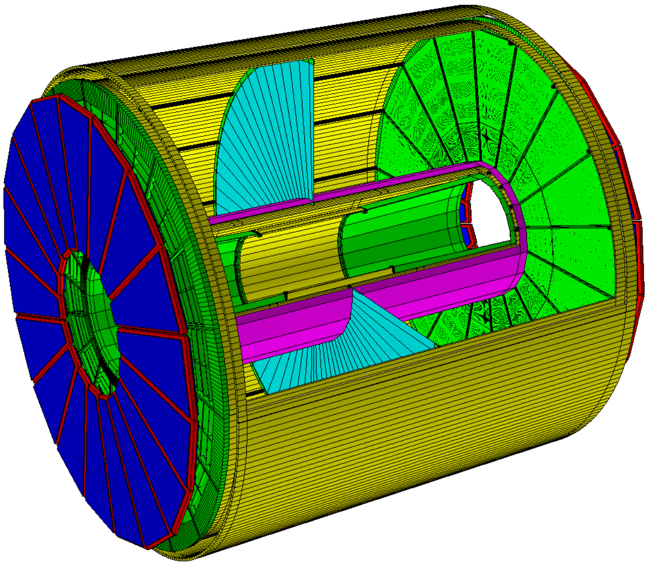

Figure 3.4: Internal and external view of the TPC, the high-voltage electrode is located at the middle (light blue). The end plates with the readout chambers are also visible (green and blue).

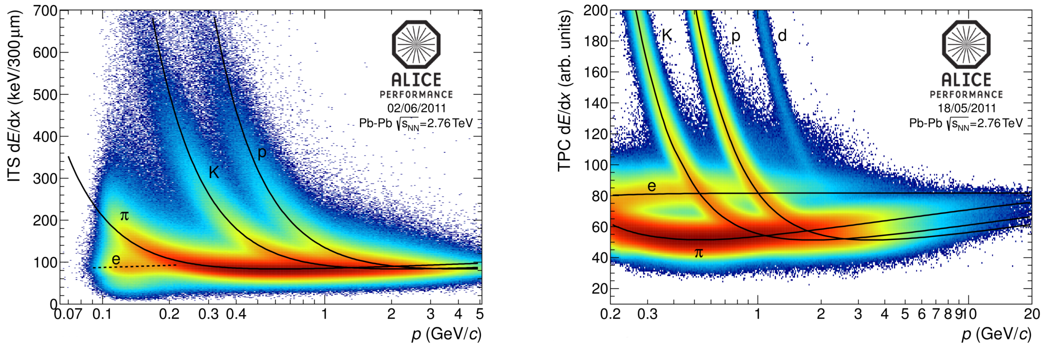

Figure 3.5: Stand-alone PID performance vs p for ITS (*left*) and TPC (*right*) in Pb-Pb collisions.

3.2.3 Transition Radiation Detector

The TRD [80] working principle relies on photon radiation by charged particles crossing two media with different dielectric constants. The photon is emitted in the soft X-ray region (figure 3.6). This radiation is strongly dependent on the relativistic γ factor: for $1 \leq p \leq 100$ GeV/c only electrons produce the transition radiation. However, the probability to emit such radiation is too low, for this reason many layers are used.

This detector also provides electron identification in the central barrel for momenta above 1 GeV/c (left panel of figure 3.8). Below this momentum electrons can be identified via specific energy loss measurement in the TPC. Above 1 GeV/c transition radiation from electrons passing a radiator can be used together with the specific energy loss in a suitable gas mixture to obtain the necessary pion rejection capability. In conjunction with data from the ITS and the TPC it is possible to study the production of light and heavy vector-meson resonances and the dilepton continuum both in pp as well as in Pb-Pb collisions. Exploiting the excellent impact parameter resolution of the ITS it is furthermore possible to reconstruct open charm and open beauty in semi-leptonic decays.

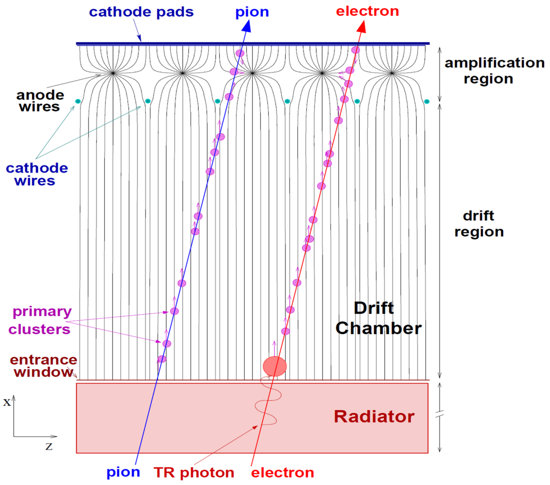

Figure 3.6: TRD working principle

3.2.4 Time-Of-Flight

The working principle of the TOF [81, 82] relies on the Multi-gap Resistive-Plate Chamber (MRPC), where a high and uniform electric field is applied over the full sensitive gaseous volume of the detector. Any ionisation produced by a traversing charged particle immediately starts a gas avalanche process which generates the observed signals on the pick-up electrodes (figure 3.7).

The TOF detector provides PID in the intermediate momentum range, below about 2.5 GeV/c for pions and kaons, up to 4 GeV/c for protons, with a π/K and K/p separation better than 3 σ (right panel of figure 3.8). Coupled with the ITS and TPC for track and vertex reconstruction and for dE/dx measurements in the low-momentum range (up to about 1 GeV/c), it provides an event-by-event identification of large samples of pions, kaons and protons. At the inclusive level it allows invariant mass studies, in particular the detection of open heavy-flavoured states and vector meson resonances.

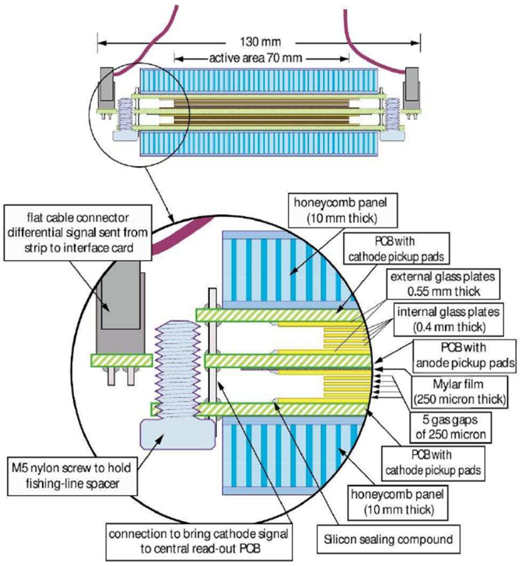

Figure 3.7: Transversal view of a TOF module, a zoom-in is made to provide an insight into the MRPC.

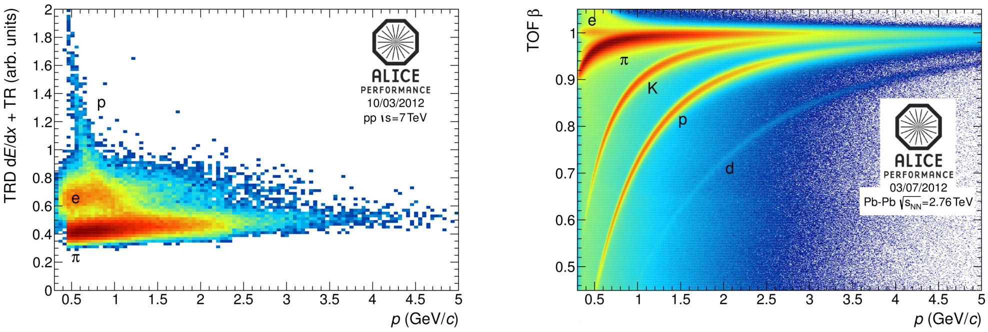

Figure 3.8: *Left:* TRD truncated mean signal vs p in pp collisions (a TPC dE/dx selection has been previously applied). *Right:* β vs p measured by the TOF in Pb-Pb[3].

---

[3] $\beta = \lambda/(t_{\mathrm{TOF}} - t_0)$ where λ is the path length travelled by the particle and t_0 the time at the interaction point.

3.2.5 High-Momentum Particle Identification Detector

The HMPID [83] is dedicated to inclusive measurements of identified hadrons at $p_{\mathrm{T}} > 1$ GeV/c. It enhances the PID capability of ALICE by enabling identification of charged hadrons beyond the momentum interval attainable through energy-loss (in ITS and TPC) and time-of-flight measurements (in TOF). The detector extends the useful range for π/K and K/p discrimination, on a track-by-track basis, up to 3 and 5 GeV/c, respectively (right panel of figure 3.9). The geometry of the detector was optimized with respect to the particle yields in pp and heavy-ion collisions at LHC energies, and with respect to the large opening angle required for two-particle correlation measurements. In addition, the identification of light nuclei and anti-nuclei (d, t, ^{3}He, α) at high-p_{T} in the central rapidity region can also be performed with this detector.

The HMPID is based on proximity-focusing Ring Imaging Cherenkov (RICH): fast charged particles traversing the detector emit Cherenkov radiation that is collected by a CsI photon counter located in the pad cathode of a Multi-Wire Pad Chamber (MWPC).

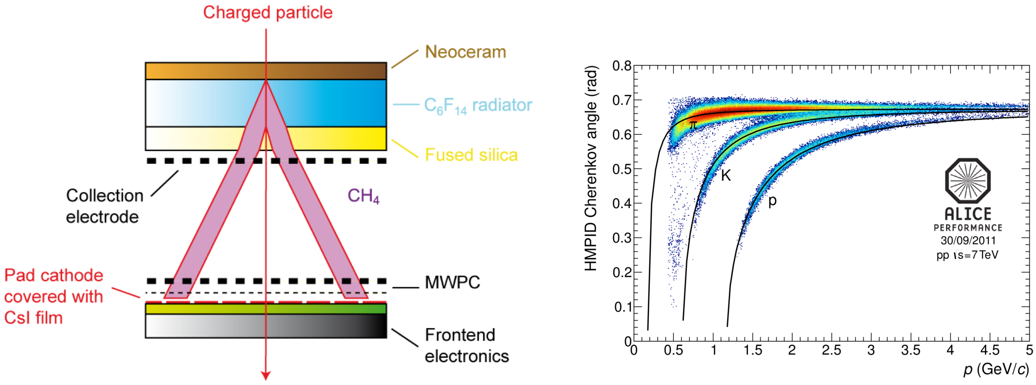

Figure 3.9: *Left:* Transversal view and working principle of the HMPID. *Right:* PID performance of the detector in pp collisions.

3.2.6 PHOton Spectrometer

The main physics objectives of this electromagnetic spectrometer are the study of thermal and dynamical properties of the initial phase of the collision extracted from low p_{T} direct photon measurements and the study of jet quenching through the measurement of high-p_{T} π^0 and γ-jet correlations [84].

Photon identification requires high discrimination power against charged hadrons, neutrons and anti-neutrons. Topological analysis of the shower development in the electromagnetic calorimeter, time of flight measurement and charged particle identification provide the discriminating criteria. The required performance is met through a high granularity electromagnetic calorimeter made out of lead-tungstate ($PbWO_4$), a timing resolution of the individual detector cells of the order of a few ns and a charged particle detector in front of the calorimeter.

The Charged-Particle Veto (CPV) detector is a Multi-Wire Proportional Chamber (MWPC) with cathode-pad readout. Its charged-particle detection efficiency is better than 99%. The CPV is placed on top of the PHOS modules at a distance of about 5 mm and the active volume is filled with a gas mixture 80% Ar/20% CO_2.

3.2.7 ElectroMagnetic CALorimeter

The EMCal [85] enables ALICE to explore the physics of jet quenching over the large kinematical range accessible in heavy-ion collisions at the LHC. The EMCal is a large lead-scintillator calorimeter adjacent to the ALICE magnet coil and approximately opposite in azimuth to the PHOS. It also provides a fast and efficient trigger for hard jets, photons and electrons. The EMCal also measures the neutral energy component of jets, enabling full jet reconstruction in all collision systems. The combination of the EMCal, the excellent ALICE charged particle tracking capabilities, and the modest ALICE magnetic-field strength, is a preferred configuration for jet reconstruction in the high-background environment of heavy-ion collisions. This allows the optimization of background rejection while preserving the crucial jet-quenching signals at moderate transverse momentum.

3.2.8 ALICE COsmic Ray DEtector

ACORDE is an array of plastic scintillator counters placed on the upper surface of the L3 magnet, it plays a two-fold role:

1. Provide a fast trigger signal, for the commissioning, calibration and alignment procedures of some of the tracking detectors.
2. Detect, in combination with the TPC, TRD and TOF, single atmospheric muons, thus allowing to study high-energy cosmic rays.

3.2.9 Zero Degree Calorimeter

The ZDC [86] measures the energy carried in the forward direction by non-interacting nucleons in order to extract the number of participant nucleons in the Pb-Pb collisions. It also provides an estimate of the reaction plane of the nuclear collisions.

Two sets of hadronic ZDC are located at 116 m on either side of the Interaction Point (IP) and two electromagnetic calorimeters (ZEM) are placed at 7 m from the IP, on both sides of the LHC beam pipe along the positive z axis.

There are two distinct ZDC detectors: one for spectator neutrons (ZN) located between the beam pipes at $0°$ relative to the z axis and another one for spectator protons (ZP) placed externally to the outgoing beam pipe on the side where positive particles are deflected. Both are installed on lifting platforms in order to lower them out of the horizontal beam plane, where the radiation levels are the highest, when they are not in use.

The hadronic ZDCs are quartz fibres sampling calorimeters; the shower generated by incident particles in a dense absorber (passive material) produces Cherenkov radiation in quartz fibres (active material) distributed in the absorber.

The ZEM measure the energy of particles emitted at forward rapidity (mainly photons generated from π^0 decays). This increases monotonically with the collision centrality and is used to discriminate between central and peripheral collisions. The detection technique is similar to the one used for the hadronic calorimeters.

3.2.10 Photon Multiplicity Detector

The PMD [87] measures the multiplicity and spatial distribution of photons in order to estimate the transverse electromagnetic energy and the reaction plane. This provides information in terms of limiting fragmentation, order of phase transition, the equation of state of matter and the formation of disoriented chiral condensates.

Due to the large particle density in the forward region, calorimetric techniques for photon measurements are not feasible. The PMD uses the preshower method where a thick converter is sandwiched between two planes of highly granular gas proportional counters. The granularity and the converter thickness are optimized for high particle density so that the overlap of photon showers is minimal. The information from the detector plane placed in front of the converter is used as a CPV and the preshower data from the second detector plane is used for photon identification.

3.2.11 Forward Multiplicity Detector

The FMD measures the charged-particle multiplicity at forward pseudo-rapidity [88]. The overlap between the FMD silicon rings and the ITS inner pixel layer provides redundancy and cross-checks of measurements between subdetectors and ensures continuous coverage for a distribution of vertices along the z axis.

Additionally, high radial detector segmentation allows for the study of multiplicity fluctuations on an event-by-event basis while azimuthal segmentation allows for the determination of the reaction plane for each event and the analysis of flow within the FMD's pseudo-rapidity coverage.

The FMD is subdivided in FMD1, FMD2 and FMD3. The last two consist of both an inner and an outer ring of silicon sensors and are located on either side of the ITS detector. They are positioned to have approximately the same acceptance, however, the presence of the T0 detector required a different placement for the FMD3 inner ring. The FMD1 was placed further from the interaction point opposite to the muon spectrometer to extend the charged particle multiplicity coverage. The upper limit on this additional coverage is constrained by the increasing number of secondary particle contributions at very forward rapidity.

3.2.12 V0

The V0 (Vertex 0) is a small angle detector consisting of two arrays of scintillator counters, called V0A and V0C, which are installed on either side of the IP, it provides the minimum-bias trigger and luminosity measurements [88].

As the dependence between the number of registered particles on the V0 arrays and the number of primary emitted particles is monotone, the V0 also serves as an indicator of the centrality of the collision via the multiplicity measured.

3.2.13 T0

The T0 (Time 0) consists of two arrays of Cherenkov counters, 12 counters per array. Each Cherenkov counter is based on a photomultiplier tube that is in turn optically coupled to a quartz [88].

The detector generates a start time for the TOF detector, this timing signal (with a precision of about 50 ps) corresponds to the real time of the collision (plus a fixed time delay) and is independent of the position of the vertex. It also measures the vertex position and discriminates against beam-gas interactions providing redundancy to the V0 minimum bias and multiplicity triggers.

3.2.14 Central Trigger Processor (CTP)

The CTP is a hardware trigger responsible of the correct selection of physically interesting events that are not commonly produced [89].

In order to accept/reject an event as fast as possible, detectors with similar trigger latencies[4] are grouped together in trigger levels:

- L0: arrives at the CTP within 800 ns of the interaction and is delivered to the detectors 1.2 μs after the collision. The CTP can handle up to 24 L0 trigger inputs and takes a decision in 100 ns, the remaining latency is due to the generation time of the trigger input itself and by the cable delays.
- L1: it is sent to the detectors 6.5 μs after the collision, in fact, this is a second stage of the fast level trigger that ALICE has split in two.
- L2: reaches the detectors after 100 μs, a value constrained by the TPC drift time.

Following the same idea of the trigger levels, detectors with similar read out times are grouped into clusters. These, together with the trigger conditions define a trigger class. A single event can generate more than one trigger class.

Finally, another important feature of the CTP is the past-future protection, a specific time window centred in a given event to protect against pile-up. As different detectors are busy for different periods after triggering, the past-future protection vetoes the event once a critical number of events occur in the past-future window.

3.2.15 High-Level Trigger (HLT)

This is a software trigger that processes the data in parallel allowing an online analysis of the events [89]. The HLT reduces the stored data volume by selecting regions of interest and by applying compression algorithms on the accepted and selected data. It is also divided in layers: the first one is in charge of receiving the raw data of all ALICE detectors; the second layer performs basic detector calibrations; the third one reconstructs the event in a detector per detector basis; the forth layer performs the global reconstruction of the event by combining the processed and calibrated information of all detectors; finally the fifth layer selects the events or regions of interest.

3.2.16 Upgrades

After the long shut down 2, scheduled for 2018, the LHC will reach an interaction rate of about 50 kHz in Pb-Pb collisions. With such big instantaneous luminosity (L = 6 x 10^{27} cm^{-2}s^{-1}) ALICE aims to register 10 nb^{-1} of Pb-Pb

---

[4] The time between the collision and when the piece of information is delivered to the trigger system.

collisions. It is then mandatory to improve the previous described detectors to fully exploit the scientific potential from the LHC and its upgrades [90].

3.2.16.1 Beam pipe

In order to improve the impact parameter resolution, the Beryllium beam pipe inner radius will be shrunk from 29 mm to 17.2 mm in the vicinity of the nominal IP. Beyond a distance of 2 m from the IP, a larger beam pipe radius has to be considered. Meanwhile, the thickness has been fixed (up to now) to 0.8 mm as it is still not clear if smaller values can provide reliable mechanical stability.

3.2.16.2 ITS

With the new beam pipe, the first ITS layer will be located closer to the beam line [91]. The material budget will be reduced down to 0.3 % of X_0 per layer improving the impact parameter resolution and reducing the probability of photon conversion. The upgraded ITS will consist of 7 layers of silicon tracking detectors, nevertheless the final layout has not been decided yet and two options are still considered:

1. All layers made of silicon pixel detectors. This scenario will provide a better standalone tracking efficiency and p_{T} resolution.
2. The first 3 inner layers made of silicon pixel detectors and the remaining ones of double sided silicon strip detectors. This configuration significantly improve the PID.

3.2.16.3 Other detectors

The actual MWPC in the TPC will be replaced by Gas Electron Multiplier (GEM) detectors which can block ions without additional gating.

For the remaining detectors minor improvements are considered, most of these being related to the substitution of the electronics in order to support the expected high read out rates.

3.2.16.4 Very High-Momentum Particle IDentificator

The Very High-Momentum Particle IDentificator (VHMPID) [92] was proposed[5] to identify charged pions, kaons, protons and antiprotons in the momentum range 5 GeV/c $< p <$ 25 GeV/c. Its main purpose is to determine

---

[5] Detector finally not approved by the ALICE collaboration in March 2013.

hadron specific effects in the fragmentation of partons and subsequent formation of jets in vacuum and in medium. These measurements will be unique to ALICE, since no other LHC experiment has such specific PID capabilities or is planning to employ a similar device in the future.

This detector was supposed to be assembled in 3 stages, the first two during the second long shutdown of the LHC and the last one in the third long shutdown. The VHMPID would be located next to the actual PHOS position, providing a 30% coverage of the ALICE central barrel. It will employ the same RICH working principle used in the HMPID but using a gas radiator with a refraction index closer to unity, as this defines the threshold of Cherenkov emission and amount of produced photons.

3.2.16.5 Forward Electromagnetic Calorimeter

The Forward Electromagnetic Calorimeter (FoCal) [93] detector was proposed[5] in order to measure photons in the forward pseudorapidity region for energies up to $E \approx 500$ GeV/c. It would provide jet energy measurements as well as discrimination between direct photons and neutral pions.

The position of this proposed detector has not been fully established as it could be located at 3.5 from IP, replacing the existing PMD, covering a pseudorapidity range of 2.5 to 4.3. The second option is to place it 15 m from IP, reaching $\eta \approx 5.5$ and significantly enhancing the p_{T} relative to the previous position. The weakness of this point is that the beam pipe would have to be modified.

Chapter 4

The Muon Spectrometer

The present chapter describes in detail the detector that is used in the data analysis of the present thesis. It will begin by explaining in detail the parts that compose the muon spectrometer: the absorbers, the dipole magnet, the tracking and the trigger system. The chapter is then complemented by a section describing the trigger principle and the tracking algorithm. Finally a brief summary on the, already approved, upgrade plans for the detector is given.

4.1 Overview

The muon spectrometer [94, 95] was designed to measure the quarkonium (J/ψ, ψ', Υ, Υ' and Υ") and the low-mass vector mesons (ϕ, ω and ρ) production via their dimuon decay channel, but also open heavy flavours (D^+, D^-, B^+ and B^-) through their semimuonic desintegration.

In order to maximise the particle detection the acceptance of the detector was chosen as large as possible and the p_{T} coverage extended down to zero. At large p_{T} a sizeable fraction of the detected J/ψ are produced via B-decays: experimental results [96] show that the amount of J/ψ from B feed down is approximately 10% for $p_{\mathrm{T}} < 3-4$ GeV/c, reaching up to 40% for $p_{\mathrm{T}} \approx 15-18$ GeV/c.

For description purposes of this thesis, the parts composing the muons spectrometer are divided into three groups: the absorbers and the dipole magnet, the tracking and the trigger systems.

Table 4.1 presents a summary of the most important characteristics of the muon spectrometer, while figure 4.1 shows a schematic view of the detector.

Table 4.1: A summary of the main characteristics of the muon spectrometer.

Muon detection	
Polar, azimuthal angle coverage Minimum muon momentum	$171^\circ \leq \theta \leq 178^\circ$, 360° $4\,\mathrm{GeV}/c$
Pseudo-rapidity coverage	$-4.0 < \eta < -2.5$
Front absorber	
Longitudinal position (from IP) Total thickness (materials)	$-5030\,\mathrm{mm} \leq z \leq -900\,\mathrm{mm}$ ($\sim$10 λ_{int}, $\sim$60 X_0) (carbon-concrete–steel)
Dipole magnet	
Nominal magnetic field, field integral Free gap between poles Overall magnet length Longitudinal position (from IP)	$0.67\,\mathrm{T}$, $3\,\mathrm{T\,m}$ 2.972–$3.956\,\mathrm{m}$ $4.97\,\mathrm{m}$ $-z = 9.94\,\mathrm{m}$ (centre of the dipole coils)
Tracking chambers	
No. of stations, no. of planes per station Longitudinal position of stations Anode-cathode gap (equal to wire pitch) Gas mixture Pad size st. 1 (bending plane) Pad size st. 2 (bending plane) Pad size st. 3, 4 and 5 (bending plane) Max. hit dens. st. 1–5 (central Pb-Pb × 2) Spatial resolution (bending plane)	5, 2 $-z = 5\,357, 6\,860, 9\,830, 12\,920, 14\,221\,\mathrm{mm}$ 2.1 mm for st. 1; 2.5 mm for st. 2–5 $80\,\%\mathrm{Ar}/20\,\%\mathrm{CO}_2$ $4.2 \times 6.3,\ 4.2 \times 12.6,\ 4.2 \times 25.2\ \mathrm{mm}^2$ $5 \times 7.5,\ 5 \times 15,\ 5 \times 30\,\mathrm{mm}^2$ $5 \times 25,\ 5 \times 50,\ 5 \times 100\,\mathrm{mm}^2$ $5.0, 2.1, 0.7, 0.5, 0.6 \cdot 10^{-2}\,\mathrm{hits}/\mathrm{cm}^2$ $\simeq 70\,\mu\mathrm{m}$
Tracking electronics	
Total no. of FEE channels Shaping amplifier peaking time	1.08×10^6 $1.2\,\mu\mathrm{s}$
Trigger chambers	
No. of stations, no. of planes per station Longitudinal position of stations Total no. of RPCs, total active surface Gas gap Electrode material and resistivity Gas mixture Pitch of readout strips (bending plane) Max. strip occupancy bend. (non bend.) plane Maximum hit rate on RPCs	2, 2 $-z = 16\,120, 17\,120\,\mathrm{mm}$ 72, $\sim 140\,\mathrm{m}^2$ single, 2 mm Bakelite$^{\mathrm{TM}}$, $\rho = 2$–$8 \times 10^9\,\Omega\,\mathrm{cm}$ Ar/$\mathrm{C_2H_2F_4}$/i-buthane/$\mathrm{SF_6}$ (50.5/41.3/7.2/1) 10.6, 21.2, 42.5 mm (for trigger st. 1) $3\%(10\%)$ in central Pb-Pb 3 (40) Hz/cm^2 in Pb-Pb (Ar-Ar)
Trigger electronics	
Total no. of FEE channels No. of local trigger cards	2.1×10^4 $234 + 8$

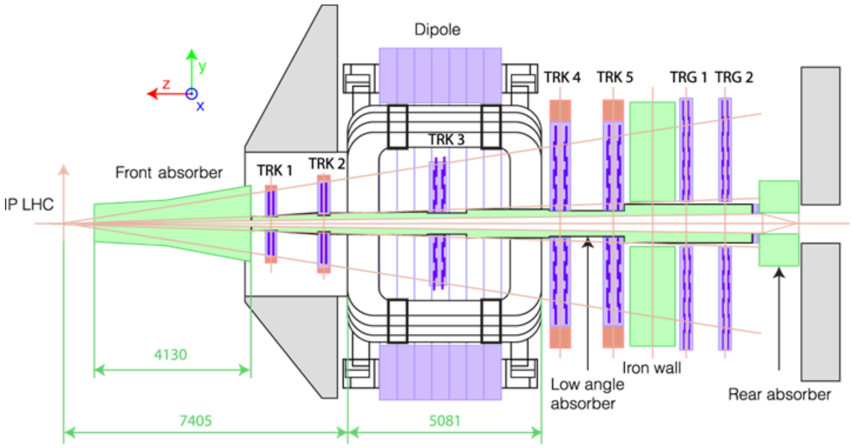

Figure 4.1: Longitudinal view of the muon spectrometer and its components.

4.2 Absorbers and dipole magnet

The absorbers protects the detector from the high background originated in central Pb-Pb collisions. There are four absorbers: the front absorber, the beam shield, the iron wall and the rear absorber.

4.2.1 Front absorber

The front absorber is located at 90 cm from the nominal IP in order to absorb, as soon as possible, the large flux of particles resulting from the collision. The distance from the IP is constrained by the ITS dimension along the z axis.

The materials chosen to make up the front absorber had to fulfill the following requirements:

1. A small interaction length (λ_{int}) to efficiently absorb the hadrons.
2. A large radiation length (X_0) to minimise the multiple scattering.

The absorber (figure 4.2) is then composed by carbon in its closest half to the vertex while the second half is made out of concrete. The end cap is a composite of lead and CH2 boronated at 50%, the first one diminishes the flux of gammas thanks to its large atomic number and the second material operates as a moderator absorbing neutrons. Finally, a layer of lead wraps the whole structure avoiding back-scattering particles into the TPC.

The front absorber has an impact on the detector performance as it introduces a lower limit cut of $p = 4$ GeV/c on the muons in order to overcome all this amount of material and to be detected.

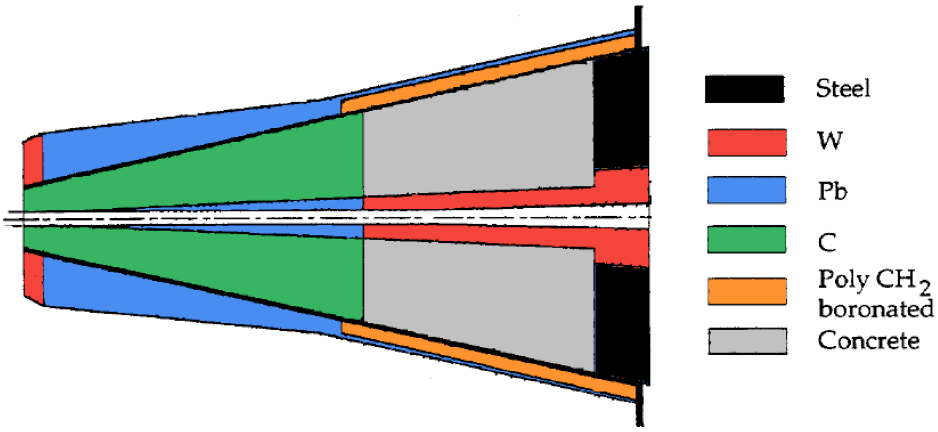

Figure 4.2: Longitudinal view of the front absorber.

4.2.2 Beam shield

The goal of the low angle absorber is to minimize the high background on the detectors, produced by the interactions with the beam pipe of large rapidity (up to 2°) particles (mainly pions and kaons). This shielding was optimized in shape, dimensions and materials choice [97].

The beam shield is made of tungsten and lead, allowing a low cost absorber, and finally covered by a stainless steel layer.

4.2.3 Iron wall

The iron wall, located between the last tracking chamber and the first trigger chamber, is made of a 1.2 m thickness (7 λ_{int}) iron. The iron wall stops hadrons that punch through the front absorber and secondaries. As it is located downstream the tracking chambers, it has no effect on the mass resolution of the particles reconstructed.

4.2.4 Rear absorber

It is also mandatory to protect the trigger chambers from the background generated by the accelerator (beam-gas residual interactions). This background is proportional to the beam luminosity and as a consequence, not negligible during the pp runs.

4.2.5 Dipole magnet

The dipole magnet is a warm magnet that deflects the muons according to their electric charge (q) allowing their momentum (p) to be measured via the relation $R = p/|qB|$, with R the curvature radius of the particle and B the magnetic field of the dipole. The dipole structure is also used as a support for the front absorber and the beam shield. The magnetic field is along the x-axis, so the deflection of the particles is in the yz plane.

4.3 Tracking system

The tracking system reconstructs the trajectory of the tracks that pass through the muon spectrometer. There are five tracking stations, each one containing two chambers. Taking the IP as the reference, the first two stations are located right after the front absorber, the third one is embedded into the dipole and the last two are located between the magnet and the iron wall.

The active surface of each station increases (from 2.5 to 20 m^2) along the z axis in the direction of the trigger chambers, reaching a total covered area of approximately 100 m^2. The active area of the first two stations is the geometrical projection of the front absorber; the third station dimensions increase, but they are limited by the magnet; finally the last two stations are the biggest ones as they have to detect the muons deflected by the dipole.

4.3.1 Required performance

To disentangle the Υ family, the tracking chambers must have a resolution better than 100 μm in the bending (y axis) plane. In the non-bending plane (x axis), a 2 mm resolution is enough to efficiently reconstruct the angle between the two muons and their trajectories. These values must include the misalignment effects and mechanical deformations because if the detector performance improves by a factor two, the mass resolution improves only by 10 MeV.

The chamber thickness must be inferior to 3 X_0 in order to limit the multiple scattering effects that can lead to a spatial resolution degradation and as a consequence worsening the mass resolution of the reconstructed particle.

The tracking chambers are also expected to provide a reliable performance in the high multiplicity environment created in central nucleus-nucleus collisions. For example, the design of the first station was studied to limit the occupancy at 5%.

4.3.2 Working principle

The type of detector that better satisfies the previous requirements are the Multiwire Proportional Chambers (MWPC) with segmented cathodes, usually called Cathode Pad Chambers (CPC). Their advantage is that they can be segmented as a function of the local hit density which decreases with the chamber radius. This means that the largest occupancy of the detector is in the region surrounding the beam pipe.

A chamber is made by a central anode plane with wires equally spaced parallel to the y axis (bending plane) and sandwiched between two outer cathode planes. A high voltage (1650 V) is applied to the wires while the cathode planes are grounded, generating an electric field with its maximum value at the wire surface and that decreases as r^{-1} near the wires.

When a particle crosses the detector (figure 4.3), a primary ionization starts and the electrons (ions) follow the field lines towards the anode wires (cathode planes). The electric field induces an acceleration of the electrons, ionizing the gas and creating an avalanche. The multiplication factor between primary electrons and the total amount of electrons collected in the anode is related to the Townsend coefficient[1].

The filling gas is Argon, characterised by its high specific ionization[2] and low cost relative to other noble gases as Xenon or Krypton. Nevertheless, a typical problem presented is that, during the avalanche formation, the Ar excited molecules return to the ground state by emitting a photon that can ionize the cathode material, producing a spurious avalanche. This problem is solved by introducing a small amount of polyatomic molecules, in this case 20% of CO_2. This acts as a quencher, absorbing the radiated photons and dissipating this energy through elastic collisions or by dissociation into simpler radicals.

4.3.3 Chambers structure

A schematic design of a CPC from the first station can be seen in figure 4.4. The chamber is in a sandwich structure with the wires in the middle and the pads equally spaced from the anode plane. The pads made of cooper and gold are then drawn directly on the Printed Circuit Board (PCB). The next component is an internal high density frame that provides rigidity and avoid the multiple scattering. Finally an external frame is used to reinforce the stiffness of the ensemble.

---

[1] Number of produced pairs per unit path length created by a free electron immersed in an electric field.

[2] Number of ion pairs formed per unit distance along the track of an ion passing through matter.

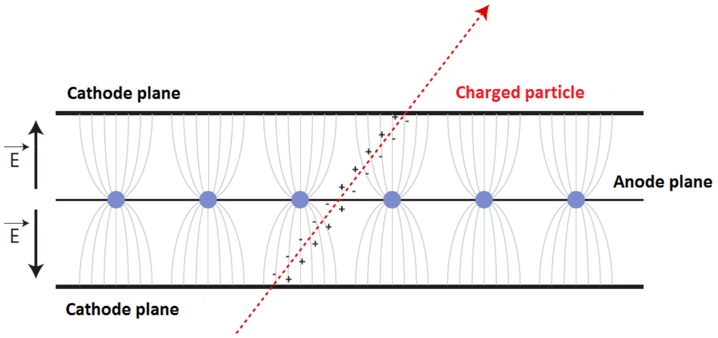

Figure 4.3: Working principle of a Multiwire Proportional Chamber.

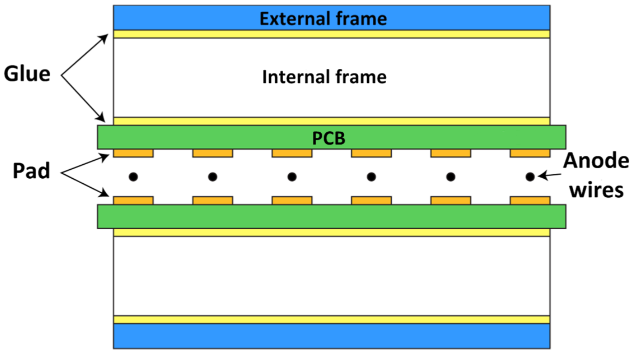

Figure 4.4: Generic structure of a CPC from station 1.

The previous description is also valid for the chambers of the remaining stations. For the first two stations, the smallest ones, the tracking chambers have a quadrant geometry and the last 6 chambers, as they have to cover a larger area, are made up of horizontal modules called *slats*.

Figure 4.5 shows the cathode segmentation in a quadrant of station 1, but it is similar to the chambers from the different stations. The quadrant is divided in three regions and in each one the size of the pads is different. In the first region, around the beam pipe, the detector presents its largest granularity, where the maximum multiplicity is expected. In the outer edges of the chambers the granularity decreases and, as a consequence, the size of the pads increase.

4.3.4 Electronics

The readout mechanism [98] in the tracking chambers begins with the Front End Electronics (FEE), this is, the NUmerical MAnas (MANU) that are embedded in the detectors. They deal with the analogical signals coming from 64 pads through 4 Multiplexed ANAlog Signal (MANAS). The MANAS insure

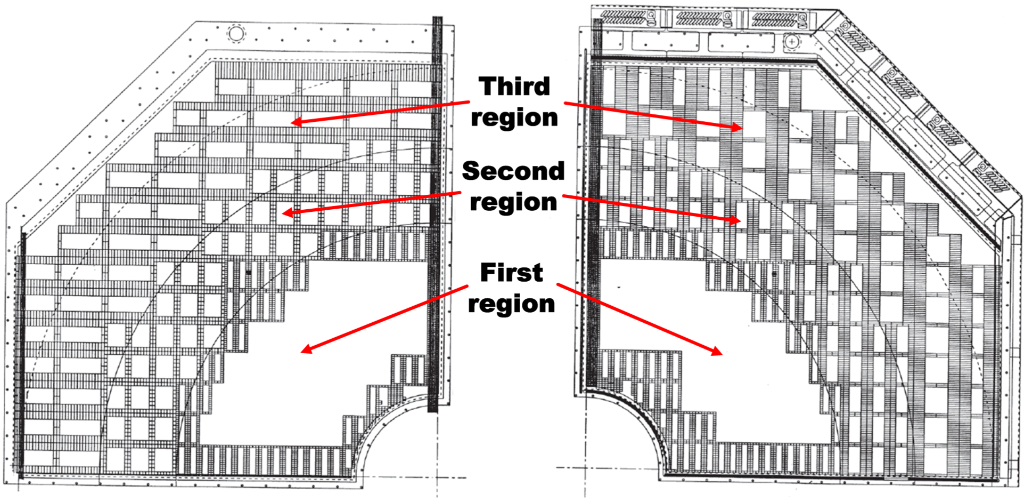

Figure 4.5: Chamber cathode segmentation in station 1 for the non-bending (*left*) and the bending (*right*) plane.

the signal amplification, shaping with a 1.2 μs peaking time and multiplexing of the 16 channels.

The output signal of 2 MANAS are then sent to one of the two ADC located in the MANU. These ADC convert the analogue signal to a numerical one. The last component of a MANU is the Muon Arm Readdout Chip (MARC) that controls the functioning of the MANAS and the zero suppression.

The tracking system consists of more than one million electronic channels to be read. The zero suppression mechanism optimizes this readout. A threshold value for each pad is stored in the MARC. When the signal arrives it is compared to the one available in the memory of the MARC. If the signal is above the threshold it is processed.

Once the signal has been converted to a numerical one, it is sent to the Concentrator Readout Cluster Unit System (CROCUS) through the Protocol for Alice Tracking Chamber (PATCH). The PATCH is then a bus communication between the detector and the CROCUS over a long distance. The CROCUS has several tasks, for example, retrieve the data from the detector, calibrate the MANU and transmit the data to the Data AcQuisition (DAQ). A CROCUS crate is composed by 5 FRonT (FRT) and one ConcentRaTor (CRT) board; each FRT manages 10 bus PATCH while the CRT concentrates the information of the FRT. Each CROCUS is in charge of half chamber, so the tracking system includes a total of 20 CROCUS crates.

The last element is the Trigger Crocus Interface (TCI) that manages the trigger information sent by the CTP. The TCI receives the trigger level signals in the Frontal Fan-out Trigger (FFT), then it sends the trigger level signal

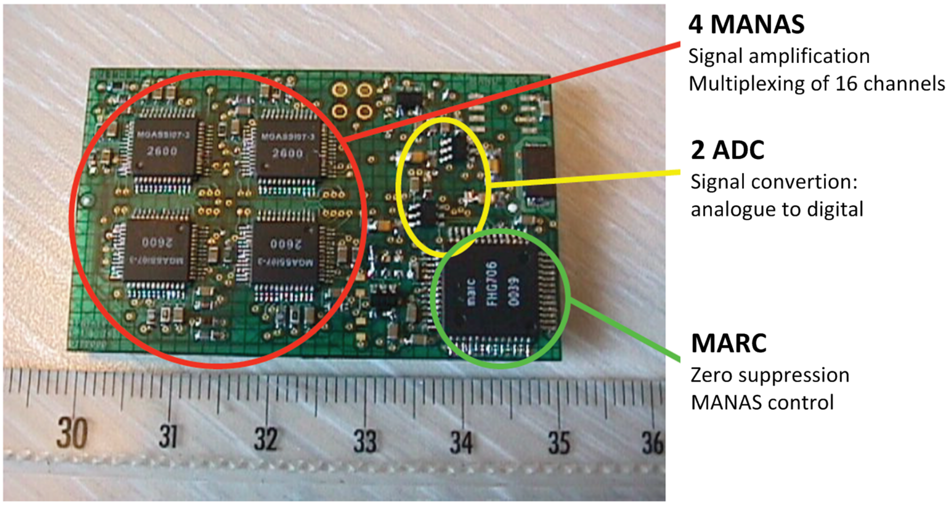

Figure 4.6: Example of a MANU with its 4 MANAS, 2 ADC and 1 MARC.

to the Frontal Trigger Dispatching (FTD) that finally distributes the signal to each CROCUS. For the L0 trigger level, it is dispatched to the MANU through the TCI and CROCUS without delay, so L0 trigger can be received in the scheduled 1.2 μs after the interaction.

4.4 Trigger system

The trigger system is responsible to select interesting events containing dimuons coming from the decay of quarkonia or low mass resonances, but also single muons originated from the desintegration of open heavy flavours. The main sources of background are low-p_{T} muons from pion and kaon decays. To remove the undesirable muons, the trigger applies p_{T} cuts ranging from 0.5 up to 4 GeV/c. The threshold for the low-p_{T} (high-p_{T}) triggers are a compromise between background rejection and signal detection efficiency in the mass regions of the J/ψ (Υ) family [99].

There are two trigger stations, each one consisting of two chambers and located downstream the iron wall. The active surface of the planes in both stations is approximately 30 m^2.

4.4.1 Required performance

The efficiency of the trigger must be higher than 95% for charged particles, but it should be less than 10^{-2} (10^{-3}) for photons (neutrons).

During the LHC operations a high flux of particles is expected. This flux depends on the luminosity and the colliding system (pp, A-A, p-A). It is thus mandatory to have a high efficiency for radiation rates of the order of 100 Hz/cm^2.

At its nominal operation with proton beams, the LHC will deliver 2 808 bunches per beam separated by 25 ns. The muon trigger should have a time resolution better than the bunch separation to make sure that all muons produced in a given collision come from the same bunch crossing.

In the muon trigger system the spatial resolution is defined in terms of the cluster size: the number of strips fired by a single tracks that crosses the chamber. To provide a highly selective trigger, the cluster size must be of the order of a centimetre.

4.4.2 Working principle

The Resistive Plate Chambers (RPC) have been chosen by the LHC experiments to work as the muon triggers (figure 4.7). These detectors are based on the traditional spark chambers, where a charged particle crossing a gas immersed in an electric field between two metallic and parallel plates creates a spark. A multiplication process is then created, electrons are driven to the anode and the ions towards the cathode.

In the RPC, due to its planar geometry, the electric field doesn't decrease as a function of the distance from the anode, hence multiplication occurs in the whole gas volume. The difference between ordinary spark chambers and RPC relies on the resistive material of which the electrodes are made in the latter, preventing the signal from propagating beyond a small region and in this way allowing to get the refereed sparks under control.

Different gas mixtures and HV values lead to different behaviours of the RPC, each one having its own advantages [100]:

- The streamer mode is used in A-A collisions where the main constraint is the high multiplicity. It allows a large signal amplification in the detector and therefore is less sensitive to electronics noise.
- The avalanche configuration has a very good time resolution and slower ageing are achieved. It is employed during pp runs where the main restrictions are the high luminosity and collision rate.

4.4.3 Chambers structure

The signal generated in the RPC is picked-up by conductive strips electrically insulated from the electrodes. Strips are located in both sides of the chambers,

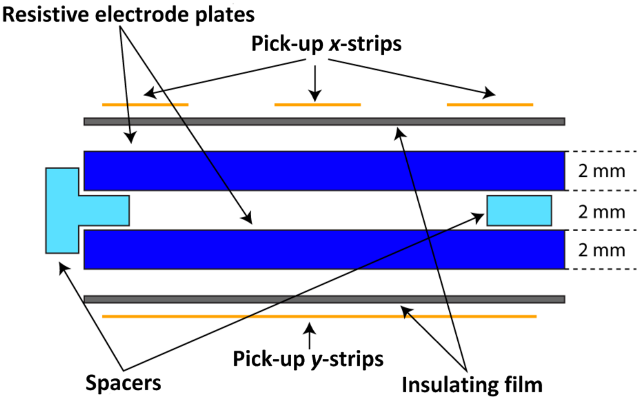

Figure 4.7: View of a RPC used in the muon trigger system.

those located in the front face are orthogonal to the ones in the rear. This configuration provides a two dimensional reconstruction of the tracks. The read-out strips along the bending coordinate are called X strips and those providing the non-bending coordinate measurements are the Y strips.

Figure 4.8 shows the structure of the trigger chambers. The colors represent the different sizes of the strip segmentation used in a given area. The segmentation decreases with the increasing radius of the chamber. Notice the X strips are the most conditioned by the requirement on the spatial resolution. The numbers indicate the number of strips placed in the signalled region, this granularity is higher around the beam pipe as in the tracking chambers.

4.4.4 Electronics

The FEE of the trigger chambers is composed by a system called A DUaL Threshold (ADULT), that allows to improve the temporal resolution in the *streamer* configuration [101]. The signal from the FEE is collected by the trigger boards that are in charge of applying the trigger algorithm. Local trigger boards are accommodated in regional crates, each one of these is controlled by a regional board that collects the trigger decisions from the local boards. Regional boards receive single or double local trigger decisions and sends the information to the last step of the trigger decision, gathered by the global board. The total latency of the L0 trigger signal of the muon trigger system is 800 ns.

The data read-out is performed by two DAta Read out Card (DARC): they receive the L0 signals from the CTP, dispatch the order of track and hold to the regional, and global boards and transfer the data, after reception of the L2 trigger, to the DAQ.

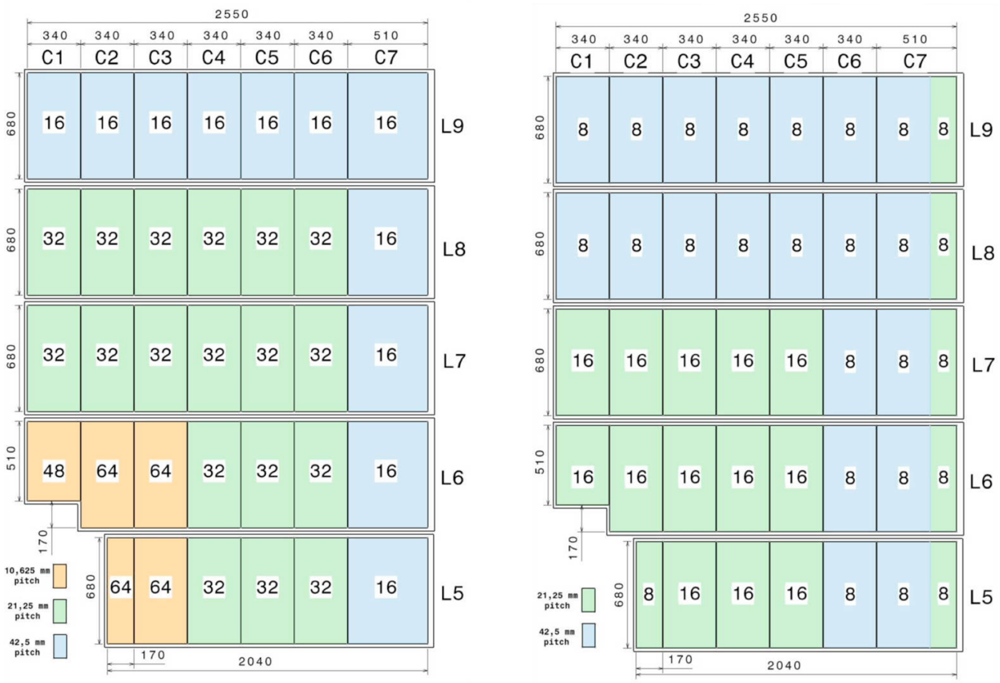

Figure 4.8: Structure and segmentation of a trigger chamber: X strips (*left*) and Y strips (*right*). The dimensions are expressed in millimeters.

4.5 Track reconstruction

Up to now only the hardware structure of the muon has been described. The following section will detail how the trigger selects a track according to its p_{T} and how the tracking algorithm reconstructs the trajectory of the particles.

4.5.1 Trigger principle

A muon coming from the IP is deviated by an angle θ_d due to the magnetic field generated by the dipole magnet (figure 4.9). The particle is then detected by the trigger stations 1 and 2 in the coordinates (X_1,Y_1,Z_1) and (X_2,Y_2,Z_2) respectively. The muon survives the p_{T} selection of the trigger if its deviation ($\delta Y_2 = Y_2 - Y_2^{\infty}$) relative to a muon with infinite transverse momentum (p_{T}^{∞}) is smaller than a given fixed limit [94].

In the yx (bending) plane, for small deviation angles and at first order, the momentum of a muon is given by:

$$p_{\mathrm{y,z}} = \left| \frac{qBL}{\theta_d} \right| , \tag{4.1}$$

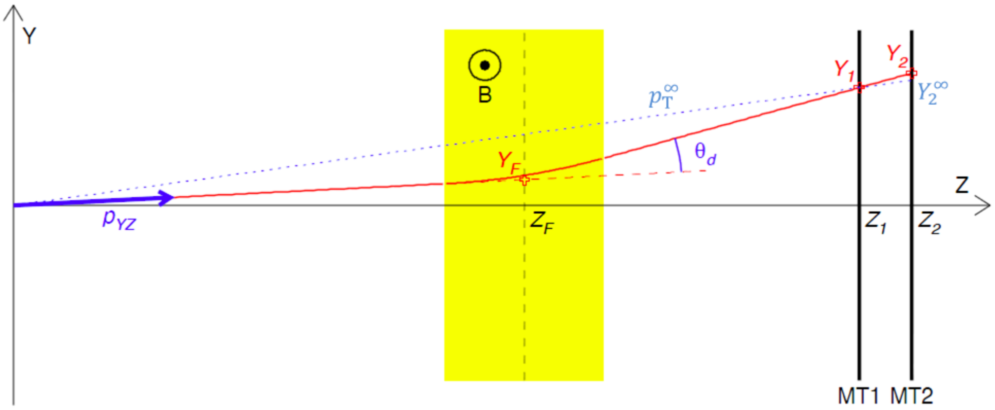

Figure 4.9: Working principle of the trigger algorithm.

where q is the charge of the particle, B the magnetic field and L the length of the dipole, while the expression for the deviation angle is:

$$\theta_d = \frac{1}{Z_F}\left(\frac{Z_1Y_2 - Z_2Y_1}{Z_2 - Z_1}\right), \tag{4.2}$$

with Z_F the position of the centre of the dipole along the z axis. The transverse momentum of the muon is then:

$$p_T = p_{YZ}\frac{\sqrt{X_F^2 + Y_F^2}}{Z_F}, \tag{4.3}$$

that can be solved using equations 4.1, 4.2 where

$$X_F = X_1 Z_F / Z_1 \qquad Y_F = Y_2 - \frac{(Y_2 - Y_1)(Z_2 - Z_F)}{Z_2 - Z_1}.$$

Two different p_{T} thresholds, corresponding to the low and high thresholds, are pre-loaded in the look-up tables located in the trigger electronics.

4.5.2 Tracking algorithm

The hit finding algorithm is based on a Maximum Likelihood Expectation Maximization technique. It assumes that the pad charge distribution, released by a muon passing through a chamber, can be described by a two-dimensional integral of the Mathieson function [102]. The algorithm starts by finding groups of adjacent pads on one cathode and overlapping them with the pads on the other cathode to form a pre-cluster. This is a recursive procedure to determine the number and position of clusters into the pre-clusters. Each group of clusters is then fitted with the 2D Mathieson function to extract its exact position.

Once the clusters distributions have been extracted in all the chambers, the tracking reconstruction procedure begins [103, 104, 105]:

- Build all combinations of clusters between the two chambers of stations 5(4), computing for each one the local position, orientation of the track and bending momentum by assuming the particle was originated from the IP. Extrapolate the track candidates from station 5(4) to station 4(5) looking for at least one compatible cluster and recomputing the track parameters.
- Remove track candidates sharing the same clusters and those whose estimated bending momentum and non-bending impact parameter at vertex are not within the limits defined by the reconstruction parameters.
- Propagate the track to stations 3, 2 and 1, searching for at least one cluster per station and extracting at each step the reconstruction parameter. If several compatible clusters are found in the same chamber, the track candidate is duplicated to consider all the possibilities.
- Remove connected tracks, keeping the one with the largest number of clusters or the one with the lowest χ^2 in case of equality.
- Reconstructed tracks are matched with the trigger tracks to identify the muons responsible for the trigger signal.
- Finally the tracks are corrected for energy loss and multiple scattering in the front absorber and extrapolated to the vertex of the collision.

The tracking reconstruction algorithm is represented in figure 4.10.

4.6 Upgrades

The upgrade of the muon spectrometer will be focused on the tracking electronics in order to work at a trigger rate of 50 kHz [90].

At a luminosity of $\mathcal{L}$ = 6x10^{27} cm^{-2} s^{-1} and assuming $\sigma_{\mathrm{Pb-Pb}} \approx 8$ b, a maximum of 50 kHz Pb-Pb interaction rate is expected. The goal is to accumulate 10 nb^{-1} of Pb-Pb collisions and 6 pb^{-1} in pp collisions at a 500 kHz rate during one month.

At these conditions, some changes will be needed:

- No more muon trigger. The muon trigger will become a muon ID.

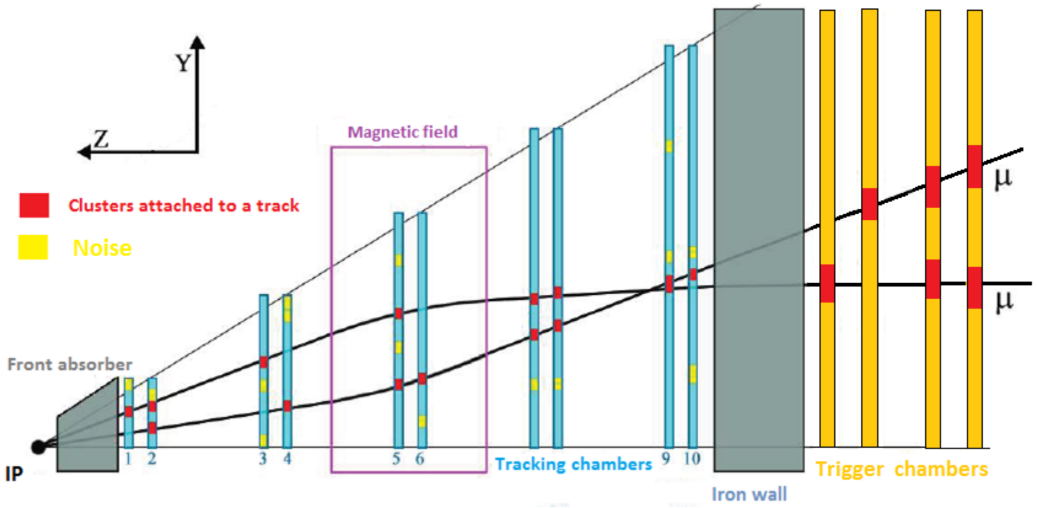

Figure 4.10: Tracking reconstruction algorithm.

- No more CROCUS. The detector will be read continuously at 10 MHz with a sampling of the signal in pipeline mode. In case of a Minimum Bias trigger, the data will be sent to the HLT and next to the DAQ. Up to 40 GB/s of information is expected to be processed on the tracking apparatus.

4.6.1 Muon Forward Tracker

The presence of the front absorber imposes serious limitations to the physics capabilities of the muon spectrometer. The multiple scattering of the muons when going through the absorber compromises the access to an accurate and detailed information on the position of the primary vertex. It is then impossible to disentangle the prompt from non-prompt contribution of the measured J/ψ. The mass resolution for low mass resonances is also affected by the degradation of the kinematics and by the difficulty to reject background muons from the semimuonic decays of pions and kaons.

The Muon Forward Tracker (MFT) is proposed[3], among the ALICE upgrades, to cope with these problematic [106]. The MFT will be a silicon pixel detector that will be added in the muon spectrometer acceptance upstream the front absorber, between the V0C and the IP. Its main purpose is to match the extrapolated muon tracks, registered by the tracking system, before they arrive to the front absorber. This will in turn ensure a correct measurement of their origin with respect to the primary vertex of the interaction.

The MFT (figure 4.11) is planed to consist of an ensemble of 5 circular

---

[3] Detector finally approved by the ALICE collaboration in March 2013. The project is going to be submitted to the LHCC for final decision in September.

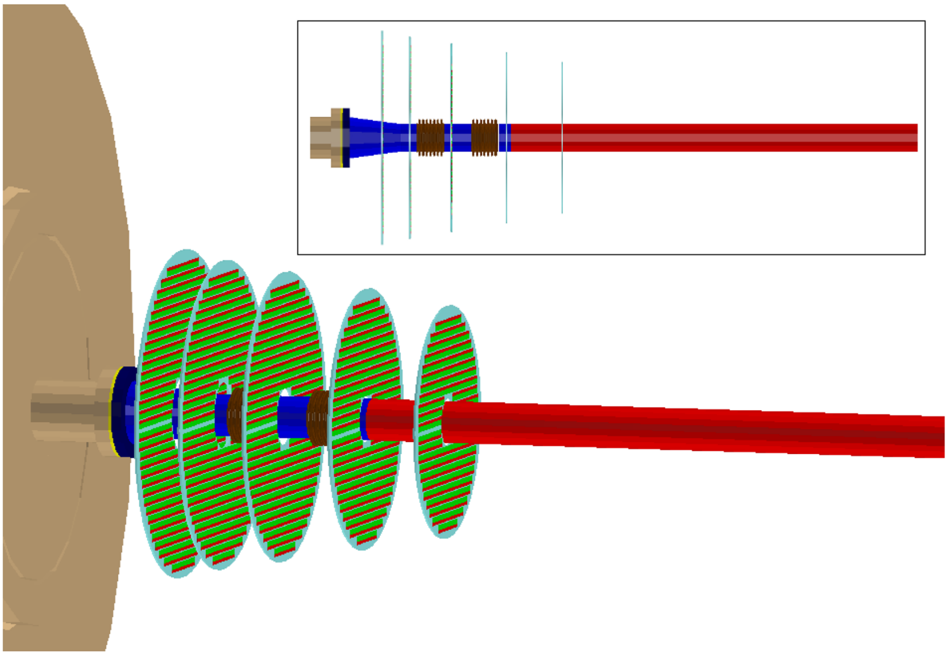

Figure 4.11: Simulation of the MFT planes installed in ALICE.

pixel planes, each one having a 400 μm thickness of silicon ($\approx$ 0.4 % of X_0). The external radius of each planes is chosen in order to reach a polar angle of 10° for tracks coming from the nominal interaction point; the internal radius is constrained by the presence of the beam pipe.

The final configuration of the MFT has not been decided yet, indeed, a 6^{th} plane is also under consideration to provide redundancy to the detector and improving its tracking performance. The definitive position and dimensions are also still undefined, they depend on the ultimate design of the upgraded ITS and beam pipe.

The tracking strategy will be similar to the actual one described in the previous section. The muon tracks reconstructed by the tracking system, while extrapolated to the vertex region, are evaluated at the last plane of the MFT (the one closest to the absorber) estimating for each cluster in this plane their compatibility. For each compatible cluster a new candidate track is created, whose parameters and uncertainties are updated with the information given by the added cluster by means of a Kalman filter algorithm. Each candidate track is then extrapolated to the next MFT plane, where a search for compatible clusters is performed. The steps proceed towards the vertex region where the number of candidate tracks converge, but if more than one final coinciding track is found, the one with the best global fit quality is chosen.

Chapter 5

Tracking chambers efficiency studies

The previous chapter presented a detailed description of the muon spectrometer. The following chapter focuses on how the tracking efficiency of the muon tracking chambers is computed. The efficiency is studied as a function of the centrality, p_{T} and y. The comparison of the efficiencies obtained between data and simulation is used to estimate the systematics uncertainties on the tracking chambers efficiency. These studies were performed along one year of data taking and include two periods of Pb-Pb collisions and one of pp, all of them at $\sqrt{s_{NN}} = 2.76$ TeV.

5.1 Acceptance and efficiencies

The number of reconstructed J/ψ ($N_{\mathrm{J}/\psi}$) in the muon spectrometer is just a fraction of the total amount of J/ψ produced in a collision (N_{prod})[1]. This is a consequence of the limited acceptance and efficiency of the detector. In order to compute cross sections or Nuclear Modification Factors, the employed quantity is the invariant yield:

$$Y = \frac{N_{\mathrm{J}/\psi}}{BR_{\mathrm{J}/\psi\rightarrow\mu^+\mu^-} \times N_{\mathrm{MB}} \times A \times \epsilon} \ ,$$

where BR is the decay branching ratio of the J/ψ into muons, N_{MB} the number of Minimum Bias collisions used in the analysis and $A \times \epsilon$ the acceptance times efficiency term.

---

[1] Although the present description has been made for the J/$\psi \rightarrow \mu^+\mu^-$ process in the muon spectrometer, it can also be applied to any other process employing any other detector.

5.1.1 Acceptance

The acceptance of the muon spectrometer is computed from Monte Carlo simulations. It is given by the ratio $A = N_{\text{det}}/N_{\text{prod}}$, where the numerator indicates the J/ψ that are emitted in the detector angular coverage and that are subject to be detected.

At the single muon level, the -4 $< \eta <$ -2.5 track selection ensures that muons are in the acceptance of the muon spectrometer. At the J/ψ level the acceptance requirement is extended by asking for -4 $< y <$ -2.5.

5.1.2 Efficiency

The efficiency of the muon spectrometer is given by the ratio $\epsilon_{\text{MS}} = N_{\text{rec}}/N_{\text{det}}$, this is, the number of J/ψ reconstructed out of the detectable ones. The efficiency of the muon spectrometer can be factorized as [107]:

$$\epsilon_{MS} = \epsilon_{\text{Trackable}}\,\epsilon_{\text{Tracking}}\,\epsilon_{\text{Triggerable}}\,\epsilon_{\text{Trigger}},$$

where:

- $\epsilon_{\text{Trackable}}$ is the fraction of the tracks that cross the tracking chambers through their active areas.
- $\epsilon_{\text{Tracking}}$ estimates if the tracking chambers respond to the crossing tracks. It is an indicator of the tracking chambers intrinsic performance.
- $\epsilon_{\text{Triggerable}}$ estimates the proportion of tracks that reach the trigger stations.
- $\epsilon_{\text{Trigger}}$ corresponds to the intrinsic trigger chambers response. It evaluates the probability that the trigger chambers respond to the passage of a particle.

5.2 Determination of the tracking efficiency

In general the $A \times \epsilon$ term is computed from Monte-Carlo simulation, as some of its components (acceptance, $\epsilon_{\text{Triggerable}}$ and $\epsilon_{\text{Trackable}}$) cannot be estimated from the data itself. Nevertheless, the remaining ones ($\epsilon_{\text{Tracking}}$ and $\epsilon_{\text{Trigger}}$) must be evaluated with simulation and compared to the results obtained by using real data. This comparison is an indicator of how well the simulation reproduces the data and the difference between them is used to assess the systematics on the tracking and trigger efficiencies. From now on, the chapter will stick to the $\epsilon_{\text{Tracking}}$ calculations.

As the comparison to real data is crucial, the simulations must use realistic conditions. In particular, for the tracking chambers, these conditions include the alignment and the response function of the chambers. By performing the simulations in a run-per-run basis, all the possible variations of the status of the tracking chambers are taken into account: HV trips, pedestal values, electronic noise, etc.

5.2.1 The method

The tracking reconstruction algorithm, described in the previous chapter, requires that a track leaves one cluster in each of the first three stations and at least three clusters in the last two in order to be reconstructed. Thanks to the redundancy of the detector, a particle going through a tracking station (figure 5.1) can leave a cluster in both chambers (N_{i-j}), a cluster only in chamber i (N_{i-0}), a cluster only in chamber j (N_{0-j}) or no cluster at all (N_{0-0}). However, according to the tracking reconstruction requirements, a track with N_{0-0} cluster configuration in any station can not be reconstructed. The total number of tracks that cross a tracking station can be written as:

$$N_{\text{Tot}} = N_{i-j} + N_{i-0} + N_{0-j} + N_{0-0}.$$

The efficiency (ϵ) of a chamber is the number of tracks detected divided by the total number of tracks:

$$\epsilon_{\text{Ch}\,i} = \frac{N_{i-j} + N_{i-0}}{N_{\text{Tot}}},$$

$$\epsilon_{\text{Ch}\,j} = \frac{N_{i-j} + N_{0-j}}{N_{\text{Tot}}}.$$

Considering the efficiency of chamber i independent of the efficiency from chamber j ($N_{i-j} = \epsilon_{\text{Ch}\,i}\epsilon_{\text{Ch}\,j}N_{\text{Tot}}$) and that $\epsilon_{\text{Ch}\,i,j} \neq 0$, it is possible to write the efficiency of chamber i and j in terms of measurable quantities:

$$\epsilon_{\text{Ch}\,i} = \frac{N_{i-j}}{N_{i-j} + N_{0-j}}, \tag{5.1}$$

$$\epsilon_{\text{Ch}\,j} = \frac{N_{i-j}}{N_{i-j} + N_{i-0}}. \tag{5.2}$$

The error on the efficiency of the chambers is computed considering a binomial distribution because in the previous equations the numerator (N_{Num}) is a subset of the denominator (N_{Den}):

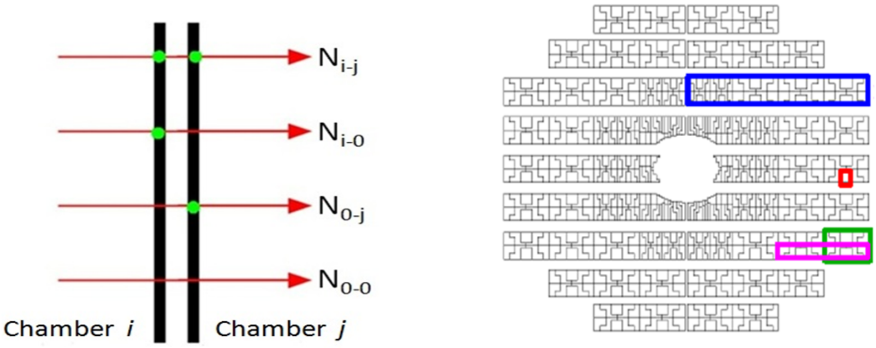

Figure 5.1: *Left:* Possible configurations for a track going through a muon tracking station. *Right:* Chamber elements; colours indicate the Detection Elements (blue), Bus Patch (pink), PCB (green) and MANU (red).

$$\Delta\epsilon_{\mathrm{Ch}\,i,\,j} = \frac{1}{N_{\mathrm{Den}}}\sqrt{N_{\mathrm{Num}}\left(1-\frac{N_{\mathrm{Num}}}{N_{\mathrm{Den}}}\right)}.$$

However, when $N_{\mathrm{Num}} \approx 0$ or $N_{\mathrm{Num}} \approx N_{\mathrm{Den}}$ the ordinary binomial approach to calculate errors breaks down: efficiencies, within the uncertainties, could become inferior to zero or superior to 1. It is then necessary to employ asymmetric error ranges to avoid unphysical results.

The procedure followed up to now is also valid at the Detection Element (DE) level (see right panel of figure 5.1). The efficiency of Detections Elements i ($\epsilon_{\mathrm{DE}\,i}$) and j ($\epsilon_{\mathrm{DE}\,j}$) has exactly the same form as equations 5.1 and 5.2.

The efficiency of a station is estimated according to the tracking reconstruction algorithm, that demands at least one cluster in each one of the first three stations, so:

$$\epsilon_{\mathrm{St}\,k} = 1-(1-\epsilon_{\mathrm{Ch}\,i})(1-\epsilon_{\mathrm{Ch}\,j}), \tag{5.3}$$

with $k \in \{1,\,2,\,3\}$. For the last two stations, due to the requirement of at least three clusters among the four chambers, their efficiency is computed as a single one:

$$\begin{aligned}\epsilon_{\mathrm{St}\,4-5} \;=\;& (1-\epsilon_{\mathrm{Ch}\,7})\epsilon_{\mathrm{Ch}\,8}\epsilon_{\mathrm{Ch}\,9}\epsilon_{\mathrm{Ch}\,10} + \epsilon_{\mathrm{Ch}\,7}(1-\epsilon_{\mathrm{Ch}\,8})\epsilon_{\mathrm{Ch}\,9}\epsilon_{\mathrm{Ch}\,10}\\ &+ \epsilon_{\mathrm{Ch}\,7}\epsilon_{\mathrm{Ch}\,8}(1-\epsilon_{\mathrm{Ch}\,9})\epsilon_{\mathrm{Ch}\,10} + \epsilon_{\mathrm{Ch}\,7}\epsilon_{\mathrm{Ch}\,8}\epsilon_{\mathrm{Ch}\,9}(1-\epsilon_{\mathrm{Ch}\,10})\\ &\epsilon_{\mathrm{Ch}\,7}\epsilon_{\mathrm{Ch}\,8}\epsilon_{\mathrm{Ch}\,9}\epsilon_{\mathrm{Ch}\,10}.\end{aligned} \tag{5.4}$$

The total tracking efficiency is given by the following expression:

$$\epsilon_{\mathrm{Tracking}} = \epsilon_{\mathrm{St\,1}}\epsilon_{\mathrm{St\,2}}\epsilon_{\mathrm{St\,3}}\epsilon_{\mathrm{St\,4-5}}\,. \tag{5.5}$$

5.2.2 Results

The tracking efficiency studies that will be described were performed along one year of data taking in the ALICE Muon Spectrometer, from November 2010 up to December 2011 and for two different collisions systems (Pb-Pb and pp) at $\sqrt{s_{\mathrm{NN}}} = 2.76$ TeV. The results are divided according to the respective periods, defined as:

- LHC10h: Pb-Pb collisions during November-December 2010.
- LHC11a: pp collisions in March 2011.
- LHC11h: Pb-Pb collisions during November-December 2011.

5.2.2.1 LHC10h

This was the first heavy-ion run at the LHC and for this reason measuring the efficiency of the chambers as a function of the centrality of the collision was a primary item. For this analysis the events were selected using the Minimum Bias trigger. The following standard cuts at the single muon level were applied:

- $-4.0 < \eta < -2.5$ to ensure muons are within the acceptance of the muon spectrometer.
- Tracks must match the all-p_{T} trigger threshold (0.5 GeV/c).
- The track transverse radius coordinate at the end of the front absorber (R_{Abs}) must be in the range $17.6 < R_{\mathrm{Abs}} < 80$ cm, or equivalently, $2° < \Theta_{\mathrm{Abs}} < 9°$ (figure 5.2). The latter is defined as the angle of the track at the end of the front absorber relative to the horizontal plane. The motivation is to avoid tracks that went through the beam shield (small angles) and the outer most layer of front absorber.

Figure 5.3 show the efficiency of the tracking chambers as a function of the centrality of the events extracted by applying:

- Only the standard cuts (black points).
- Standard cuts plus $p \times DCA$ (blue points). Where p is the momentum and DCA is the Distance of Closest Approach of the extrapolated track to the vertex in the X-Y plane [108].

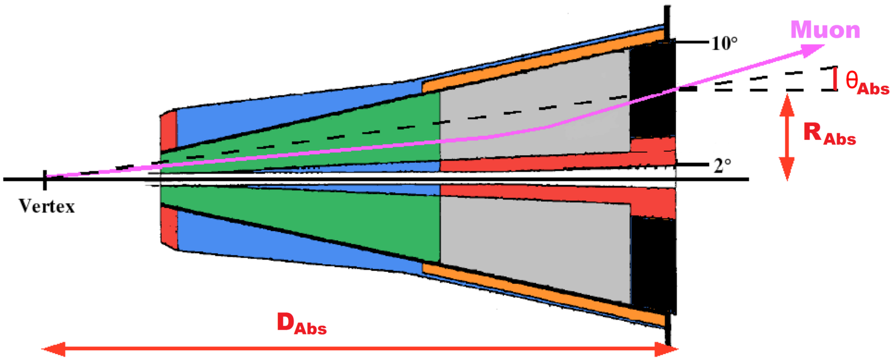

Figure 5.2: Graphical explanation of R_{Abs} and Θ_{Abs}.

- Standard cuts plus $p \times DCA$ plus a χ^2 cut on the reconstructed tracks (red points). The χ^2 indicates the goodness of the reconstructed track.

For the three set of points, the efficiency is basically flat (87%) in the 40-80% centrality bins, but for the most central collisions the efficiency drops due to the presence of fake tracks that contain less clusters. In particular, by applying only the standard cuts the efficiency loss is 5%.

In addition to the standard selection criteria, the $p \times DCA < 5\,\sigma_{\mathrm{pDCA}}$[2] is required. The objective is to clean up the fake tracks when the chambers have a large occupancy (central events). A second extra requirement ($\chi^2 < 3.5$) is applied to further reduce the remaining contamination at low transverse momentum ($p_{\mathrm{T}} <$ 1-2 GeV/c). Despite the application of these two extra requirements, the efficiency in the 20-80% centrality range is basically the same as if only the standard cuts are applied. The $p \times DCA$ and χ^2 are then rejected as track selection criteria and only the standard requirements are used.

As the comparison data-simulation for the tracking efficiency is performed using a single muon parametrization or a pure J/ψ generator it is not possible to reproduce the occupancy effect due to the central collisions. The centrality range used for this comparison, in the LHC10h period, is then restricted to the 40-80% centrality range.

Figure 5.4 presents the measured tracking efficiency for each run, both for data and a pure J/ψ simulation. The increase of the run number (time line of the data taking) is from left to right. From the upper part of the plot it is clear that the efficiency is constant along the period with very small fluctuations. Furthermore, the simulation perfectly reproduces the behaviour of the data. The relative integrated difference between the efficiency computed in the data and simulation ($\epsilon_{\mathrm{Data}}/\epsilon_{\mathrm{Sim}}$) is used as the systematic uncertainty on the tracking efficiency: 1.5% at the single muon level and 3.0% for dimuons, assuming the two muons are fully independent.

---

[2] σ_{pDCA} is the width of the $p \times DCA$ distribution.

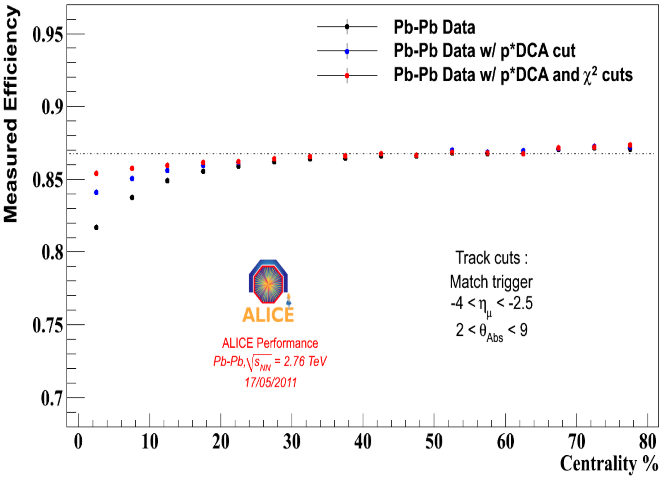

Figure 5.3: Centrality dependence of the tracking efficiency during the 2010 Pb-Pb collisions. Dotted lines indicate the integrated value in the 40-80% range

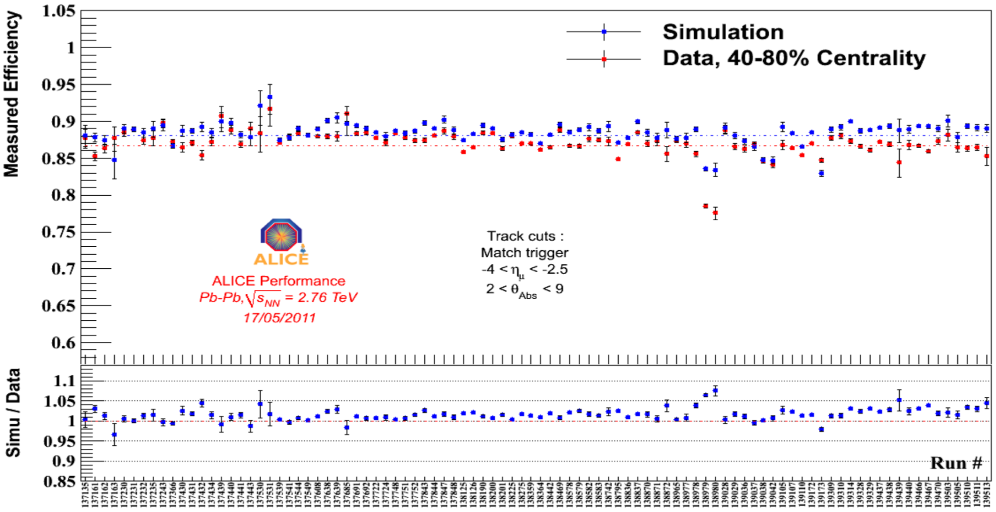

Figure 5.4: Run-per-run tracking efficiency during the LHC10h period, a pure J/ψ generator was used for the simulation. Dotted lines indicate the integrated values.

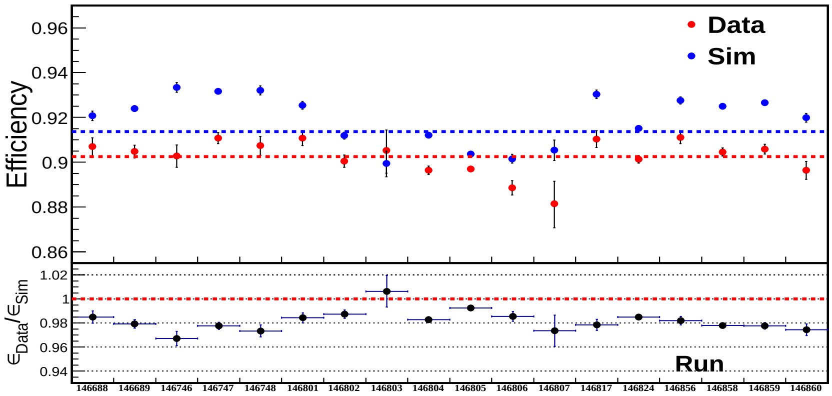

Figure 5.5: Run-per-run tracking efficiency during the LHC11a period, a pure J/ψ generator was used for the simulation. Dotted lines indicate the integrated values.

5.2.2.2 LHC11a

The pp collisions at $\sqrt{s}$ = 2.76 TeV were the first data recorded in 2011. The analysis employs the same event and track selections applied in the LHC10h period.

Figure 5.5 shows that the tracking efficiency obtained from real data is quite constant along the runs, oscillating around the integrated value (90.25 ± 0.01 %). For the pure J/ψ simulation, the computed integrated tracking efficiency was 91.37 ± 0.03 %. The associated systematic uncertainty is assessed as 1% at the single muon and 2% at the dimuon level.

5.2.2.3 LHC11h

For this period the selection criteria were partially changed compared to LHC10h and LHC11a, because the dimuon unlike sign trigger was used. As a result it was necessary to require that the tracks match the low-p_T trigger threshold (1 GeV/c) and to introduce a sharp $p_T > 1$ GeV/c cut because below this value, the trigger description in the simulation could not properly describe the data. In addition, the requirement at the end of the front absorber was set as 17.6 $< R_{Abs} <$ 89.5 cm ($2° < \Theta_{Abs} < 10°$) in order to recover some acceptance.

The first observable to be measured was the tracking efficiency as a function of the centrality of the event (left plot of figure 5.6). A flat centrality dependence was found in the 30-90% centrality range, with a 7% drop of the efficiency for the most central collisions. The real data analysis is then restricted to this 30-90% interval where the tracking efficiency presents no centrality dependence.

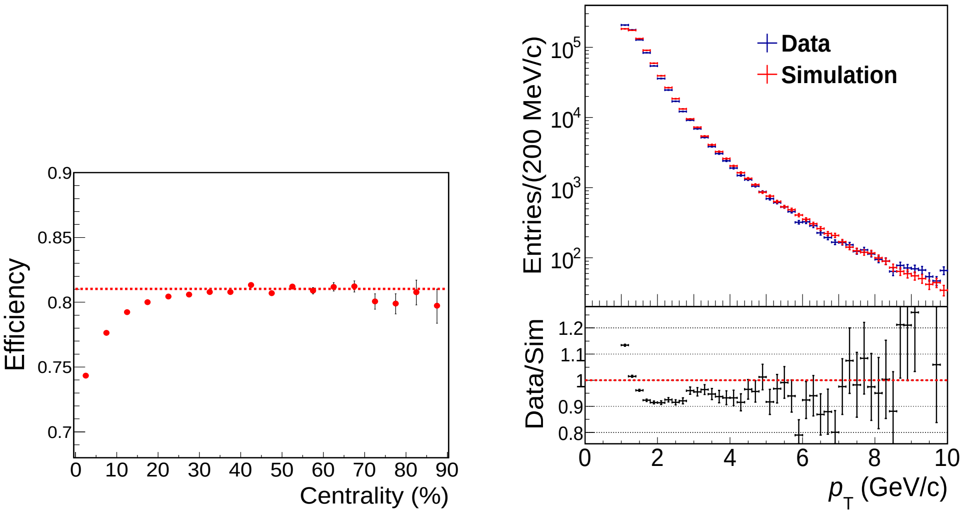

Figure 5.6: *Left*: Centrality dependence of the tracking efficiency during the 2011 Pb-Pb collisions. Dotted line indicates the integrated value in the 30-90% range. *Right*: Comparison of the reconstructed kinematic distributions between data and the tuned Monte Carlo simulation as a function of p_{T}.

Thanks to the large statistics collected in the 2011 Pb-Pb collisions, it was possible to compute the tracking efficiency as a function of p_{T} and y. Muons from a pure J/ψ generator did not match the kinematic distributions from the data. For this reason a Monte Carlo tuned single muon parametrization was used. This tune was performed on the single muon kinematic distributions from real data in the 30-90% centrality interval. Figure 5.7 and the right plot of figure 5.6 show the comparison between the reconstructed tuned single muon parametrisation and the real data. A fair agreement was found for the p_{T}, y and ϕ distributions.

Figure 5.8 shows the measured tracking efficiency as a function of the 134 runs of the period. The efficiency is rather constant for the first 107 runs but then there is a first drop of 6% due to a HV trip in chamber 8. After 16 runs the efficiency presents a second drop of 7%, once again because of a HV trip but now in chamber 10. After 5 runs, the latter problem was resolved and the tracking efficiency increases by 6% for the last 6 runs. Despite these variations in the run configuration the simulation always follows the trend of the data, indicating that the aforementioned readout problems are well reproduced.

The integrated p_{T} and y ratio, $\epsilon_{\mathrm{Data}}/\epsilon_{\mathrm{sim}} \approx 0.96$, indicates that the systematic uncertainty for single muons is 4% and 8% for dimuons. However, this estimation was made by assuming that the two muons are fully independent and it was then decided to find out a more realistic effect at the J/ψ level.

For the integrated case, and running over a pure J/ψ simulation, a global

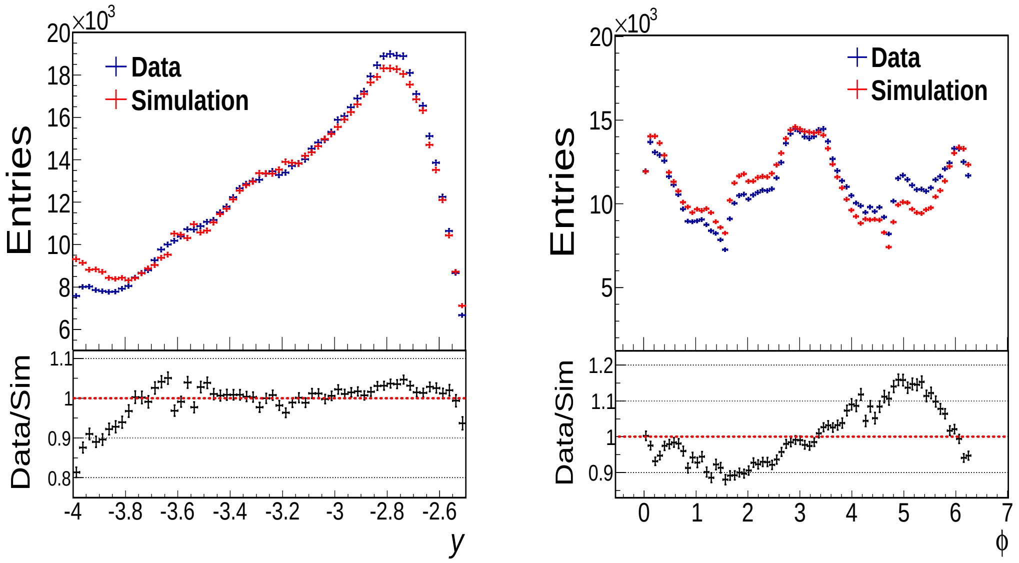

Figure 5.7: Comparison of the kinematic distributions between data and the tuned Monte Carlo simulation as a function of y (*left*) and ϕ (*right*).

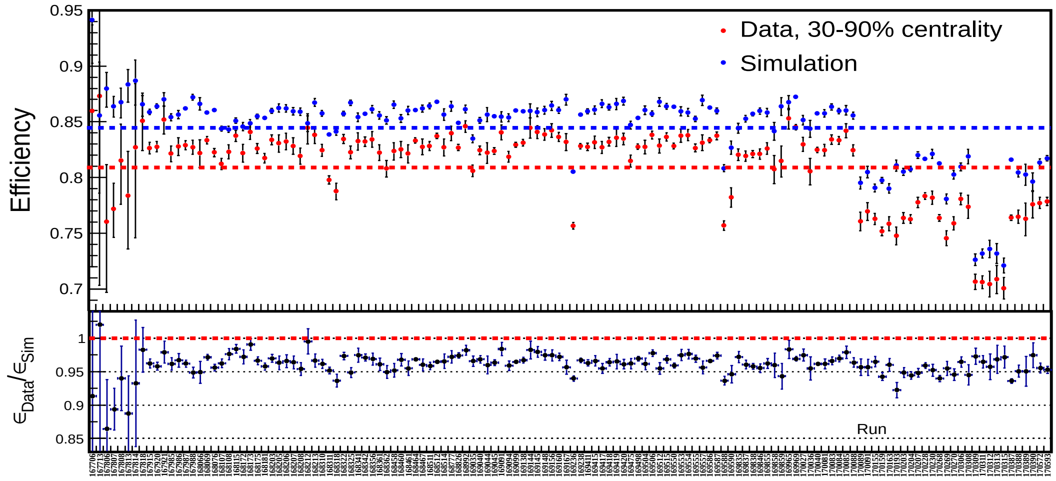

Figure 5.8: Run per run tracking efficiency during the LHC11h period, a generator of parametrized single muons was used for the simulation. Dotted lines indicate the integrated values.

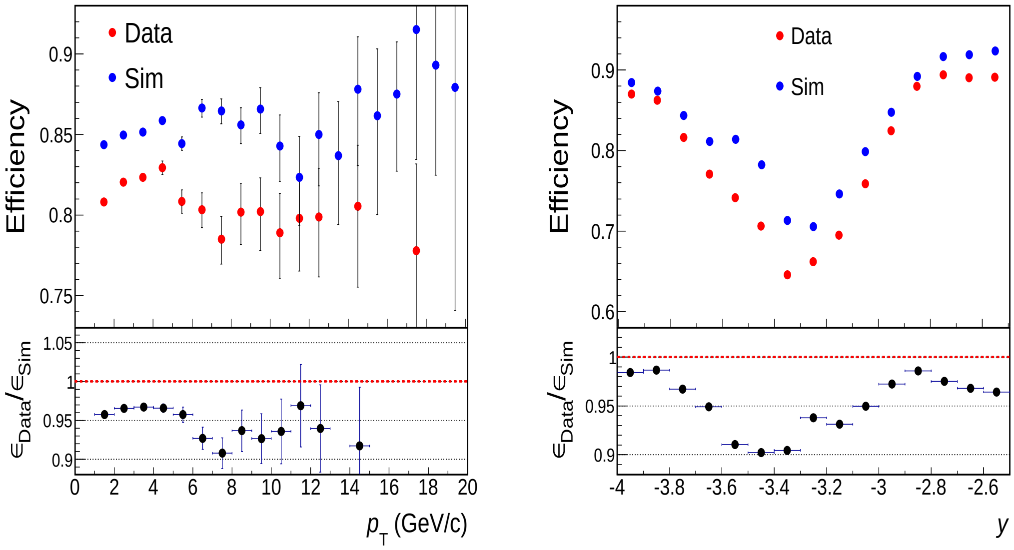

Figure 5.9: Comparison of the tracking efficiency obtained from data and the simulated single muon parametrisation as a function of p_T (*left*) and y (*right*).

survival probability of 0.96 (obtained from the integrated ratio $\epsilon_{\text{Data}}/\epsilon_{\text{sim}}$ in figure 5.8) is assigned to all the muons. A random number generator produces uniformly distributed numbers that are associated to all muons, and if the generated number results to be larger than the global one the track is rejected. The surviving opposite sign tracks are then paired into a J/ψ^S. The procedure is repeated keeping all the muons to form J/ψ. The ratio $J/\psi^S/J/\psi$ quantifies the systematic uncertainty for the J/ψ: 9% for the integrated p_T and y.

The corresponding comparison of the tracking efficiency vs p_T and y between data and simulation, with the tuned single muon parametrization, is shown in figure 5.9. It is clear that there is not a good agreement between both data sets: differences range from 3 to 9% for p_T and from 1 to 10% for y. If the two decaying muons from the J/ψ are considered fully independent the systematic uncertainties for dimuons with, for example, $-3.6 < y < -3.3$ would amount up to 20%.

As in the integrated p_T and y case, it was necessary to compute the effect of the single muon inefficiencies at the J/ψ level. The difference was that the p_T/y global survival probabilities (given by $\epsilon_{\text{Data}}/\epsilon_{\text{sim}}$) of the muons vary from bin to bin as shown in figure 5.9. The ratio $J/\psi^S/J/\psi$, where the systematic uncertainties are extracted, is shown in figure 5.10.

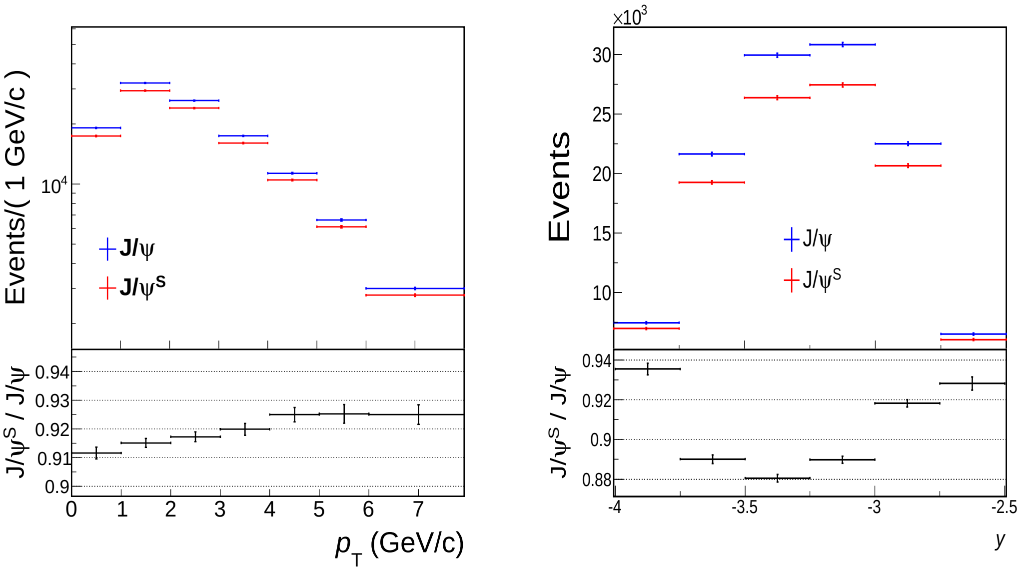

Figure 5.10: Comparison between J/ψ^S and J/ψ vs p_{T} (*left*) and y (*right*).

5.2.3 Chambers efficiency evolution

As the tracking efficiency studies described in this chapter were performed along one year of data taking in the ALICE muon spectrometer, it is then worth to take a look to the evolution of the efficiency of the tracking chambers. From the left panel of figure 5.11 it is clear that, except for chambers 1 and 2, the efficiency of the chambers varies from one period to another. The tracking efficiency is better at the beginning of the year, after the winter shutdown once the chambers have been repaired. In particular chamber 3 had an efficiency of 96% in March 2011 (LHC11a) while for the Pb-Pb collisions at the end of the same year (LHC11h) this value dropped down to 58%. The chambers from the station 4 and 5 had a poor performance as their efficiencies were always below 90%.

In the right plot of figure 5.11 shows the ratio $\epsilon_{\mathrm{Sim}}/\epsilon_{\mathrm{Data}}$ for each chamber. The agreement between data and simulation, except for chambers 3, 9 and 10, is fairly good as the difference is never more than 3%. Chamber 3 presents the worst ratio among all in the last period, indicating that the more damaged a chamber is, the more difficult is to be correctly reproduced by the simulation. In chambers 3, 8 and 9, the simulation is systematically overestimating the efficiency in all the periods.

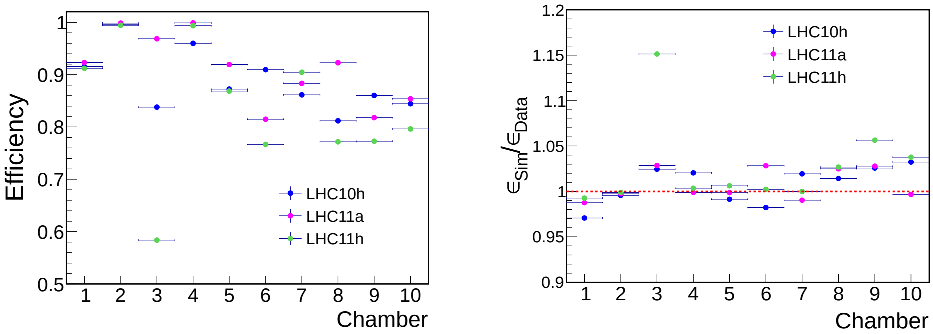

Figure 5.11: Evolution of the efficiency of the tracking chambers (*left*) and $\epsilon_{\text{Sim}}/\epsilon_{\text{Data}}$ ratio (*right*) along the three periods studied.

5.3 Correlated effects

During data taking, or offline reconstruction, parts of the detector are removed when not fulfilling the quality requirements (voltage trips, high occupancies, missing pedestals, etc). In a station, two inefficient areas located in front of each other lead to a correlated inefficiency. All particles crossing these Correlated Dead Areas (CDA) will not be reconstructed because they will be a N_{0-0} type (see left panel of figure 5.1).

Figure 5.12 shows the cluster distribution of station 5 during one run of the 2010 Pb-Pb collisions. The white areas indicate parts of the detector that are either removed from the readout configuration or either inefficient (no high voltage) for particle detection. The orange rectangles highlight a CDA in the DE 25 of chamber 9 and 10. As a consequence, the computed efficiency of the chambers (equations 5.1 and 5.2) will be overestimated: there are more particles going through the chambers than originally computed. This indicates that the efficiency formulas expressed up to now only take into account the uncorrelated inefficiencies present in the chambers, but they are blind to the correlated ones. It is then necessary to correct equations 5.1 to 5.5 by including the effect of the CDA found in the tracking chambers.

The identification of the Correlated Dead Areas is done by exploiting the X-Y symmetry of each chamber (figure 5.13): symmetrical DE must, approximately, detect the same amount of tracks. A deficit in the number of tracks measured by a detection element relative to its symmetrical ones would indicate the presence of a CDA.

First, it is necessary to compute the number of clusters detected by DE i:

$$N_{\text{Cluster}}^{\text{DE}\,i} = N_{i-j} + N_{i-0},$$

and then use $\epsilon_{\text{DE}\,i}$ (analogous to equation 5.1) to correct $N_{\text{Cluster}}^{\text{DE}\,i}$ by the

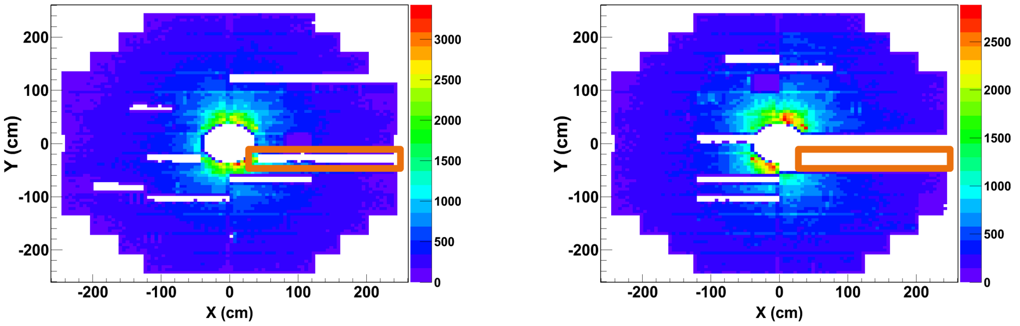

Figure 5.12: Example of the cluster distribution in station 5, chambers 9 (*left*) and 10 (*right*), during one run of the 2010 Pb-Pb collisions. The orange rectangles highlight a CDA in the DE 25 of both chambers.

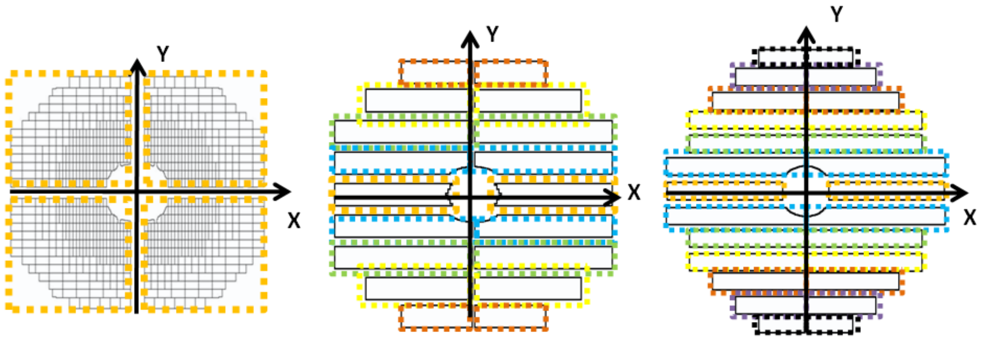

Figure 5.13: Symmetric X-Y detection elements marked by rectangles of the same colour in stations 1 and 2 (*left*), 3 (*middle*) and 4 and 5 (*right*).

uncorrelated inefficiencies present in the DE:

$$\text{Corrected } N^{\mathrm{DE}\,i}_{\mathrm{Cluster}} = \frac{N^{\mathrm{DE}\,i}_{\mathrm{Cluster}}}{\epsilon_{\mathrm{DE}\,i}}.$$

The Corrected $N^{\mathrm{DE}\,i}_{\mathrm{Cluster}}$ of symmetric detection elements in each station are plotted together (figure 5.14). For each group of symmetric DE the mean of the Corrected $N^{\mathrm{DE}\,i}_{\mathrm{Cluster}}$ is computed and a band of ±20% the mean is drawn.

All DE whose Corrected $N^{\mathrm{DE}\,i}_{\mathrm{Cluster}}$ lie in or above this safe band are considered to have the same number of entries, while those below this area would signal a CDA. The left plot of figure 5.14 shows how a well behaved (no CDA) symmetric DE look like, while the right plot indicates how a CDA is visible by using the Corrected N^{i}_{Cluster}. In fact the CDA detected in this figure corresponds to the one signaled in figure 5.12.

Once a CDA has been detected, the missing number of tracks relative to the mean of the three properly working DE gives access to an estimation of

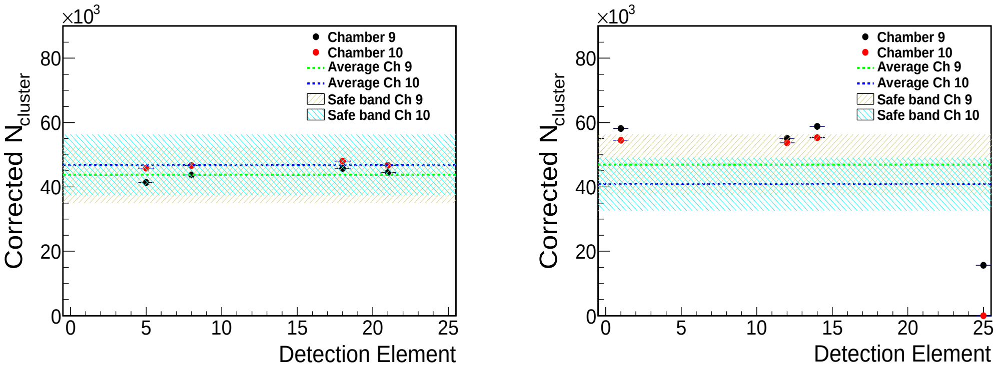

Figure 5.14: Example of symmetric X-Y detection elements in station 5: no CDA (*left*) and CDA (*Right*) found during the LHC10h period.

N_{0-0} that is called N_{0-0}^{est}. The next step is to use N_{0-0}^{est} to correct the efficiencies previously computed for the chamber i or j (equation 5.1 or 5.2):

$$\epsilon'_{\text{Ch}\,i} = \frac{N_{i-j}}{N_{i-j} + N_{0-j} + N_{0-0}^{\text{est}}} \ ,$$

$$\epsilon'_{\text{Ch}\,j} = \frac{N_{i-j}}{N_{i-j} + N_{i-0} + N_{0-0}^{\text{est}}} .$$

It is important to emphasize that only the efficiency of one chamber per station is corrected. Indeed, correcting both chambers would erroneously imply that the tracking reconstruction algorithm requires two cluster per station to reconstruct a track in the muon spectrometer.

The loss on the efficiency affects the whole muon spectrometer by the same amount and not only to one station: the number of tracks not detected (N_{0-0}^{est}) by the station where the CDA was found are the same number of tracks not detected by all the stations because these tracks are not reconstructed. The correction of the total tracking efficiency (equation 5.5) is then performed as:

$$\epsilon'_{\text{Tracking}} = \epsilon_{\text{Tracking}} \left(\frac{\epsilon'_{\text{Ch}}}{\epsilon_{\text{Ch}}} \right) . \tag{5.6}$$

The CDA corrected tracking efficiency is then compared to the true tracking efficiency that is obtained directly from the Monte Carlo generator.

5.3.1 Results

As the method relies on the occupancy distribution of tracks in the chambers at the detection element level, the simulated muons must have a kinematical distribution as close as possible to the muons from real data.

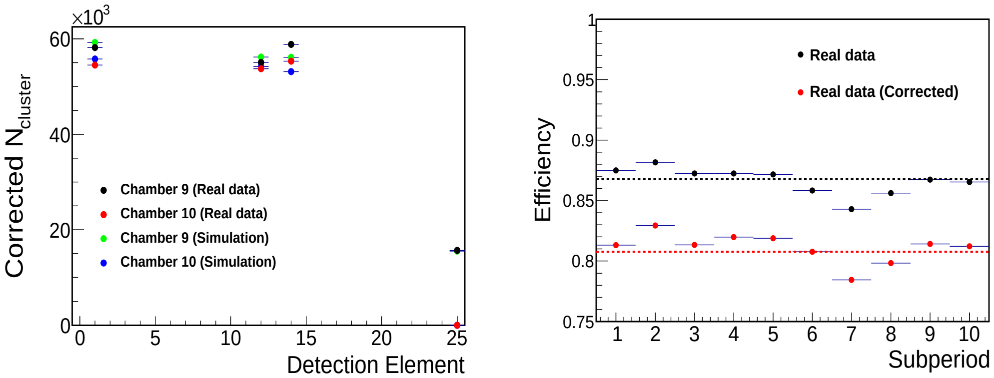

Figure 5.15: *Left:* Principal correlated inefficiency during the 2010 Pb-Pb collisions. *Right:* Tracking efficiency extracted from real data for ten subperiods before and after the correction from CDA, dotted lines indicate the integrated values.

5.3.1.1 LHC10h

The pure J/ψ simulation used to extract the tracking efficiency in section 5.2.2.1 could not reproduce the distribution of the clusters found in the data. It was necessary to use a single muon parametrisation tuned to the kinematic distributions of the muons from real data. Left plot of figure 5.15 shows that the simulation reproduces correctly the cluster distribution and that the detected CDA of figures 5.12 and 5.14 is also visible in the simulation. In fact, this is the most important CDA present in this period as it is responsible for a decrease of 5% in the total tracking efficiency. The second CDA was spotted in the DE 3 of station 3, causing a decrease of an additonal 1%.

This study can not be performed run-per-run because large statistics are needed to compute the efficiencies at the DE level, specially for those detection elements located in the borders of the chambers. In order to study the evolution of these correlated inefficiencies, the 94 runs were divided in 10 subperiods, all of them containing approximately the same number of reconstructed tracks. For each subperiod the tracking efficiency was computed (equation 5.5) and, if necessary, corrected by the correlated inefficiencies (equation 5.6).

The CDA uncorrected and corrected tracking efficiency are presented in figure 5.15. The ten subperiods present the same CDA (DE 25 in station 5 and DE 3 in station 3), and they are all corrected by the same amount (6%). This is a confirmation of the stability of the detector along the data taking, as already observed in figure 5.4. The tracking efficiency in real data, after correction due to CDA, is 80.77 ± 0.03 %.

The procedure described above was applied to the simulation. The same CDA found in real data were also detected in this case, requiring the tracking efficiency computed from the simulation to be corrected by 6% (integrated and

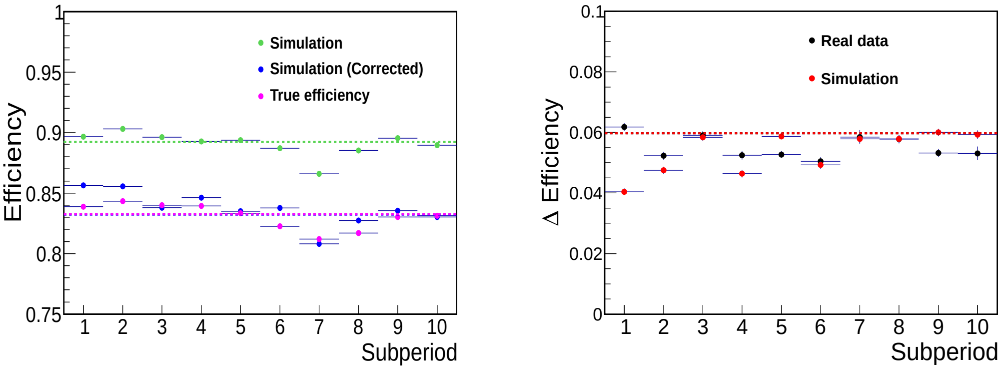

Figure 5.16: *Left*: Tracking efficiency extracted from simulation for ten subperiods before and after the correction from CDA, dotted lines indicate the integrated values. *Right*: ΔEfficiency for real data and simulation, dotted lines indicate the integrated values (overlapped).

per subperiod). The left plot of figure 5.16 compares the corrected tracking efficiency from simulation to the true efficiency, yielding a very good agreement, both integrated and per subperiods. This is a confirmation of the applicability of the method developed here. The tracking efficiency obtained from simulations, after correction due to CDA, is 83.24 ± 0.03 %.

In order to define the systematic uncertainty from the correlated inefficiencies, it is necessary to compare the amount of correction due to correlated inefficiencies in data and simulation. The variable ΔEfficiency is created, and is defined as the difference between the CDA uncorrected and the corrected tracking efficiency. The relative difference between the ΔEfficiency extracted from real data and the ΔEfficiency obtained from the simulation is taken as the systematic uncertainty associated to the correlated inefficiencies.

The right plot of figure 5.16 shows that the integrated ΔEfficiency for data and simulation has the same value of 6% (dotted lines are overlapped), indicating that the tracking efficiency from data and simulation is corrected by the same amount. A conservative 1% was then established as the systematic uncertainty arising from correlated inefficiencies at the single muon level and 2% for dimuons.

The total systematic uncertainty arising from the tracking efficiency is computed by adding[3] the systematic uncertainties due to the uncorrelated plus the correlated effects, this is, 1.5% + 1% = 2.5% for single muons and 3% + 2% = 5% for dimuons.

---

[3] The systematic uncertainty arising from the uncorrelated and correlated inefficiencies are not independent so they must not be added in quadrature.

5.3.1.2 LHC11a

Due to the very good status of the tracking chambers in this period it was possible to study the correlated effects with the pure J/ψ Monte Carlo used to extract the tracking efficiency in section 5.2.2.2.

Only a very small correlated inefficiency was found in the data, causing a decrease of less than 1% in the tracking efficiency. The final CDA corrected tracking efficiency is then 89.93 ± 0.01 %. In the simulation no CDA was found. The systematic uncertainty due to the correlated inefficiencies was then established as 1% for single muons and 2% for dimuons.

The total systematic uncertainty at the single muon level includes the systematic uncertainty due to uncorrelated (1%) and correlated effects (1%), adding up to 2%. For dimuons, the total systematic uncertainty is taken as 4%.

Unlike the 2010 Pb-Pb collisions, in this period the true efficiency (97%) was found to be in disagreement to the measured tracking efficiencies from the simulation by 6%. This difference shows that the tracking efficiency determination has a bias for this data set. However, since the bias is the same in the simulation and in the real data, it does not have an impact on the method that gives the systematic uncertainties on the tracking efficiency.

5.3.1.3 LHC11h

The same single muon parametrization employed to extract the tracking efficiency in section 5.2.2.3 was used to detect the CDA.

In this case only one CDA (figure 5.17) was found when analysing the integrated period, both in real data and in simulation. In figure 5.18 it is possible to observe the signature of the correlated inefficiency: DE 18 of chambers 7 and 8 contains less clusters than their symmetrics.

In 2011 the heavy-ion data taking took place during almost one month. For this reason the LHC11h period was divided in subperiods to study the evolution of the CDA. The right plot of figure 5.18 depicts the tracking efficiency calculated from real data with and without the correction due to the correlated inefficiencies. For the first subperiod no correction was needed, the CDA (DE 18 of chambers 7 and 8) appears at the end of the second subperiod so the correction is small. Subperiods three to six are affected by this same CDA, but at the end of the LHC11h period there is an increase on the amount of the correction: from 2% in the sixth subperiod up to 9% in the last one. The reason is because a new CDA (DE 25 from station 5, as in LHC10h) appears at the end of the seventh subperiod. The corrected tracking efficiency for real data is computed as 79.26 ± 0.04 %.

The same procedure was carried out on the simulation (left plot of figure

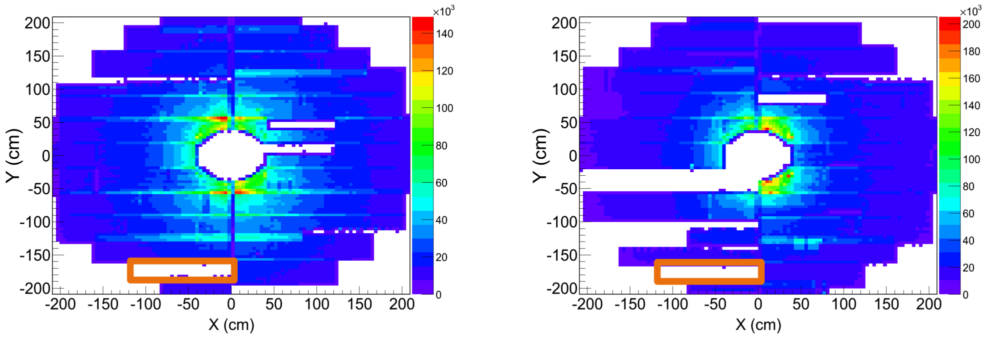

Figure 5.17: Example of the cluster distribution in station 4, chambers 7 (*left*) and 8 (*right*), during the LHC11h period. The orange rectangle signal a CDA in the DE 18 of both chambers.

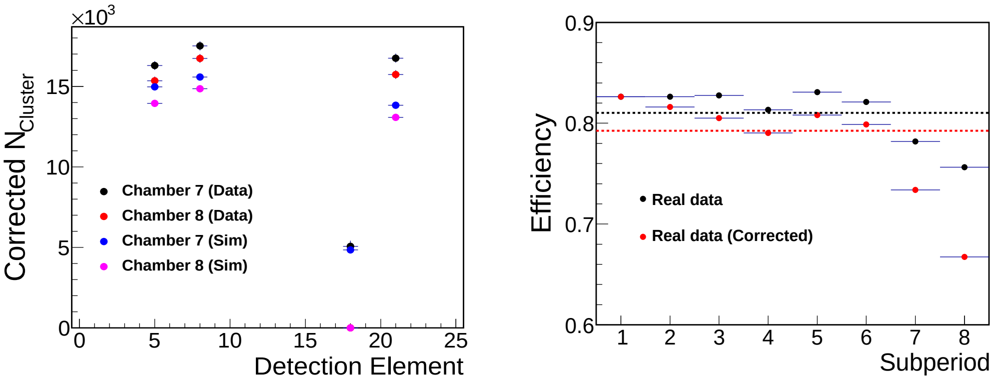

Figure 5.18: *Left:* Principal correlated inefficiency during the 2011 Pb-Pb collisions. *Right:* Tracking efficiency extracted from real data for eight subperiods before and after the correction from CDA, dotted lines indicate the integrated values.

5.19), with similar results to real data, so the recomputed tracking efficiency is 82.72 ± 0.02 %. The difference between the true tracking efficiency (87.5%) and the corrected tracking efficiency from simulation amounts to 5%. This bias is comparable to the one observed in the LHC11a period.

The ΔEfficiency variable (right panel of figure 5.19) indicates the amount of correction due to CDA, applied to the tracking efficiency obtained in real data and simulation. In both data sets the integrated correction is about 2%, indicated by the (overlapped) dotted lines. The presence of the CDA lowers the efficiencies in a similar percentage in all the subperiods, except for the last two.

The systematic uncertainties due to correlated inefficiencies is then 1% at the single muon level and 2% for dimuons.

The total integrated p_{T} and y systematic uncertainty for dimuons includes

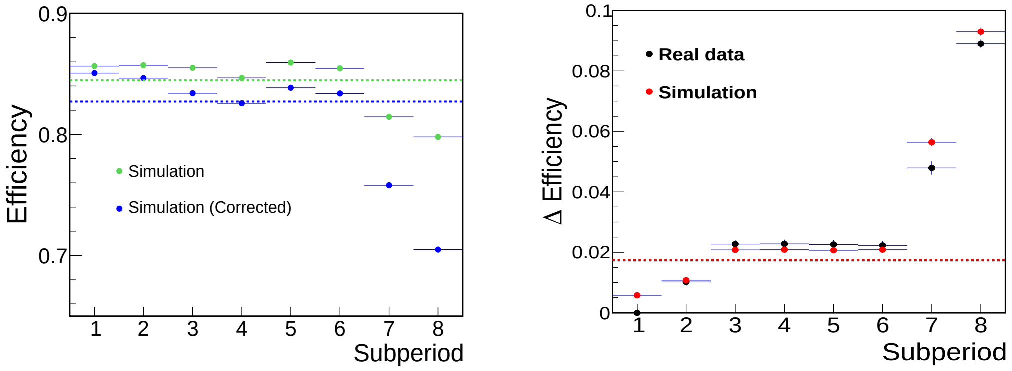

Figure 5.19: *Left*: Tracking efficiency extracted from simulation for eight subperiods before and after the correction from CDA, dotted lines indicate the integrated values. *Right*: ΔEfficiency for real data and simulation, dotted lines indicate the integrated values (overlapped).

the systematic uncertainty due to uncorrelated (9%) and correlated effects (2%), adding up to 11%. For the transverse momentum and rapidity, the total systematic uncertainty is obtained by adding the 2% due to the correlated effects to each $J/\psi^S/J/\psi$ bin shown in the plots of figure 5.10 (systematic uncertainty due to uncorrelated effects).

Chapter 6

J/ψ analysis in the 2011 Pb-Pb collisions

This chapter contains the main physics results of the thesis. The first part is the description of the data recorded during the 2011 Pb-Pb collisions, the J/ψ signal extraction, the normalization procedure and the technique used to determine the $A \times \epsilon$ corrections. The second part is dedicated to the estimation of the systematic uncertainties arising from different sources. Finally, the last part presents the inclusive J/ψ R_{AA}, $\langle p_{\mathrm{T}} \rangle$ and $\langle p_{\mathrm{T}}^2 \rangle$ together with comparisons to theoretical models and other experiments.

6.1 The 2011 Pb-Pb collisions

The analysis is based on 136 runs collected during the LHC11h period, all of these runs passed the Quality Assurance checks: trigger and tracking efficiencies, number of tracks per trigger, number of clusters per track, cluster sizes, etc.

The Minimum Bias (MB) trigger is defined as the coincidence of a signal in VZERO-A and VZERO-C detectors synchronized with the passage of two colliding lead bunches. This MB trigger provides high triggering efficiency ($\geq 95\%$) for hadronic interactions. To improve the purity, a threshold on the energy deposited in the neutron ZDCs reject the contribution from electromagnetic processes at L1 trigger level. Beam induced background was further reduced at the offline (physics selection) level by timing cuts on the signals from the VZERO and from the ZDC.

After a limited number of colliding bunches (low luminosity) period, the MB trigger was down-scaled at the L0 trigger level to open the DAQ bandwidth to more rare triggers. In particular several muon specific triggers were activated:

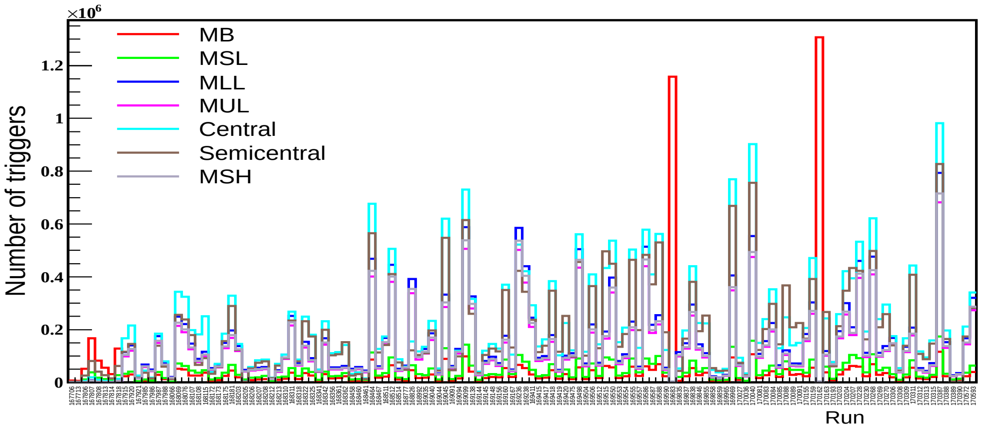

Figure 6.1: Distribution of triggers along the LHC11h period.

- Single muon low-p_{T} ($p_{\mathrm{T}}^{\mu} \geq 1$ GeV/c) or MSL.
- Single muon high-p_{T} ($p_{\mathrm{T}}^{\mu} \geq 4$ GeV/c) or MSH.
- Unlike-sign dimuon low-p_{T} ($p_{\mathrm{T}}^{\mu} \geq 1$ GeV/c on each muon) or MUL.
- Like-sign dimuon low-p_{T} ($p_{\mathrm{T}}^{\mu} \geq 1$ GeV/c on each muon) or MLL.

In addition two other triggers, relevant for the present thesis, were used: the Central and Semicentral. These are triggers generated with the V0 detector but with an online selection on the centrality. The Central trigger is defined in the 0-10% centrality range and the Semicentral in the 10-50% interval.

Figure 6.1 shows the distribution of the number of the different triggers along the 136 runs. The downscaling of the MB trigger occurred at the very beginning of the period. Also notice there are two runs (169683 and 170162) that only contain this Minimum Bias trigger.

The first goal of this chapter is to compute the inclusive Nuclear Modification Factor for the J/ψ in Pb-Pb collisions as a function of three different observables: centrality, p_{T} and y. For this purpose equation 1.6 is used, however, for practical purposes it will be re-written here as:

$$R_{\mathrm{AA}} = \frac{Y^{AA}_{J/\psi}(\Delta p_{\mathrm{T}}, \Delta y)}{\langle T_{\mathrm{AA}} \rangle \times \sigma^{pp}_{J/\psi}(\Delta p_{\mathrm{T}}, \Delta y)}, \tag{6.1}$$

where $\langle T_{\mathrm{AA}} \rangle$ is the Nuclear Overlap Function (see appendix A), $\sigma^{pp}_{J/\psi}(\Delta p_{\mathrm{T}}, \Delta y)$ is the inclusive J/ψ cross section measured at the same energy[1] and $Y^{AA}_{J/\psi}(\Delta p_{\mathrm{T}}, \Delta y)$ the inclusive invariant J/ψ yield:

---

[1] In the text this will also be called as the *pp reference*.

$$Y^{\mathrm{AA}}_{J/\psi}(\Delta p_{\mathrm{T}}, \Delta y) = \frac{N_{J/\psi}}{BR_{J/\psi\to\mu^+\mu^-} \times N_{MB} \times A \times \epsilon}. \tag{6.2}$$

The Nuclear Modification Factors are divided in two groups: single differential and multidifferential. In the first one the R_{AA} is extracted as a function of:

- The centrality with $p_{\mathrm{T}} < 8$ GeV/c and $2.5 < y < 4$.
- p_{T} with $2.5 < y < 4$ and centrality 0-90%.
- y with $p_{\mathrm{T}} < 8$ GeV/c and centrality 0-90%.

The multidifferential R_{AA} are extracted as a function of:

- p_{T} for three centrality bins (0-20%, 20-40% and 40-90%) with $2.5 < y < 4$.
- The centrality for three p_{T} bins (0-2 GeV/c, 2-5 GeV/c and 5-8 GeV/c,) with $2.5 < y < 4$.
- The centrality for three rapidity bins (2.5-3, 3-3.5 and 3.5-4) with $p_{\mathrm{T}} < 8$ GeV/c.

The second goal is to extract the J/ψ $\langle p_{\mathrm{T}} \rangle$ and $\langle p^2_{\mathrm{T}} \rangle$. They are computed from equation 6.2 as a function of p_{T} for three centrality bins (0-20%, 20-40% and 40-90%) with $2.5 < y < 4$.

In the following sections the required quantities and their uncertainties needed to achieve the desired objectives will be determined.

6.2 Signal extraction

A total amount of 17 347 100 events selected with the MUL trigger in the 0-90% centrality range (MUL_{events}) was used in the present studies. At the single muon level, the selection criteria include:

- $-4.0 < \eta < -2.5$ to ensure muons are within the acceptance of the muon spectrometer.
- Tracks must match the low-p_{T} trigger threshold to have a concordance with the MUL trigger.
- $17.6 < R_{\mathrm{Abs}} < 89.5$ cm, or equivalently, $2^\circ < \Theta_{\mathrm{Abs}} < 10^\circ$.

At the dimuon level the requirements are:

- $2.5 < y < 4.0$ to restrict the analysis on dimuons within the acceptance of the detector.
- $p_T < 8.0$ GeV/c. This cut insures that the maximum transverse momentum is common to the one used in the pp reference[2].

The extraction of the number of J/ψ ($N_{\mathrm{J}/\psi}$) is performed via two methods: the first one is based directly on fits to the invariant mass unlike-sign dimuon spectrum while the second one uses the Event Mixing (EM) technique to subtract the combinatorial background. In both cases $N_{\mathrm{J}/\psi}$ is obtained by integrating the signal contribution in the whole fitting range (2-5 GeV/c).

6.2.1 Raw spectrum

The J/ψ candidates are formed by pairing opposite-sign tracks. As can be seen in figure 6.2, the J/ψ peak is clearly visible, even without any kind of background subtraction. The signal is fitted using an Extended Crystal Ball (CB2) function and the background is described with a Variable Width Gaussian (VWG), both functions are described in appendix B.

In all centrality, p_{T} and y bins, the mass (M) and width (σ) are left as free parameters, although none of them show an important p_{T}/y dependence. For the centrality studies, the number of J/ψ given by the fit shows no variation if M and σ are fixed to the 0-90% values. In all cases a negligible variation of the J/ψ yield was found by including the ψ(2S) in the invariant mass fit.

The mass value extracted from the fit in all the centrality/p_{T}/y bins is found to be systematically above the value found in the literature (3.097 GeV), however, the discrepancy is never larger than 0.5% [5]. Although not always, the σ is 15-20% larger than the width obtained by fitting the invariant mass from the embedding Monte Carlo.

The tail parameters present in the CB2 are fixed to the values obtained from the embbeding technique (explained below). On one side, these parameters are constant as a function of the centrality; on the other side, there is a strong variation among the different p_{T}/y bins. Therefore, in order to take into account such modification, the CB2 tails values used are fixed to those extracted from the embedding simulation in the corresponding kinematical bin.

The signal over background ratio (S/B) and significance ($S/\sqrt{S+B}$) are evaluated within three standard deviations with respect to the J/ψ mass pole. The S/B ranges from 0.2 at low-p_{T} up to 1 at high-p_{T}. As a function of the rapidity, the S/B varies from 0.2 for $2.5 < y < 2.75$ up to 0.6 in the most forward rapidity bin. The S/B versus centrality improves from 0.15 to 6 when the centrality of the collisions decreases.

---

[2] In the $\langle p_{\mathrm{T}} \rangle$ and $\langle p_{\mathrm{T}}^2 \rangle$ analysis this cut is not needed as the pp reference is not used.

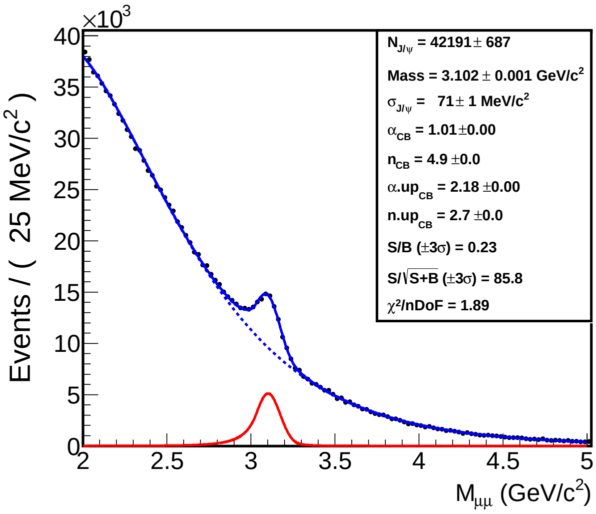

Figure 6.2: Invariant mass spectra of opposite-sign dimuons with $p_{\mathrm{T}} < 8$ GeV/c, $2.5 < y < 4$ and centrality 0-90%.

Figure 6.2 shows the integrated opposite-sign dimuon invariant mass spectrum. Figures 6.3, 6.4 and 6.5 present the signal for the different centrality ($p_{\mathrm{T}} < 8$ GeV/c and $2.5 < y < 4$), p_{T} (centrality 0-90% and $2.5 < y < 4$) and y ($p_{\mathrm{T}} < 8$ GeV/c and centrality 0-90%) bins.

6.2.2 Background subtraction via Event Mixing

The event mixing technique is commonly used in heavy-ion collisions in order to subtract the large combinatorial background that is present, in particular, in the most central collisions. This technique consists in combining tracks from different events. In such case, any possible correlation between the tracks is lost and the mixed pairs give a good description of the uncorrelated part of the dimuon background.

In the present analysis, opposite-sign mixed muons are paired by combining tracks corresponding to events selected with the MSL[3] trigger belonging to the same run and in the same centrality range. In order to have enough statistics, each MSL triggered event is mixed with the following 25 events that fired the MSL condition. The generated mixed spectra is then normalized to the data using the combination of the measured like-sign pairs [109]:

---

[3] Although the raw invariant mass spectra are extracted with the MUL trigger, different tests demonstrated that the invariant mass, p_{T} and y distributions of the unlike/like-sign mixed pairs from the MSL trigger reproduced the best the corresponding distributions obtained with the MUL trigger.

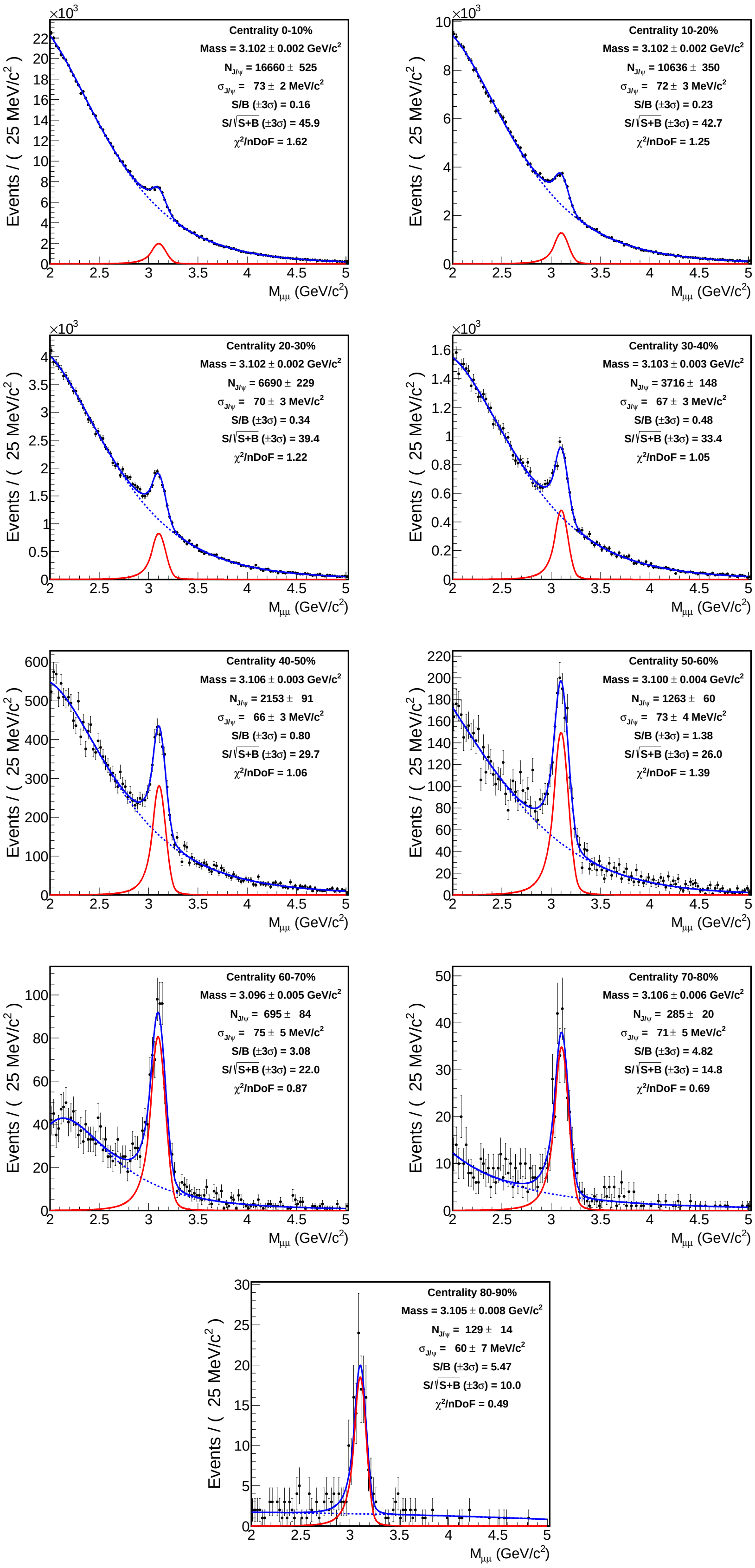

Figure 6.3: Invariant mass spectra of opposite-sign dimuons for different centralities ($p_{\mathrm{T}} < 8$ GeV/c and $2.5 < y < 4$).

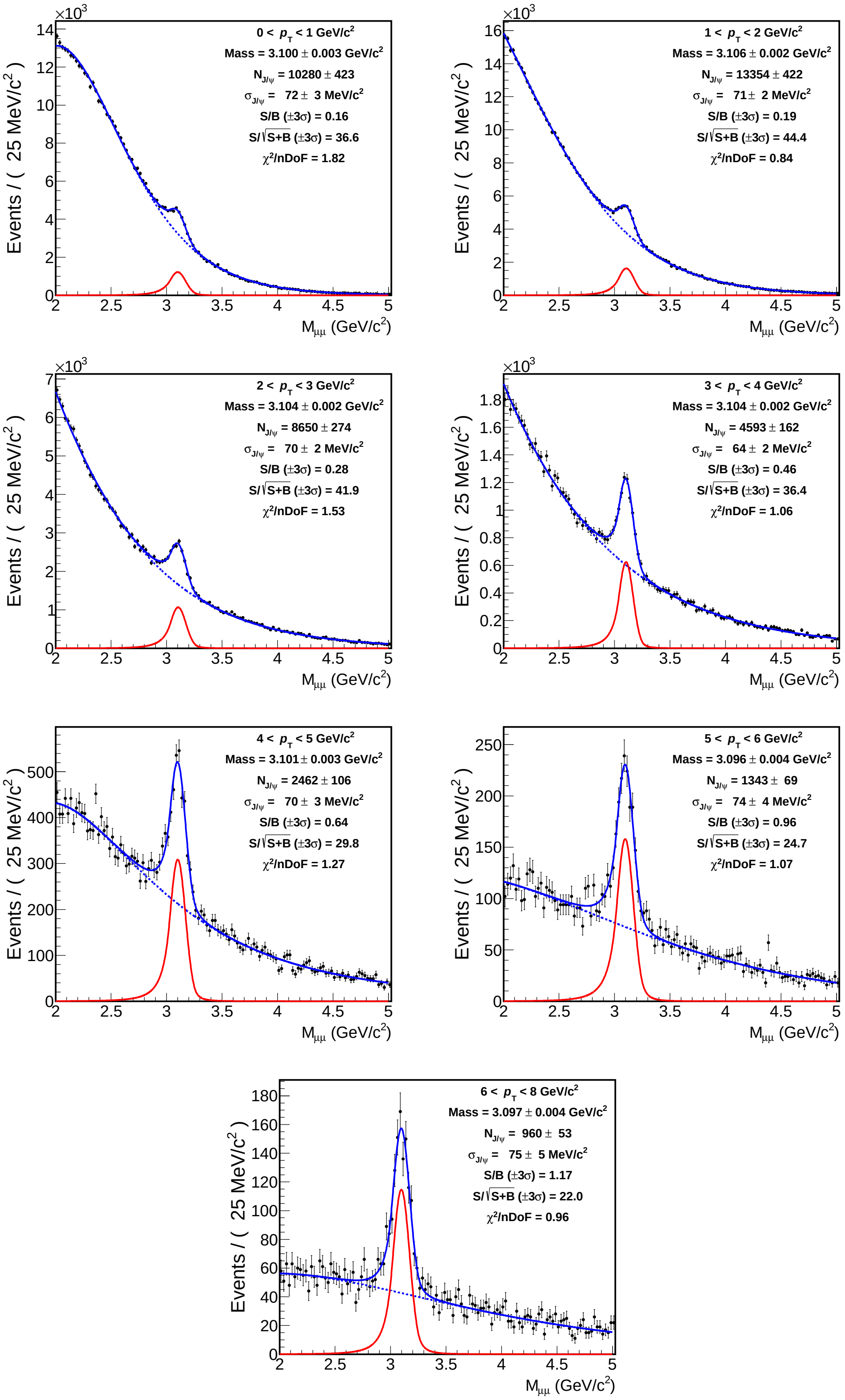

Figure 6.4: Invariant mass spectra of opposite-sign dimuons for different p_{T} ($2.5 < y < 4$ and centrality 0-90%).

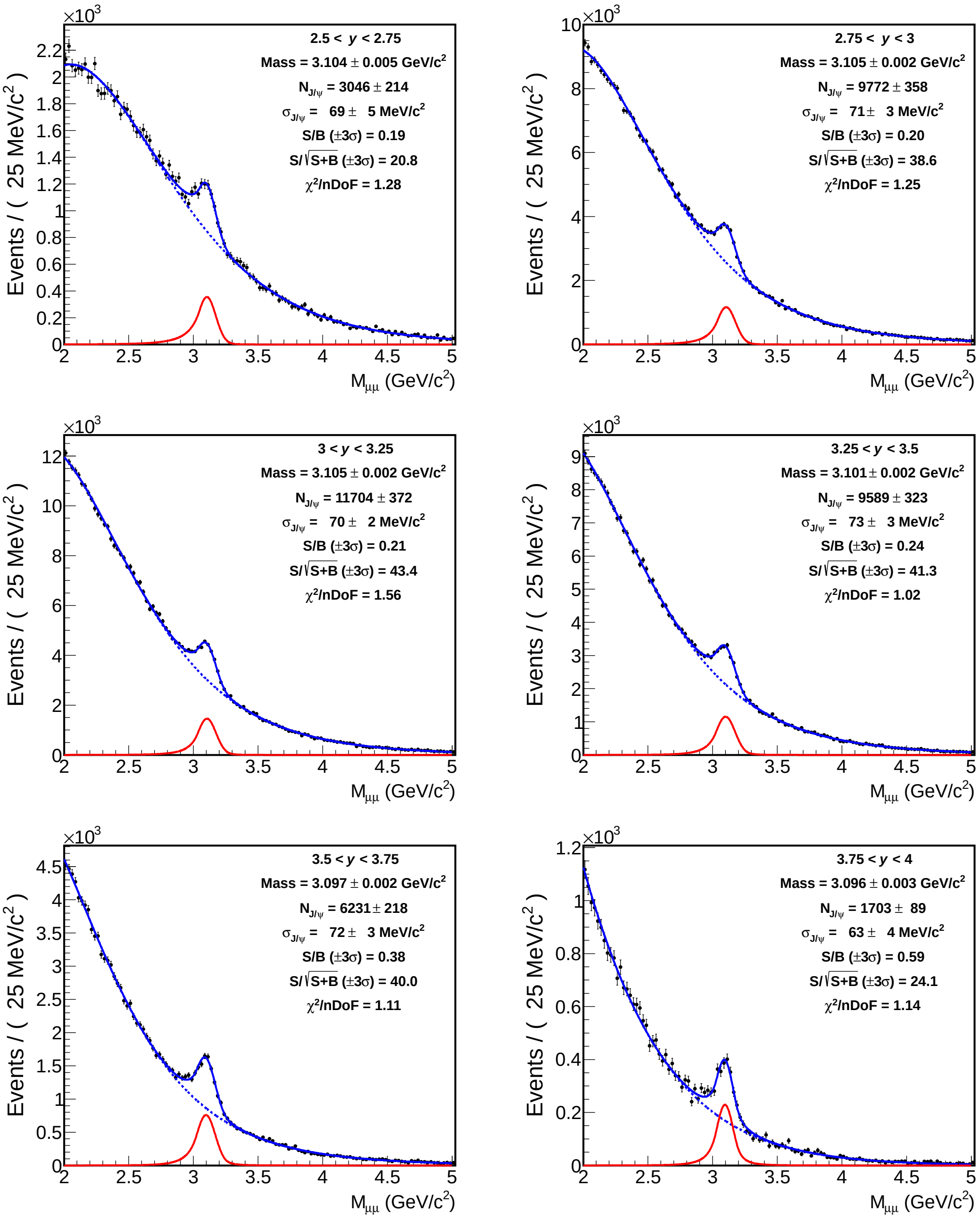

Figure 6.5: Invariant mass spectra of opposite-sign dimuons for different rapidities ($p_{\mathrm{T}} < 8$ GeV/c and centrality 0-90%).

$$\int N_{+-}^{\text{mixed}}\, dM = \int 2\, R_{\text{Mix}} \sqrt{N_{++}N_{--}}\ dM, \tag{6.3}$$

$$R_{\text{Mix}} = \frac{N_{+-}^{\text{mixed}}}{2\sqrt{N_{++}^{\text{mixed}} N_{--}^{\text{mixed}}}}\,. \tag{6.4}$$

The R_{Mix} factor, corresponding to the 0-90% centrality bin, shows deviations from unity smaller than 1% above the dimuon invariant mass of 1.5 GeV/c (figure 6.6). Comparisons of the invariant mass, p_{T} and rapidity distributions of the unlike/like-sign pairs from the same and mixed events are present in figures 6.7, 6.8 and 6.9. In all cases the ratios are compatible with the unity in the region of interest (2-5 GeV/c^2 for the invariant masses), indicating the good status of the EM.

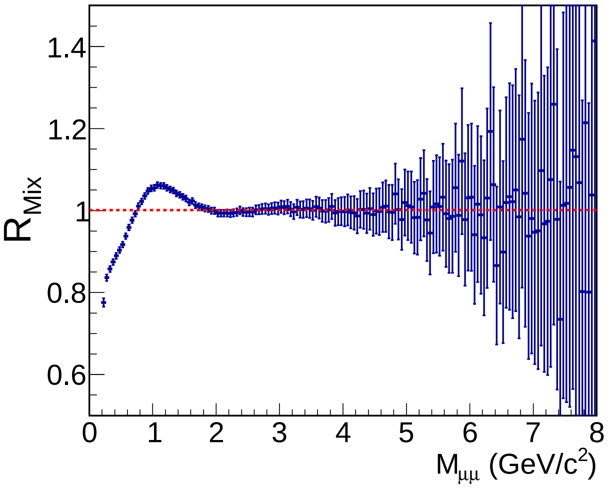

Figure 6.6: R_{Mix} factor (equation 6.4) corresponding to the 0-90% centrality bin.

The opposite-sign pair mixed spectra, once normalized to the data, is subtracted. The resulting combinatorial background subtracted spectra is, as in the previous case, fitted with a CB2 for the signal with the tails tuned to the values extracted from the embedding Monte Carlo. The remaining background is fitted with an exponential function. It was verified that choosing another function, as for example a first degree polynomial, leads to differences smaller than 1% in the extracted $N_{\text{J}/\psi}$. It was also found that variations on the integration range of equation 6.3 led to negligible differences on the number of J/ψ.

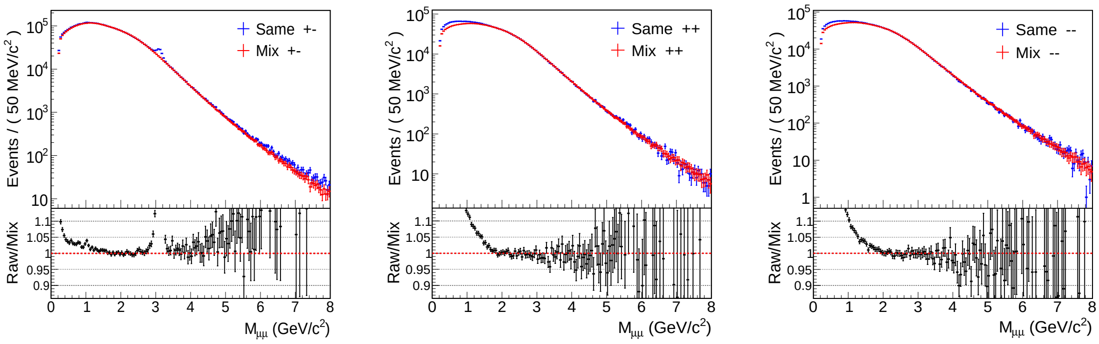

Figure 6.7: Comparison of the invariant mass spectra of unlike (*left*) and like-sign (*middle* and *right*) pairs from the same and mixed event corresponding to the 0-90% centrality.

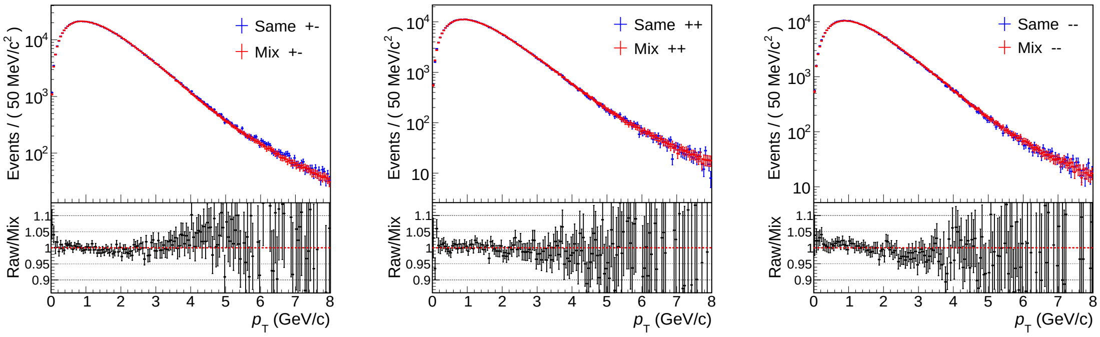

Figure 6.8: Comparison of the p_T spectra of unlike (*left*) and like-sign (*middle* and *right*) pairs from the same and mixed event corresponding to the 0-90% centrality.

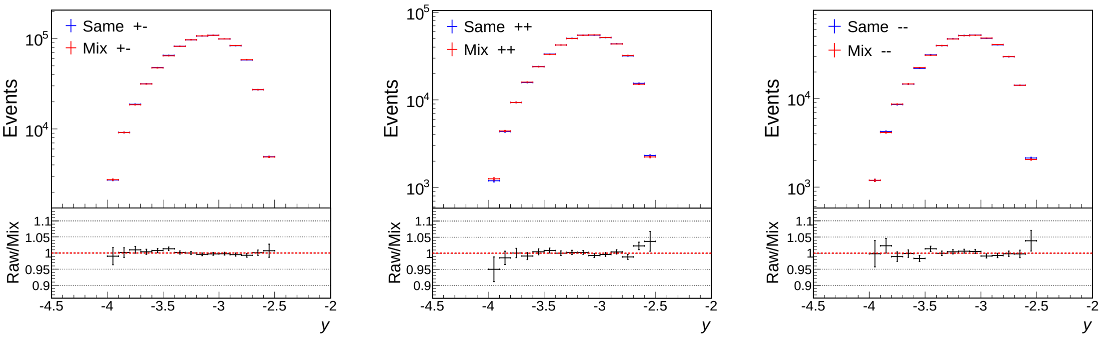

Figure 6.9: Comparison of the y spectra of unlike (*left*) and like-sign (*middle* and *right*) pairs from the same and mixed corresponding to the 0-90% centrality.

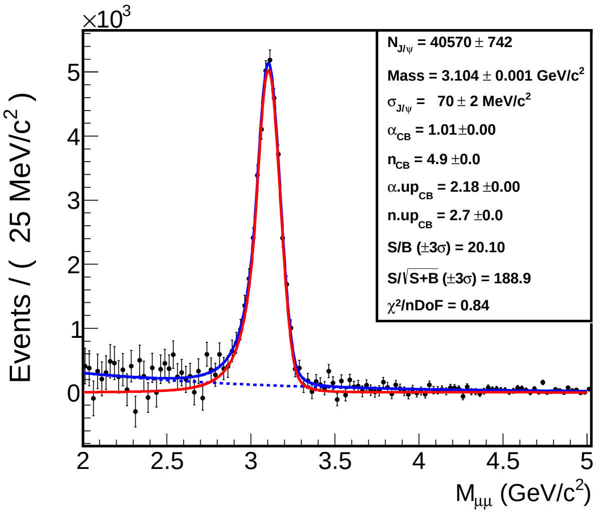

Figure 6.10: Opposite-sign dimuon invariant mass spectrum after background subtraction ($p_{\mathrm{T}} < 8$ GeV/c, $2.5 < y < 4$ and centrality 0-90%).

Figure 6.10 shows the integrated invariant mass spectra after background subtraction. Figures 6.11, 6.12 and 6.13 present the signal for the different centrality ($p_{\mathrm{T}} < 8$ GeV/c and $2.5 < y < 4$), p_{T} (centrality 0-90% and $2.5 < y < 4$) and y ($p_{\mathrm{T}} < 8$ GeV/c and centrality 0-90%) bins. In all cases the masses and widths obtained by fitting the resulting background subtracted spectra is in agreement with the corresponding M and σ extracted in the raw spectrum. Plots from figure 6.12 and 6.13 contain a dimuon invariant mass cut ($2.7 < M_{\mu\mu} < 4$) in order to reject any contribution from the J/ψ and ψ(2S).

6.3 Normalization

The MUL trigger was used to select events with higher probability to contain a J/ψ. However, in order to compute the invariant yield (equation 6.2) the number of events needed are those from the MB trigger. It is then mandatory to compute a normalization factor (F_{Norm}) that gives the probability of having a dimuon trigger when the MB condition is verified. This link can only be done with triggers having an unbiased (flat) centrality distributions, a characteristic that the MUL trigger does not fulfill. Indeed, left panel of figure 6.14 shows the centrality distribution of MUL triggers that is highly biased towards the most central events.

The reference triggers that have a flat centrality dependence are the MB, Central and Semicentral. The MB trigger (right panel of figure 6.14) presents a flat centrality distribution in the 0-90% range. The Central trigger (left panel of figure 6.15) is defined in the 0-10% range, nevertheless, it presents

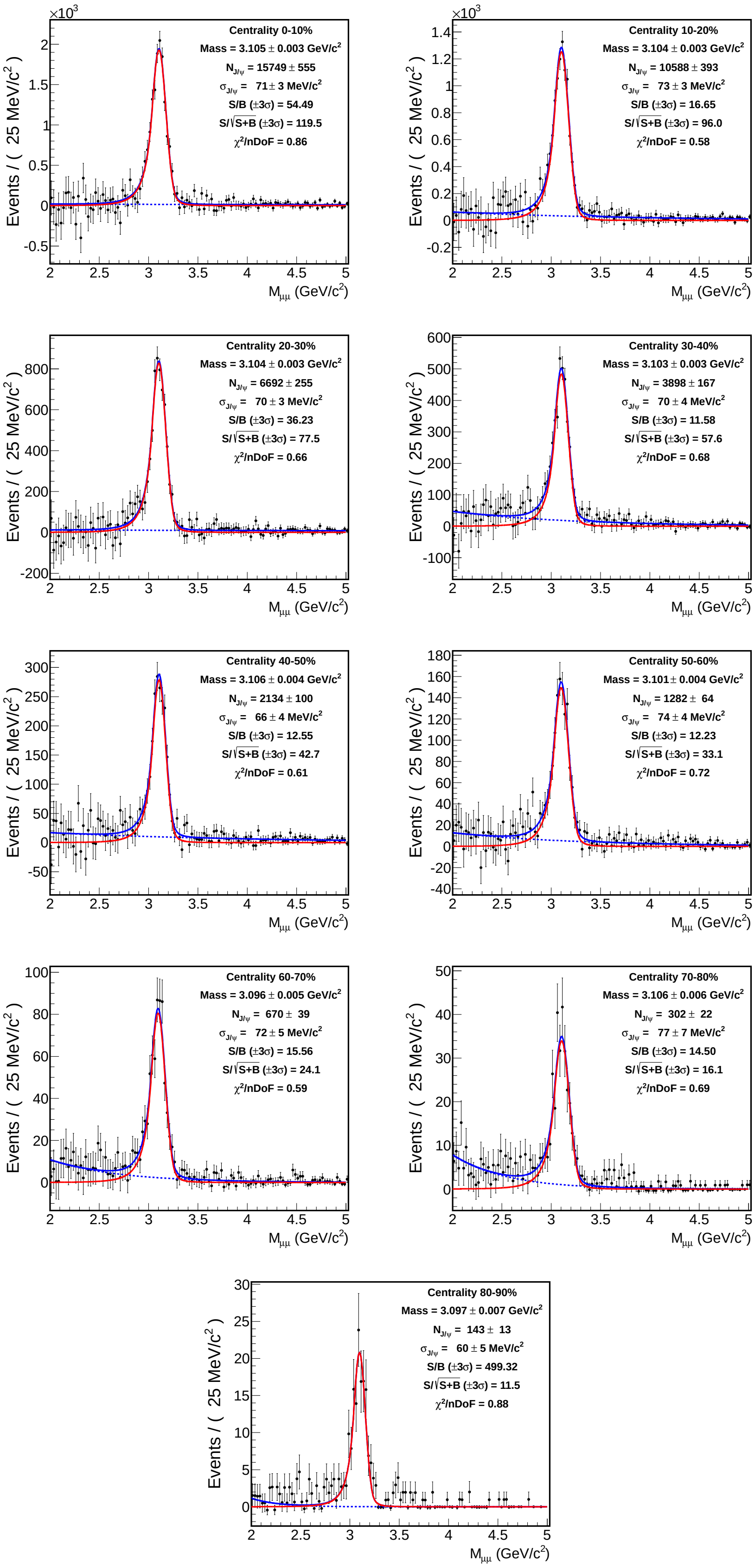

Figure 6.11: Invariant mass spectra of opposite-sign dimuons for different centralities after background subtraction ($p_T < 8$ GeV/c and $2.5 < y < 4$).

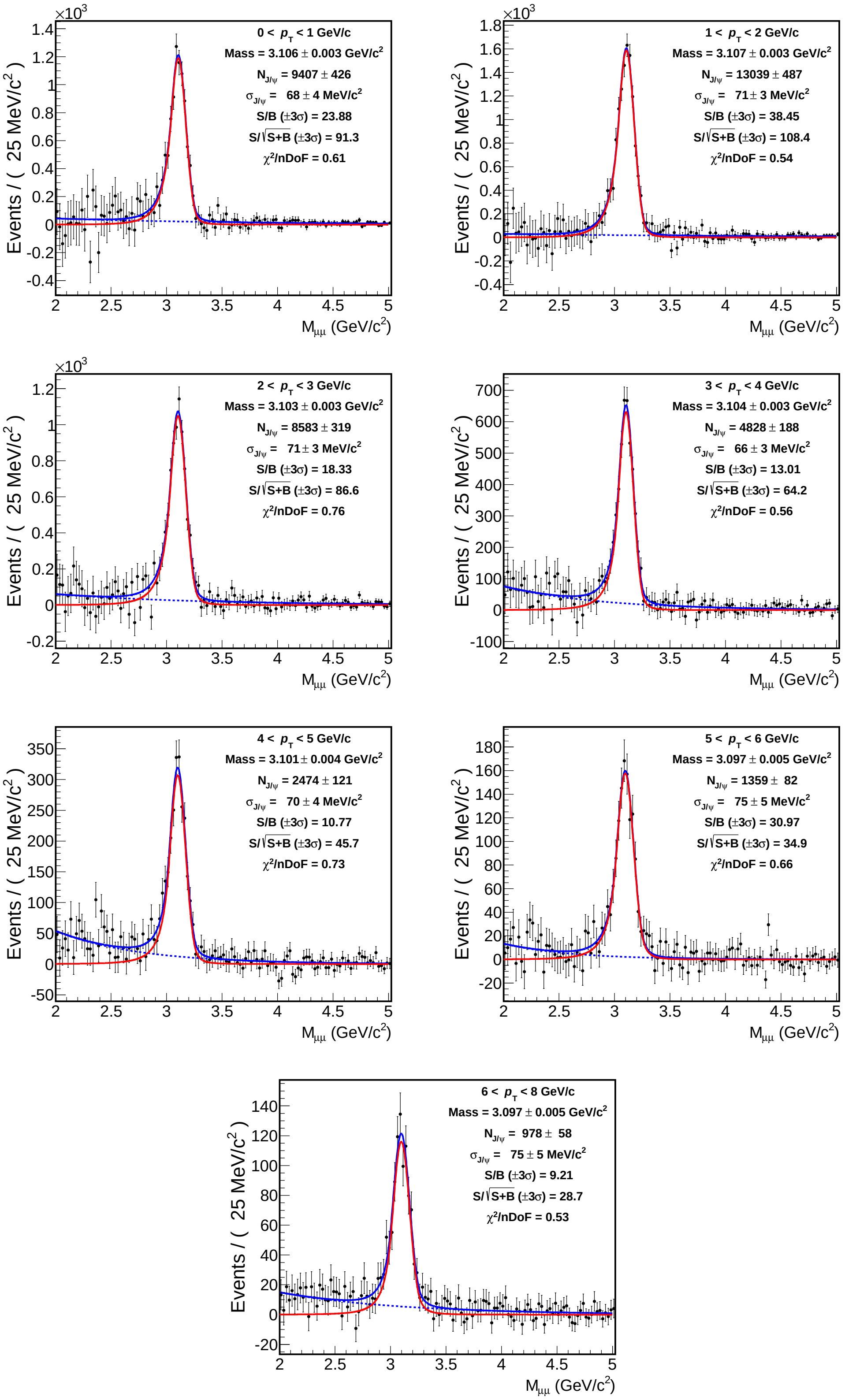

Figure 6.12: Invariant mass spectra of opposite-sign dimuons for different p_T ($2.5 < y < 4$ and centrality 0-90%) after background subtraction.

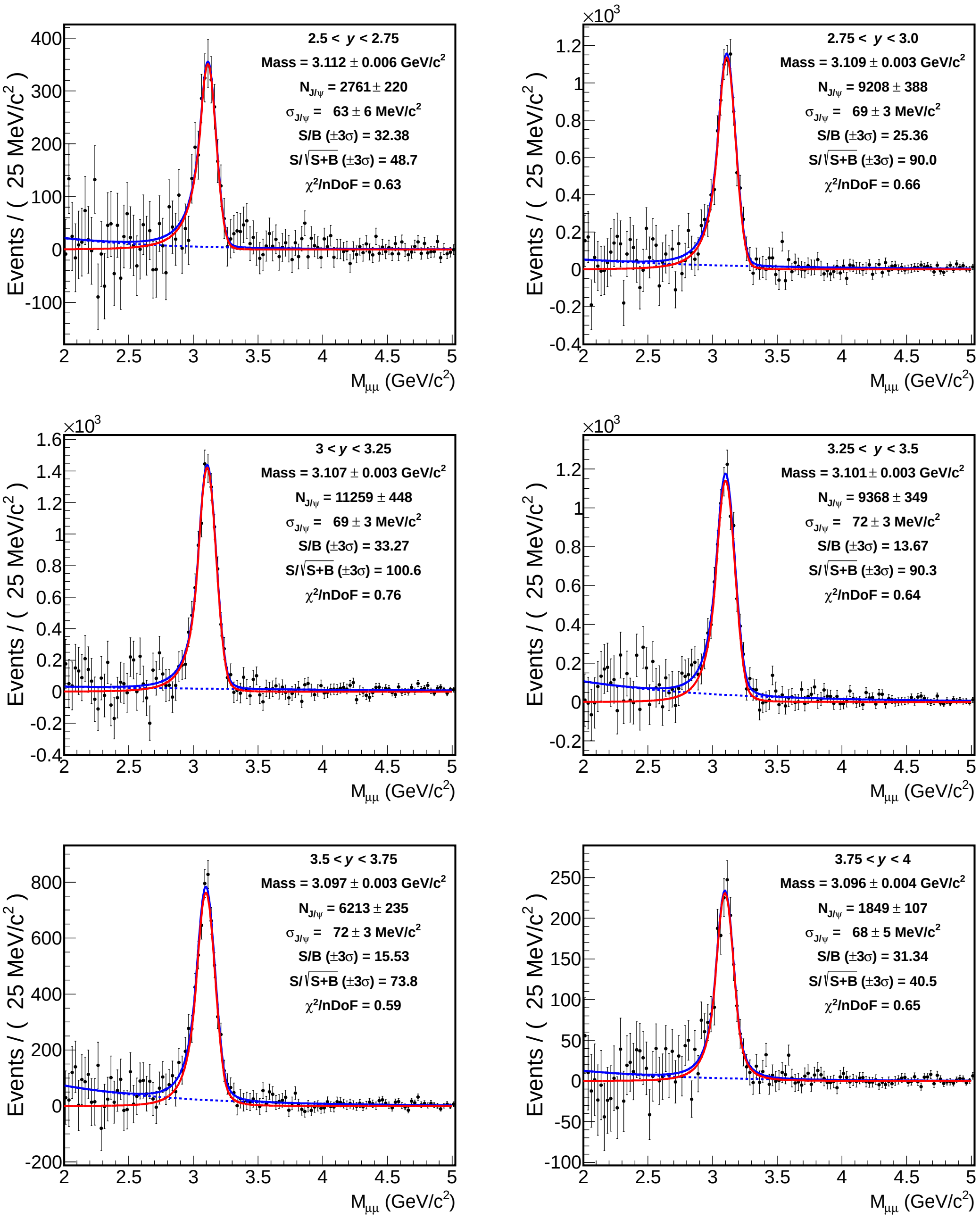

Figure 6.13: Invariant mass spectra of opposite-sign dimuons for different rapidities ($p_{\mathrm{T}} < 8$ GeV/c and centrality 0-90%) after background subtraction.

a bias in its centrality distribution at the end of this interval that extends beyond its centrality range[4]. To avoid this problem, the Central trigger was restricted up to 8% (red arrow). Finally, the Semicentral trigger (right panel of figure 6.15) is defined in the 10-50% (red arrows) centrality range, but it also presents bias at the edges at the offline level (blue markers). The bias at 10% is due to the Physics Selection, while the bias at the upper edge is due to the online selection, where the trigger is defined in the 0-50% (green markers). The Semicentral trigger at the online level (without Physics Selection) is then used for the present normalization.

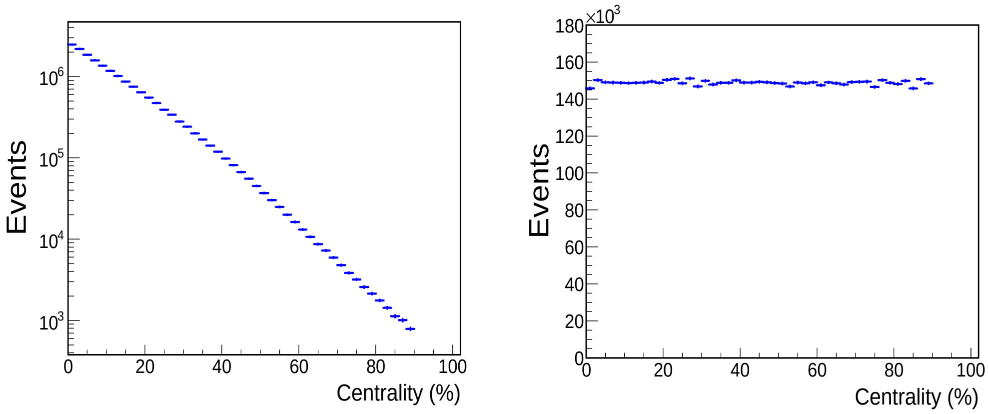

Figure 6.14: Centrality distributions from MUL (*left*) and MB (*right*) triggers.

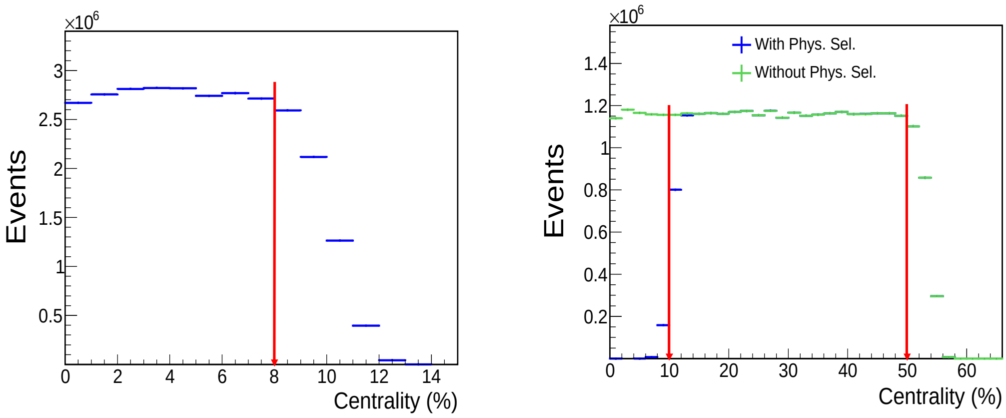

Figure 6.15: Centrality distributions from Central (*left*) and Semicentral (*right*) triggers.

Once the trigger and their centrality ranges have been properly delimited the next step is to compute, in a run-per-run basis, the following quantities:

---

[4] The online centrality selection for the Central and Semicentral trigger is performed with a threshold on the multiplicity of the V0 detector rather than a sharp cut.

1. *nTrigClass*: number of events per reference trigger class in the proper centrality range.
2. *nMULinTrigClass*: number of *nTrigClass* that also contain a MUL trigger.
3. *nMUL*: number of MUL triggers in the centrality range of the given reference trigger.
4. $R_{\mathrm{Trigger}} = nTrigClass/nMULinTrigClass$.
   - $R_{\mathrm{MB}} \approx 27$.
   - $R_{\mathrm{Central}} \approx 5.2$.
   - $R_{\mathrm{Semi}} \approx 27$.
5. Extend R_{Trigger} to the 0-90% centrality range by the correction factors C_{Trigger}
   - $C_{\mathrm{MB}} = 1$.
   - $C_{\mathrm{Central}} = 0.9/0.08$.
   - C_{Semi} 0.9/0.4.
6. Once again correct R_{Trigger} by the ratio $R_{\mathrm{MUL}} = nMUL/MUL_{\mathrm{events}}$:
   - $R_{\mathrm{MUL}} = 1$ in the 0-90% centrality range.
   - $R_{\mathrm{MUL}} \approx 0.46$ in 0-8%.
   - $R_{\mathrm{MUL}} \approx 0.45$ in the 10-50%.

Using R_{MUL}, C_{Trigger} and R_{Trigger}, $Norm_{\mathrm{Trigger}}$ is defined as

$$Norm_{\mathrm{Trigger}} = R_{\mathrm{MUL}}\, C_{\mathrm{Trigger}}\, R_{\mathrm{Trigger}}$$

for each run and for the three trigger references (figures 6.16, 6.17 and 6.18). A zero degree polynomial fit on the $Norm_{\mathrm{Trigger}}$ distribution of each trigger is used to obtain F_{Trigger} and its statistical error. The systematic uncertainty is taken as the RMS from the distribution of $Norm_{\mathrm{Trigger}}$ weighted by one over the square of the statistical errors (figure 6.19).

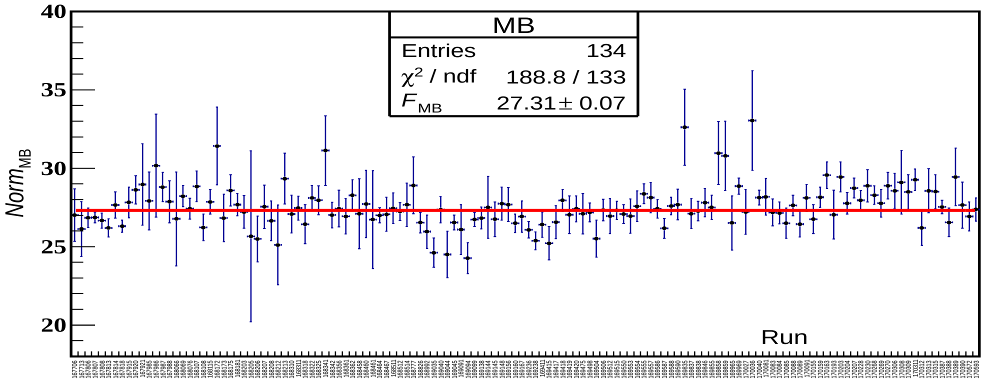

Figure 6.16: Run-per-run *Norm* using the MB trigger.

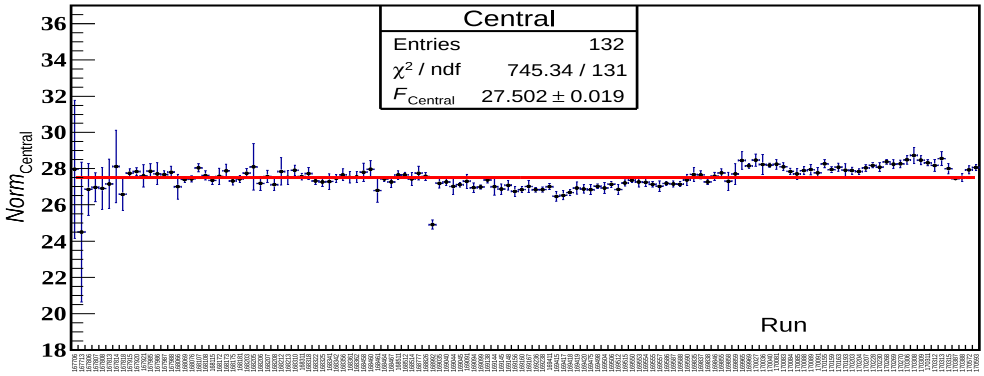

Figure 6.17: Run-per-run *Norm* using the Central trigger.

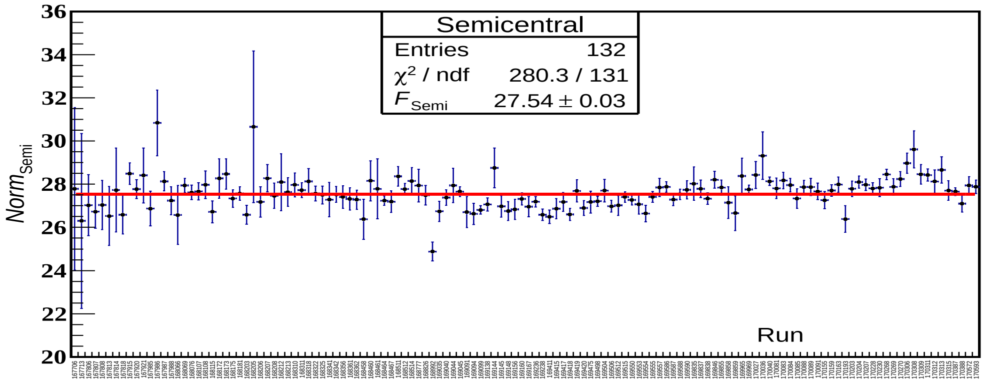

Figure 6.18: Run-per-run *Norm* using the Semicentral trigger.

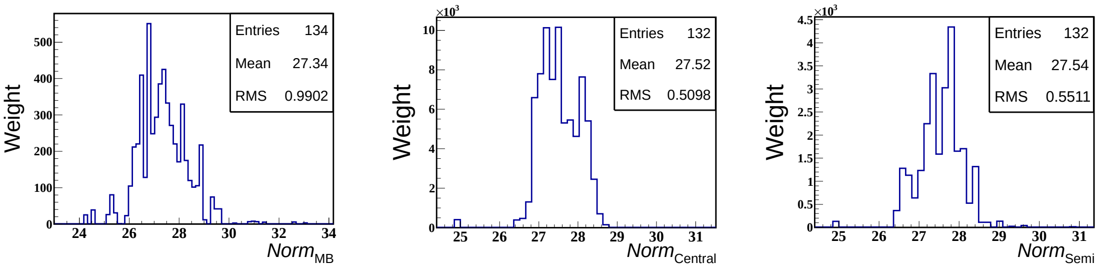

Figure 6.19: Weighted $Norm_{\mathrm{Trigger}}$ distributions from the MB (*left*), Central (*middle*) and Semicentral (*right*) triggers.

The resulting F_{Trigger} are:

$$F_{\mathrm{MB}} = 27.31 \pm 0.07 \text{ (stat.)} \pm 0.99 \text{ (syst.)},$$

$$F_{\mathrm{Central}} = 27.50 \pm 0.01 \text{ (stat.)} \pm 0.50 \text{ (syst.)},$$

$$F_{\mathrm{Semi}} = 27.54 \pm 0.03 \text{ (stat.)} \pm 0.55 \text{ (syst.)}.$$

These values are then combined using [110]:

$$F_{\mathrm{Norm}} = \frac{\sum F_{\mathrm{Trig}}/\sigma^2_{\mathrm{Stat}}}{\sum 1/\sigma^2_{\mathrm{Stat}}},$$

$$\Delta\mathrm{Stat} = \sqrt{\frac{1}{\sum 1/\sigma^2_{\mathrm{Stat}}}},$$

$$\Delta\mathrm{Syst}/F_{\mathrm{Norm}} = \mathrm{Max}\left\{\frac{\sigma^{MB}_{\mathrm{Syst}}}{F_{\mathrm{MB}}}, \frac{\sigma^{Central}_{\mathrm{Syst}}}{F_{\mathrm{Central}}}, \frac{\sigma^{Semi}_{\mathrm{Syst}}}{F_{\mathrm{Semi}}}\right\}.$$

where the summation is performed over the three different triggers. So, finally, the normalization factor is:

$$F_{\mathrm{Norm}} = 27.50 \pm 0.02 \text{ (stat.)} \pm 0.99 \text{ (syst.)} \tag{6.5}$$

The number of MB events in the 0-90% centrality range, equivalent to the number of unlike-sign dimuon triggers, and that will be used in equation 6.2, is:

$$N_{\mathrm{MB}} = MUL_{\mathrm{events}} \times F_{\mathrm{Norm}} = 477\ 045\ 250 \pm 3.6\% \text{ (syst. } F_{\mathrm{Norm}}).$$

The integrated luminosity recorded in the 2011 Pb-Pb collisions is then given by:

$$\mathcal{L}_{\mathrm{int}} = \frac{N_{\mathrm{MB}}/0.9}{\sigma_{\mathrm{Pb-Pb}}} = 69.4 \pm 3.6\% \text{ (syst. } F_{\mathrm{Norm}}) \pm 2.9\% \text{ (syst. } \sigma_{\mathrm{Pb-Pb}}) \;\; \mu b^{-1},$$

where $\sigma_{\mathrm{Pb-Pb}} = 7.64 \pm 0.22$ (syst.) b is the hadronic Pb-Pb cross section at $\sqrt{s_{\mathrm{NN}}} = 2.76$ TeV [111] and N_{MB} has been divided by 0.9 to obtain the number of MB events in the 0-100% interval. This integrated luminosity was found to be in very good agreement with the preliminary result from a van der Meer scan that yielded $\mathcal{L}_{\mathrm{int}} = 71.4^{+2\%}_{-4\%}$ (syst.) μb^{-1}.

6.4 The embedding technique

The embedding Monte Carlo technique consists in simulating a signal particle (a J/ψ in this analysis) and embedding the detector response into a real event raw data (before the reconstruction). The embedded event is then reconstructed as if it were a normal real event. The embedding technique has the advantage of providing the most realistic background conditions. Such realistic description is necessary if the environment can alter the track reconstruction efficiency, as it is the case in central Pb-Pb collisions with its high particle multiplicity: for example, at $\eta = 3.25$, $\mathrm{d}N_{\mathrm{ch}}/\mathrm{d}\eta \approx 1\,450$ for the 0-5% most central Pb-Pb collisions [112]. This increase of the detector occupancy with the centrality of the collision could alter the reconstruction efficiency, which is not taken into account in pure J/ψ simulations. The raw data of a real event is first converted into Summable Digits (SDigits)[5], then the particle of interest is generated, decayed and propagated through our detector and the charge deposited and merged with the background SDigits. The resulting merged SDigits are then processed by the normal reconstruction chain. One J/ψ per event is simulated at the position of the real event primary vertex for 80% of the Minimum Bias events in each run used in the analysis.

6.4.1 $A \times \epsilon$ corrections

The main motivation to perform the embedding simulations is to compute an unbiased acceptance times efficiency factor in centrality, p_{T} and y bins. Since the embedding is done in MB events and the analysis uses unlike-sign dimuon triggers, a weighting is applied to account for the fact that runs with a large numbers of MB events may have a small number of MUL. The result

---

[5] A SDigit is a pad with its associated charge, but no noise or electronics response function applied. It is one of the first steps during the reconstruction chain.

is then integrated over the full period, ensuring that $A \times \epsilon$ fluctuations on a run-per-run basis are properly propagated to the final result.

Figure 6.20 shows the J/ψ acceptance times efficiency as a function of collision centrality obtained from these simulations in the rapidity domain $2.5 < y < 4.0$ and $p_{\rm T} < 8.0$ GeV/c. It is possible to observe a small decrease of 7.4% of the J/ψ reconstruction efficiency from 0.1316 in the 80-90% centrality bin to 0.1219 in the 0-10% centrality class[6].

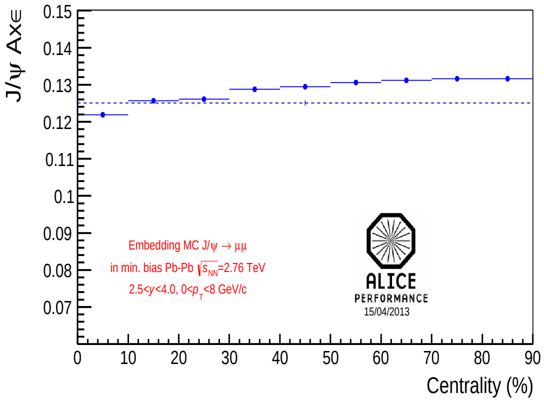

Figure 6.20: J/ψ acceptance times efficiency versus collision centrality ($p_{\rm T} < 8$ GeV/c and $2.5 < y < 4$). The dash line represents the average value integrated over the centrality range 0-90%.

The 0-90% centrality integrated value of $A \times \epsilon$ is 0.1250. In order to account for the real distribution of J/ψ as a function of centrality, this value was calculated using the $N_{{\rm J}/\psi}$ weighted by the $A \times \epsilon$ from each centrality bin. The same calculations were performed replacing the corrected number of J/ψ by the average number of binary nucleon-nucleon collisions ($\langle N_{\rm Coll} \rangle$) or the average number of participant nucleons ($\langle N_{\rm Part} \rangle$). Results were found to be consistent with less than 0.6% relative difference.

Left plot of figure 6.21 shows the $A \times \epsilon$ vs $p_{\rm T}$ ($p_{\rm T} < 8$ GeV/c and 0-90% centrality), while the right panel of the same figure depicts the acceptance times efficiency value as a function of the rapidity ($p_{\rm T} < 8$ GeV/c and 0-90% centrality), the shape of the distribution reflects the acceptance of the muon spectrometer.

6.4.2 Signal shape parameters

The parameters from the Extended Crystal Ball function are obtained by fitting the invariant mass distributions of reconstructed Monte Carlo J/ψ in the

---

[6] Statistical errors on $A \times \epsilon$ are negligible.

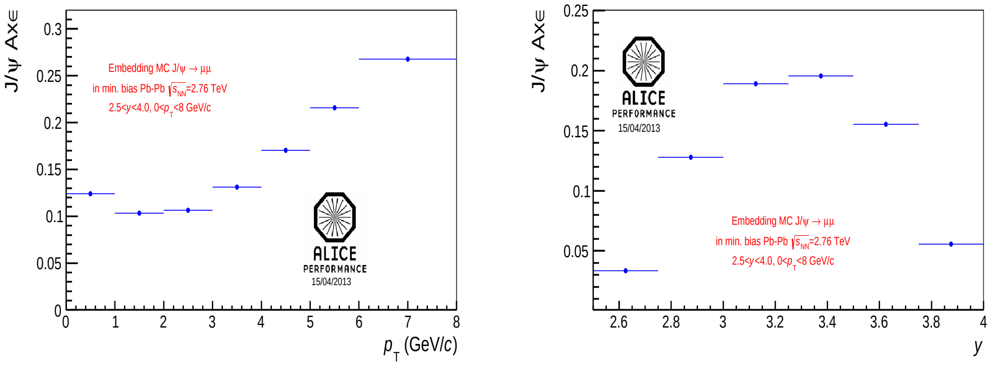

Figure 6.21: *Left*: J/ψ acceptance times efficiency versus p_{T} ($2.5 < y < 4$ and 0-90% centrality). *Right*: J/ψ $A \times \epsilon$ vs y ($p_{\mathrm{T}} < 8$ GeV/c and 0-90% centrality).

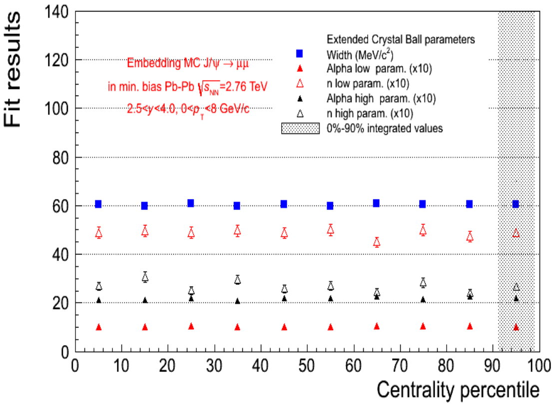

Figure 6.22: Centrality dependence of the J/ψ signal shape parameters obtained from the embedding ($p_{\mathrm{T}} < 8$ GeV/c and $2.5 < y < 4$).

embedding. For the 0-90% centrality, $p_{\mathrm{T}} < 8$ GeV/c and $2.5 < y < 4$, the tails values found are:

$$\alpha = 1.01 \pm 0.01,\ \ n = 4.86 \pm 0.08,\ \ \alpha' = 2.18 \pm 0.02\ \ \text{and}\ \ n' = 2.68 \pm 0.06$$

Figure 6.22 indicates that the CB2 tails parameters and width of the J/ψ are constant as a function of the centrality. This is not the same for p_{T} and y (figure 6.23), where important variations from bin to bin are observed. This dependence is taken into account by using p_{T}/y dependent tails parameters in the function describing the signal.

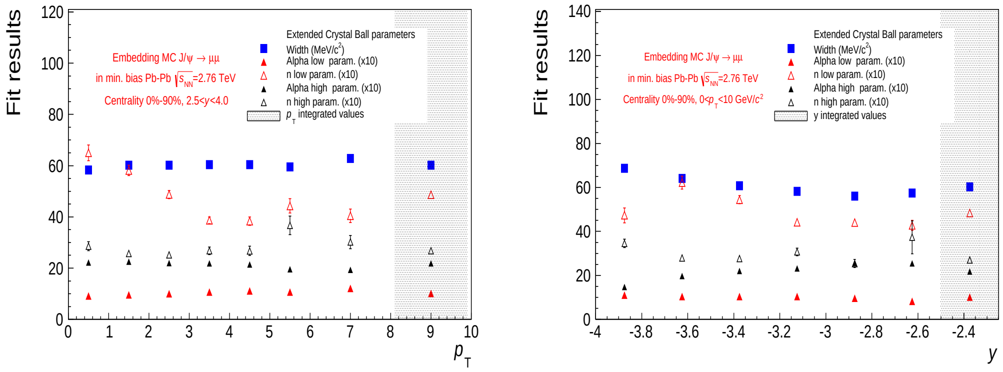

Figure 6.23: Signal shape parameters as a function of p_{T} ($2.5 < y < 4$ and 0-90% centrality) and y ($p_{\mathrm{T}} < 8$ GeV/c and 0-90% centrality).

6.5 pp reference

ALICE has already performed detailed studies on the inclusive production of the J/ψ in pp collisions at $\sqrt{s} = 2.76$ TeV [56]. These values are used as reference for the Nuclear Modification Factors that will be presented (table 6.1). For instance, the integrated p_{T} and y cross section obtained by the collaboration at this energy is:

$$\sigma^{\mathrm{pp}}_{J/\psi}(2.5 < y < 4) = 3.34 \pm 0.13(\mathrm{stat.}) \pm 0.24(\mathrm{syst.}) \pm 0.12(\mathrm{lumi.})\ ^{+0.53}_{-1.07}(\mathrm{pol.})\mu\mathrm{b}.$$

6.6 Systematic uncertainties

All the ingredients needed to extract the J/ψ R_{AA}, $\langle p_{\mathrm{T}} \rangle$ and $\langle p_{\mathrm{T}}^2 \rangle$ have been determined. In the following section the methods used to compute the systematic uncertainties from the different sources are described.

6.6.1 Signal extraction

The number of J/ψ is extracted by fitting the opposite-sign invariant mass dimuon spectra from the raw and the background subtracted distributions. However, systematics associated to the background fitting range and signal line shapes were also explored.

The signal line and background shapes were estimated using different functions and methods. For the signal, apart from the tails extracted from the

Table 6.1: Summary of the inclusive J/ψ differential cross sections for pp at $\sqrt{s}$ = 2.76 TeV.

p_{T} (GeV/c)	$\mathrm{d}^2\sigma_{J/\psi}/\mathrm{d}p_{\mathrm{T}}\mathrm{d}y$ (μb/(GeV/c))	Systematic uncertainties Correl. (μb/(GeV/c))	Non-correl. (μb/(GeV/c))	Polariz., CS (μb/(GeV/c))	Polariz., HE (μb/(GeV/c))
		2.5 <y< 4			
[0; 1]	0.380±0.033	0.022	0.021	+0.074, −0.141	+0.069, −0.133
[1; 2]	0.705±0.042	0.041	0.040	+0.122, −0.271	+0.098, −0.211
[2; 3]	0.583±0.038	0.034	0.033	+0.100, −0.203	+0.069, −0.127
[3; 4]	0.321±0.027	0.019	0.018	+0.050, −0.089	+0.029, −0.047
[4; 5]	0.135±0.017	0.008	0.008	+0.014, −0.027	+0.009, −0.018
[5; 6]	0.073±0.011	0.004	0.004	+0.005, −0.011	+0.005, −0.009
[6; 8]	0.019±0.004	0.001	0.001	+0.001, −0.001	+0.001, −0.002
y	$\mathrm{d}\sigma_{J/\psi}/\mathrm{d}y$ (μb)	(μb)	(μb)	(μb)	(μb)
[2.5; 2.75]	3.05±0.35	0.18	0.17	+0.67, −1.41	+0.52, −1.04
[2.75; 3]	2.37±0.19	0.14	0.13	+0.42, −0.84	+0.39, −0.78
[3; 3.25]	2.26±0.15	0.13	0.13	+0.29, −0.65	+0.31, −0.61
[3.25; 3.5]	2.01±0.14	0.12	0.11	+0.27, −0.54	+0.21, −0.38
[3.5; 3.75]	2.00±0.16	0.12	0.11	+0.33, −0.67	+0.15, −0.30
[3.75; 4]	1.68±0.19	0.10	0.09	+0.36, −0.69	+0.16, −0.26

embedding simulation, another set from a pure J/ψ simulation was used. The integrated values are (left plot on figure 6.24):

$$\alpha = 1.06 \pm 0.01,\ n = 5.0 \pm 0.1,\ \alpha' = 2.12 \pm 0.03 \text{ and } n' = 2.9 \pm 0.1$$

and in this case the parameters also vary from bin to bin as a function of p_{T}/y.

Another set of tails was obtained from pp collisions at $\sqrt{s}$ = 7 TeV. The invariant mass spectrum shown on the right plot of figure 6.24 was extracted using the same event and track selection used for the Pb-Pb collisions. The high-mass tail was fixed to the values from a pure J/ψ simulation while the low-mass tail was let free. The values obtained from the fit to the pp data together with those from the simulation are used in the Pb-Pb signal extraction:

$$\alpha = 0.98 \pm 0.04,\ n = 6.4 \pm 1.6,\ \alpha' = 2.26 \text{ and } n' = 2.6$$

Due to the lack of statistics, it was not possible to extract the tails parameters from pp collisions in different p_{T} nor y bins.

Two fitting ranges on the invariant mass were used: $2.0 < M_{\mathrm{J}/\psi} < 5.0$ GeV/c^2 and $2.3 < M_{\mathrm{J}/\psi} < 4.7$ GeV/c^2.

So, the total number of combinations to extract $N_{\mathrm{J}/\psi}$ amounts to 12 for each centrality, transverse momentum and rapidity bin. The final $N_{\mathrm{J}/\psi}$ is estimated by weighting each test by the statistical uncertainty of its result and

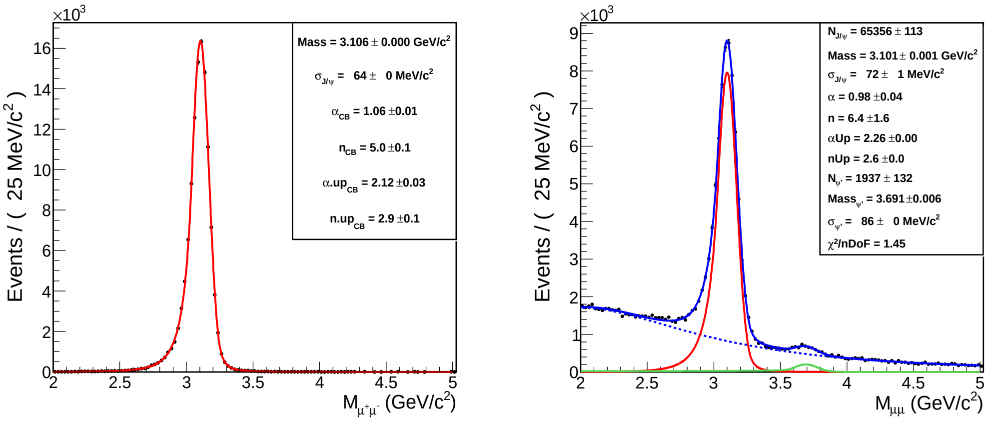

Figure 6.24: CB2 tails extraction from pure J/ψ simulation (*left*) and pp data (*right*). In the latter, the green curve corresponds to the ψ(2S) signal where the width is fixed to $\sigma_{\psi(2S)} = \sigma_{J/\psi} \times M_{\psi(2S)}/M_{J/\psi}$.

by taking the average value of the 12 tests. The statistical and systematic uncertainties correspond to the statistical uncertainty and the RMS of the weighted distribution. Figure 6.25 offers a graphical explanation on how the aforementioned tests are displayed in figure 6.26: signal extracted in the raw or background subtracted spectrum (green), the CB2 tails used (purple), the fitting range (red), the weighted mean (orange) and the ± 1 RMS (pink).

Tables from 6.2 to 6.7 summarize the number of J/ψ extracted in all centrality, p_{T} and y bins after the 12 tests performed. The maximum $N_{\mathrm{J}/\psi}$ dispersion from the weighted mean is never larger than 2.4 RMS, indicating that the fit results are very stable.

Table 6.2: Extracted $N_{\mathrm{J}/\psi}$ as a function of the centrality with $p_{\mathrm{T}} < 8$ GeV/c and $2.5 < y < 4$.

$p_{\mathrm{T}} < 8$ GeV/c, $2.5 < y < 4$	
Cent.	$N_{\mathrm{J}/\psi}$ ± stat. ± syst.
0-90%	40 878 ± 719 ± 673
0-10%	16 009 ± 534 ± 385
10-20%	10 420 ± 371 ± 190
20-30%	6 590 ± 242 ± 71
30-40%	3 736 ± 157 ± 82
40-50%	2 119 ± 96 ± 16
50-60%	1 254 ± 63 ± 20
60-70%	673 ± 40 ± 13
70-80%	284 ± 23 ± 9
80-90%	136 ± 13 ± 6

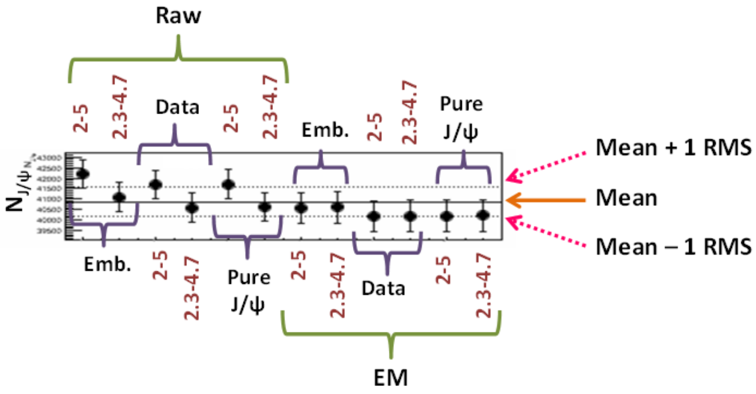

Figure 6.25: Graphical explanation of tests performed for the signal extraction. The points correspond to the $N_{J/\psi}$ from the 0-90% centrality, $p_T <$ 8 GeV/c and $2.5 < y < 4$ spectra.

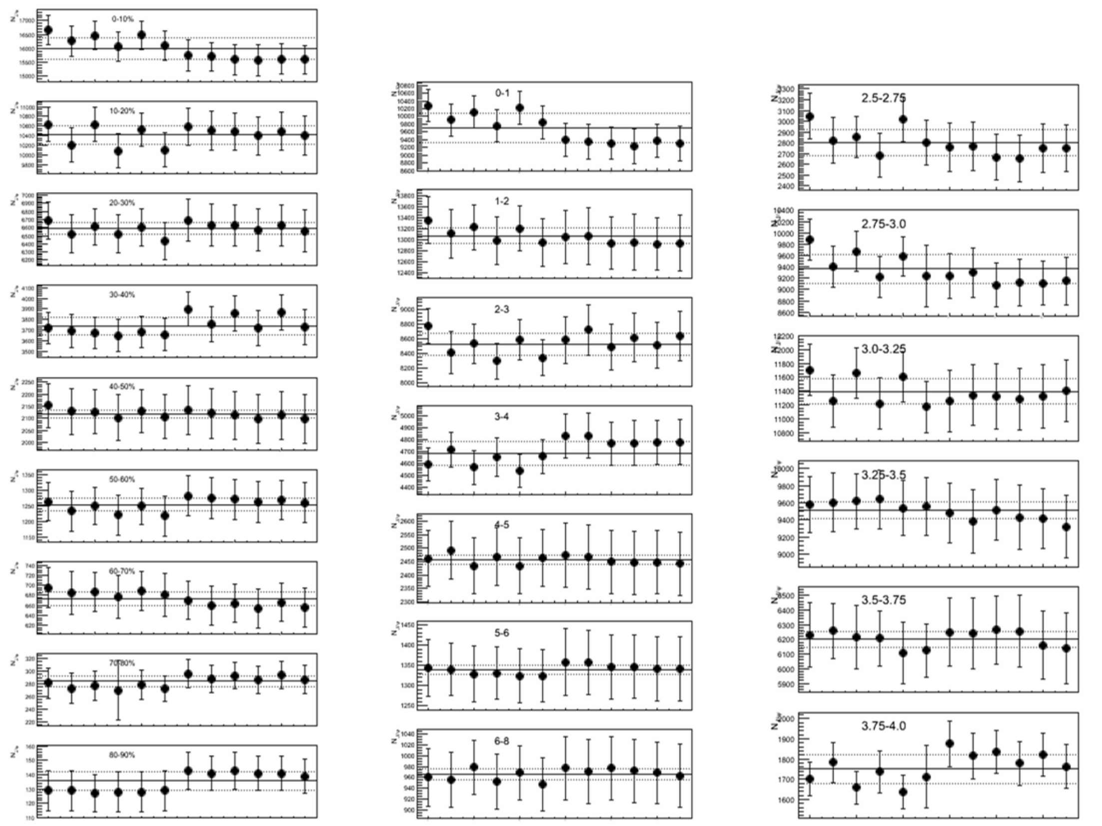

Figure 6.26: From *left* to *right*: results of the 12 tests for signal extraction as a function of the centrality ($p_T < 8$ GeV/c and $2.5 < y < 4$), p_T (2.5 $< y <$ 4 and centrality 0-90%) and y ($p_T < 8$ GeV/c and centrality 0-90%) in different bins. The centrality (p_T/y) decreases (increases) from the top to the bottom.

Table 6.3: *Left*: $N_{\mathrm{J}/\psi}$ as a function of p_{T} ($2.5 < y < 4$ and centrality 0-90%). *Right*: $N_{\mathrm{J}/\psi}$ as a function of y ($p_{\mathrm{T}} < 8$ GeV/c and centrality 0-90%).

0-90%, $2.5 < y < 4$	
p_{T} (GeV/c)	$N_{\mathrm{J}/\psi}$ ± stat. ± syst.
$[0, 1]$	9 668 ± 428 ± 377
$[1, 2]$	13 070 ± 458 ± 142
$[2, 3]$	8 531 ± 288 ± 151
$[3, 4]$	4 684 ± 162 ± 99
$[4, 5]$	2 457 ± 112 ± 17
$[5, 6]$	1 339 ± 72 ± 11
$[6, 8]$	965 ± 54 ± 10

0-90%, $p_{\mathrm{T}} < 8$ GeV/c	
y	$N_{\mathrm{J}/\psi}$ ± stat. ± syst.
$[2.5, 2.75]$	2 803 ± 213 ± 123
$[2.75, 3.0]$	9 362 ± 392 ± 256
$[3.0, 3.25]$	11 393 ± 406 ± 186
$[3.25, 3.5]$	9 514 ± 344 ± 95
$[3.5, 3.75]$	6 202 ± 216 ± 55
$[3.75, 4.0]$	1 750 ± 101 ± 74

Table 6.4: $N_{\mathrm{J}/\psi}$ as a function of p_{T} in three centrality bins ($2.5 < y < 4$).

p_{T} (GeV/c)	Cent. 0-20%	Cent. 20-40%	Cent. 40-90%
	$N_{\mathrm{J}/\psi}$ ± stat. ± syst.	$N_{\mathrm{J}/\psi}$ ± stat. ± syst.	$N_{\mathrm{J}/\psi}$ ± stat. ± syst.
$[0, 8]$	26 423 ± 665 ± 453	10 403 ± 289 ± 103	4 444 ± 118 ± 44
$[0, 1]$	6 610 ± 395 ± 361	2 227 ± 169 ± 47	914 ± 62 ± 25
$[1, 2]$	8 714 ± 393 ± 104	3 142 ± 168 ± 40	1 265 ± 75 ± 17
$[2, 3]$	5 457 ± 281 ± 104	2 196 ± 119 ± 54	924 ± 54 ± 14
$[3, 4]$	2 775 ± 140 ± 89	1 303 ± 70 ± 32	624 ± 37 ± 6
$[4, 5]$	1 410 ± 107 ± 32	663 ± 47 ± 4	384 ± 26 ± 3
$[5, 6]$	762 ± 60 ± 8	405 ± 33 ± 5	174 ± 16 ± 6
$[6, 8]$	484 ± 44 ± 11	338 ± 27 ± 6	163 ± 14 ± 3

Table 6.5: $N_{\mathrm{J}/\psi}$ as a function of the centrality in three p_{T} bins ($2.5 < y < 4$).

Cent.	$0 < p_{\mathrm{T}} < 2$ GeV/c	$2 < p_{\mathrm{T}} < 5$ GeV/c	$5 < p_{\mathrm{T}} < 8$ GeV/c
	$N_{\mathrm{J}/\psi}$ ± stat. ± syst.	$N_{\mathrm{J}/\psi}$ ± stat. ± syst.	$N_{\mathrm{J}/\psi}$ ± stat. ± syst.
0-90%	23 019 ± 644 ± 515	15 736 ± 336 ± 146	2 297 ± 89 ± 18
0-10%	9 440 ± 460 ± 482	5 719 ± 251 ± 100	764 ± 59 ± 9
10-20%	5 985 ± 324 ± 156	3 883 ± 173 ± 52	468 ± 45 ± 6
20-30%	3 460 ± 199 ± 30	2 675 ± 116 ± 36	419 ± 32 ± 4
30-40%	1 904 ± 128 ± 54	1 488 ± 80 ± 51	330 ± 27 ± 2
40-50%	972 ± 74 ± 15	970 ± 52 ± 12	179 ± 17 ± 2
50-60%	643 ± 50 ± 8	533 ± 36 ± 3	169 ± 15 ± 3
60-90%	606 ± 37 ± 14	425 ± 26 ± 3	

Table 6.6: $N_{J/\psi}$ as a function of the centrality in three y bins ($p_T < 8$ GeV/c).

Cent.	$2.5 < y < 3.0$ $N_{J/\psi}$ ± stat. ± syst.	$3.0 < y < 3.5$ $N_{J/\psi}$ ± stat. ± syst.	$3.5 < y < 4.0$ $N_{J/\psi}$ ± stat. ± syst.
0-90%	12 106 ± 429 ± 346	20 811 ± 522 ± 317	7 934 ± 249 ± 87
0-10%	4 631 ± 336 ± 188	8 251 ± 375 ± 332	3 268 ± 192 ± 55
10-20%	3 404 ± 210 ± 84	5 196 ± 285 ± 82	1 736 ± 117 ± 51
20-30%	1 898 ± 138 ± 41	3 412 ± 178 ± 43	1 304 ± 85 ± 26
30-40%	964 ± 87 ± 40	2 030 ± 115 ± 45	737 ± 58 ± 11
40-50%	614 ± 54 ± 10	1 050 ± 70 ± 10	448 ± 35 ± 6
50-60%	384 ± 36 ± 10	657 ± 46 ± 6	261 ± 23 ± 5
60-90%	297 ± 25 ± 4	540 ± 32 ± 9	257 ± 19 ± 7

Table 6.7: $N_{J/\psi}$ as a function of p_T in three centrality bins ($2.5 < y < 4$), used to compute the $\langle p_T \rangle$ and $\langle p_T^2 \rangle$.

p_T (GeV/c)	Cent. 0-20% $N_{J/\psi}$ ± stat. ± syst.	Cent. 20-40% $N_{J/\psi}$ ± stat. ± syst.	Cent. 40-90% $N_{J/\psi}$ ± stat. ± syst.
$[0.0, 0.5]$	1 979 ± 240 ± 119	801 ± 125 ± 27	418 ± 34 ± 11
$[0.5, 1.0]$	4 701 ± 328 ± 297	1 464 ± 139 ± 30	519 ± 53 ± 12
$[1.0, 1.5]$	4 814 ± 304 ± 224	1 738 ± 134 ± 60	669 ± 53 ± 13
$[1.5, 2.0]$	3 940 ± 327 ± 151	1 395 ± 104 ± 38	606 ± 49 ± 9
$[2.0, 2.5]$	3 037 ± 203 ± 80	1 162 ± 94 ± 22	558 ± 42 ± 9
$[2.5, 3.0]$	2 391 ± 167 ± 72	1 050 ± 76 ± 38	361 ± 31 ± 8
$[3.0, 3.5]$	1 589 ± 110 ± 45	783 ± 57 ± 30	335 ± 27 ± 5
$[3.5, 4.0]$	1 175 ± 90 ± 45	553 ± 48 ± 11	298 ± 25 ± 5
$[4.0, 4.5]$	794 ± 74 ± 17	368 ± 39 ± 17	213 ± 18 ± 3
$[4.5, 5.0]$	625 ± 64 ± 21	296 ± 28 ± 6	166 ± 15 ± 5
$[5.0, 5.5]$	423 ± 48 ± 4	275 ± 26 ± 9	174 ± 16 ± 6
$[5.5, 6.0]$	308 ± 34 ± 13	152 ± 19 ± 4	
$[6.0, 8.0]$	484 ± 44 ± 11	338 ± 27 ± 6	163 ± 14 ± 3

6.6.2 Trigger efficiency

When integrated over p_T and y, the muon trigger efficiency obtained in pure J/ψ simulations or embedded J/ψ into peripheral events is $\epsilon_{trg} \approx 97\%$. A small decrease of about 3.5% of this efficiency is observed for single muons in most central events.

The systematic uncertainty on the trigger threshold has been determined by using 3 different p_T dependent trigger response functions for the threshold used in this analysis. These functions have been computed by fitting the resulting low-p_{T}/all-p_{T} trigger threshold ratio[7] at the single muon level from LHC11h pass2, muons from J/ψ decay in embedding productions and muons from a pure J/ψ simulation (left column of figure 6.27).

Opposite-sign invariant mass dimuon spectra from a pure J/ψ simulation were extracted for different p_{T} and y bins weighted by the trigger response functions previously obtained. The systematic uncertainties were then estimated as the maximum relative difference in $N_{\mathrm{J}/\psi}$ among the three sets.

Integrated over p_{T} and y the systematic on the trigger efficiency is 1%. As a function of p_{T} the systematic on the trigger efficiency is applied bin to bin (uncorrelated) and it is 3% in the p_{T} range from 0 to 1 GeV/c (right column of figure 6.27) and 1% in all others bins. As a function of y, an uncorrelated systematic uncertainty of 1% was considered.

It is also necessary to take into account the systematic uncertainty arising from the intrinsic chambers efficiency which amounts to 1% for single muons and 2% for J/ψ. This systematic uncertainty is taken correlated as a function of centrality and uncorrelated as a function of p_{T} and y since variations from one local board to the other may exist. This uncertainty is added in quadrature with the one arising from the trigger threshold.

Finally, as a function of the centrality (increasing multiplicity in the trigger chambers), the systematic uncertainty has been assessed by changing the detector response to the passage of particles. Two embedding simulations have been performed with and without activating the trigger cluster size[8]; the relative central to peripheral J/ψ $A \times \epsilon$ difference provides an estimate of the systematic uncertainty. Since it is clearly an extreme case to deactivate the cluster size in the simulation, the systematic uncertainty is taken as half of the difference: 1% in 0%–10% and 10%–20% and 0.5% in 20%–30% and 30%–40%.

6.6.3 Tracking efficiency

The previous chapter was dedicated to the calculation of the tracking efficiency and its associated systematic uncertainties.

A last uncorrelated systematic uncertainty is related to the centrality dependence of the tracking efficiency. Comparisons between the embedding simulation and the real data have shown small systematic difference that is added as an uncertainty in the most central bins: 1% in the 0-10% and 0.5 in the 10-20%.

---

[7] In the LHC11h period, the all-p_{T} trigger threshold is defined at 0.5 GeV/c while the low-p_{T} one at 1 GeV/c.

[8] Number of adjacent strips giving a signal. Activating the cluster size allows a better description of the trigger in the simulations.

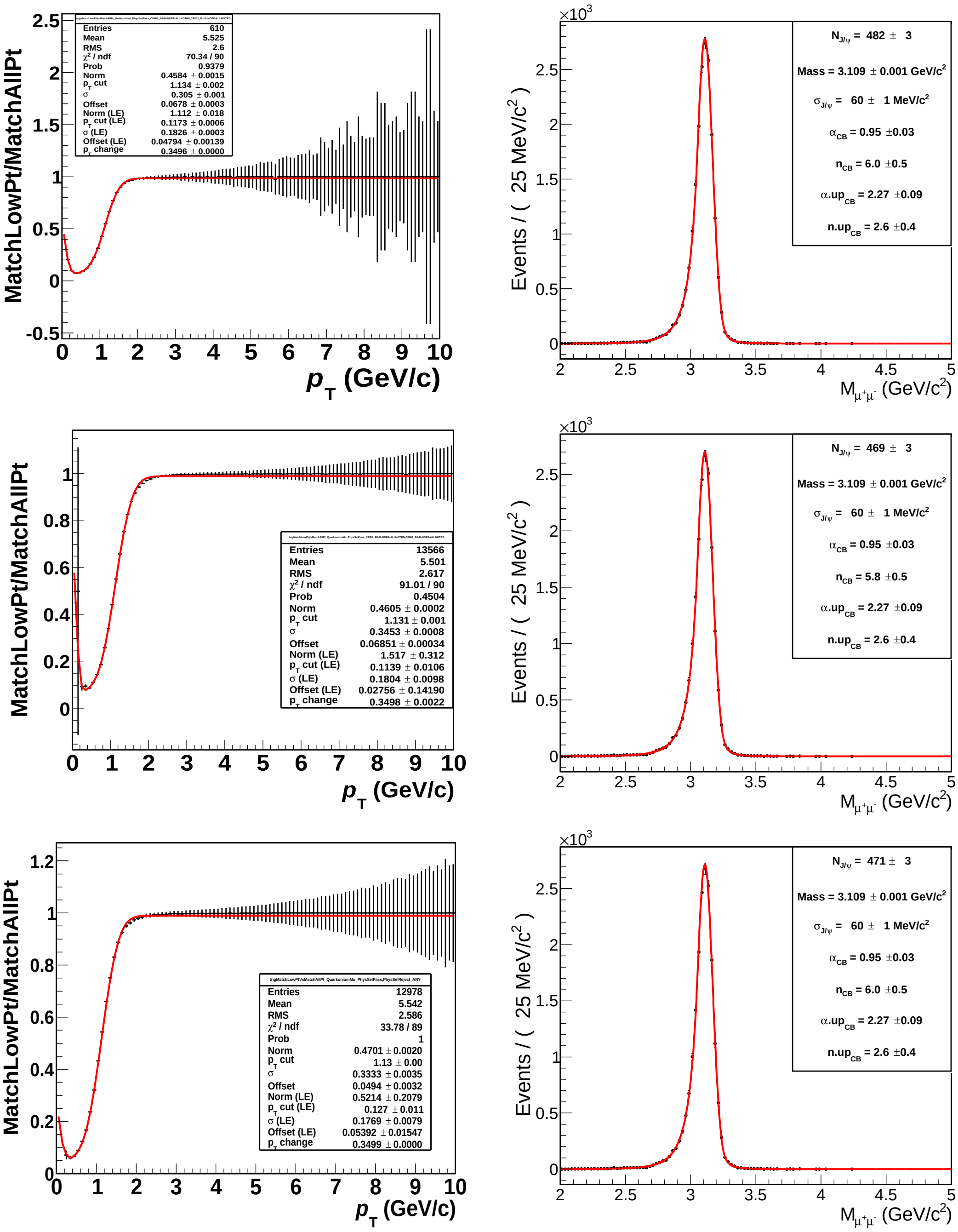

Figure 6.27: *Left*: fit to the low-p_{T}/all-p_{T} trigger threshold ratio from data (*top*), embedding (*middle*) and pure J/ψ simulation (*bottom*). *Right*: fit to the corresponding invariant mass spectra weighted by trigger response functions obtained from data (*top*), embedding (*middle*) and pure J/ψ simulation (*bottom*). The three invariant mass plots correspond to the $0 < p_{\mathrm{T}} < 1$ GeV/c and $2.5 < y < 4$ bin. The maximum relative difference in $N_{\mathrm{J}/\psi}$ among the three spectra (3%) is used as the systematic uncertainty on the trigger threshold.

6.6.4 MC input

As the estimated $A \times \epsilon$ values might depend on the J/ψ p_{T} and y shapes used as input distributions in the MC simulations, it is necessary to evaluate the sensitivity of the results on these initial choices. The extraction of the systematics uncertainties used a three steps method:

- Evaluate the systematic uncertainty starting from the available Pb-Pb data: for each p_{T}/y bin (centrality integrated) the data points are displaced following a Gaussian distribution with a width $\sigma = \sqrt{\sigma^2_{\mathrm{Stat}} + \sigma^2_{\mathrm{Syst}}}$, fitting the new distribution and computing from this an $A \times \epsilon$ value. This procedure is repeated one thousand times. The RMS from the 1 000 acceptance times efficiency results is taken as the sytematic uncertainty.
- p_{T}-y correlation: results for J/ψ at $\sqrt{s}$ = 7 TeV [113] indicate these kinematical variables exhibit a certain degree of correlation. This was estimated by computing $A \times \epsilon$ values from extreme cases of p_{T}-y distributions.
- p_{T}/y-centrality correlation: similar approach to the previous one, but now the correction factors are computed using p_{T}/y-centrality distributions.

The results from these three steps are added in quadrature to assess the final values. The systematic uncertainties are dominated by the p_{T}/y-centrality correlation.

6.6.5 Matching efficiency

The systematic uncertainty on the matching efficiency between the tracking and the trigger tracks has been taken to 1%. Its origin lies in the difference observed between data and simulations when applying different χ^2 cuts on the matching between the track reconstructed in the tracking chambers and the one reconstructed in the trigger chambers. This error is correlated as a function of the centrality and uncorrelated as a function of p_{T} and y.

6.6.6 Other sources

Systematic uncertainties on T_{AA} range from 3% for the most central up to 8% for the most peripheral collisions (table A.1). The systematic uncertainty on F_{Norm} is 3.6%, as can be seen from equation 6.5.

The J/ψ is assumed to be unpolarized, both in pp and Pb-Pb collisions, so no systematic uncertainty is associated on this subject.

6.6.7 Correlated, uncorrelated and partially correlated

All the different sources of systematic uncertainties have been quantified, but some of them vary from bin to bin (uncorrelated) and some others are common to all the centrality/p_{T}/y ranges (correlated). For the single differential R_{AA}, table 6.8 presents a summary of the systematic uncertainties: the origin, value and type (correlated or uncorrelated). Table 6.9 presents the same information but for the multidifferential R_{AA}. In both single and multidifferential R_{AA} vs centrality, the statistical error comes from the signal extraction in Pb-Pb. For the R_{AA} vs p_{T}/y (single and multidifferential) the statistical errors are obtained by adding in quadrature the errors from the signal extraction in Pb-Pb and pp.

In the next section, where the Nuclear Modification Factors are shown, the statistical errors appear as bars while the uncorrelated systematics are indicated as boxes at each point. The correlated uncertainties are quoted at the top of the plots.

Finally, the treatment of the systematics uncertainties when more than one multidifferential set is plotted is particularly delicate. Indeed, some systematic uncertainties may have a certain degree of correlation within a given group of points and/or within different sets. The degree of correlation can not be easily quantified and it is not possible to disentangle the correlated and uncorrelated contributions. Therefore, these kind of systematic uncertainties are grouped as partially correlated and are included as shaded areas around each point in the plots.

Table 6.8: Summary of systematic uncertainties for the single differential R_{AA}. Type I (II) indicates correlated (uncorrelated).

Source	Centrality		p_{T}/y	
	Value (%)	Type	Value (%)	Type
Signal	1 - 5	II	1 - 4	II
MC input	3	I	0 - 1 / 3 - 8	II
Tracking	11 and 0 - 1	I and II	9 - 11 / 8 - 14	II
Trigger	2 and 0 - 1	I and II	2 - 4 / 2	II
Matching	1	I	1	II
T_{AA}	3 - 8	II	3	I
σ^{pp}	9	I	6 and 5 - 6	I and II
F_{Norm}	4	I	4	I

Table 6.9: Summary of systematic uncertainties for the multidifferential R_{AA}. Type I (II) indicates correlated (uncorrelated).

Source	vs p_{T} in cent. bins		vs cent. in p_{T} bins		vs cent. in y bins	
	Value (%)	Type	Value (%)	Type	Value (%)	Type
Signal	1 - 5	II	1-5	II	1 - 4	II
MC input	0 - 1	II	3	I	3	I
Tracking	0 - 1 / 9 - 11	I / II	9 - 11 / 0 - 1	I / II	10 - 14 / 0 - 1	I / II
Trigger	1 / 2 - 4	I / II	2 / 0 - 1	I / II	2 / 0 - 1	I / II
Matching	1	II	1	I	1	I
T_{AA}	3 - 5	I	3 - 6	II	3 - 6	II
σ^{pp}	6 and 5 - 6	I and II	8 - 14	I	8 - 10	I
F_{Norm}	4	I	4	I	4	I

Table 6.10: Different kind of systematics for the multidifferential R_{AA} when more than one set is plotted. Type I/II/III indicates correlated/uncorrelated/partially correlated.

Source	vs p_{T}, cent. bins	vs cent., p_{T}/y bins
	Type	Type
Signal	II	II
MC input	II	III
Tracking	III	III
Trigger	III	III
Matching	II	III
T_{AA}	III	III
σ^{pp}	I and III	I and III
F_{Norm}	I	I

6.7 Nuclear Modification Factors

At forward rapidity ALICE can only measure inclusive J/ψ, as a consequence the following R_{AA} present additional contributions with respect to the initial $gg \rightarrow c\bar{c}$

- J/ψ from B-hadron decays (see appendix C).
- J/ψ from photoproduction (see appendix D).

In both cases, the effect on the J/ψ production is estimated as a function of the centrality, p_{T} and y.

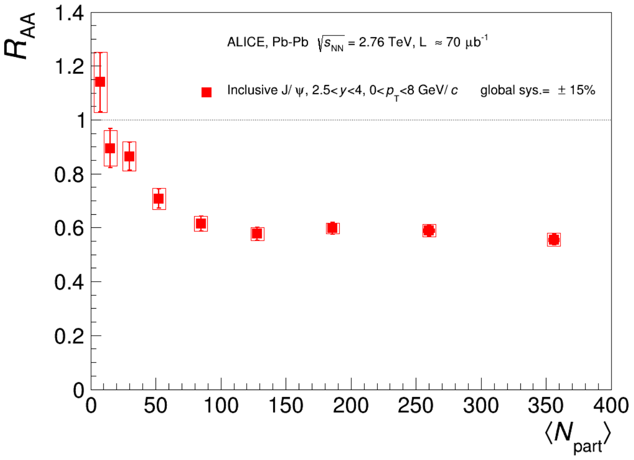

Figure 6.28: J/ψ $R_{\rm AA}$ vs $N_{\rm part}$ with $0 < p_{\rm T} < 8$ GeV/c and $2.5 < y < 4$.

6.7.1 Single differential

The inclusive J/ψ $R_{\rm AA}$ measured by ALICE at $\sqrt{s_{\rm NN}} = 2.76$ TeV in the range $2.5 < y < 4$ and $0 < p_{\rm T} < 8$ GeV/c is shown on figure 6.28 as a function of $N_{\rm part}$. The centrality integrated values is $R_{\rm AA}^{0-90\%} = 0.574 \pm 0.010$ (stat.) $\pm$ 0.089 (syst.), indicating a clear J/ψ suppression with no significant centrality dependence for $N_{\rm part} \gtrsim 70$.

On the left panel of figure 6.29, the centrality dependent $R_{\rm AA}$ obtained from the 2011 Pb-Pb collisions is compared to the one extracted from the 2010 data [61], where $R_{\rm AA}^{0\%-80\%} = 0.545 \pm 0.032$ (stat.) $\pm$ 0.083 (syst.). Results are in very good agreement, both point-per-point and in the integrated value. The common correlated systematic uncertainty between both sets[9] has been removed for a proper comparison.

On the right plot of figure 6.29 ALICE results are compared to PHENIX [114]: Au-Au collisions at $\sqrt{s_{\rm NN}} = 0.2$ TeV with $p_{\rm T} > 0$ GeV/c and $1.2 < |y| < 2.2$. The differences between both experiments is noticeable in the most central collisions, in particular, $R_{\rm AA}^{\rm ALICE} \approx 3 \times R_{\rm AA}^{\rm PHENIX}$ for $N_{\rm part} \gtrsim 250$. This indicates that, despite the larger energy of the collisions at the LHC, PHENIX measures a larger suppression of inclusive J/ψ for $N_{\rm part} \gtrsim 130$ with a remarkable centrality dependence. In the most peripheral bins ($N_{\rm part} \lesssim 50$) both set of results are in very good agreement.

The left panel of figure 6.30 presents the $R_{\rm AA}$ vs transverse momentum, the amount of suppression is larger at high-$p_{\rm T}$ compared to the low-$p_{\rm T}$ regime by approximately 50%. The right panel of the same figure contains the comparison to CMS inclusive J/ψ $R_{\rm AA}$ [115]. The CMS values are obtained in

---

[9] $\sigma^{\rm pp} = 9\%$, that is quoted at the bottom of the plot as ALICE common global systematic uncertainty.

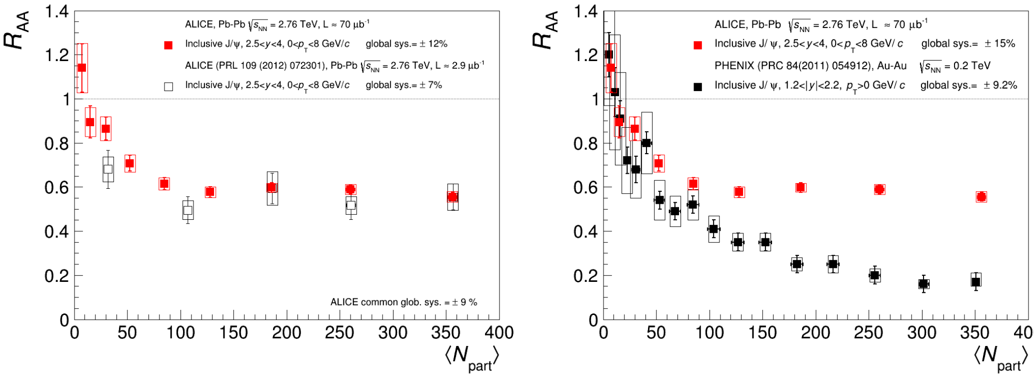

Figure 6.29: *Left*: R_{AA} vs N_{part} compared to the published 2010 results. *Right*: R_{AA} vs N_{part} compared to PHENIX results.

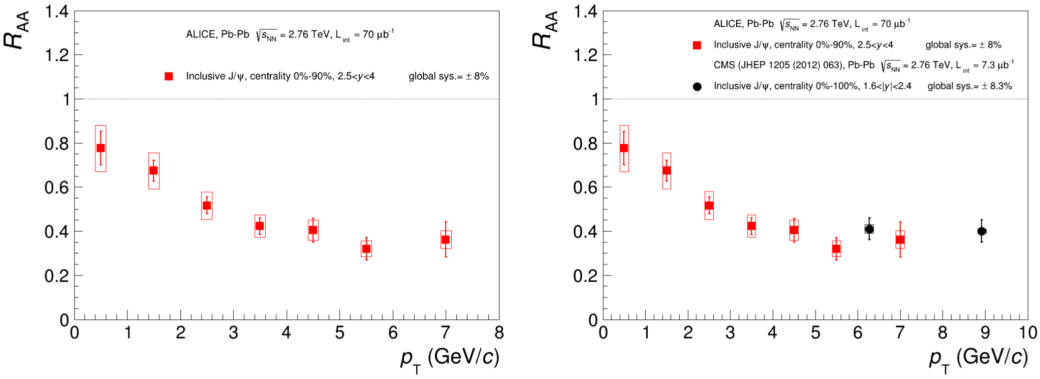

Figure 6.30: *Left*: R_{AA} vs p_{T}. *Right*: R_{AA} vs p_{T} compared to CMS results.

a different rapidity range, closer to mid-rapidity ($1.6 < |y| < 2.4$) and in overlapping p_{T} ranges: $3 \leq p_{\mathrm{T}} \leq 30$ GeV/c with $\langle p_{\mathrm{T}} \rangle = 6.27$ GeV/c and $6.5 \leq p_{\mathrm{T}} \leq 30$ GeV/c with $\langle p_{\mathrm{T}} \rangle = 8.92$ GeV/c.

The rapidity dependence of the Nuclear Modification Factor is shown on the left plot of figure 6.31, where the R_{AA} shows a decrease of almost 30% from $y = 2.5$ to $y = 4$. On the right panel of the same figure, both forward and mid rapidity ($R_{\mathrm{AA}}^{0-90\%} = 0.772 \pm 0.057$ (stat.) $\pm$ 0.102 (syst.)) results are plotted together[10]. The correlated error common to both measurements is indicated at the bottom and contains the uncertainty on the luminosity and on the T_{AA}. The result from the J/$\psi \to e^{+}e^{-}$ decaying channel suggests a decreasing trend of the R_{AA} towards the forward/backward rapidity.

---

[10] Mid rapidity results include the 2010 and the 2011 Pb-Pb periods.

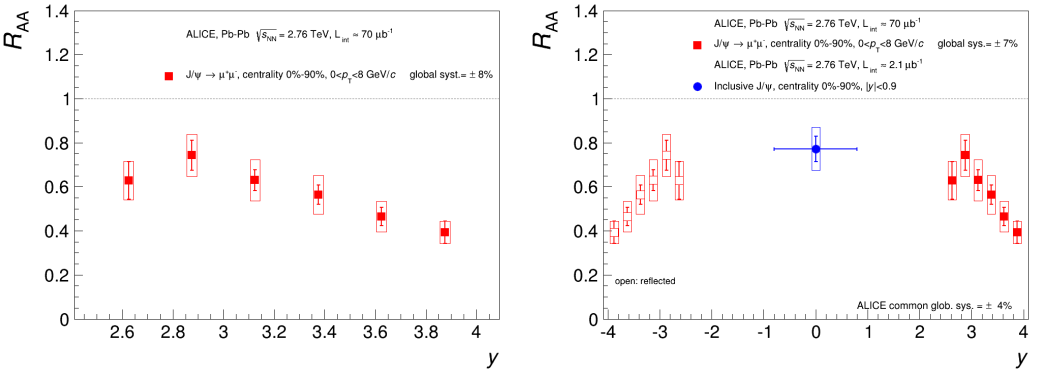

Figure 6.31: *Left*: R_{AA} vs y at forward rapidity. *Right*: R_{AA} vs y at mid and forward rapidity.

6.7.2 Multidifferential

Figure 6.32 presents the R_{AA} vs p_{T} for different centrality ranges. In the most central collisions (left panel) the suppression is clearly increasing from the low to high-p_{T} domain. However this behaviour is less pronounced for the intermediate centrality (middle panel). For peripheral collisions (right panel), the difference between low and high-p_{T} bins is not significant anymore.

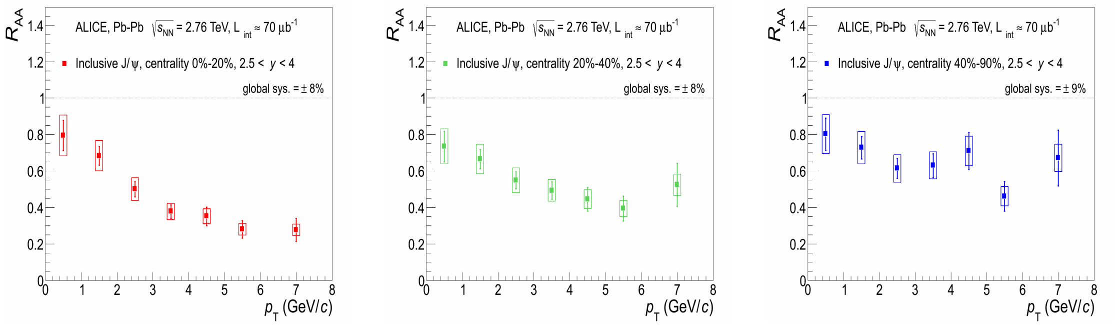

Figure 6.32: R_{AA} vs p_{T} in 0-20% (*left*), 20-40% (*middle*) and 40-90% (*right*) centrality bins.

On the left side of figure 6.33 the most central and peripheral bins are plotted together. For $p_{\mathrm{T}} > 3$ GeV/c the R_{AA} from the 0-20% centrality range show a larger suppression. On the right side of the same figure, the R_{AA} vs p_{T} for the most central collisions is compared to a lower energy measurement from the PHENIX experiment. Although the rapidity coverage and CNM effects can play an important role, the difference is evident and is a possible indicator that the production of low-p_{T} J/ψ is favoured at the LHC.

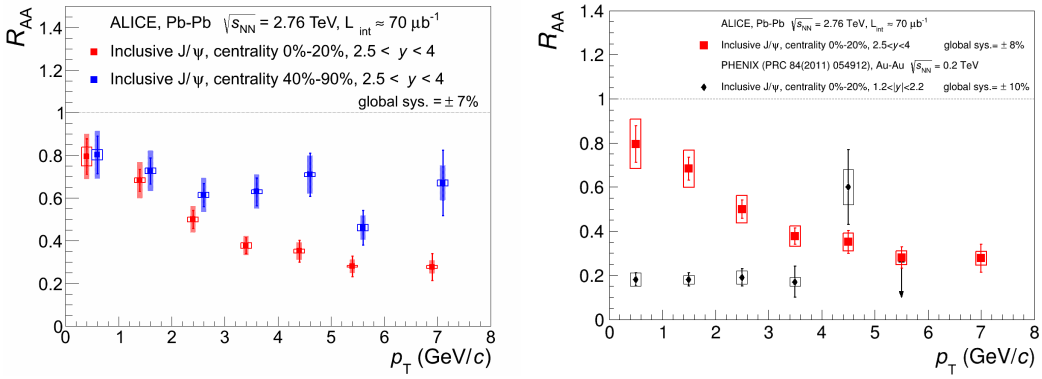

Figure 6.33: *Left*: Comparison of R_{AA} vs p_T for different centrality bins. *Right*: R_{AA} vs p_T in the 0-20% centrality bin compared to PHENIX results.

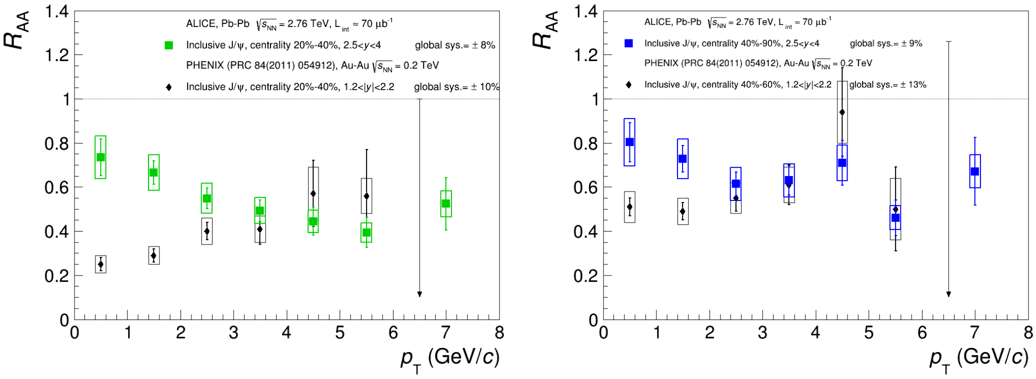

Figure 6.34: R_{AA} vs p_T in the 20-40% (*left*) and 40-90% (*right*) centrality bin compared to PHENIX results.

Left (right) plot of figure 6.34 contains the R_{AA} vs p_T for semicentral (peripheral) collisions compared to PHENIX. For the semicentral collisions, the difference between both results is, once again, striking: ALICE measurements show a decreasing trend from low to high p_T, while PHENIX R_{AA} has the opposite behaviour. For the peripheral collisions the difference is reduced, indeed for $p_T > 2$ GeV/c both measurements are fully consistent.

Figure 6.35 shows the R_{AA} vs N_{part} in three different p_T ranges. In the low-p_T regime (left) the Nuclear Modification Factor shows very little centrality dependence for $N_{part} \gtrsim 100$, that tends to disappear as the p_T is increased.

The R_{AA} vs N_{part} for the low and high p_T J/ψ are plotted together on the left panel of figure 6.36 showing that, for $N_{part} \gtrsim 150$, results corresponding to the $5 < p_T < 8$ GeV/c bin present a larger suppression. On the right plot of the same figure the R_{AA} vs N_{part} for the high-p_T bin is compared to the CMS results in the $|y| < 2.4$ and $6.5 < p_T < 30$ GeV/c bins. Despite the

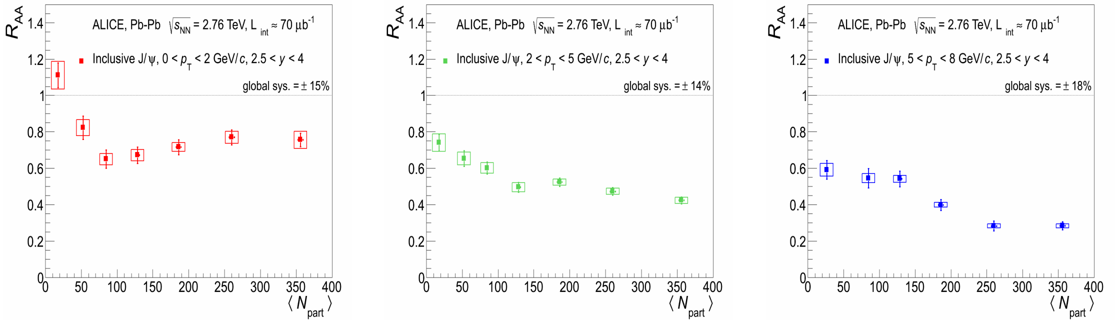

Figure 6.35: R_{AA} vs N_{part} for $p_{\mathrm{T}} < 2$ GeV/c (*left*), $2 < p_{\mathrm{T}} < 5$ GeV/c (*middle*) and $5 < p_{\mathrm{T}} < 8$ GeV/c (*right*).

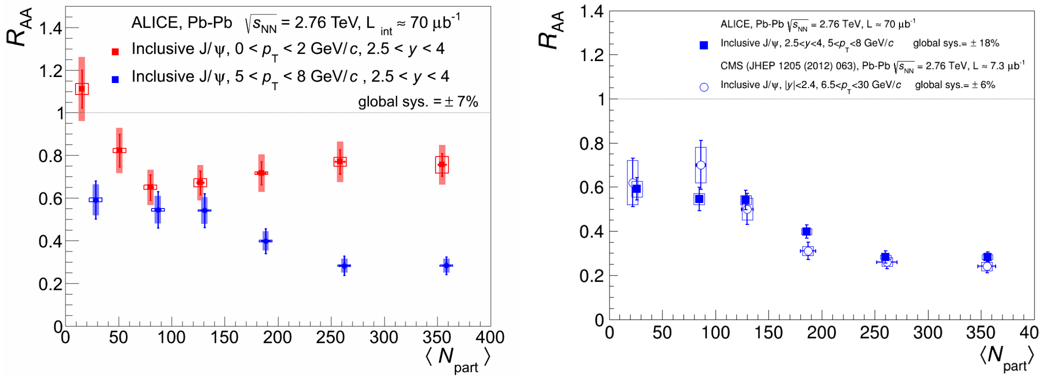

Figure 6.36: *Left*: Comparison between R_{AA} vs N_{part} for low and high p_{T} J/ψ. *Right*: Comparison between ALICE high-p_{T} J/ψ and CMS.

different rapidity and transverse momentum ranges, both results present the same centrality dependence and amount of suppression.

Figure 6.37 contains the R_{AA} as a function of N_{part} in three different rapidity ranges. In all cases the Nuclear Modification Factor is weakly dependent on the centrality when $N_{\mathrm{part}} \gtrsim 150$. Figure 6.38 shows the comparison between the $2.5 < y < 3$ and $3.5 < y < 4$ bins, where the R_{AA} in the most forward region is systematically lower.

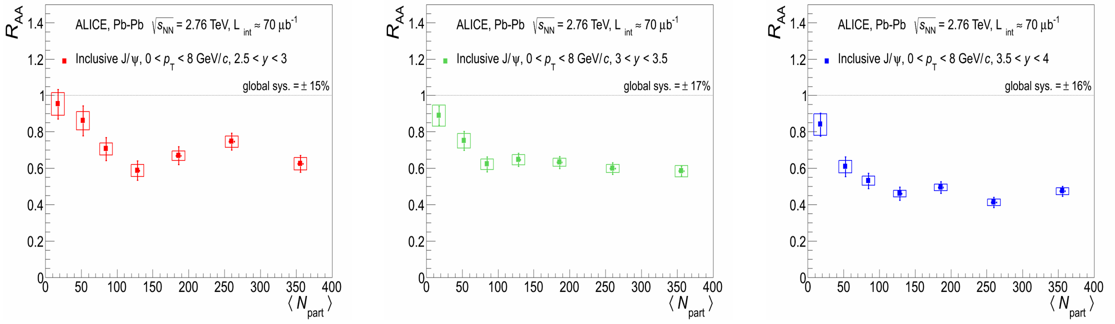

Figure 6.37: $R_{\rm AA}$ vs $N_{\rm part}$ for $2.5 < y < 3$ (*left*), $3 < y < 3.5$ (*middle*) and $3.5 < y < 4$ (*right*).

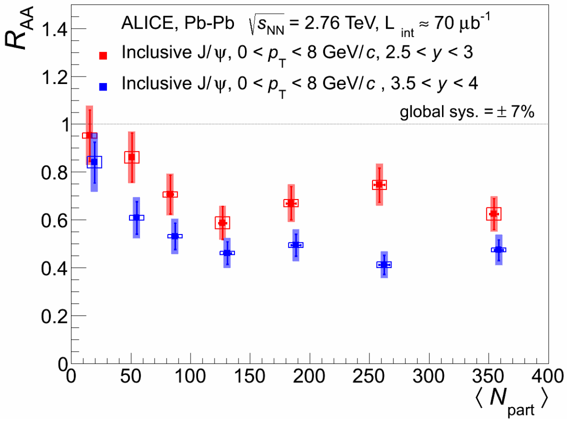

Figure 6.38: Comparison between $R_{\rm AA}$ vs $N_{\rm part}$ in two different rapidity bins.

6.8 Comparison to theoretical models

The J/ψ $R_{\rm AA}$ as a function of the number of participants is shown on figure 6.39 and it is compared to the predictions from the Statistical Hadronization Model (SHM), Transport Model (TM) and Comovers plus recombination (CpR). The two lines from the SHM indicate the predictions obtained from two different charm production cross sections in Pb-Pb collisions. The TM are shown as bands where the lower (upper) limit is the result obtained by the models with (without) shadowing. Within the large uncertainties due to the shadowing and charm cross section, all four models reproduce quite well the data for $N_{\rm part} \gtrsim 70$.

Figure 6.40 contains the J/ψ $R_{\rm AA}$ vs y and an estimate of the shadowing effects within the CSM at LO and CEM at NLO. The shadowing is computed with the nDSg [116] and EPS09 [117] parametrizations of the nPDF, respectively. For nDSG (EPS09) the upper and lower limits correspond to

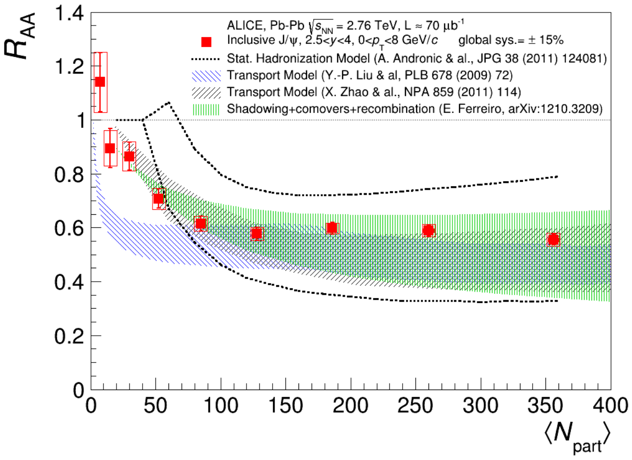

Figure 6.39: R_{AA} vs N_{part} compared to the Statistical Hadronization Model, Transport Models and Comovers plus recombination.

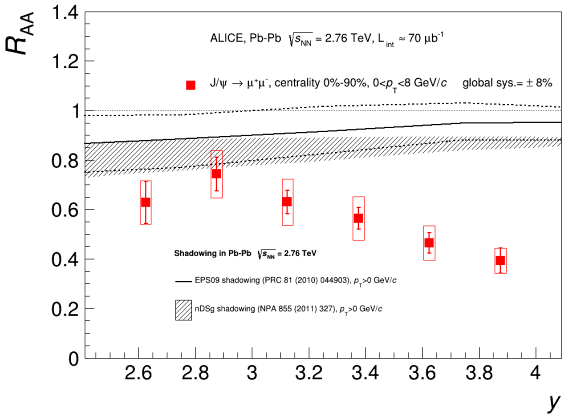

Figure 6.40: R_{AA} vs y with an estimate of the shadowing effect.

the uncertainty on the factorization scale (uncertainty of the nPDF). In both cases, according to the models, the effect of the shadowing is weaker at more forward rapidities. As a consequence, the shadowing corrected R_{AA} at low rapidity would be barely suppressed by QGP effects.

Figure 6.41 shows the R_{AA} vs p_T compared to the Transport Models, where the contribution of regenerated J/ψ at low-p_T amounts to approximately 25% (left panel) and 50% (right panel) of the measured yield, while it vanishes at high-p_T. The remaining contribution comes from the initial produced J/ψ. A noticeable difference between the models is that in one of them (left plot) the primordial component dominates the J/ψ production over the whole p_T range and only for transverse momentum below 3 GeV/c there is a sizeable production from recombination. For the other one, J/ψ production from recombination clearly dominates for p_T < 2 GeV/c and exceeds the primordial

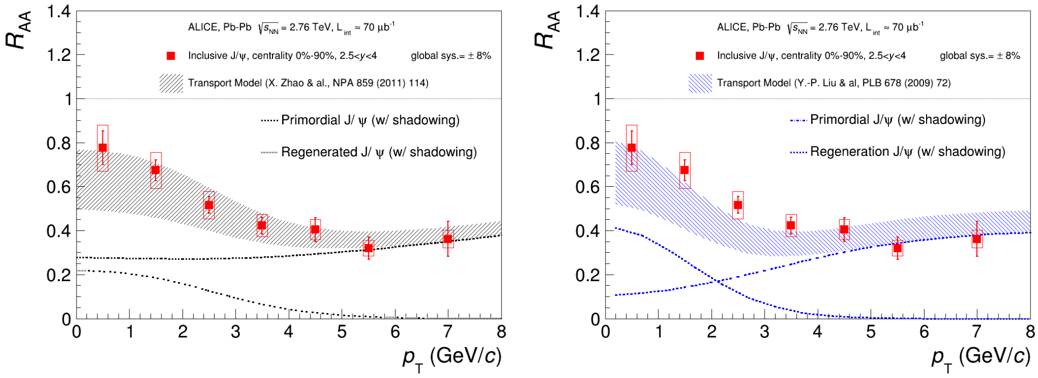

Figure 6.41: R_{AA} vs p_T compared to Transport Models.

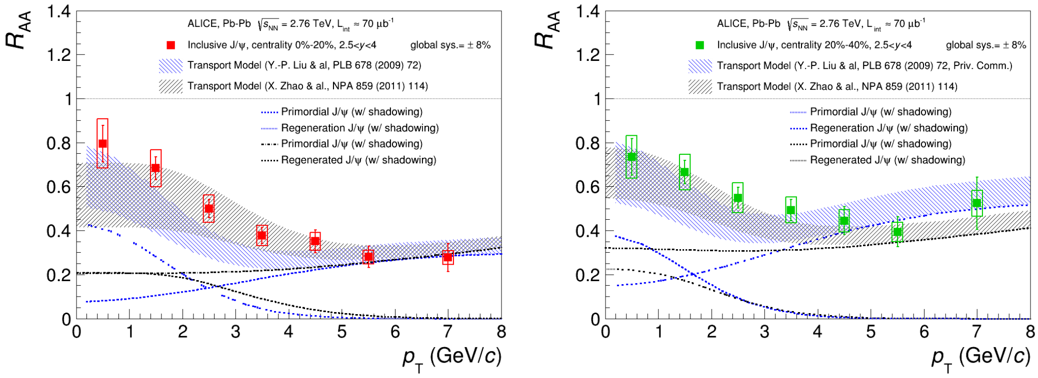

Figure 6.42: R_{AA} vs p_T for central (*left*) and semicentral (*right*) collisions compared to Transport Models.

production by 60% in this range. Both models underestimate the data for p_T < 3 GeV/c.

In figure 6.42 the R_{AA} as a function of p_T for the 0-20% (left plot) and 20-40% (right plot) centrality ranges are compared to the Transport Models. In both models the contribution from regeneration is present in the low-p_T regime, while it vanishes at high transverse momentum. The difference between the models relies on the amount of the regenerated contribution in the low-p_T range for both centralities: Liu & et al. propose a 50% of recombined J/ψ while Zhao et al. 25%. For the most central collisions both models reproduce the data for p_T > 5 GeV/c, below this value the prediction from Liu & et al. tends to underestimate the results. Similar conclusion can be drawn for the 20-40% centrality bin.

The comparison between the Transport Models and the R_{AA} vs p_T in the 40-90% centrality range is presented in figure 6.43. In this case, according to the models, the contribution from regeneration in the low-p_T regime decreases as compared to the figure 6.42. Another interesting point is that, opposite to

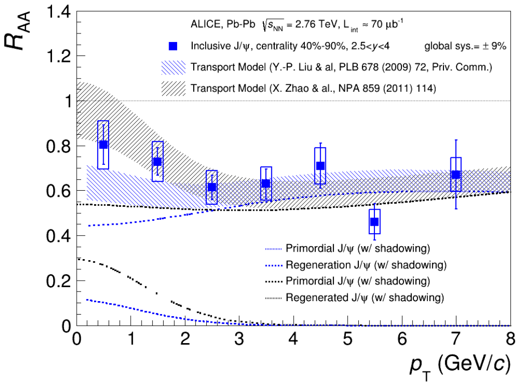

Figure 6.43: R_{AA} vs p_T in the 40-90% centrality range compared to Transport Models.

the 0-20% and 20-40% centrality bins, the prediction from Zhao et al. proposes a larger amount of regenerated J/ψ (40%) than Liu et al. (15%). The curve that better fits the data comes from Zhao et al.

The R_{AA} as a function of the centrality for $0 < p_T < 2$ GeV/c is compared to both Transport Models in figure 6.44. In the left panel the regenerated (primary) component dominates for $N_{part} \gtrsim 150$ ($N_{part} \lesssim 100$); however, the global prediction of the model underestimates the results. In the right panel the contribution from regenerated J/ψ is basically constant for $N_{part} \gtrsim 50$ and is dominated by the primary component up to the most central collisions. Another important fact is that the yield from primaries amounts up to 90% for the most peripheral bins. This model provides a good description of the data for $N_{part} \lesssim 170$.

Figure 6.45 performes the same comparison but in the $2 < p_T < 5$ GeV/c bin. In this case both models present a similar amount of contribution due to regenerated J/ψ (30-40%) that decreases until it vanishes in the peripheral collisions. The difference between the predictions relies in the primary component: it is larger in the peripheral bins for the model show in the right panel. Although the model from the left panel reproduces the trend of the data, it systematically underestimates it. The best description of the R_{AA} comes, once again, from X. Zhao & et al.

The R_{AA} vs N_{part} for $5 < p_T < 8$ GeV/c is also compared to the Transport Models in figure 6.46. In this case both models adjust to the data indicating that the contribution from regenerated J/ψ is negligible (even in the most central collisions). The difference is once again the amount of the primary component in the most peripheral collisions, where the model present in the right panel overestimates the R_{AA}.

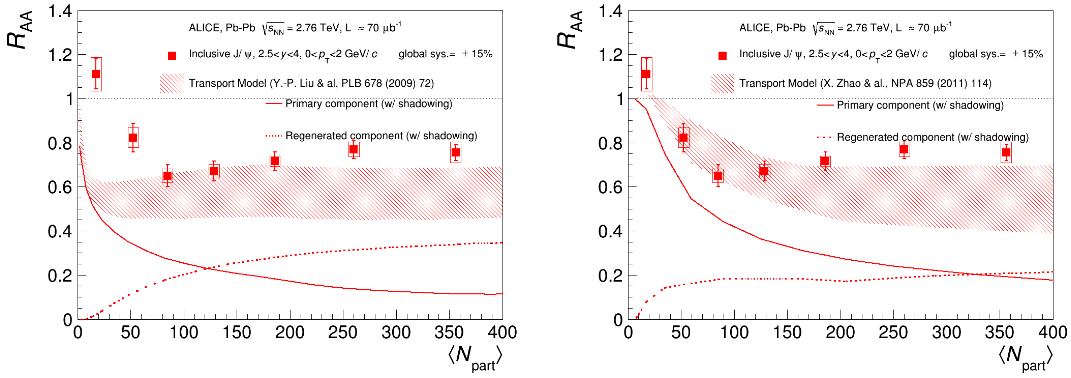

Figure 6.44: R_{AA} vs N_{part} for $0 < p_T < 2$ GeV/c bins compared to Transport Models.

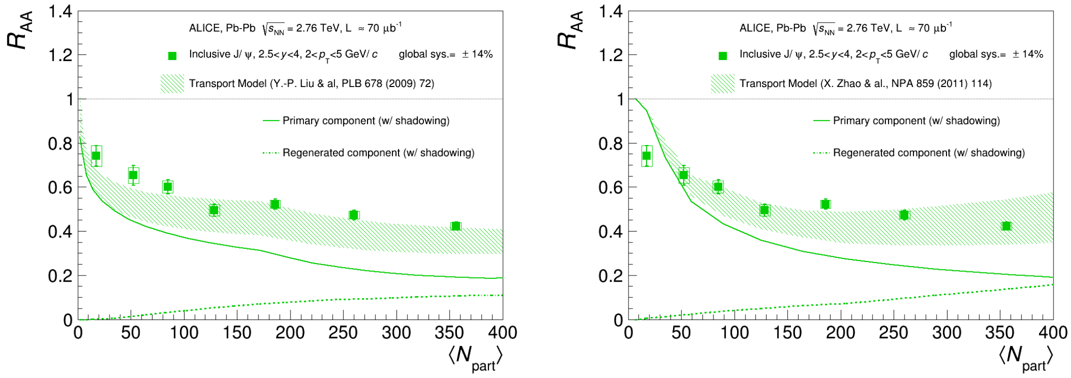

Figure 6.45: R_{AA} vs N_{part} for $2 < p_T < 5$ GeV/c bins compared to Transport Models.

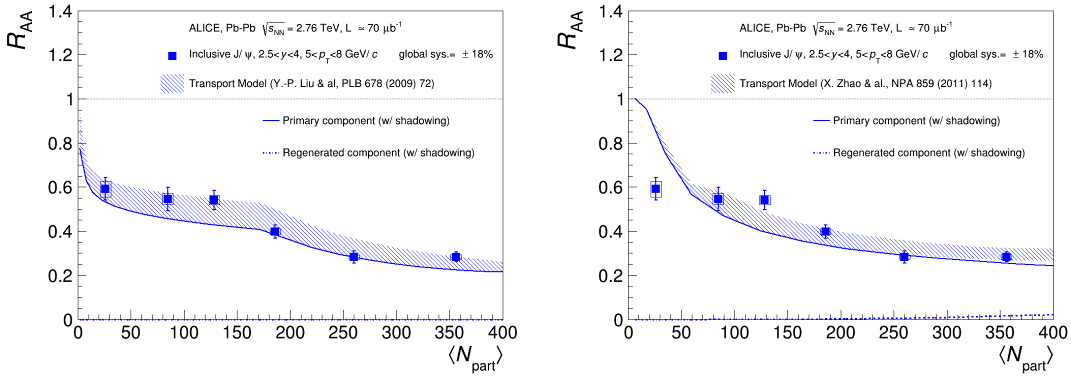

Figure 6.46: R_{AA} vs N_{part} for $5 < p_T < 8$ GeV/c bins compared to Transport Models.

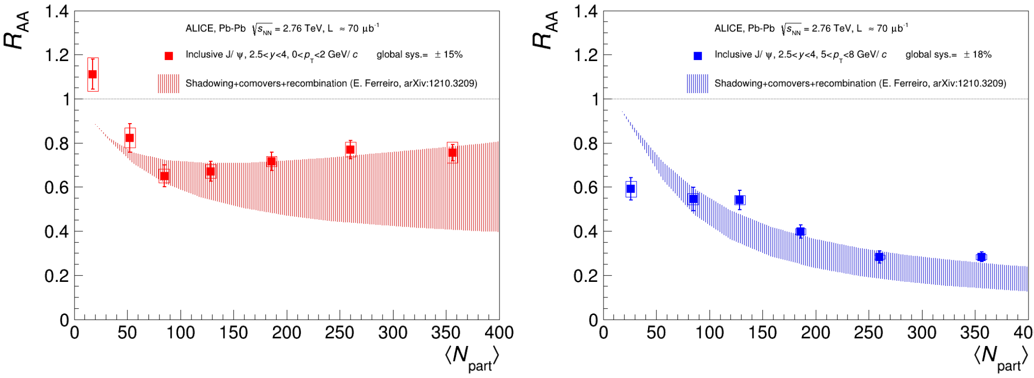

Figure 6.47: R_{AA} vs N_{part} for low (*left*) and high-p_{T} (*right*) J/ψ compared to the CpR model.

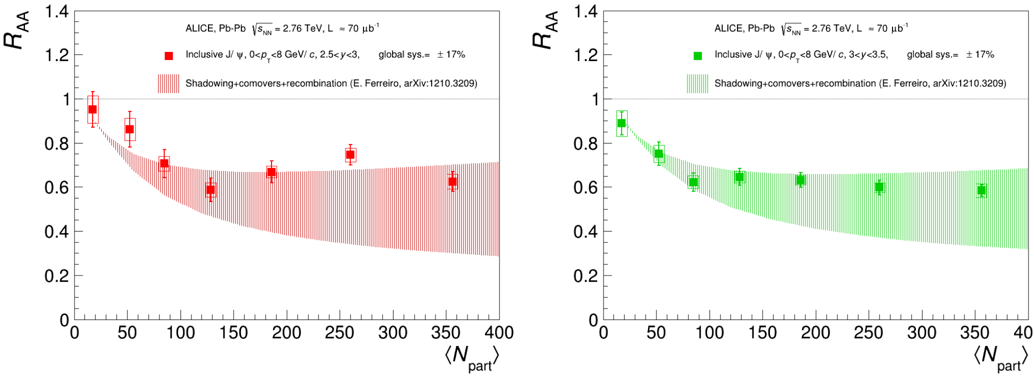

Figure 6.48: R_{AA} vs N_{part} for $2.5 < y < 3$ (*left*) and $3.0 < y < 3.5$ (*right*) compared to the CpR model.

Figure 6.47 contains the R_{AA} vs N_{part} for $0 < p_{\mathrm{T}} < 2$ GeV/c (left panel) and $5 < p_{\mathrm{T}} < 8$ GeV/c (right panel) p_{T} J/ψ compared to the CpR model. Contrary to the previous Transport Models, the CpR adjusts to the data in the $p_{\mathrm{T}} < 2$ GeV/c bin, but this is mainly due to its large uncertainty band. In the $5 < p_{\mathrm{T}} < 8$ GeV/c range it also describes the data, although in this regime the uncertainty on the prediction is much smaller.

Figure 6.48 shows the comparison between the CpR and the R_{AA} vs N_{part} for $2.5 < y < 3$ (left) and $3.0 < y < 3.5$ (right). In both cases the model, with a rather large uncertainty, presents a good description of the data. Finally figure 6.49 shows the same comparison but for the most forward rapidity bin where the prediction clearly overestimates the results for $N_{\mathrm{part}} \lesssim 150$.

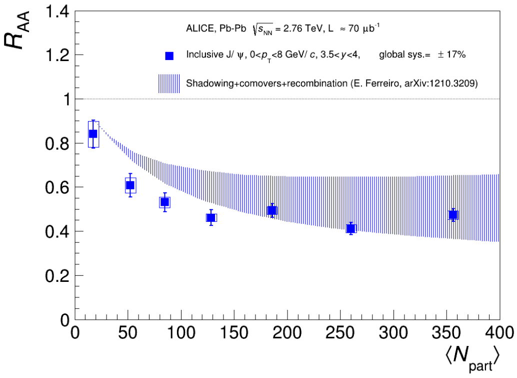

Figure 6.49: R_{AA} vs N_{part} for $3.5 < y < 4$ compared to the CpR model.

6.9 $\langle p_{\mathrm{T}} \rangle$ and $\langle p_{\mathrm{T}}^2 \rangle$

The inclusive J/ψ $d^2\sigma/dp_{\mathrm{T}}dy$ distribution was studied in three different centrality bins (0-20%, 20-40% and 40-90%). It is obtained from the invariant yield (equation 6.2), the total Pb-Pb cross section ($\sigma_{\mathrm{Pb-Pb}}$), the rapidity width covered by the muon spectrometer (Δy) and the width of the p_{T} interval (Δp_{T}):

$$\frac{d^2\sigma}{dydp_{\mathrm{T}}} = \sigma_{\mathrm{Pb-Pb}} \frac{Y^{\mathrm{AA}}_{J/\psi}(\Delta p_{\mathrm{T}}, \Delta y)}{\Delta y \Delta p_{\mathrm{T}}}. \tag{6.6}$$

Because in this case the pp reference was not needed, the signal extraction was performed in finer p_{T} bins (table 6.7), allowing to better define the $d^2\sigma/dp_{\mathrm{T}}dy$ shapes. The resulting distributions (figure 6.50) are fitted with the function:

$$f(p_{\mathrm{T}}) = C \frac{p_{\mathrm{T}}}{\left[1 + \left(\frac{p_{\mathrm{T}}}{p_0}\right)^2\right]^n}, \tag{6.7}$$

where C, p_0 and n are free parameters.

In the $d^2\sigma/dp_{\mathrm{T}}dy$ plot corresponding to the 40-90% centrality range (right panel of figure 6.50), the first p_{T} bin (0-0.5 GeV/c) is shifted up relative to the expected hadroproduced J/ψ indicated by the fit. At low-p_{T} and in peripheral collisions, the J/ψ are affected by coherent photoproduction (see appendix D). The three $d^2\sigma/dp_{\mathrm{T}}dy$ distributions are plotted together in figure 6.51.

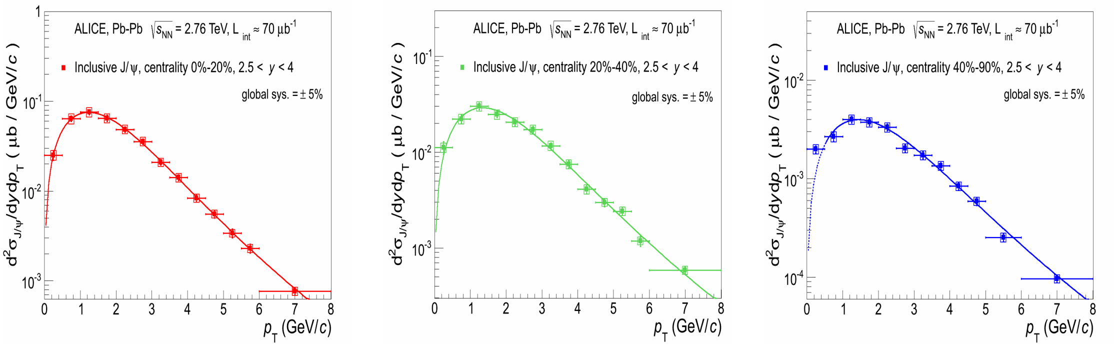

Figure 6.50: $d^2\sigma/dp_Tdy$ for different centrality bins: 0-20% (*left*), 20-40% (*middle*) and 40-90% (*right*).

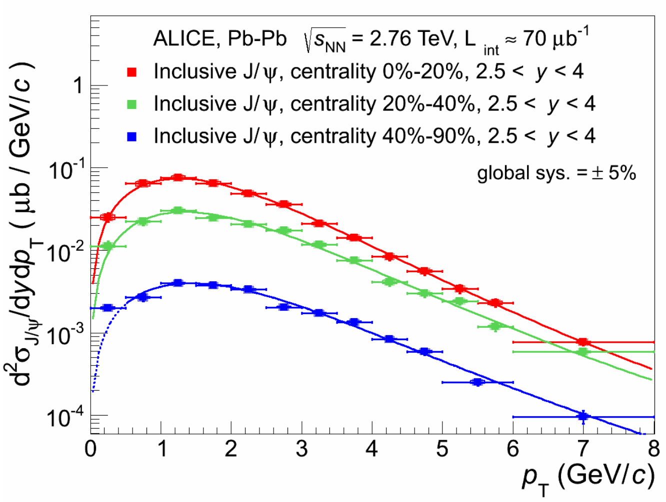

Figure 6.51: Comparison between the $d^2\sigma/dydp_T$ obtained in three centrality bins: 0-20%, 20-40% and 40-90%.

The $\langle p_T \rangle$ and $\langle p_T^2 \rangle$ can be obtained by integrating the fitting function in the interval $0 < p_T < 8$ GeV/c. The statistical uncertainties are computed in the following way:

1. Fit the $d^2\sigma/dp_Tdy$ distributions with statistical uncertainties only, using equation 6.7.
2. Draw a 1σ variation contour plot of p_0 and n parameters[11]. Each point along the contour corresponds to a variation of p_0 and n within 1σ (figure 6.52).

---

[11] C is the normalization so it has no influence on the $\langle p_T \rangle$ nor $\langle p_T^2 \rangle$ values.

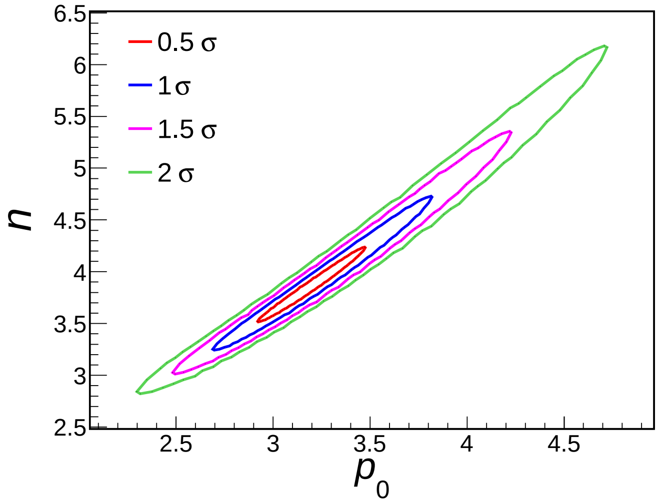

Figure 6.52: Example of the n σ variation contour plot for the p_0 and n parameters corresponding to the statistical error of the $d^2\sigma/dp_{\mathrm{T}}dy$ distribution in the 0-20% centrality bin.

3. Re-compute the $\langle p_{\mathrm{T}} \rangle$ and $\langle p_{\mathrm{T}}^2 \rangle$ fixing p_0 and n to a point (p_0', n') along the contour. The re-calculation is repeated 500 times using different points from the 1σ contour plot, performing a closed orbit.
4. The extreme case of this distribution, made out of 500 $\langle p_{\mathrm{T}} \rangle$ and $\langle p_{\mathrm{T}}^2 \rangle$ values, is taken as the statistical uncertainty (figure 6.53).

The systematic uncertainties are extracted in the same way (figure 6.54), but replacing the statistical errors by the systematic ones. Table 6.11 presents the J/ψ $\langle p_{\mathrm{T}} \rangle$ and $\langle p_{\mathrm{T}}^2 \rangle$ values obtained. The results indicate a decreasing trend for increasing centrality.

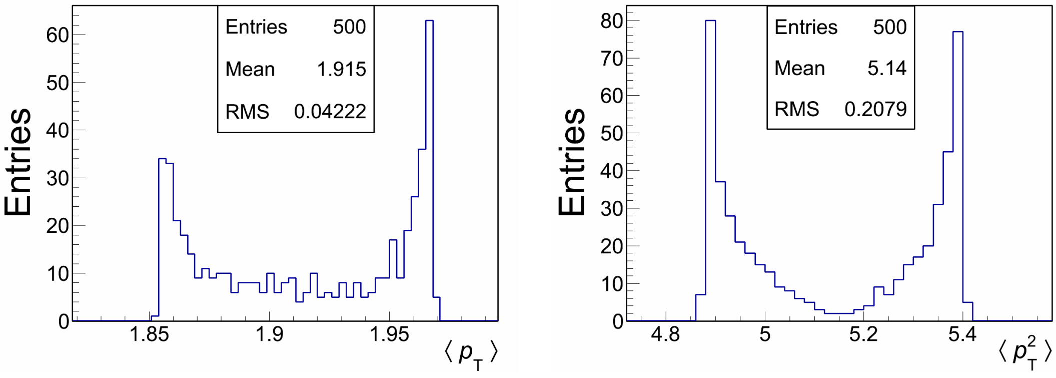

Figure 6.53: Distribution of the J/ψ $\langle p_{\mathrm{T}} \rangle$ (*left*) and $\langle p_{\mathrm{T}}^2 \rangle$ (*right*) evaluated along the 1σ variation contour plot corresponding to the statistical uncertainties.

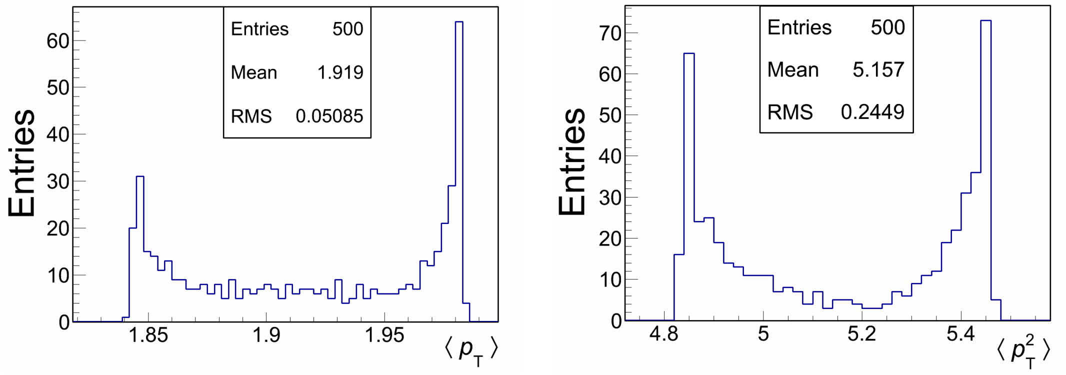

Figure 6.54: Distribution of the J/ψ $\langle p_{\mathrm{T}} \rangle$ (*left*) and $\langle p_{\mathrm{T}}^2 \rangle$ (*right*) evaluated along the 1σ variation contour plot corresponding to the systematic uncertainties.

Table 6.11: J/ψ $\langle p_{\mathrm{T}} \rangle$ and $\langle p_{\mathrm{T}}^2 \rangle$.

	$0 < p_{\mathrm{T}} < 8$ GeV/c, $2.5 < y < 4$	
Cent.	$\langle p_{\mathrm{T}} \rangle$ ± stat. ± syst. (GeV/c)	$\langle p_{\mathrm{T}}^2 \rangle$ ± stat. ± syst. (GeV/c)^2
0-20%	1.91 ± 0.06 ± 0.07	5.1 ± 0.3 ± 0.3
20-40%	2.08 ± 0.07 ± 0.09	6.0 ± 0.4 ± 0.4
40-90%	2.22 ± 0.08 ± 0.09	6.8 ± 0.6 ± 0.6

In the left panel of figure 6.55, the J/ψ $\langle p_{\mathrm{T}} \rangle$ measured by ALICE is shown as a function of the centrality. The $\langle p_{\mathrm{T}} \rangle$ presents a clear decreasing trend, a striking difference with respect to the trend shown by the PHENIX experiment in Au-Au and Cu-Cu collisions at $\sqrt{s_{\mathrm{NN}}} = 200$ GeV/c in the rapidity interval $1.2 < |y| < 2.2$ [118, 119]. The pp results from both experiments are also shown. The right panel presents a compilation of J/ψ $\langle p_{\mathrm{T}}^2 \rangle$ results as a function of the number of participant nucleons. The decrease already observed in the $\langle p_{\mathrm{T}} \rangle$ is confirmed in the $\langle p_{\mathrm{T}}^2 \rangle$ behaviour, once again, an opposite trend compared to PHENIX results.

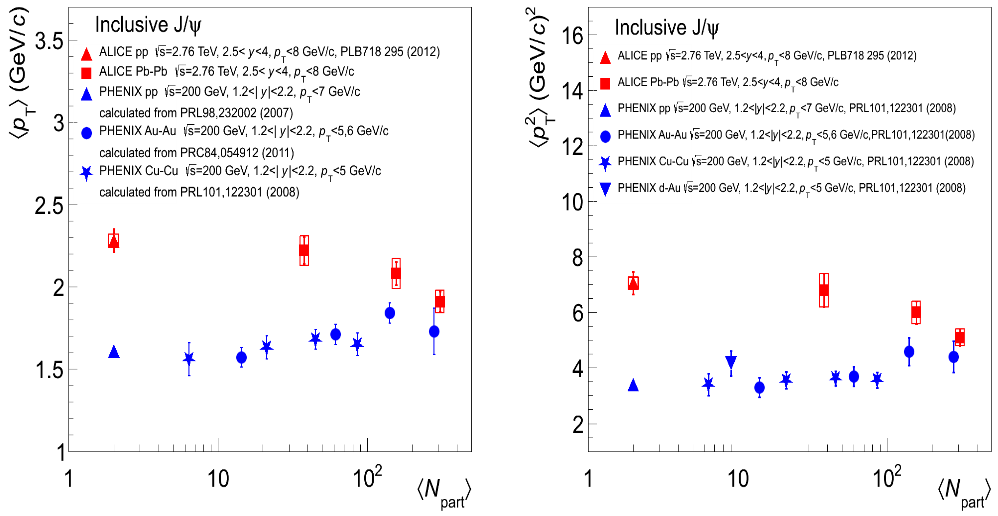

Figure 6.55: J/ψ $\langle p_{\mathrm{T}} \rangle$ (*left*) and $\langle p_{\mathrm{T}}^2 \rangle$ (*right*) compared to PHENIX experiment.

Chapter 7

Conclusions

This thesis has presented a detailed study of the tracking efficiency of the muon chambers in the ALICE experiment and of the inclusive J/ψ production, down to $p_{\mathrm{T}} = 0$ GeV/c, at forward rapidity in Pb-Pb collisions.

The tracking efficiency of the muon chambers was studied along one year of data taking for two different colliding systems (Pb-Pb and pp) at $\sqrt{s_{\mathrm{NN}}} =$ 2.76 TeV and as a function of different variables: time (run number), centrality, p_{T} and y. In Pb-Pb collisions the efficiency presented a remarkable dependence on the centrality of the event due to the high multiplicity created in central collisions. In the 2010 Pb-Pb period the efficiency was found to be constant during all the data taking, while in 2011 important fluctuations appeared in the last runs because of some HV trips. In general, the best performance of the chambers was reached at the beginning of the year, after the winter shut down, once the chambers have been repaired. It was also shown that more damaged a chamber is, more difficult is to be correctly reproduced by the simulation. In the three periods studied, a precise analysis of the correlated effects were performed by exploiting the X-Y symmetry of each chamber and it was shown that these effects are correctly reproduced by the simulation. As an open issue remains the disagreement observed between the measured efficiency in real data/simulation and the true efficiency that is directly computed from the Monte Carlo generator.

Concerning the inclusive J/ψ production measurement in the 2011 Pb-Pb collisions at $\sqrt{s_{\mathrm{NN}}} = 2.76$ TeV, the analysis included the normalization of the number of events, signal extraction, detector acceptance and efficiency corrections and the estimation of the systematic uncertainties from the different sources: signal extraction, MC input, normalization, pp reference, trigger, tracking and matching efficiency. The resulting Nuclear Modification Factor presents a suppression that suggests a decreasing trend towards forward rapidities. The R_{AA} has no significant centrality dependence for $N_{\mathrm{part}} \gtrsim 70$ and, for the most central collisions, it is approximately three times larger than the one measured at forward rapidity at RHIC. The R_{AA} exhibits a strong p_{T} dependence, decreasing for increasing p_{T}, a completely different behaviour relative to PHENIX results. The clear decrease of the $\langle p_{\mathrm{T}} \rangle$ and $\langle p_{\mathrm{T}}^2 \rangle$ with increasing N_{part} indicates that low-p_{T} J/ψ are less suppressed in central collisions, a striking difference with respect to lower energy results. Theoretical models which include a full and partial J/ψ production from charm quarks in a dense partonic phase successfully describe the data. In all the theoretical predictions, the (re)generation component is dominant in the low-p_{T} regime. However, a main source of uncertainty in the models is the amount of shadowing and the $c\bar{c}$ cross section, demonstrating the importance to quantify the Cold Nuclear Matter effects.

References

[1] A. Quadt, “Top quark physics at hadron colliders,” *Eur. Phys. J. C*, vol. 48, p. 835, 2006.

[2] ATLAS Collaboration, “Observation of a new particle in the search for the Standard Model Higgs boson with the ATLAS detector at the LHC,” *Phys.Lett.*, vol. B716, pp. 1–29, 2012.

[3] CMS Collaboration, “Observation of a new boson at a mass of 125 GeV with the CMS experiment at the LHC,” *Phys.Lett.*, vol. B716, pp. 30–61, 2012.

[4] LHC Study Group, “The Large Hadron Collider: Conceptual Design,” CERN-AC-95-05-LHC, 1995.

[5] Particle Data Group *Phys. Rev. D*, vol. 86, p. 010001, 2012.

[6] F. Halzen and A. Martin, *Quarks and Leptons: An Introductory Course in Modern Particle Physics.* John Wiley & Sons, 1984.

[7] S. Bethke, “World Summary of α_s (2012),” 2012, arXiv:1210.0325.

[8] R. Vogt, *Ultrarelativistic Heavy-Ion Collisions.* 1^{st} ed., 2007.

[9] A. Bazavov *et al.*, “Equation of state and QCD transition at finite temperature,” *Phys.Rev. D*, vol. 80, p. 014504, 2009.

[10] H. Satz, “The Thermodynamics of Quarks and Gluons,” *Lect.Notes Phys.*, vol. 785, pp. 1–21, 2010.

[11] K. Yagi, T. Hatsuda, and Y. Miake, “Quark-gluon plasma: From big bang to little bang,” *Camb.Monogr.Part.Phys.Nucl.Phys.Cosmol.*, vol. 23, pp. 1–446, 2005.

[12] PHENIX Collaboration, “Scaling properties of azimuthal anisotropy in Au+Au and Cu+Cu collisions at $\sqrt{s_{\mathrm{NN}}} = 200$ GeV,” *Phys.Rev.Lett.*, vol. 98, p. 162301, 2007.

[13] STAR Collaboration, "Enhanced strange baryon production in Au + Au collisions compared to p + p at $\sqrt{s_{\mathrm{NN}}} = 200$ GeV," *Phys.Rev.*, vol. C77, p. 044908, 2008.

[14] NA60 Collaboration, "First measurement of the ρ spectral function in high-energy nuclear collisions," *Phys.Rev.Lett.*, vol. 96, p. 162302, 2006.

[15] NA60 Collaboration, "A Comparative measurement of $\phi \to K^+K^-$ and $\phi \to \mu^+\mu^-$ in In-In collisions at the CERN SPS," *Phys.Lett.*, vol. B699, pp. 325–329, 2011.

[16] PHENIX Collaboration, "Dihadron azimuthal correlations in Au+Au collisions at $\sqrt{s_{\mathrm{NN}}} = 200$ GeV," *Phys.Rev.*, vol. C78, p. 014901, 2008.

[17] PHENIX Collaboration, "Energy Loss and Flow of Heavy Quarks in Au+Au Collisions at $\sqrt{s_{\mathrm{NN}}} = 200$ GeV," *Phys.Rev.Lett.*, vol. 98, p. 172301, 2007.

[18] ALICE Collaboration, "ALICE: Technical Proposal for a Large Hadron Collider Experiment at the CERN LHC," CERN-LHCC 95-71, 1995.

[19] B. Mueller, J. Schukraft, and B. Wyslouch, "First Results from Pb+Pb collisions at the LHC," *Ann.Rev.Nucl.Part.Sci.*, vol. 62, pp. 361–386, 2012.

[20] ALICE Collaboration, "Charged-particle multiplicity density at midrapidity in central pb-pb collisions at $\sqrt{s_{NN}} = 2.76$ TeV," *Phys. Rev. Lett.*, vol. 105, p. 252301, Dec 2010.

[21] ALICE Collaboration, "Centrality dependence of the charged-particle multiplicity density at midrapidity in pb-pb collisions at $\sqrt{s_{\mathrm{NN}}} = 2.76$ TeV," *Phys. Rev. Lett.*, vol. 106, p. 032301, Jan 2011.

[22] ALICE Collaboration, "Two-pion Bose-Einstein correlations in central Pb-Pb collisions at $\sqrt{s_{\mathrm{NN}}} = 2.76$ TeV," *Phys.Lett.*, vol. B696, pp. 328–337, 2011.

[23] ALICE Collaboration, "Elliptic flow of charged particles in Pb-Pb collisions at $\sqrt{s_{\mathrm{NN}}} = 2.76$ TeV," *Phys.Rev.Lett.*, vol. 105, p. 252302, 2010.

[24] ALICE Collaboration, "Higher harmonic anisotropic flow measurements of charged particles in Pb-Pb collisions at $\sqrt{s_{\mathrm{NN}}} = 2.76$ TeV," *Phys.Rev.Lett.*, vol. 107, p. 032301, 2011.

[25] ALICE Collaboration, "Suppression of Charged Particle Production at Large Transverse Momentum in Central Pb–Pb Collisions at $\sqrt{s_{\mathrm{NN}}} = 2.76$ TeV," *Phys.Lett.*, vol. B696, pp. 30–39, 2011.

[26] ALICE Collaboration, "Suppression of high transverse momentum D mesons in central Pb-Pb collisions at $\sqrt{s_{\rm NN}} = 2.76$ TeV," *JHEP*, vol. 1209, p. 112, 2012.

[27] ALICE Collaboration, "Production of muons from heavy flavour decays at forward rapidity in pp and Pb-Pb collisions at $\sqrt{s_{\rm NN}} = 2.76$ TeV," *Phys.Rev.Lett.*, vol. 109, p. 112301, 2012.

[28] E598 Collaboration, "Experimental observation of a heavy particle J," *Phys.Rev.Lett.*, vol. 33, pp. 1404–1406, 1974.

[29] SLAC-SP-017 Collaboration, "Discovery of a narrow resonance in e^+ e^- annihilation," *Phys.Rev.Lett.*, vol. 33, pp. 1406–1408, 1974.

[30] H. Satz, "Colour deconfinement and quarkonium binding," *J.Phys.*, vol. G32, p. R25, 2006.

[31] N. Brambilla *et al.*, "Heavy quarkonium: progress, puzzles, and opportunities," *Eur.Phys.J.*, vol. C71, p. 1534, 2011.

[32] M. Kramer, "Quarkonium production at high-energy colliders," *Prog.Part.Nucl.Phys.*, vol. 47, pp. 141–201, 2001.

[33] R. Vogt, "J/ψ production and suppression," *Phys.Rept.*, vol. 310, pp. 197–260, 1999.

[34] G. A. Schuler, "Production of heavy quarks and heavy quarkonia," *Z.Phys.*, vol. C71, pp. 317–328, 1996.

[35] T. Matsui and H. Satz, "J/ψ suppression by Quark-Gluon Plasma formation," *Phys.Lett.*, vol. B178, p. 416, 1986.

[36] S. Digal, P. Petreczky, and H. Satz, "Quarkonium feed down and sequential suppression," *Phys.Rev.*, vol. D64, p. 094015, 2001.

[37] F. Karsch, D. Kharzeev, and H. Satz, "Sequential charmonium dissociation," *Phys.Lett.*, vol. B637, pp. 75–80, 2006.

[38] K. Eskola, V. Kolhinen, and P. Ruuskanen, "Scale evolution of nuclear parton distributions," *Nucl.Phys.*, vol. B535, pp. 351–371, 1998.

[39] N. Armesto, "Nuclear shadowing," *J.Phys.*, vol. G32, pp. R367–R394, 2006.

[40] J. Albacete, "Shadowing, saturation, CGC and other initial state effects on heavy quark production." 1st Sapore Gravis Meeting, November 2012.

[41] J.-P. Blaizot and J.-Y. Ollitrault, "J/ψ suppression in Pb Pb collisions: A hint of quark - gluon plasma production?," *Phys.Rev.Lett.*, vol. 77, pp. 1703–1706, 1996.

[42] A. Capella and E. Ferreiro, "J/ψ suppression and the decrease of nuclear absorption with increasing energy," *Phys.Rev.*, vol. C76, p. 064906, 2007.

[43] P. Braun-Munzinger and J. Stachel, "(Non)thermal aspects of charmonium production and a new look at J/ψ suppression," *Phys.Lett.*, vol. B490, pp. 196–202, 2000.

[44] A. Andronic *et al.*, "Heavy quark(onium) at LHC: the statistical hadronization case," *J.Phys.*, vol. G37, p. 094014, 2010.

[45] A. Andronic *et al.*, "Evidence for charmonium generation at the phase boundary in ultra-relativistic nuclear collisions," *Phys.Lett.*, vol. B652, pp. 259–261, 2007.

[46] X. Zhao and R. Rapp, "Medium Modifications and Production of Charmonia at LHC," *Nucl.Phys.*, vol. A859, pp. 114–125, 2011.

[47] Y.-p. Liu *et al.*, "J/ψ Transverse Momentum Distribution in High Energy Nuclear Collisions at RHIC," *Phys.Lett.*, vol. B678, pp. 72–76, 2009.

[48] E. Ferreiro, "Charmonium dissociation and recombination at LHC: Revisiting comovers," 2012, arXiv:1210.3209.

[49] NA38 Collaboration, "Study of J/ψ production in p U, O U and S U interactions at 200-GeV per nucleon.," *Phys.Lett.*, vol. B255, pp. 459–465, 1991.

[50] NA50 Collaboration, "Evidence for deconfinement of quarks and gluons from the J/ψ suppression pattern measured in Pb + Pb collisions at the CERN SPS," *Phys.Lett.*, vol. B477, pp. 28–36, 2000.

[51] NA50 Collaboration, "A New measurement of J/ψ suppression in Pb-Pb collisions at 158-GeV per nucleon," *Eur.Phys.J.*, vol. C39, pp. 335–345, 2005.

[52] NA60 Collaboration, "J/ψ Production in Indium-Indium Collisions at 158 GeV/Nucleon," *Phys. Rev. Lett.*, vol. 99, p. 132302, Sep 2007.

[53] PHENIX, "J/ψ Production vs Centrality, Transverse Momentum, and Rapidity in Au+Au Collisions at $\sqrt{s_{NN}}$ = 200-GeV," *Phys.Rev.Lett.*, vol. 98, p. 232301, 2007.

[54] NA60 Collaboration, "Highlights from the NA60 experiment," 2007, arXiv:0705.3339.

[55] ALICE Collaboration, "Rapidity and transverse momentum dependence of inclusive J/ψ production in pp collisions at $\sqrt{s} = 7$ TeV," *Phys.Lett.*, vol. B704, pp. 442–455, 2011.

[56] ALICE Collaboration, "Inclusive J/ψ production in pp collisions at $\sqrt{s}$ = 2.76 TeV," *Phys.Lett.*, vol. B718, pp. 295–306, 2012.

[57] ALICE Collaboration, "J/ψ polarization in pp collisions at $\sqrt{s} = 7$ TeV," *Phys.Rev.Lett.*, vol. 108, p. 082001, 2012.

[58] M. Butenschoen and B. A. Kniehl, "J/ψ polarization at Tevatron and LHC: Nonrelativistic-QCD factorization at the crossroads," *Phys.Rev.Lett.*, vol. 108, p. 172002, 2012.

[59] ALICE Collaboration, "J/ψ production as a function of charged particle multiplicity in pp collisions at $\sqrt{s} = 7$ TeV," *Phys.Lett.*, vol. B712, pp. 165–175, 2012.

[60] ALICE Collaboration, "Measurement of prompt J/ψ and beauty hadron production cross sections at mid-rapidity in pp collisions at $\sqrt{s} = 7$ TeV," *JHEP*, vol. 1211, p. 065, 2012.

[61] ALICE Collaboration, "J/ψ suppression at forward rapidity in Pb-Pb collisions at $\sqrt{s_{NN}} = 2.76$ TeV," *Phys.Rev.Lett.*, vol. 109, p. 072301, 2012.

[62] ALICE Collaboration, "Coherent J/ψ photoproduction in ultra-peripheral Pb-Pb collisions at $\sqrt{s_{NN}} = 2.76$ TeV," *Phys.Lett.*, vol. B718, pp. 1273–1283, 2013.

[63] M. Bajko *et al.*, "Interim summary report of the analysis of the 19 September 2008 incident at the LHC," CERN-LHC-PROJECT-Report-1168, 2008.

[64] ALICE Collaboration, "First proton-proton collisions at the LHC as observed with the ALICE detector: Measurement of the charged particle pseudorapidity density at $\sqrt{s} = 900$ GeV," *Eur. Phys. J. C*, vol. 65, pp. 111–125, 2010.

[65] P. Bryant and L. Evans, "LHC Machine," *JINST 3 S08001*, 2008.

[66] F. Zimmermann, "LHC: the machine." SLAC Summer Institute, July 2012.

[67] ATLAS Collaboration, "The ATLAS Experiment at the CERN Large Hadron Collider," *JINST 3 S08003*, 2008.

[68] CMS Collaboration, "The CMS experiment at the CERN LHC," *JINST 3 S08004*, 2008.

[69] LHCb Collaboration, "The LHCb Detector at the LHC," *JINST 3 S08005*, 2008.

[70] LHCf Collaboration, "The LHCf detector at the CERN Large Hadron Collider," *JINST 3 S08006*, 2008.

[71] TOTEM Collaboration, "The TOTEM Experiment at the CERN Large Hadron Collider," *JINST 3 S08007*, 2008.

[72] K. Schindl, "The injector chain for the LHC," CERN-PS-99-018-DI, 1999.

[73] A. Beuret, "The LHC lead injector chain," in *Proceedings of EPAC 2004*, (Lucerne, Switzerland), 2004.

[74] K. Kahle and L. Rossi, "Designs on higher luminosity." CERN courier, February 2012.

[75] ALICE Collaboration, "ALICE: Physics Performance Report, Volume 1," *J. Phys. G: Nucl. Part. Phys. 30 1517*, vol. 19, September 2004.

[76] ALICE Collaboration, "ALICE: Physics Performance Report, Volume 2," *J. Phys. G: Nucl. Part. Phys. 32 1295*, vol. 32, November 2006.

[77] ALICE Collaboration, "The ALICE experiment at the CERN LHC," *JINST 3 S08002*, 2008.

[78] ALICE Collaboration, "ALICE Technical Design Report of the Inner Tracking System," CERN-LHCC-1999-012, 1999.

[79] ALICE Collaboration, "ALICE Technical Design Report of the Time Projection Chamber," CERN-LHCC-2000-001, 2000.

[80] ALICE Collaboration, "ALICE Technical Design Report of the Transision Radiaton Detector," CERN-LHCC-2001-021, 2001.

[81] ALICE Collaboration, "ALICE Technical Design Report of the Time of Flight system," CERN-LHCC-2000-012, 2000.

[82] ALICE Collaboration, "Addendum to the ALICE Technical Design Report of the Time of Flight system," CERN-LHCC-2002-016, 2002.

[83] ALICE Collaboration, "ALICE Technical Design Report of the High Momentum Particle Identification Detector," CERN-LHCC-1998-19, 1998.

[84] ALICE Collaboration, "ALICE Technical Design Report of the Photon Spectrometer," CERN-LHCC-1999-4, 1999.

[85] ALICE Collaboration, "ALICE Technical Design Report of the Electromagnetic Calorimeter," CERN-LHCC-2008-014, 2008.

[86] ALICE Collaboration, "ALICE Technical Design Report of the Zero Degree Calorimeter," CERN-LHCC-1999-5, 1999.

[87] ALICE Collaboration, “ALICE Technical Design Report of the Photon Multiplicity Detector,” CERN-LHCC-1999-032, 1999.

[88] ALICE Collaboration, “ALICE Technical Design Report on Forward Detectors: FMD, T0 and V0,” CERN-LHCC-2004-025, 2004.

[89] ALICE Collaboration, “ALICE Technical Design Report of the Trigger, Data Acquisition, High Level Trigger and Control System,” CERN-LHCC-2003-062, 2003.

[90] ALICE Collaboration, “Upgrade of the ALICE experiment Letter Of Intent,” CERN-LHCC-2012-012, 2012.

[91] ALICE Collaboration, “Upgrade of the Inner Tracking System Conceptual Design Report,” CERN-LHCC-2012-013, 2012.

[92] ALICE Collaboration, “A Very High Momentum Particle Identification Detector for ALICE Letter of Intent,” tech. rep., 2013.

[93] ALICE Collaboration, “A Forward Calorimeter (FoCal) for the ALICE experiment Letter of Intent,” tech. rep., 2013.

[94] ALICE Collaboration, “ALICE Technical Design Report of the Dimuon Forward Spectrometer,” CERN-LHCC-1999-022, 1999.

[95] ALICE Collaboration, “Addendum to the ALICE Technical Design Report of the Dimuon Forward Spectrometer,” CERN-LHCC-2000-046, 2000.

[96] CDF Collaboration, “Measurement of the J/ψ meson and b-hadron production cross sections in $p\overline{p}$ collisions at $\sqrt{s} = 1960$ GeV,” *Phys. Rev. D*, vol. 71, p. 032001, Feb 2005.

[97] N. Bastid *et al.*, “Test experiment for the Beam Shielding in ALICE,” ALICE-INT-1996-14, 1996.

[98] ALICE Collaboration, “The electronics of the ALICE dimuon tracking chambers,” ALICE-INT-2004-026, 2004.

[99] P. Dupieux *et al.*, “ALICE Muon Trigger Performance,” ALICE-INT-2006-002, 2006.

[100] R. Arnaldi *et al.*, “Study of the resistive plate chambers for the ALICE Dimuon Arm,” *Nucl. Instrum. Methods Phys. Res. A*, vol. 456, pp. 73–76, 2000.

[101] R. Arnaldi *et al.*, “A dual threshold technique to improve the time resolution of resistive plate chambers in streamer mode,” *Nucl. Instrum. Methods Phys. Res. A*, vol. 457, pp. 117–125, 2001.

[102] G. Chabratova and A. Zinchenko, "A new approach to cluster finding and hit reconstruction in cathode pad chambers and its development for the forward muon spectrometer of ALICE," *Nucl. Instrum. Methods Phys. Res. A*, vol. 502, pp. 778–780, 2003.

[103] L. Aphecetche *et al.*, "Numerical simulations and offline reconstruction of the muon spectrometer of ALICE," ALICE-INT-2009-044, 2009.

[104] G. Chabratova *et al.*, "Development of the Kalman filter for the tracking in the forward muon spectrometer of ALICE," ALICE-INT-2003-002, 2003.

[105] G. Chabratova *et al.*, "Further development of the Kalman filter for the muon spectrometer of ALICE and its comparison with the default method," ALICE-INT-2003-053, 2003.

[106] ALICE Collaboration, "A Muon Forward Tracker for the ALICE experiment Letter of Intent," tech. rep., 2013.

[107] N. L. Bris, *Étude des décroissances semi-muoniques de saveurs lourdes à bas* p_{T}*, et de l'efficacité de trajectographie du spectromètre à muons d'ALICE.* PhD thesis, 2009.

[108] M. Lenhardt, *Étude du taux de production des J/ψ et muons simples en collisions proton-proton à l'aide du spectromètre à muons de l'expérience ALICE au LHC.* PhD thesis, 2011.

[109] L. Massacrier, *La physique de (di)muons dans ALICE au LHC: analyse en collisions pp* ($\sqrt{s}$ *= 7 TeV) and Pb-Pb* ($\sqrt{s_{\mathrm{NN}}}$ *= 2.76 TeV) des résonances de basse masses (ρ, ω, ϕ) et étude d'un trajectographe en pixels de Silicium dans l'ouverture du spectromètre.* PhD thesis, 2011.

[110] L. Lyons, *Statistics for nuclear and particle physicists.* Cambridge University Press, 1989.

[111] ALICE Collaboration, "Centrality determination of Pb-Pb collisions at $\sqrt{s_{\mathrm{NN}}}$ = 2.76 TeV with ALICE," 2013, arXiv:1301.4361.

[112] ALICE Collaboration, "Centrality dependence of the pseudorapidity density distribution for charged particles in Pb-Pb collisions at $\sqrt{s_{\mathrm{NN}}}$ = 2.76 TeV," 2013, arXiv:1304.0347.

[113] LHCb Collaboration, "Measurement of J/ψ production in pp collisions at $\sqrt{s}$=7 TeV," *Eur.Phys.J.*, vol. C71, p. 1645, 2011.

[114] PHENIX Collaboration, "J/ψ suppression at forward rapidity in Au+Au collisions at $\sqrt{s_{\mathrm{NN}}}$ = 200 GeV," *Phys.Rev.*, vol. C84, p. 054912, 2011.

[115] CMS Collaboration, "Suppression of non-prompt J/ψ, prompt J/ψ and Y(1S) in PbPb collisions at $\sqrt{s_{NN}} = 2.76$ TeV," *JHEP*, vol. 1205, p. 063, 2012.

[116] A. Rakotozafindrabe *et al.*, "Cold Nuclear Matter Effects on extrinsic J/ψ production at $\sqrt{s_{\mathrm{NN}}} = 2.76$ TeV at the LHC," *Nucl.Phys.*, vol. A855, pp. 327–330, 2011.

[117] R. Vogt, "Cold Nuclear Matter Effects on J/ψ and Υ Production at the LHC," *Phys.Rev.*, vol. C81, p. 044903, 2010.

[118] PHENIX Collaboration, "J/ψ production versus transverse momentum and rapidity in p+p collisions at $\sqrt{s} = 200$ GeV," *Phys.Rev.Lett.*, vol. 98, p. 232002, 2007.

[119] PHENIX Collaboration, "J/ψ production in $\sqrt{s_{\mathrm{NN}}} = 200 =$ GeV Cu+Cu collisions," *Phys.Rev.Lett.*, vol. 101, p. 122301, 2008.

[120] M. L. Miller, K. Reygers, S. J. Sanders, and P. Steinberg, "Glauber modeling in high energy nuclear collisions," *Ann.Rev.Nucl.Part.Sci.*, vol. 57, pp. 205–243, 2007.

[121] LHCb Collaboration, "Measurement of J/ψ production in *pp* collisions at $\sqrt{s} = 2.76$ TeV," *JHEP*, vol. 1302, p. 041, 2013.

Appendix A

Centrality determination

The Glauber Model of multiple collision processes provides a quantitative consideration of the geometrical configuration of the nuclei when they collide. It is based on the concept of a mean-free path with the assumption of an elementary nucleon-nucleon cross section.

In all calculations of geometric parameters using a Glauber approach, some experimental data must given as model inputs [120]. The two most importants are:

- The nuclear charge density that is usually parametrized by a Woods-Saxon or a Fermi distribution:

  $$\rho(r) = \rho_0 \, \frac{1 + w(r/R)^2}{1 + \exp(\frac{r-R}{a})} \, ,$$

  where ρ_0 is the nucleon density, w characterizes deviations from spherical shapes, $R = 6.62 \pm 0.06$ fm is the radius of the ^{208}Pb nucleus and $a = 0.546 \pm 0.01$ fm the skin thickness of the nucleus, which indicates how quickly the nuclear density falls off near the edge of the nucleus.

- The inelastic nucleon-nucleon cross section ($\sigma^{NN}_{\text{inel}}$) as it can not be calculated using pQCD. For nuclear collisions at $\sqrt{s_{\text{NN}}} = 2.76$ TeV $\sigma^{NN}_{\text{inel}} = 64 \pm 5$ mb, estimated by interpolation of pp data at different center of mass energies, subtracting the elastic scattering cross section from the total one.

Figure A.1 represents two heavy-ions colliding at relativistic speeds with impact parameter b. During the collision two flux tubes, located at a distance s with respect to the center of the target nucleus A and a distance $s - b$ from the center of the projectile B, overlap. The probability per unit transverse area of a given nucleon beign located in the target flux tube is:

$$\hat{T}_A(s) = \int \hat{\rho}_A(s, z_A) \, dz_A,$$

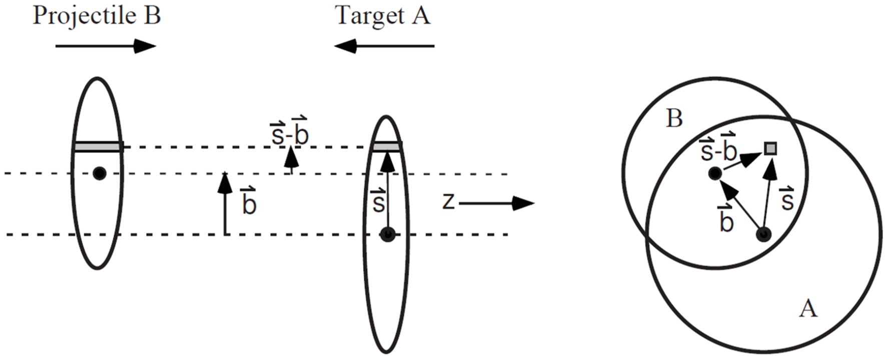

Figure A.1: Schematic representation of the Glauber Model geometry, with longitudinal (*left*) and transverse (*right*) views.

with $\hat{\rho}_A(s, z_A)$ the probability per unit volume to find a nucleon at location (s, z_A). A similar expression can be written for the projectile nucleon. The product $\hat{T}_A(s)\hat{T}_B(s-b)d^2s$ provides the joint probability per unit area of the nucleons being located in the respective overlapping target and projectile flux tubes of differential area d^2s. With this it is possible to obtain the Nuclear Thickness Function:

$$\hat{T}_{AB}(b) = \int \hat{T}_A(s)\hat{T}_B(s-b)d^2s \tag{A.1}$$

that can be interpreted as the effective overlap area for which a specific nucleon in A can interact with a given nucleon in B[1].

The probability of an interaction occurring is then $\hat{T}_{AB}(b)\sigma_{\text{inel}}^{\text{NN}}$, so the total number of nucleon-nucleon collisions is:

$$N_{\text{coll}}(b) = AB\hat{T}_{AB}(b)\sigma_{\text{inel}}^{\text{NN}}$$

and the total number of participants/wounded nucleons is given by:

$$\begin{aligned} N_{\text{part}}(b) &= A\int \hat{T}_A(s)\left\{1-\left[1-\hat{T}_B(s-b)\sigma_{\text{inel}}^{\text{NN}}\right]^B\right\}d^2s \\ &\quad + B\int \hat{T}_B(s-b)\left\{1-\left[1-\hat{T}_A(s)\sigma_{\text{inel}}^{\text{NN}}\right]^A\right\}d^2s. \end{aligned}$$

In ALICE the centrality of an event is classified in percentiles of the hadronic cross section using the charged particle multiplicity [111]. It is then necessary to know the particle multiplicity at which the purity of the event

---

[1] For this reason $\hat{T}_{AB}$ in equation A.1 is also called Nuclear Overlap Function.

sample and the efficiency of the event selection becomes 100%. The Anchor Point (AP) is defined as the amplitude of the VZERO detector equivalent to 90% of the hadronic cross section, which determines the absolute scale of the centrality (figure A.2).

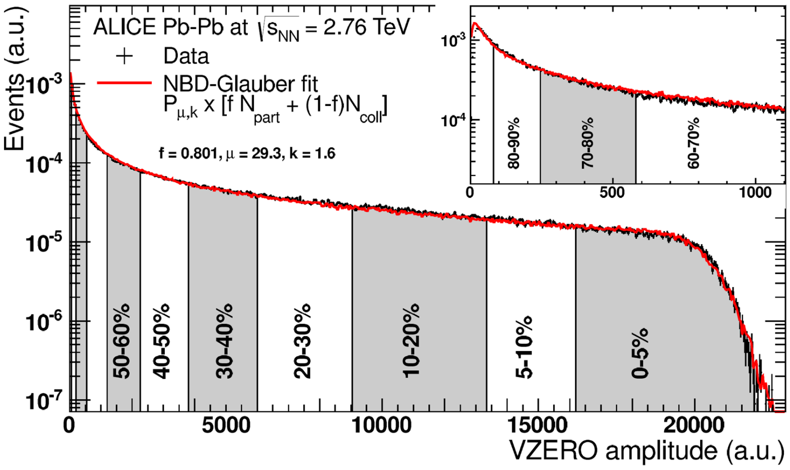

Figure A.2: Amplitude of the V0 detector, the red line is a Glauber Monte Carlo fit.

The measured event sample can be divided in centrality classes that correspond to well defined percentiles of the hadronic cross section using two methods. The first one uses the charged particle multiplicity measured by different detectors with different rapidity coverages as the VZERO, SPD and TPC. The second approach uses the ZDC, which measures the nucleon spectators. Table A.1 presents the results on the relevant geometrical quantities for different centrality bins.

Table A.1: N_{coll}, N_{part} and T_{AA} for different centralities of Pb-Pb collisions.

Centrality	N_{coll}	N_{part}	T_{AA} (mb^{-1})
0%–10%	1500±165	356±4	23.7±0.8
10%–20%	921±96	260±4	14.5±0.45
20%–30%	557±54	186±3	8.70±0.27
30%–40%	320±30	128±3	5.00±0.18
40%–50%	171±16	84.7±2.4	2.65±0.12
50%–60%	84.3±7.0	52.4±1.6	1.35±0.07
60%–70%	37.8±2.8	29.8±0.9	0.59±0.036
70%–80%	15.6±1.0	15.3±0.5	0.24±0.016
80%–90%	6.23±0.32	7.48±0.22	0.098±0.008
0%–90%	401±41	124±2	6.31±0.21

Appendix B

Fitting functions

The Crystal Ball (CB) function consists of a Gaussian core portion and a power-law tail at low mass defined by the parameters α and n:

$$\begin{aligned} f(x;\bar{x},\sigma,\alpha,n,) &= N\cdot\begin{cases}\exp(-\frac{(x-\bar{x})2}{2\sigma 2}), & \text{for } \frac{x-\bar{x}}{\sigma} > -\alpha \\ A\cdot(B-\frac{x-\bar{x}}{\sigma})^{-n}, & \text{for } \frac{x-\bar{x}}{\sigma} \leqslant -\alpha\end{cases} \\ A &= \left(\frac{n}{|\alpha|}\right)^{n}\cdot\exp\left(-\frac{|\alpha|^{2}}{2}\right) \\ B &= \frac{n}{|\alpha|}-|\alpha| \end{aligned} \tag{B.1}$$

where the power-law part reproduces non Gaussian fluctuations due to energy loss processes. On the left side of figure B.1, the shape of the CB for various set of parameters of the power-law tail is visible.

However, the signal shape obtained from J/ψ simulations can not be fully reproduced with the CB function described above. This is shown on the right side of figure B.1, where the signal is given by a Monte Carlo J/ψ embedded into real Pb-Pb events, after a full reconstruction. The combinatorial background has been removed by selecting only the muons for which the MC label correspond to simulated/embedded J/ψ. In the high mass tail of the distribution, a deviation from a simple Gaussian behaviour can be observed. This is attributed to multiple scattering and residual misalignment effects.

For this reason the original CB function has been modified to include a second power-law tail in the high mass region. This new function is called Extended Crystal Ball (CB2):

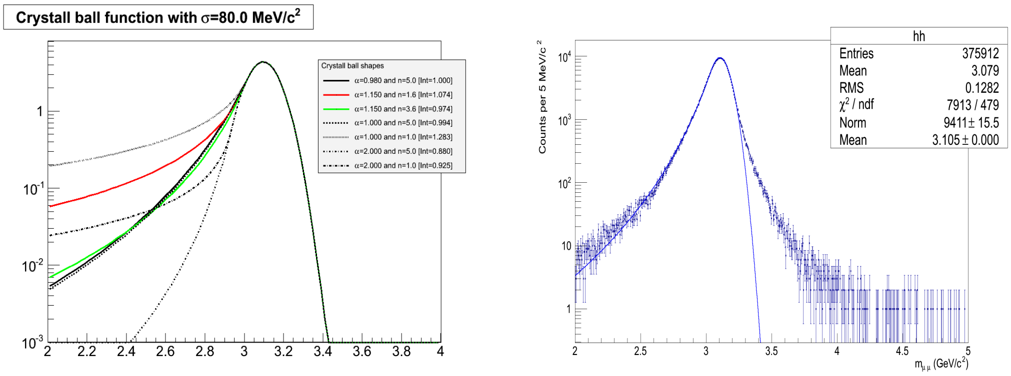

Figure B.1: *Left*: Crystal Ball shape for different power-law parameters. *Right*: CB fit on a J/ψ sample from embedding simulation in Pb-Pb collisions.

$$f(x;\bar{x},\sigma,\alpha,n,\alpha',n') = N\cdot\begin{cases}\exp(-\frac{(x-\bar{x})^2}{2\sigma^2}), & \text{for } \alpha' > \frac{x-\bar{x}}{\sigma} > -\alpha\\ A\cdot(B-\frac{x-\bar{x}}{\sigma})^{-n}, & \text{for } \frac{x-\bar{x}}{\sigma} \leqslant -\alpha\\ C\cdot(D+\frac{x-\bar{x}}{\sigma})^{-n'}, & \text{for } \frac{x-\bar{x}}{\sigma} \geqslant \alpha'\end{cases} \tag{B.2}$$

$$A = \left(\frac{n}{|\alpha|}\right)^n\cdot\exp\left(-\frac{|\alpha|^2}{2}\right)$$

$$B = \frac{n}{|\alpha|} - |\alpha|$$

$$C = \left(\frac{n'}{|\alpha'|}\right)^{n'}\cdot\exp\left(-\frac{|\alpha'|^2}{2}\right)$$

$$D = \frac{n'}{|\alpha'|} - |\alpha'|$$

The result of the CB2 fit to the J/ψ invariant mass distribution from embedding simulation is shown on the left side of figure B.2. On the right panel of the same figure it is possible to observe 3 line shapes used in the analysis, extracted from J/ψ embedded in Pb-Pb events, pure J/ψ simulations with the Pb-Pb database conditions and 7 TeV pp collisions.

For the background description a Gaussian with a width (σ) which varies as a function of the mass values has been adopted:

$$f(x) = N\cdot\exp(-(x-\alpha)^2/(2\ \sigma^2)), \tag{B.3}$$

$$\sigma = \beta + \gamma * ((x-\alpha)/\alpha).$$

This function is called Variable Width Gaussian (VWG). The shape describing the background corresponding to the 0-90% centrality integrated spectrum is plotted in figure B.3. The free parameters are tuned directly on the data in each centrality, p_T or y bin.

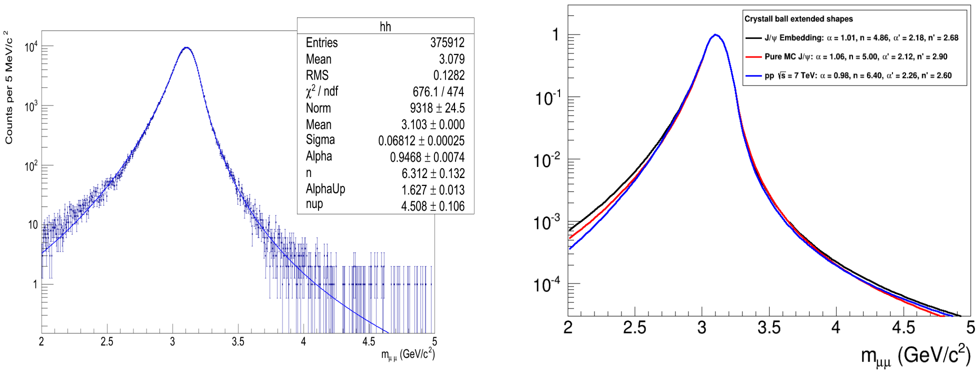

Figure B.2: *Left*: CB2 fit on a J/ψ sample from embedding simulation in Pb-Pb collisions. *Right*: CB2 shape with 3 line shapes used in the analysis.

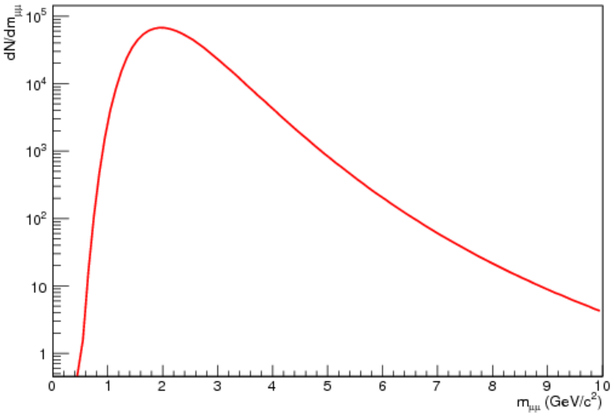

Figure B.3: Example of the Variable Width Gaussian function that describes the background in the centrality integrated invariant mass spectrum.

Appendix C

Effect of non-prompt J/ψ on the inclusive $R_{\rm AA}$

Although prompt J/ψ $R_{\rm AA}$ cannot be directly measured with the muon spectrometer, it can be evaluated once the inclusive J/ψ $R_{\rm AA}$ has been determined together with:

1. The fraction of J/ψ coming from B-hadron decays in pp collisions at $\sqrt{s}$ = 2.76 TeV, in the kinematic coverage of the muon spectrometer.
2. The suppression of B-hadron production in Pb-Pb collisions due to initial and final state nuclear effects.

As a function of $p_{\rm T}$, $R_{\rm AA}^{\rm pro}(p_{\rm T})$ can be obtained starting from $R_{\rm AA}^{\rm inc}(p_{\rm T})$:

$$\begin{aligned}
\frac{Y_{\rm AA}^{\rm inc}}{T_{\rm AA}\sigma_{\rm pp}^{\rm inc}} &= R_{\rm AA}^{\rm inc} \\
Y_{\rm AA}^{\rm pro} + Y_{\rm AA}^{\rm npro} &= R_{\rm AA}^{\rm inc} T_{\rm AA}(\sigma_{\rm pp}^{\rm pro} + \sigma_{\rm pp}^{\rm npro}) \\
Y_{\rm AA}^{\rm pro} &= R_{\rm AA}^{\rm inc} T_{\rm AA}\sigma_{\rm pp}^{\rm pro} + R_{\rm AA}^{\rm inc} T_{\rm AA}\sigma_{\rm pp}^{\rm npro} - Y_{\rm AA}^{\rm npro} \\
\frac{Y_{\rm AA}^{\rm pro}}{T_{\rm AA}\sigma_{\rm pp}^{\rm pro}} &= \frac{1}{T_{\rm AA}\sigma_{\rm pp}^{\rm pro}}(R_{\rm AA}^{\rm inc} T_{\rm AA}\sigma_{\rm pp}^{\rm pro} + R_{\rm AA}^{\rm inc} T_{\rm AA}\sigma_{\rm pp}^{\rm npro} - Y_{\rm AA}^{\rm npro}) \\
R_{\rm AA}^{\rm pro} &= R_{\rm AA}^{\rm inc} + \frac{R_{\rm AA}^{\rm inc} T_{\rm AA}\sigma_{\rm pp}^{\rm npro}}{T_{\rm AA}\sigma_{\rm pp}^{\rm pro}} - \frac{Y_{\rm AA}^{\rm npro}}{T_{\rm AA}\sigma_{\rm pp}^{\rm pro}} \\
R_{\rm AA}^{\rm pro} &= R_{\rm AA}^{\rm inc} + R_{\rm AA}^{\rm inc} f_B - \frac{Y_{\rm AA}^{\rm npro}\sigma_{\rm pp}^{\rm npro}}{T_{\rm AA}\sigma_{\rm pp}^{\rm pro}\sigma_{\rm pp}^{\rm npro}} \\
R_{\rm AA}^{\rm pro} &= R_{\rm AA}^{\rm inc} + R_{\rm AA}^{\rm inc} f_B - R_{\rm AA}^{\rm npro} f_B, \qquad \text{(C.1)}
\end{aligned}$$

where f_B is the fraction of non-prompt to prompt J/ψ measured in pp collisions and $R_{\rm AA}^{\rm npro}$ is the suppression factor of B-hadron production in Pb-Pb collisions. The upper indexes *inc*, *pro* and *npro* refer to the inclusive, prompt and non-prompt production of J/ψ, respectively.

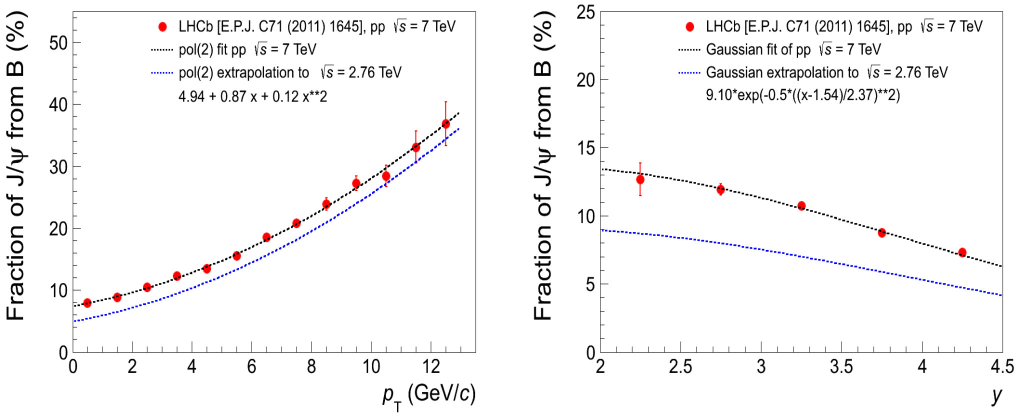

Figure C.1: Fraction of non-prompt to prompt J/ψ measured as a function of p_T (*left*) and rapidity (*right*).

The differential cross sections of non-prompt and prompt J/ψ as a function of p_T and y have been measured in pp collisions at $\sqrt{s}$= 7 TeV in a kinematic range overlapping with the muon spectrometer [113]. It is then possible to extract f_B very precisely from these data as shown on figure C.1, where a fit of the p_T and y dependence of this ratio is also given.

The integrated measurement for unpolarized J/ψ is f_B ($\sqrt{s}$ = 7 TeV, p_T < 14 GeV/c , 2.0 < y < 4.5) = 10.84 ± 0.04 ± 1.41 %. More recently, another measurement at $\sqrt{s}$ = 2.76 TeV, established f_B ($\sqrt{s}$ = 2.76 TeV, p_T < 12 GeV/c, 2.0 < y < 4.5) = 7.1 ± 0.6 ± 0.7 % [121].

These results indicate a reduction factor in the f_B of 1.53 going from $\sqrt{s}$ = 7 TeV to $\sqrt{s}$ = 2.76 TeV. Figure C.1 shows the extrapolation of f_B down to $\sqrt{s}$ = 2.76 TeV (blue dashed lines) assuming that:

1. This $\sqrt{s}$ scaling factor is independent of p_T and y for the kinematic range considered.
2. The p_T dependence of f_B can be parametrized with a second degree polynomial function.
3. The y dependence of f_B can be parametrized with a Gaussian function.

For R_{AA}^{npro}, two inputs are considered:

1. For non-prompt J/ψ with $\langle p_T \rangle \approx 9$ GeV/c and $y < 2.4$, $R_{AA} = 0.37 \pm 0.08 \pm 0.02$ [115]. Preliminary results with 2011 data analysis show that non-prompt J/ψ $R_{AA} \approx 0.3$ (0.5) for a J/ψ p_T = 17 (7) GeV/c.
2. Radiative energy loss predictions suggest that $R_{AA}^{B} > R_{AA}^{D}$. ALICE measurements at mid rapidity show that D mesons can be suppressed down to $R_{AA} \approx 0.2$ in the most central Pb-Pb collisions.

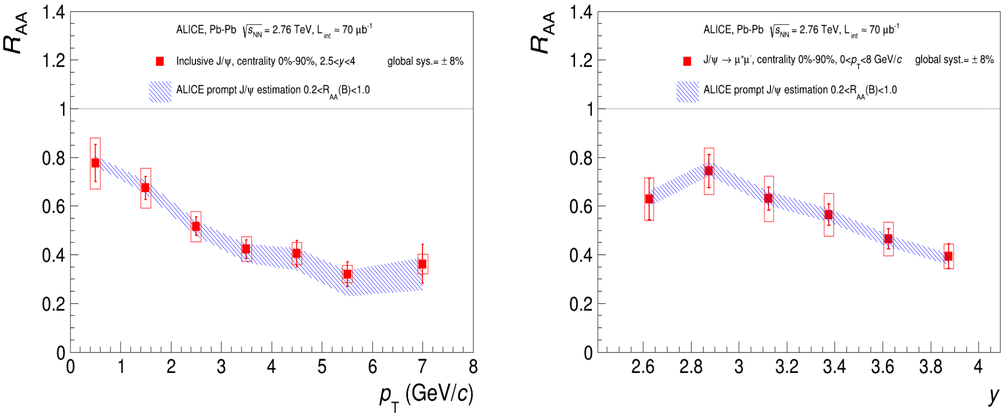

Figure C.2: Inclusive J/ψ R_{AA} measured as a function of p_{T} (*left*) and rapidity (*right*). The blue band is an estimation of the prompt J/ψ R_{AA} taking into account the non-prompt J/ψ and beauty hadrons R_{AA} ranging between 0.2 (higher limit) and 1.0 (lower limit).

Thus it has been decided to vary $R_{\mathrm{AA}}^{\mathrm{npro}}$ from 0.2 to 1.0 and keep the chosen value constant for the whole p_{T} range. The result is given on figure C.2 which displays, on top of the current measurement of the inclusive J/ψ R_{AA}, a blue band representing the expected prompt J/ψ R_{AA} . The high (low) limit of the blue band corresponds to the low (high) value of the factor $R_{\mathrm{AA}}^{\mathrm{npro}}$, i.e. B-hadrons are strongly (weakly) suppressed in heavy ion collisions.

As a function of centrality, assuming no quenching of B-hadrons ($R_{\mathrm{AA}}^{\mathrm{npro}} = 1$), the prompt J/$\psi$ R_{AA} could be 6% lower than the inclusive J/ψ R_{AA} for the 0%–10% most central collisions. This difference vanishes when going towards more peripheral collisions. However, if the B-hadrons quenching is large ($R_{\mathrm{AA}}^{\mathrm{npro}} = 0.2$), the inclusive J/$\psi$ R_{AA} would be 4% to 6% higher depending on the centrality.

In conclusion, non-prompt J/ψ from B-hadrons decay do not introduce a strong bias in the inclusive J/ψ R_{AA} presented in this thesis and the estimated prompt J/ψ R_{AA} fall inside the current statistical/systematic uncertainties for most of the p_{T} and y ranges covered. Only for p_{T} larger than 3 GeV/c B-hadrons decay would have a significant effect on the measured inclusive J/ψ R_{AA}.

Appendix D

Effect of photoproduced J/ψ on the inclusive R_{AA}

J/ψ from coherent photoproduction is an additional source of J/ψ in the very low-p_{T} region ($p_{\mathrm{T}} < 300$ MeV/c). This contribution is expected to be negligible in central collisions in which hadronic production is largely dominant. This is not the case for peripheral collisions, where the photoproduction of J/ψ may give rise to a non-negligible source of J/ψ which must be taken into account. This can be seen in the plots from figure D.1, where and excess of low-p_{T} dimuon pairs with mass $\pm 3\sigma$ around the J/ψ pole are present.

In order to quantify this effect, the J/ψ R_{AA} has been evaluated by removing dimuon pairs with transverse momentum below 300 MeV/c and computing specific $A \times \epsilon$ corrections with the embedding technique, while the same pp reference was used. The latter is equivalent to say that the J/ψ photoproduction was considered to be negligible in pp collisions at $\sqrt{s} = 2.76$ TeV.

For $0 < p_{\mathrm{T}} < 1$ GeV/c, removing the photoproduced J/ψ leads to a 4.2% decrease of the R_{AA}. Table D.1 indicates the effect on the R_{AA} vs N_{part} if only J/ψ with $p_{\mathrm{T}} > 300$ MeV/c are considered. For the 0-60% most central events a purely hadronic inclusive R_{AA} would remain inside the uncertainties, while for the most peripheral bins a significant decrease is expected. For the R_{AA} as a function of y (table D.2) the effect on the Nuclear Modification Factor seems to be rather small.

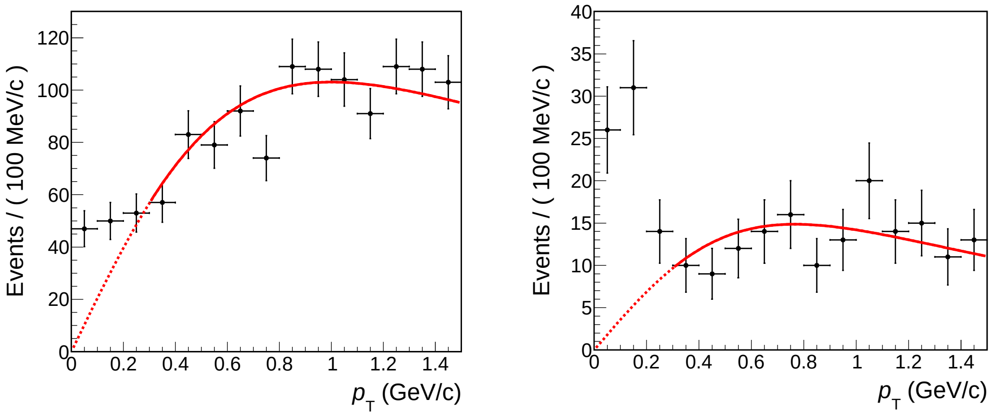

Figure D.1: Low-p_{T} J/ψ excess in the 50-70% (*left*) and 70-90% (*right*) centrality. The red line indicates the trend expected from purely hadronic production.

Table D.1: Effect on the R_{AA} vs centrality once photoproduced J/ψ are removed.

$0.3 < p_{\mathrm{T}} < 8$ GeV/c, $2.5 < y < 4$	
Cent.	R_{AA} shift (%)
0-90%	-1.0%
0-10%	-1.0%
10-20%	-1.1%
20-30%	+0.1%
30-40%	-1.7%
40-50%	-1.7%
50-60%	-1.5%
60-70%	-3.0%
70-80%	-7.8%
80-90%	-17.7%

Table D.2: Effect on the R_{AA} vs rapidity once photoproduced J/ψ are removed.

$0.3 < p_{\mathrm{T}} < 8$ GeV/c, 0-90% cent.	
y	R_{AA} shift (%)
$[2.5, 2.75]$	-0.3%
$[2.75, 3.0]$	-1.0%
$[3.0, 3.25]$	-1.2%
$[3.25, 3.5]$	-0.8%
$[3.5, 3.75]$	-0.6%
$[3.75, 4.0]$	-1.0%